The University Of Sheffield.

The Development of an Ultrasonic Standing Wave Method to Measure Liquid Viscosity

Olivia F. Manfredi

May 2019

Thesis submitted for the degree of doctor of philosophy

The Department of Mechanical Engineering

The University of Sheffield

Supervisors: Professor Rob Dwyer-Joyce and Professor Matthew Marshall

Acknowledgements

I would first and foremost like to thank Professor Rob Dwyer-Joyce for his continued enthusiasm and encouragement, and for always having faith in me right from the very beginning! This support has enabled me to persevere and gain new skills and experiences which I otherwise would not have attained. Thank you to Professor Matthew Marshall for also providing guidance and positivity throughout. I am so grateful to have been given the opportunities and experiences that I have had while working with you both.

I must also thank Dr Mathias Stark and Mr Simon Digglemann at WinG&D for their exceptional ability to adapt and go above and beyond to help with ultrasonic instrumentation, your expertise have been vital to the work in this PhD. Thanks must also go to Mr Dave Butcher for the technical support and last minute machining which inevitably led to the success of this project.

I would also like to thank Mrs Kimberley Hyde for being the most supportive iT-CDT Center Manager a PhD student could wish for. I have had a fantastic time being part of the iT-CDT, and I am extremely grateful and proud of all the experiences and variety of work we have achieved together. I would also like to thank all my colleagues in the CDT and The Leonardo Center for their continuous support and friendship, your enthusiasm and willingness to help with tribological and ultrasonic aspects is greatly appreciated. A special thanks must however go to Xiangwei, Tomos, Joe, Alan, Sushil, Matt, and Marcello, and also Nadia, Rachel and Mahdiyar, it's been a privilege!

Sincerest thanks to Dr Robin Mills for involving me in his STAMINA brainchild from the start. Thank you for all the technical support, and for always helping out in times of trouble!

Finally, it is only fitting to thank my family and friends for their patience and understanding, enabling me to achieve my goals and ambitions.

Abstract

Any industry which uses a fluid to lubricate a contact will require the viscosity of the lubricant to be known, and may periodically measure the viscosity of the liquid in order to maintain and optimise the efficiency of the system. This can be a timely process as a liquid sample may need to be removed for the measurement to be made as conventional viscometers contain rotating components which prevent in-situ measurement. Here the development of a novel standing wave method to measure viscosity in-situ has been developed. The use of a standing wave to determine physical properties of liquids has previously been overlooked, hence its use here as a viscometry technique is novel. The technique shows greater sensitivity to a wider range of viscosities than conventional ultrasonic techniques by taking advantage of the measurement enhancing effects of standing waves.

In 2014, a novel ultrasonic method using a continuous repeated chirp to produce a quasi-static standing wave signal was invented. This thesis focuses on the development and understanding of this method as a means to combat the limits of acoustic mismatch for viscosity measurement at metallic interfaces, and the assessment of the method with and without a matching layer.

Evaluation of the method in comparison to a conventional approach was firstly made through practical experimentation. The capabilities of the standing wave method with and without the matching layer were defined and evaluated with respect to a standard ultrasonic pulsed method. The standing wave method was shown to improve upon the conventional pulsed method, reducing associated errors by an order of magnitude. However, ultrasonic viscometry using the standing wave method was still found to be incapable of low viscosity measurements (2-500 mPa.s) at an aluminium interface without the addition of a matching layer. The lower limit of viscosity measurement here could however be reduced through optimisation of material properties as shown by the analysis of controllable physical parameters in this thesis.

An alternative signal analysis approach to eliminate the need of a prior reference signal was investigated and found to produce significantly similar results to those achieved using a conventional referencing technique. This analysis method therefore expands the range of applications for this technique. An analytical model produced to simulate the standing wave response to viscosity provided valuable information on key factors to consider when optimising the method. Good agreement between analytical and experimental results were found for the standing wave method with and without the matching layer ($P=0.0039$). Hence the model may prove to be a useful tool to predict the viscosity of a liquid after further refinement.

The standing wave method was then used to measure the viscosity of a liquid within the common rail system of a marine diesel test engine at an R&D facility for WinG&D, Winterthur, manufacturers of marine diesel engines. Ultrasonic viscosity measurements followed the same trend predicted using the temperature of the lubricant, an encouraging finding, as thermal effects are entirely removed from the ultrasonic apparatus through prior thermal calibration. This demonstrates the capability of the technique in thermally dynamic applications and provides evidence of the robust and stable nature of ultrasonic devices when instrumented on metallic components.

Contents

Nomenclature

Symbol	Description	Units
$\boldsymbol{A}$	Area of wet surface	m^2
$\boldsymbol{A_0}$	Initial wave amplitude	V
$\boldsymbol{A_m}$	Amplitude of measurement signal	V
$\boldsymbol{A_r}$	Amplitude of reference signal	V
$\boldsymbol{a, b, c}$	Constants	N/A
$\boldsymbol{B}$	Bulk modulus	Pa
$\boldsymbol{c_{sliding}}$	Sliding velocity	m/s
$\boldsymbol{c_m}$	Matching layer velocity of sound	m/s
$\boldsymbol{c_i}$	Incident wave speed of sound	m/s
$\boldsymbol{c_{r/t}}$	Transmission or reflection speed of sound	m/s
$\boldsymbol{f}$	Frequency	Hz
$\boldsymbol{f_t}$	Resonant frequency of the transducer	Hz
$\boldsymbol{f_s}$	Resonant frequency of the solid	Hz
$\boldsymbol{F}$	Force	N
$\boldsymbol{g}$	Acceleration due to gravity	N
$\boldsymbol{G}$	Shear modulus	Pa
$\boldsymbol{G'}$	Storage modulus	Pa
$\boldsymbol{G''}$	Loss modulus	Pa
$\boldsymbol{h}$	Lubricant film thickness	m
$\boldsymbol{k_m}$	Matching layer wavenumber	Dimensionless
$\boldsymbol{L}$	Component length	m
$\boldsymbol{N}$	Natural integer	N/A
$\boldsymbol{n}$	Number of reflections	N/A
$\boldsymbol{P}$	Pressure	MPa
$\boldsymbol{r_s}$	Radius of a sphere	m
$\boldsymbol{R}$	Reflection coefficient at the measurement interface	Dimensionless
$\boldsymbol{R'}$	Reflection coefficient at the transducer interface	Dimensionless
$\boldsymbol{S}$	Standing wave reflection coefficient	Dimensionless
$\boldsymbol{S_{pk}}$	Standing wave reflection coefficient at the resonant peaks	Dimensionless
$\boldsymbol{T}$	Temperature	°C
$\boldsymbol{t_m}$	Matching layer thickness	m
$\boldsymbol{t}$	Time	s
$\boldsymbol{U}$	Rotational speed	rpm
$\boldsymbol{U_t}$	Terminal velocity	m/s
$\boldsymbol{u}$	Shear velocity	m/s
$\boldsymbol{W}$	Load	N

$\boldsymbol{\mu}$	Coefficient of friction	Dimensionless
$\boldsymbol{z_s}$	Solid acoustic impedance	Rayl (Pa.s/m)
$\boldsymbol{z_{Al}}$	Aluminium acoustic impedance	Rayl (Pa.s/m)
$\boldsymbol{z_l}$	Liquid acoustic impedance	Rayl (Pa.s/m)
$\boldsymbol{z_{PZT}}$	Transducer acoustic impedance	Rayl (Pa.s/m)
$\boldsymbol{z_m}$	Matching layer acoustic impedance	Rayl (Pa.s/m)
$\boldsymbol{z_a}$	Air acoustic impedance	Rayl (Pa.s/m)
$\boldsymbol{\alpha}$	Attenuation coefficient	Np/m
$\boldsymbol{\alpha_p}$	Pressure viscosity coefficient	m^2/N
$\boldsymbol{\beta}$	Roelands Equation constant	Dimensionless
$\boldsymbol{\dot{\gamma}}$	Shear rate	s^{-1}
$\boldsymbol{\eta}$	Dynamic viscosity	Pa.s
$\boldsymbol{\eta_{0VI40}}$	Viscosity of a 0 VI oil at 40℃ ($\eta\_0VI40 = \eta\_0VI100$)	Pa.s
$\boldsymbol{\eta_{100VI100}}$	Viscosity of a 100 VI oil at 40℃ ($\eta\_0VI40 = \eta\_0VI100$)	Pa.s
$\boldsymbol{\theta_i}$	Incident angle	Degrees
$\boldsymbol{\theta_{r/t}}$	Angle at which reflection or transmission occurs	Degrees
$\boldsymbol{\phi'}$	Phase at the transducer interface	Radians
$\boldsymbol{\lambda}$	Wavelength	m
$\boldsymbol{\mu_1}$	Limiting low shear first Newtonian viscosity	Pa.s
$\boldsymbol{\mu_2}$	Viscosity limit at infinite shear rate	Pa.s
$\boldsymbol{\phi}$	Phase at the measurement interface	Radians
$\boldsymbol{\rho}$	Density	kg/m^3
$\boldsymbol{\rho_0}$	Density at ambient pressure	kg/m^3
$\boldsymbol{\rho_l}$	Liquid density	kg/m^3
$\boldsymbol{\rho_s}$	Solid density	kg/m^3
$\boldsymbol{\tau}$	Shear stress	Pa
$\boldsymbol{\upsilon}$	Kinematic viscosity	cP
$\boldsymbol{\Psi}$	First normal stress difference coefficient	Dimensionless
$\boldsymbol{\omega}$	Angular frequency	Hz

Abbreviations and Acronyms

Abbreviation	
AFG	Arbitrary Function Generator
ASTM	American Society for Testing and Materials
BCC	Body-Centred Cubic
PW	Pulsed Wave
COD	Coefficient of Determination
ECA	Emission Control Area
ELV	Engine Lubricant Viscometer
FFT	Fast Fourier Transform
HTHS	High Temperature High Shear
IP	Institute of Petroleum
ISO	International Organisation for Standardisation
LOSS	Lubricant Oil System Simulator
ML	Matching Layer
NDT	Non Destructive Testing
NI	National Instruments
OEM's	Original Equipment Manufacturers
P	Probability of the occurrence of a given event representing the smallest level of significance at which the null hypothesis would be rejected.
PC	Personal Computer
PZT	Lead-Zirconate Titanate
RMS	Root Mean Square
SAE	Society of Automotive Engineers
SW	Standing Wave
TBN	Total Base Number
USB	Universal Serial Bus
VI	Viscosity Index

1. Introduction

As the capabilities of lubricants improve, so does the need for monitoring devices to enable optimal efficiencies through lubrication. This could be achieved through advanced evaluation of lubricant properties during operation. It is the viscosity of the lubricant which provides the greatest overall performance indication of the oil, encapsulating information regarding film thickness capabilities, temperature, shear rate and the operation of the entire tribosystem.

The importance of lubricant monitoring systems has become ever more prevalent in recent years as industries are under increasing pressure to meet emission targets. Many manufacturers have already reached efficiency limits which can be achieved by design modification, thus the movement towards the development and optimisation of lubricants is under scrutiny. Complex mechanisms which synergistically affect a lubricant are difficult to replicate in a laboratory environment, hence the gold standard for viscosity characterisation is measurement of the lubricant within the engineering system itself, such as within a cylinder, bearing or oil line. A review of in-situ viscosity monitoring methods was made by (Markova et al. 2010), ultimately concluding acoustic techniques as those with the most promise.

Acoustic viscosity measurements are non-invasive and can be made in real time, however current acoustic systems rely on pulsed methods of sound generation which require relatively complex hardware, hence the use of acoustic monitoring devices within engineering is not commonplace. A technique for in-situ viscosity measurement presented herein however requires simplistic signal generation and acquisition hardware with the ability to exceed existing capabilities in terms of the sensitivity of viscosity measurement. The viscosity of a lubricating engine oil can range from 5 to 80 mPa.s at room temperature, hence correct selection of the lubricant is essential to achieve optimal performance. The transport industry is one which could benefit from the use of ultrasonic viscosity monitoring devices, for use as a low cost tool for lubricant performance monitoring. However this is only one of numerous industries which routinely require viscosity measurement capability.

1.1. Statement of the Problem

1.1.1. Common Rail Viscosity Monitoring in a Marine Diesel Engine

The reliability and performance of many tribo-systems depends largely on the lubricant as the viscosity of this liquid determines the capacity to provide an effective lubricating layer between two surfaces. Lubricants provide a low friction layer between two siding contacts, the thickness of which is ultimately determined by oil viscosity acting to prevent frictional wear to achieve optimal operating conditions (Williams 1994). Selection of the correct viscosity liquid depends on the load and speed during operation, high speeds at low temperatures require low viscosity oils, however low speeds with high loads and elevated temperatures require higher viscosity oils (Morgan & Wong 2017).

Engines used to power container ships are low speed diesel engines, with a speed range of between 70 and 110 rpm. The dimensions and associated tolerances of these engines are large,

meaning high viscosity lubricants are required to ensure hydrodynamic lubrication. The marine diesel industry routinely use oils to not only lubricate their engines but to also neutralise gasses produced from fuels with a high sulphur content. Fuels containing a high level of sulphur are generally cheaper as they are less refined, this however leads to the production of acidic gas during combustion which can cause corrosion of the cylinder liner and piston ring. Not only does this affect the efficiency of the engine, but high sulphur fuel emissions have been linked to climate change and issues relating the human health (European Environmental Agency 2015).

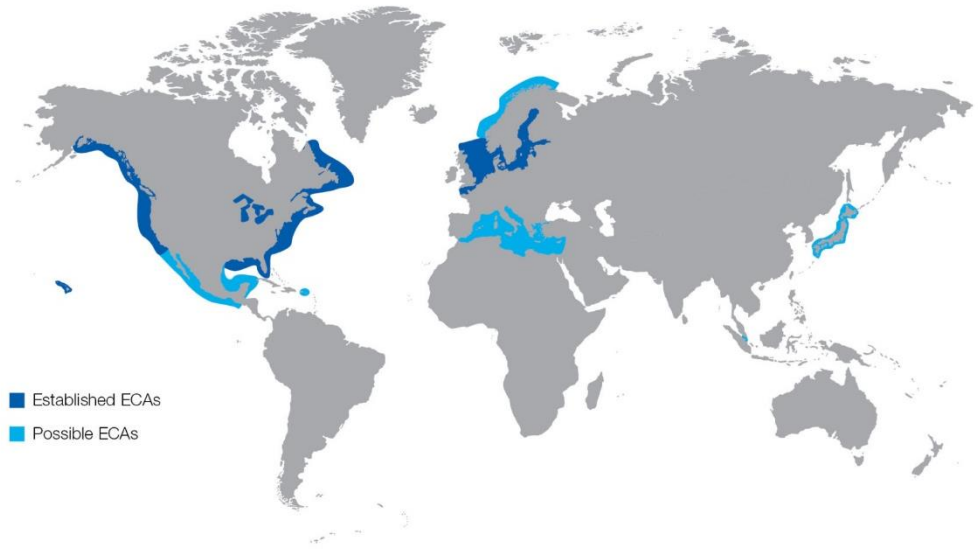

Figure 1-1: Sulphur emission control areas of the sea. (Fuels Europe 2018)

Figure 1-1 shows areas of the sea where sulphur emission from ships are controlled. Implementation of larger areas of Emission Control Areas (ECA's) are expected by 2020 when the International Maritime Organisation meet. In ECA's operators must switch to low sulphur fuels or install a scrubber which removes sulphur from the exhaust after combustion (Fuels Europe 2018). Switching fuel supply requires a change of lubricant to maintain sufficient lubrication while adequately neutralising gasses from combustion. Lubricants used for high sulphur fuels are selected for their capacity to neutralise acidic gasses from combustion while also maintaining the ability to form an effective lubricating layer between the cylinder and piston ring. Selection of the lubricant is based on the Total Base Number (TBN) which indicates the ability of the lubricant to neutralise acids and also the viscosity of the oil.

As marine vessels are required to burn low sulphur fuels in controlled areas of the seas, the need to monitor the viscosity of the lubricant becomes more important. For engines to run at their optimum efficiency, the correct lubrication regime between the cylinder and piston must be present. Optimal lubrication prevents wear of the cylinder, or liner when the surfaces move across one another, and consequently the reduction of friction for improved efficiency. The use of an in-line viscosity monitoring device could aid research and development into lubricants used within the industry, while in-line devices could provide real time measurement for test facilities.

1.1.2. Current Viscometry Techniques

A large number of commercially available viscometers have been developed, adopting familiar capillary, rotational, or falling ball configurations that measure liquid resistance to motion. The most commonly used being the rotational Couette viscometer which measures the resistance to rotational movement of a given volume of liquid. Most conventional viscometers are only capable of viscosity measurement if a sample is extracted from the system, a process costing engineering firms time and money, not only as measurement can be a timely task, but also due to loss of running time of the system under investigation.

Viscosity measurement of liquids taken using a conventional Brookfield Couette viscometer are deemed acceptable if repeatability lies within 1% of the measurement (ASTM 1998). Conventional viscometers require the removal of fluid from the point of use, so the viscosity of the oil can vary substantially as the unique combination of shear rates, pressures and temperatures in-situ are often difficult to replicate in a laboratory setting. Test rigs can be designed to reproduce these conditions however viscosity measurement in the contact often requires the modification of the contact surface, reducing the reliability of the measurement.

While the size and geometry of ultrasonic viscometers have been reduced as far as possible to prevent liquid disturbance, the devices still require immersion within the liquid of which they are required to measure. Ultrasonic viscosity measurement offers a unique opportunity to measure a liquid both non-invasively while remaining an in-situ measurement. Here we use an ultrasonic approach to oscillate the liquid using a continuous wave passing through the material of the vessel, pipeline or contact. Ultrasonic methods offer a promising measurement avenue for industrial applications as liquid measurements can be made in-situ from the counter surface of a component in real time.

Past ultrasonic viscometry techniques have adopted a pulsed configuration, where viscosity is determined by the ultrasonic loss from a single reflection at a solid-liquid boundary. When considering a metallic substrate, ultrasonic techniques suffer as a result of acoustic mismatch between solid and liquid materials. Large acoustic differences between metals and liquids result in most of the ultrasonic energy being reflected back through the material when the wave becomes incident with the interface. If the liquid has little effect on the reflection and only a small change in a reflection is detected, the method is incapable of viscosity measurement if the influence of the liquid is in the same order as the noise of the signal. This prevents viscosity measurement through a common engineering material, and so work to combat this is essential for engineering applications of ultrasonic viscometry.

The use of a continuous wave method has the potential to improve viscosity measurement sensitivity as multiple reflections, and so multiple measurements of the interface interfere to compose the standing wave signal. Theoretically, the method should have a greater sensitivity to viscosity at a metallic interface than pulsed methods. The method has not previously been used to measure viscosity in this nature, as standing wave measurements of this kind are thought to be complex and confusing as so have been avoided. The novelty of this work therefore is based upon the use of a standing wave within a component to measure viscosity on

the counter face. Additionally, novelty is present in the signal processing methods, which permit measurement without the need of a reference signal when using multiple frequency standing waves. The nature of this method permits improved measurement in comparison to pulsed techniques, and requires relatively simplistic signal generation hardware. The method could therefore transform conventional ultrasonic non-destructive testing techniques.

1.2. Project Aims and Objectives

The aim of this project was to develop a method to measure viscosity in-situ through a metal component using a continuous shear standing wave, to improve the practicality of ultrasonic viscosity measurements in engineering components. In order to achieve this the following objectives were proposed.

The objectives of the project were:

1. Develop a novel ultrasonic shear standing wave method for viscosity measurement.
2. Build and instrument a measurement apparatus to compare viscosity measurements made using the standing wave ultrasonic method, and a pulsed ultrasonic method.
3. Experimentally evaluate the influence of the implementation of a matching layer when using the standing wave method.
4. Develop a model to understand the mechanisms and parameters governing the standing wave method and validate the analytical model through comparison with experimental data.
5. Design and develop an in-line viscometer for a practical application within a marine diesel engine lubrication system.

1.3. Thesis Layout

This work is divided into eight chapters. This section reports a brief summary of each.

Chapter 1: Introduction.

Chapter 2: Literature Review. The theory outlined in this chapter concerns firstly the background of liquid viscosity, including key parameters which affect viscosity and an outline of the principal types of characterisation and conventional measurements techniques. The basic principles of ultrasound are outlined which are then used to define the physical obstacles preventing effective shear ultrasonic viscosity measurement. The fundamental principles of standing waves and resonance are also addressed in this chapter. A review of ultrasonic viscometry is then addressed, covering current state of the art viscosity measurement techniques. The chapter concludes with an evaluation of current ultrasonic viscosity measurement techniques to identify current capabilities and potential gaps within the field.

Chapter 3: The Standing Wave Method. In this chapter the novel standing wave method is presented, and the influence of the key parameters used to define the wave covered. Factors which influence the standing wave such as component geometry and material are also

discussed. Ultrasonic apparatus, hardware and signal processing along with an outline of the test oils used is also discussed.

Chapter 4: Newtonian Viscosity Measurement Using the Standing Wave Method: This chapter reports a series of viscosity measurements when using the standing wave method with and without a matching layer through an aluminium component. The standing wave method is then compared to a pulsed wave method, followed by the assessment of an auto-calibration technique, through evaluation of a fixed frequency or peak selection signal processing approach.

Chapter 5: Standing Wave Analytical Model: This chapter describes the development of an analytical model based on standing wave equations previously defined. Each input and output parameter is evaluated to verify the behaviour of the model, followed by the incorporation of a three layer reflection model to simulate the effect of a ML at the measurement surface on the standing wave behaviour with a Newtonian liquid.

Chapter 6: Experimental Validation of the Analytical Model: An evaluation of the analytical model is made through a comparison with experimental data produced in Chapter 6. The model was then assessed using input parameters from practical measurements to determine whether this is a beneficial procedure. The chapter therefore highlights the capability of the analytical model to simulate experimental results.

Chapter 7: In-situ Measurement of Marine Diesel Engine Oil Viscosity. This chapter describes the design and fabrication of an in-line ultrasonic viscometer to determine the viscosity profile of a marine diesel engine lubrication system. The viscosity of the oil was measured for a test schedule pre-determined by WinG&D (a marine diesel engine manufacturer) at variable engine loads and oil temperatures at a research and development test facility.

Chapter 8: Conclusions: A summary of the key aspects are covered here with reference to key findings of this work. The significance of the standing wave method is addressed, followed by an evaluation of the findings presented regarding the fundamentals of the method and considerations of practical applications. Further potential scope of the method is discussed for non-Newtonian validation, oblique angle measurement and shear rate spectral analysis.

2. Literature Review

This chapter consists of an overview of liquid viscosity and conventional methods to measure viscosity to outline current disadvantages of commonly used measurement methods. This is followed by an outline of the main advantages of ultrasonic viscosity measurement for in-situ applications. A theoretical explanation of ultrasonic principles is then addressed, with a focus on the fundamentals of viscosity measurement, before a review of current ultrasonic viscometry methods is made to address the variety of ultrasonic techniques available, and the capabilities of these. The main obstacles of ultrasonic viscosity measurement are then highlighted when considering engineering applications. The chapter then concludes with a summary of key ultrasonic methods which have the potential to overcome some of the obstacles which face ultrasonic viscometry within the engineering field.

2.1. Liquid Viscosity

Mineral oils are manufactured from petroleum oils through distillation and other refining processes to separate them into a few basic grades. Oil grades are widely used for lubrication identification purposes so are strictly controlled under international and national standards through the American Society for Testing and Materials, (ASTM) and the Institute of Petroleum (IP). These oils are often referred to as the base oil, but while they constitute between 75 to 95% of lubricants, additives are often supplemented to improve the function of the oil. The most important parameter of a lubricant is viscosity and the variation of this liquid property specifically with temperature and pressure.

Viscosity is a measure of resistance to shear in a fluid, which is related to interactions between molecules. This can also be referred to as the internal friction of a fluid which is caused by molecular attraction governing the tendency of a liquid to flow. The behaviour of a fluid between two parallel plates separated by a small gap, h, filled with lubricant can be seen in Figure 2-1.

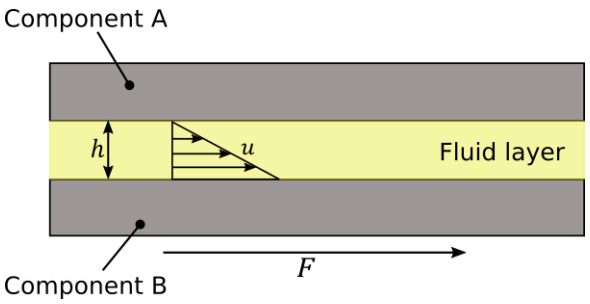

Figure 2-1: Schematic diagram of two solid plates separated by a fluid layer.

Assuming component A is stationary, the shear force applied to component B is a function of the velocity u, fluid film thickness h, viscosity of the fluid η, and the area of the wet surface, A as follows.

$$F = \eta A \frac{u}{h}$$ Equation 2-1

Shear viscosity is the resistance offered by the fluid to an applied shear stress, thus defined as the dynamic viscosity, η, with the relationship shown in Equation 2-2.

$$\eta = \frac{F}{A} \Big/ \frac{u}{h} = \frac{\tau}{\dot{\gamma}}$$ Equation 2-2

This can also be expressed in terms of shear stress τ, and shear rate $\dot{\gamma}$. The fundamental unit of dynamic viscosity is the poise, P , however viscosity measurements are often expressed in Pascal seconds Pa.s, or milli-Pascal-seconds (mPa.s), where 1 Pa.s = 1000 mPa.s = 10 P. Dynamic viscosity requires the presence of an actuated surface, alternatively kinematic viscosity, υ is the liquid resistance to flow under gravity, this being the ratio of dynamic viscosity η to the liquid density, ρ. The kinematic viscosity can therefore be expressed by Equation 2-3.

$$\upsilon = \frac{\eta}{\rho}$$ Equation 2-3

The SI unit for kinematic viscosity is the Stoke, (St) however this is often stated in centi-stoke (cSt). This work concerns the measurement of dynamic viscosity due to the selected shear based approach, thus viscosity will be expressed in terms of Pa.s or mPa.s.

2.1.1. Lubrication Mechanisms

With few exceptions, engineering components which are composed of loaded sliding surfaces will undergo significant amounts of surface damage and wear if they are not given adequate lubrication. Lubricants have many functions within engineering systems, acting to cool rubbing surfaces, remove debris from contacts, provide protection from corrosion and also, to provide a thin lubricating layer to separate surfaces. A fluid film reduces friction and wear allowing satisfactory operation of the contact. When the surfaces have no physical contact, the resistance to their motion is attributed to viscous losses in the lubricant. Frictional force will increase with tangential force if the lubricant is Newtonian, although the coefficient of friction, μ is dependent on viscosity, η, rotational speed, U, and load w per unit length, shown in Equation 2-4.

$$\mu = \frac{\eta U}{w}$$ Equation 2-4

The Stribeck curve identifies three lubrication regimes which occur between mechanical components in contact, these are boundary lubrication, mixed lubrication and hydrodynamic (Williams 1994). The curve presents friction as a function of rotating speed, viscosity and load.

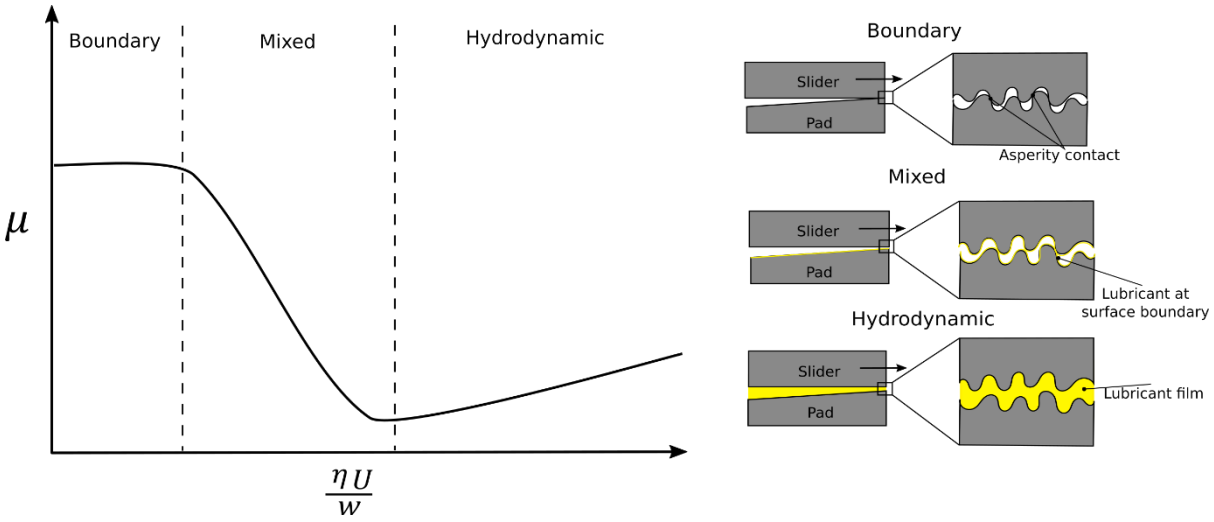

Figure 2-2: A schematic diagram of a Stribeck curve and the surfaces which characterise boundary, mixed and hydrodynamic lubrication.

The graph is split into three regions to show the areas each lubrication regime dominates. The first is boundary lubrication, in this region, the lubrication film has not yet formed and contact between the asperities of the surfaces is present, as shown by the schematic of two surfaces in Figure 2-2 under the 'Boundary' heading. The bulk properties of the substrate are significant as the load is completely resting on these, properties of the lubricant such as the viscosity are insignificant here due to the absence of hydrodynamic lift. Solid contact in this region produces high values of friction determined by the materials which form the components.

The second lubrication regime is known as mixed lubrication as it encompasses the transition from boundary lubrication to elastohydrodynamic lubrication. In this region, where components are in relative motion, the contact area between the asperities reduces as the lubricant film begins for form. This results in a sharp drop in friction as the load is now supported by the lubricant film, and asperity contact, shown schematically in Figure 2-2 under the 'Mixed' heading. The contact is therefore characterised by pockets of oil and contact between asperities.

Progression occurs as U increases, into hydrodynamic lubrication which is characterised by the formation of a full lubricating layer which reduces friction, seen as complete separation of surfaces, shown schematically in Figure 2-2 under the 'Hydrodynamic' heading. At higher speeds, the effects of viscous drag cause increased friction. In hydrodynamic bearings, lubricant film formation relies on the geometry and motion of the surfaces along with the viscous nature of the fluid. In these bearings, operation depends on the generation of a wedge shaped gap by which the lubricant is dragged into by the motion of the two surfaces. Motion of the surfaces generates a pressure which is capable of pushing the two surfaces apart by balancing the normal load on the bearing. Just as the viscosity of the oil influences the operation of a bearing, this relationship is found in all loaded sliding surfaces thus monitoring bulk properties can allow control of operational lubrication regimes.

2.1.2. Viscosity and Temperature

Liquid viscosity decreases rapidly with increasing temperature as particle bonds weaken and atomic particles increase their oscillatory speed resulting in a lower resistance to motion. The Vogel equation is thought to most precisely describe the relationship between temperature and viscosity, as shown in Equation 2-5 (Crouch & Cameron 1961).

$$\eta = ae^{\frac{b}{(T-c)}} \qquad \text{Equation 2-5}$$

In Equation 2-5, a, b and c are constants and T is temperature related to the known viscosity of the fluid at three temperatures surrounding the temperature in question. For mineral oils, c is approximately 95 and a and b are determined by dynamic viscosity measurement at two different temperatures, which are usually 40 and 100 ℃. The Vogel equation is widely used in theoretical studies of tribology due to the practical nature of the method. As ultrasonic measurement of viscosity is dynamic, the Vogel equation will be used throughout this work to determine the viscosity at specific temperatures of standard oils using dynamic viscosity measurement tables provided by the supplier (Cannon Instrument Company 2018).

2.1.3. Lubricant Viscosity Grades

Commercial mineral oils are available in a number of different viscosity grades. The grade classifies their viscosity at a standard temperature to provide the relationship of that specific oil with temperature. The two main classification systems are the International Organisation for Standardization, (ISO) and the Society of Automotive Engineers (SAE). These differ as SAE classify oil grades, whereas ISO standards more specifically include temperature variation data.

The SAE grade is the most commonly used classification for engine oils, which specifies the viscosity of the oil at high and low temperatures. The system also includes shear rate information, another parameter which affects viscosity which will be covered later in this chapter. Each year the system is revised to extend the SAE system to achieve lower High Temperature High Shear rate (HTHS) viscosities with the aim to improve engine efficiencies by using lower viscosity lubricants. As of January 2015 two new HTHS viscosity grades were added, these being SAE 12 and SAE 8, which are included in Table 2-1.

These oils were added to the system to support the development of Original Equipment Manufacturers (OEM's) to improve fuel economy. Low temperature dynamic viscosity concerns the viscosity of the oil when an engine is first started, at this point inertial effects are not considered, however these are considered by the kinematic viscosity at 100℃ where the ratio of viscous to inertial forces are of interest.

Table 2-1 SAE-J300 standard viscosity grades for engine oils.

SAE Viscosity grade	Low Temperature dynamic viscosity (mPa.s)		Low Shear Rate Kinematic Viscosity (mm^2/s) at 100℃		High temperature high shear rate (mPa.s) at 150℃.
	Cranking Viscosity	Pumping Viscosity	Minimum	Maximum	
SAE 0W	6200 at -35ºC	60000 at -40ºC	3.8	-	-
SAE 5W	6600 at -30ºC	60000 at -35ºC	3.8	-	-
SAE 10W	7000 at -25ºC	60000 at -30ºC	4.1	-	-
SAE 15W	7000 at -20ºC	60000 at -25ºC	5.6	-	-
SAE 20W	9500 at -15ºC	60000 at -20ºC	5.6	-	-
SAE 25W	13000 at -10ºC	60000 at -15ºC	9.3	-	-
SAE 8	-	-	4	<6.1	1.7
SAE 12	-	-	5	<7.1	2.0
SAE 16	-	-	6.1	<8.2	2.3
SAE 20	-	-	6.9	<9.3	2.6
SAE 30	-	-	9.3	<12.5	2.9
SAE 40	-	-	12.5	<16.3	3.5
SAE 50	-	-	16.3	<21.9	3.7
SAE 60	-	-	21.9	<26.1	3.7

Currently most automotive engine oils are multigrade which can achieve both lower and higher grading and so are functional in both summer and winter. Oils which are made for restrictive use such as in lawnmowers tend to be monograde. The SAE classification system for multigrade oils is mainly used for engine oils where the first number indicates the grade at low temperatures and the second the viscosity at high temperature, e.g. SAE 10W30.

2.1.4. Viscosity Index

The Viscosity Index (VI) system was introduced in 1929 in the USA as an empirical system based on two standard oil series. The system assigned a VI of 0 to Gulf Coast oils which were thought to have the greatest variation of viscosity with temperature, and an index of 100 given to Pennsylvanian oils which were thought to have the least variation with temperature. The VI therefore defines the behaviour of the oil with temperature. The viscosity, temperature relationship of a given oil is compared to two standard reference lubricants, (Gulf coast and Pennsylvanian) using Equation 2-6 (ASTM International 2007).

$$VI = \frac{\eta_{0VI40} - \eta_u}{\eta_{0VI40} - \eta_{100VI100}} \times 100 \qquad \text{Equation 2-6}$$

In Equation 2-6 η_{0VI40} is the viscosity of a 0 VI oil at 40ºC which has the same viscosity at 100 ºC as the oil which the VI is being calculated, $\eta_{100VI100}$ is the viscosity at 40ºC of an oil of 100 VI which has the same viscosity at 100 ºC as the oil which the VI is to be calculated. Finally,

η_u is the viscosity of the oil whose VI is to be calculated at 40ºC. These values are tabulated in the ASTM standard D2270 (ASTM 1998).

High VI lubricants shows a small change in viscosity when subject to a range of temperatures, whereas a low VI lubricant shows a greater change of viscosity with a change in temperature. Within an engine for example, high VI lubricants offer durable and stable lubrication over the full range of operating temperatures, however low VI lubricants offer lower friction and thus improved engine performance. Most mineral oils have a VI of less than 100, however synthetic oils and multi-grade oils can have VI of more than 100 due to the development of additives. For example, automobile engine oils have a VI of around 160 indicating the wide range of temperatures over which they are able to operate.

2.1.5. Viscosity and Pressure

Viscosity increases with pressure when the fluid is said to be piezo-viscous. The variation between η and pressure, P, can be expressed by the Barus equation, Equation 2-7 (Barus 1893),

$$\eta = \eta_0 e^{\alpha_p P} \qquad \text{Equation 2-7}$$

where η_0 is the dynamic viscosity at ambient pressure and α is the pressure viscosity coefficient. This relationship is important in high pressure non-conformal contacts such as rolling element bearings, gears, cams and followers which operate in the elasto-hydrodynamic regime. The Barus equation indicates that η can double from ambient pressure to 35 MPa, and triple at 55 MPa. It is however known that the Barus equation overestimates viscosity at high pressures in the order of GPa, in which case the Roeland's Equation can be recommended as a replacement, outlined in Equation 2-8 (Ghosh et al. 2013),

$$\eta = \eta_0 e^{\left\{[9.67+\ln\eta_0]\left[\left(1+\frac{P}{P_0}\right)^{\beta}\right]-1\right\}} \qquad \text{Equation 2-8}$$

where β is a constant and $P_0 \approx 2 \times 10^8$ Pa. The density of a liquid, ρ_l, is also influenced by pressure P, however to a much lesser extent. The following empirical equation describes this relationship.

$$\frac{\rho}{\rho_0} = \frac{1 + 1.27P}{1 + 1.68P} \qquad \text{Equation 2-9}$$

In Equation 2-9, ρ_0 is the density at ambient pressure, and P must be in GPa units. Density change with pressure is small, for example a pressure increase of 35 MPa will double the viscosity of SAE 30 at 100°C, but only increase the density by 2%.

2.1.6. Viscosity and Shear Rate

Depending on the state and composition, liquids can exhibit a number of behaviours when sheared. When a liquid viscosity remains the same regardless of the shear stress, the fluid is said to demonstrate Newtonian behaviour, and is therefore named a Newtonian fluid. Fluids

are said to exhibit a non-Newtonian behaviour when η is not constant with shear rate, γ. As schematically shown in Figure 2-3a, non-Newtonian fluids can show either a shear thinning behaviour, where η decreases with γ (known as pseudoplastic) or shear thickening behaviour where η increases with γ (known as dilatant). In addition to these two main non-Newtonian behaviours, fluids can also show time dependent thinning with a constant shear rate, known as thixotropy, and thickening known as rheopexy, as shown in Figure 2-3b.

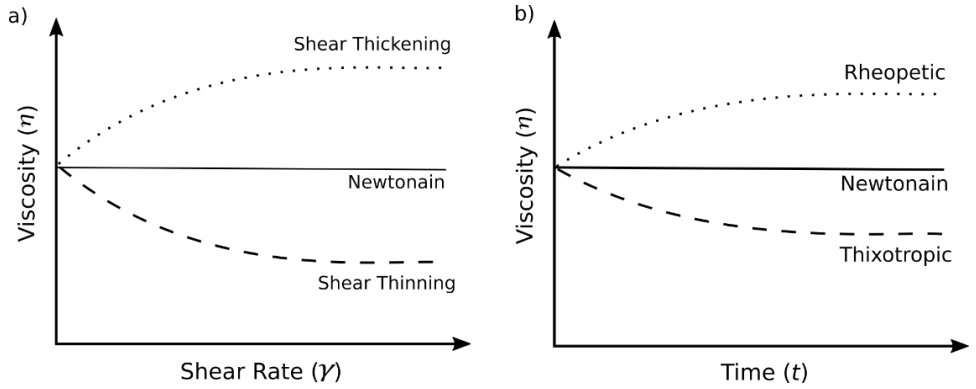

Figure 2-3: Schematic diagrams of a) viscosity and shear rate, b) varying viscosity vs time of shearing relations.

These mechanisms are determined by the molecular kinetics of the liquid when a shear rate is applied. When molecules align with the displacement produced by two surfaces within a liquid, less resistance to motion is exerted by the liquid which reduces the forces required to move the components. This behaviour is known as shear thinning as the viscosity decreases with increasing shear rate. Molecules in shear thickening fluids undergo a transition to behave like solid particles when subject to shear forces, a behaviour observed in liquids containing deflocculating solids, as particles move to expand in a way to create voids in which the liquid cannot penetrate, producing a shear thickening behaviour.

The behaviour between viscosity and shear rate must be carefully interpreted when considering shear motion produced by ultrasonic displacement. The kinetic mechanism by which shear motion is produced varies between that produced from steady shear, such as that within a conventional viscometer, to oscillatory shear produced by an ultrasonic wave (Schirru et al. 2018). Particles within the liquid align in the direction of motion when subject to steady shear, as shown in Figure 2-4. When subject to oscillatory shear motion particles within a liquid are displaced according to the frequency of the oscillation and size of the particle.

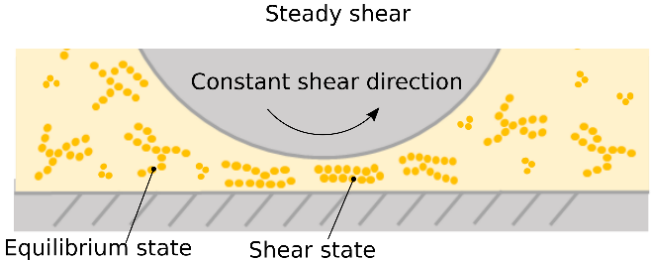

Figure 2-4. Steady shear thinning.

If the period (1/frequency) of the ultrasonic wave is shorter than the time it takes for the particles within the molecular structure of the fluid to relax, the apparent viscosity is a function of the solvent only as shown in Figure 2-5a.

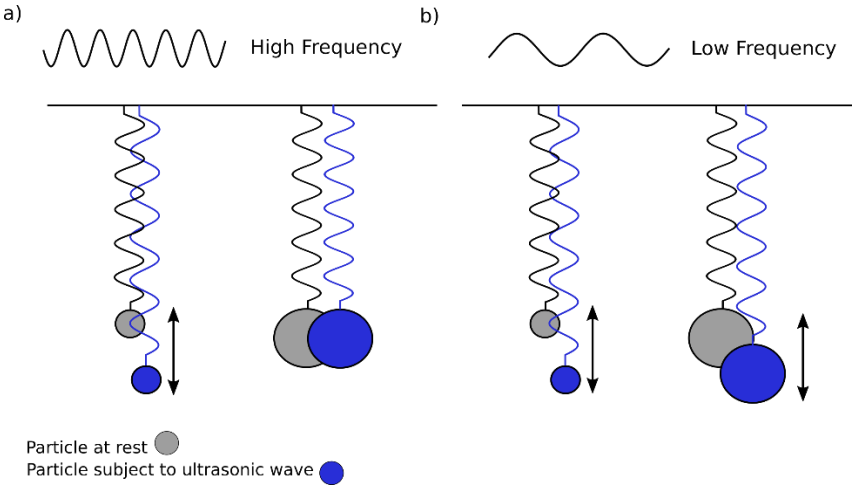

Figure 2-5: A schematic representation of the effect of a) high frequency oscillation, and b) low frequency oscillation on the movement of small and large particles within a liquid.

In contrast, if the period of the ultrasonic wave is longer than the relaxation time, the measured viscosity is a function of the larger molecules and the solvent. This gives the particles in the molecular structure time to return to their equilibrium and so contribute to the resistance to shear. As a result, a higher viscosity measurement at lower shear rates (and thus lower frequencies) is seen, as shown in Figure 2-5b. This behaviour produces a higher relative viscosity measurement at lower shear rates, than that given at high shear rates. The influence of shear rate on viscosity is shown in Figure 2-6.

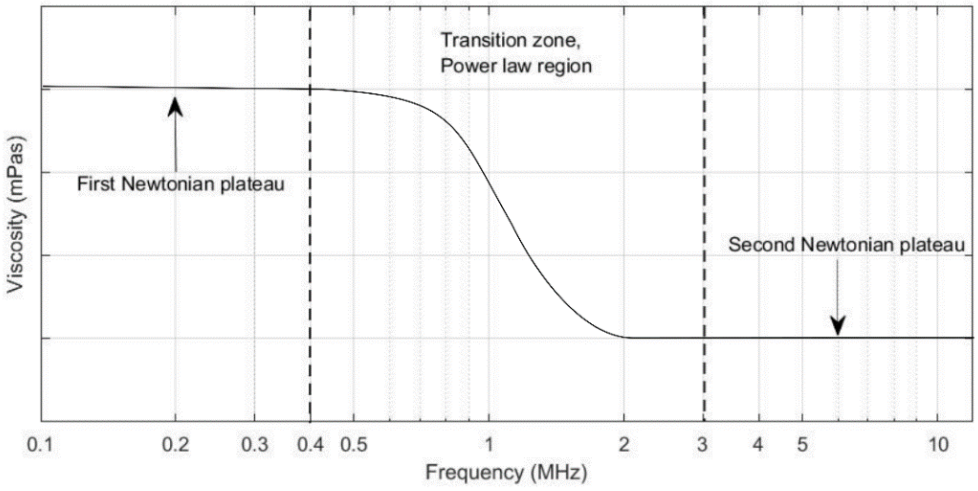

Figure 2-6: A schematic diagram of a typical viscosity-frequency spectrum from a high shear viscometer.

Engine oils are known to transition between two Newtonian plateaus with increasing shear rate as seen in Figure 2-6. At low shear rates the oil behaves like a Newtonian fluid, but then undergoes a period of transition as the shear rate increases. In the transition zone, the fluid

shows Non-Newtonian behaviour before transitioning into the second Newtonian plateau at very high shear rates. Here the viscosity is independent of shear rate once again, but at a lower viscosity value than the first Newtonian plateau. This behaviour of engine oil is important to consider when selecting the correct viscosity oil for a tribosystem, as two liquids which show the same viscosity at one shear rate may have very different viscosities under higher shear rates, the very reasoning behind multiple shear rate values in the SAE-J300.

Most engine lubricants exhibit shear thinning behaviour, however it is important to note that the viscosity does not drop to zero as this is physically impossible. In fact lubricating oils can show both Newtonian and non-Newtonian properties. Base, mineral and synthetic oils show Newtonian behaviour, however oil degradation through oxidation or contamination during service can cause non-Newtonian behaviour (Markova et al. 2010). Additives in more complex oils produce non-Newtonian shear thinning effects to improve the performance of oil in-situ. Some of the mechanisms which can influence the viscosity of an oil are outlined in Table 2-2.

Table 2-2: Parameters affecting viscosity within an engineering system.

Increased Oil Viscosity	**Decreased Oil Viscosity**
Thermal Destruction	Oil Cracking
Oxidation	Fuel ingress
Increased Pressure	Decreased pressure
Lower temperature	Increased Temperature
Additive decomposition	Fuel, water or coolant contamination

Some parameters shown in Table 2-2 may occur in isolation, while others in unison making identification of each action difficult to distinguish by a change in viscosity alone as one may compensate for another. For example lubrication oil in diesel engines can be contaminated by fuel, decreasing the viscosity, and simultaneously contaminated with soot which acts to increase viscosity (Markova et al. 2010).

2.2. Conventional Viscometers

Viscometers broadly use the resistance to shear motion as a measure of viscosity. Conventional viscometers measure the resistance to motion or the time duration for kinetic displacement of a liquid. Here viscometers have been classified according to their shear action, in brief, falling body, rotational, vibrational and capillary, as shown in Figure 2-7.

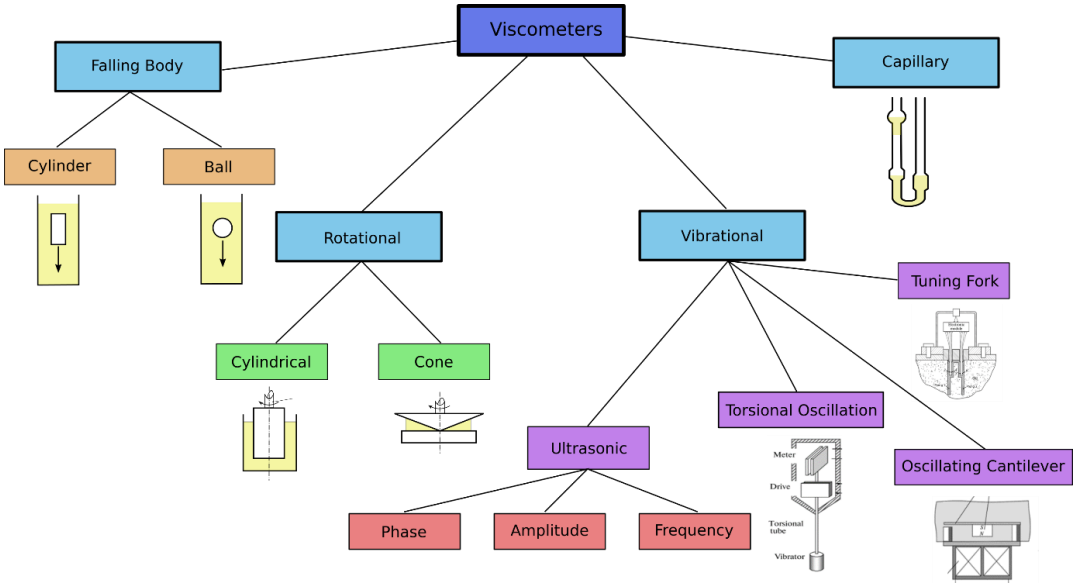

Figure 2-7: Methods for measuring on-line monitoring of the viscosity of lubricating oils.

The most commonly used conventional viscometers will now be outlined, while this list in not exhaustive, principal mechanical shear viscometers are reviewed in order to demonstrate the wide ranging methods and devices currently adopted.

2.2.1. Capillary Viscometers

Capillary viscometers equate the time it takes for the liquid to travel through a capillary to the kinematic viscosity as the technique relies on gravity and has no mechanical parts to apply shear to the liquid. An image of a capillary viscometer is shown in Figure 2-8. The viscometer is filled through the tube on the right in the image below, then drawn up the second left hand tube by suction. Prior to this, the lubricant is allowed to equilibrate within a controlled temperature bath in which the viscometer is immersed. The time taken for the meniscus to fall from the upper etched mark to the lower mark is measured (Williams 1994).

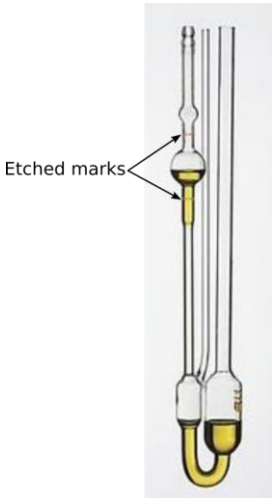

Figure 2-8: A conventional capillary viscometer. Image adapted from (IndiaMART 2018)

The time taken is proportional to the kinematic viscosity, which can be defined by the formula;

$$v = Ct \qquad \text{Equation 2-10}$$

where C is the calibration constant for the viscometer dependent upon the geometry of the device, measured in mm^2/s^2 and t is the arithmetic mean value of the flow time measured in seconds. The kinematic viscosity measured using a capillary viscometer has a relative error of $\pm 0.5 - 2.5\%$ for operating devices (Markova et al. 2010).

2.2.2. Falling Body Viscometers

Falling body viscometers measure the time taken for a body within the liquid to travel through the capillary, unlike capillary viscometers which measure the time the liquid travels. Two examples of this configuration can be seen in Figure 2-9.

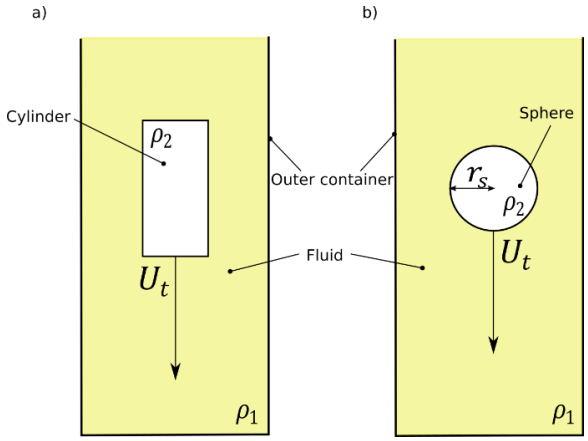

Figure 2-9: a) Falling cylinder viscometer, b) falling ball viscometer.

Stokes law is used to calculate the force, F exerted by the viscous drag of the liquid for a spherical body using:

$$F = 6\pi\eta r_s U_t, \qquad \text{Equation 2-11}$$

where r_s is the radius of the sphere, and U_t is the terminal velocity of the falling sphere. The viscosity of the liquid is then calculated by balancing the force with the buoyancy force exerted on the ball, shown in Equation 2-12.

$$\eta = 2gr_s^2 \frac{\rho_2 - \rho_1}{9U_t} \qquad \text{Equation 2-12}$$

In Equation 2-12, g is gravity, ρ_1 is the density of the liquid, and ρ_2 is the density of the solid body. A similar approach is used to calculate the viscosity of a liquid when using the falling cylinder viscometer, however the range of viscosities measurable when using these devices is dependent upon many other factors than what are considered here, such as the capillary length, ratio of the cylinder or sphere size to the diameter of the chamber and also the influence of wall effects, all of which influence liquid flow.

2.2.3. Rotational Rheometer

The measured resistance offered by the fluid to an applied shear stress is a measurement of the dynamic viscosity. Rotational viscometers thus measure the dynamic viscosity of a fluid as the viscometer consists of a rotating cylinder fixed on a shaft coaxially within a motionless cylinder, although other configurations exist, the most common will be addressed. Liquid is placed between two cylinders, producing a viscous friction force which is measurable by a torque transducer attached to the rotating shaft. The change in rotational speed for a given torque or measurement of the torque during a constant rotational speed relates to the liquid viscosity. Rotational viscometers have primarily cylinder or cone-on-plate configurations.

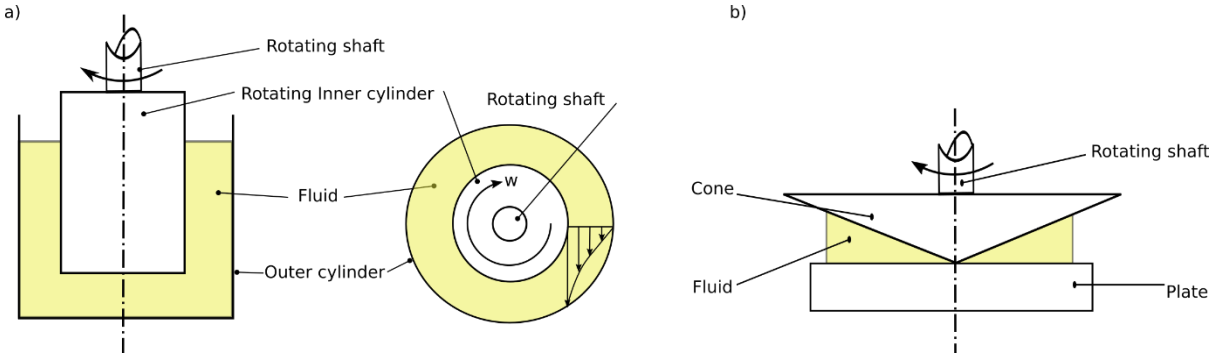

Figure 2-10: Schematic representation of a) a cylindrical rotational viscometer and b) a cone-on-plate viscometer

A cone on plate viscometer has the same operating principal but the rotating surface is conical. The setup permits a small liquid sample size and so is often favoured over alternative configurations as thin films can be analysed. The shear rate achieved using rotational viscometers varies from 10 to 10^4 s^{-1} although higher shear rates can be achieved using a plate-on-plate viscometer, otherwise known as a high shear viscometer. The high shear viscometer is based on the cylindrical rotational viscometer and can measure dynamic viscosity up to 10^7 s^{-1}. Figure 2-11 shows a schematic of a high shear viscometer.

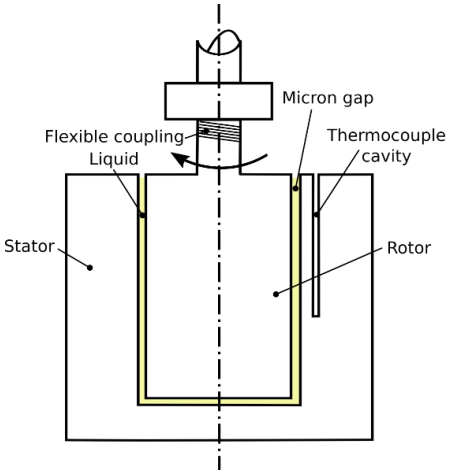

Figure 2-11: Schematic drawing of the ultra-high shear viscometer.

The temperature generated from the high shear rate is the limiting factor when considering high shear viscometers. To overcome this, measurements are taken for a short period of time, while high shear rates are generated because the stator (the stationary container of the viscometer) and the rotor are separated by only 1 μm (PCS Instruments). Less than 5 ml of liquid is required for a measurement to be made and the liquid temperature can range from 40 to 150℃ with temperature accuracy reported as $\pm$0.1℃. The viscometer is capable of viscosity measurement up to 50 mPa.s and was designed to measure automotive oils which experience high shear rate within the engine contact.

2.2.4. Vibrational Rheometers

Vibrational viscometers measure the amount of power required to displace a given quantity of liquid with either a rotational or tuning fork configuration. Quartz resonators measure the resonant frequency change Δf, when the oscillating quartz is submerged in the liquid.

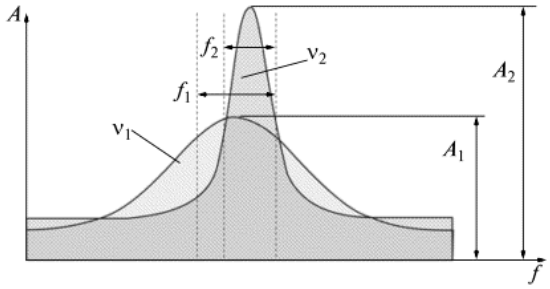

Figure 2-12: Vibrator oscillation variation of parameters with viscosity change. Where A_1 and A_2 are amplitudes, f_1 and f_2, frequency of vibrator oscillation within the liquid, and viscosity v_1 and v_2 where $v_1 > v_2$. Image from (Markova et al. 2010).

These methods use either a phase change of the resonating signal of the vibrator or the dampening effect of oscillation of the vibrator shown as an amplitude reduction. Depending on which parameter is evaluated, the viscometer can have one of two configurations. The first being the torsional oscillator, and the second a vibrating cantilever.

2.2.5. Torsional Oscillation Viscometer

Torsional oscillation viscometers are comprised of a vibrator mounted at one end of a torsional tube and a drive and turn meter at the other, shown in Figure 2-13.

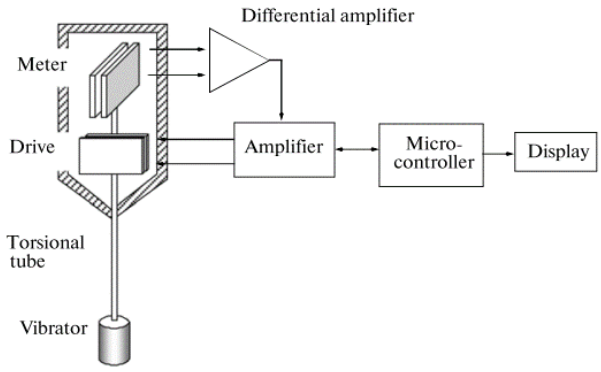

Figure 2-13: Schematic diagram of a torsional oscillation viscometer. Image adapted from (Markova et al. 2010).

The drive uses two piezoelectric elements and an alternating current to produce torsional oscillations relative to the resonant frequency of the torsional tube. A second pair of piezoelectric elements is used to record the signal in order to characterise the torsional oscillation of the bar. When the vibrator is submerged in a liquid, the phase difference in the signal is analysed to assess the damping factor of the liquid upon the vibration of the bar, a factor which is proportional to the viscosity.

2.2.6. Vibrating Cantilever

The second vibrational viscometer is based on the use of a vibrating cantilever made of a ferromagnetic material with a Teflon coating. A short pulse of current is used to excite an electromagnetic coil which in turn produces a bending motion on the cantilever at the beams natural frequency, a permanent magnet is fixed to the cantilever which is mounted over an electromagnet. Once submerged within the liquid the oscillation is dampened by the resistance of the liquid, which has a positive correlation with the dynamic viscosity of the liquid.

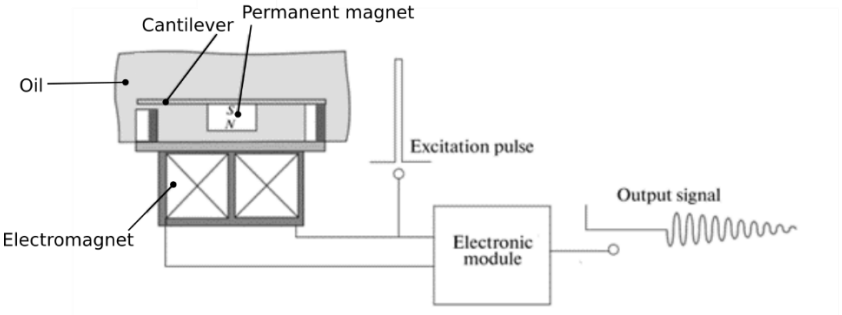

Figure 2-14: Vibrating cantilever viscometer, image adapted from (Markova et al. 2010).

The cantilever oscillates around 500 Hz a frequency which can not only be produced by the electromagnetic coil but also recorded. It is the rate of dampening of the oscillation of the cantilever which indicates the dynamic viscosity.

2.2.7. Tuning Fork Rheometer

Tuning fork viscometers use mechanical displacement of two prongs within a liquid to measure viscosity. The prongs operate at a frequency of <75 kHz and must be submerged within the liquid to produce a measurement. The prongs in Figure 2-15 are labelled 1 and 2 as protrusions into the oil.

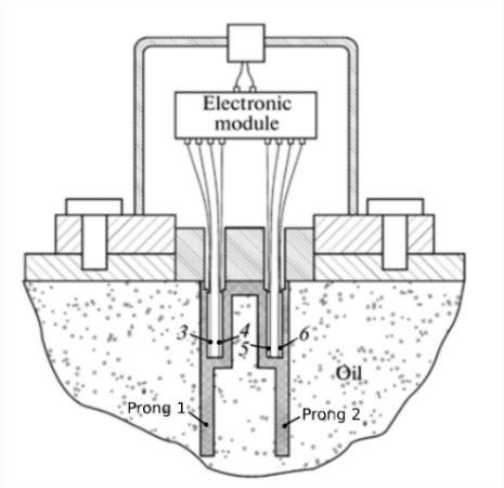

Figure 2-15: Tuning fork viscometer. Image adapted from (Markova et al. 2010).

The prongs of the forks have channels which house the piezoelectric elements shown in Figure 2-15 at positions 3 to 6. The elements act to oscillate the prongs when a voltage is applied, the oscillation of the prongs when immersed within a liquid is dependent on the shear resistance, and thus the viscosity. By changing the bandwidth of the oscillation, i.e. the range of frequencies used to excite the prongs, the density of the liquid can be obtained (Markova et al. 2010). This method measures the viscosity-density coefficient as the density of the liquid cannot be isolated from that of the viscosity. As discussed, the mechanisms by which a shear action is subject to a liquid vary rather significantly.

2.3. In-Situ Viscosity Measurement

Several devices for in-situ viscosity measurement have been proposed, however many devices require submersion of the device within the engineering system. This approach is adopted by the vibrating wire method, whereby the resistance to wire motion is related to viscosity (Schlumberger 2014), which can achieve viscosity measurement between 0.2 and 300 mPa.s with an accuracy of $\pm 10\%$. Capacitance methods which measure the ability of the oil to conduct a charge have also been developed by Shell^{TM}, with an accuracy of $\pm 1.5\%$ (Shell 2012). This method however requires a fluid reservoir to be created within the device itself, limiting the technique to bulk viscosity measurement only.

Optical in-situ viscosity measurements includes the use of a viscosity sensing fluorescent dye with molecular rotors, whose fluorescence intensity increases with viscosity permitting high spatial resolution of viscosity within a contact when an optical window is present (Morgan & Wong 2017). While a highly detailed viscosity profile can be achieved using this technique,

the system requires a transparent window to be present at the contact after the introduction of fluorescent molecules into a lubricant. The technique however has been found to measure the viscosity range between 1 to 100 Pa.s of very thin films, down to 170 nm at pressures between 200 MPa and 1.2 GPa. Ultrasonic means of viscosity measurement require no such modification to a component, and so do not specifically require the design and manufacture of a bespoke full scale rig to permit reliable measurement. Direct application to a real engineering system is most suited to the technique, as instrumentation is a fast process with potentially minimal costs.

2.4. Ultrasonic theory

Sound takes the form of pressure waves which travel through media. The human eardrum consists of a diaphragm which vibrates in response to these pressure pulses, acting as a biological transducer to convert pressure pulses into electrical signals which our brains can process. The fundamentals of human hearing show some similarity to the acquisition of ultrasound presented here, using piezoelectric elements to convert ultrasonic waves into an electric current. Audible sound waves are defined as those which lie below ~20 kHz, above this the wave becomes ultrasonic due to the frequency at which is oscillates, the sound spectrum is shown in Figure 2-16.

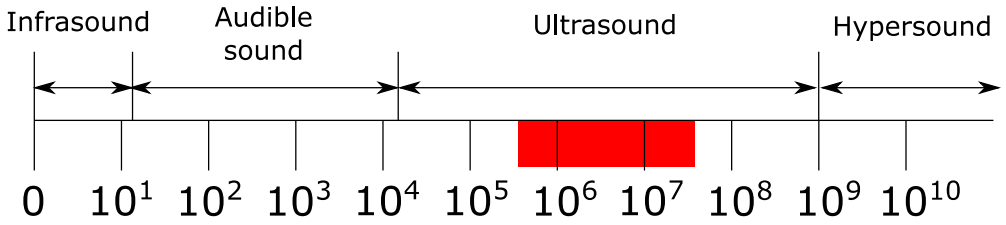

Figure 2-16: Schematic diagram of an acousic spectra in Hz.

The penetrative and reflective nature of ultrasonic waves has led to its use in the natural world as a navigation, communication and hunting device by bats, dolphins and whales, and amphibians. Ultrasound is thus capable of locating submarines or ships at sea, crack detection in solid vessels and most recently as a measurement device to measure oil film thickness, contact pressure, surface wear and lubricant properties (Krautkrämer & Krautkrämer 1968; Dwyer-Joyce & Drinkwater 2003; Dwyer-Joyce 2005; Pau et al. 2000) in the field of Non Destructive Testing (NDT).

Ultrasound is not able to propagate through a vacuum as sound requires an ordered transmission of structured kinetic energy from particle to particle through the deflection of electrostatic bonds. Propagation occurs through the transmission of kinetic energy to adjacent particles within media, which in turn transmit the energy to their adjacent counterparts, resulting in a wave of kinetic deformation; the extent of which is dependent upon the stiffness of the bonds between the particles. Due to the finite stiffness of the bonds kinetic energy is not transmitted instantaneously, but rather as a rate of propagation dependent upon the material and mode in which sound exists. Ultrasonic waves produce elastic deformations thus no permanent change is made to the material, making the technique favourable for engineering applications as the method is non-destructive and so does not interfere with the material in

which it measures. Ultrasonic waves can propagate in a series of modes depending on the source and type of wave.

Ultrasonic waves are composed of discrete particles of matter which oscillate; the path in which the oscillation takes can be characterized by a sinusoidal wave. If all particles in the first plane of the substrate are excited in unison with a sinusoidal oscillation, all particles in the plane will oscillate at the same amplitude, and frequency (Krautkrämer & Krautkrämer 1968).

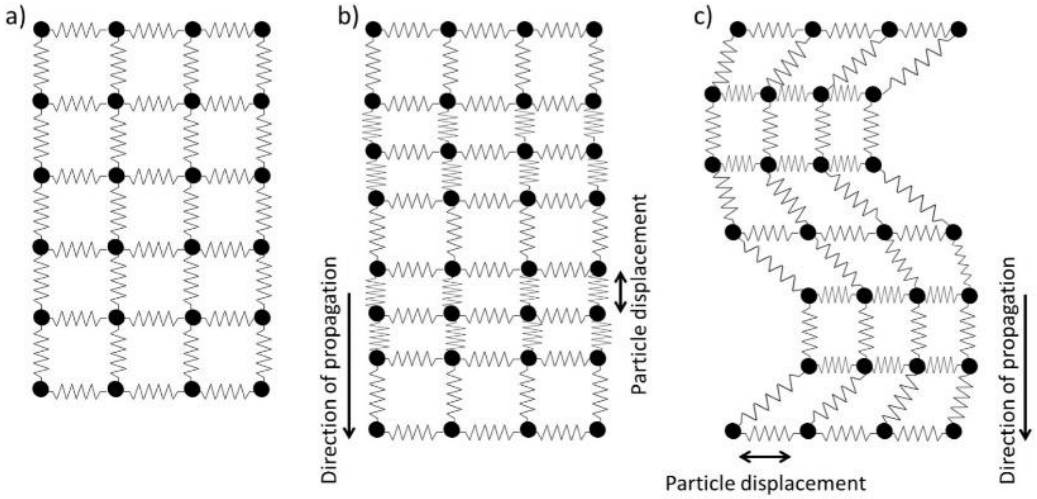

Figure 2-17: A schematic diagram of a) a material lattice at rest, b) longitudinal bulk wave propagation, c) shear bulk wave propagation. Image taken from (Schirru 2016).

If the forces between the particles were rigid, all the particles would be subject to the same phase of oscillation. The motion described here is known as a longitudinal or compression wave as the direction of propagation is parallel to the direction of particle motion, shown schematically in Figure 2-17b. Longitudinal bulk waves are thus primarily used for distance measurements, such as film thickness, component thickness, wear measurements and crack detection.

A shear or transverse bulk wave displaces particles perpendicular to the direction of propagation, as shown in Figure 2-17c. While longitudinal waves can be supported through solids, liquids and gasses, a shear wave cannot be maintained within a liquid or gas. Shear waves can however be transmitted through solid structures, acting to produce a shear motion at the surface of a component. The ability of a liquid to support shear waves however increases with viscosity, hence ultrasonic loss into a liquid increases with increasing viscosity (Greenwood & Bamberger 2002). This is the fundamental principle which governs shear wave viscometry. The work presented here concerns ultrasonic liquid viscosity measurement, therefore bulk shear waves are used throughout.

Ultrasonic surface waves have also been utilised for viscometry methods as a greater proportion of the wave exists at the interface of the liquid (Kiełczynski et al. 2008). Surface waves travel along the surface of a solid component, and if the surface is in contact with a liquid media, the liquid properties determine how the wave travels.

2.4.1. The Piezoelectric Effect

The piezoelectric effect is a material property governing the ability of the material to generate an electrical charge in response to a mechanical stress, an effect discovered in 1880 by the Curie brothers. The reverse effect whereby a material when placed between two electrodes changes form if an electrical field is applied was later discovered in 1881. The first is known as the direct piezoelectric effect, and is used when capturing a signal, whereas the latter is known as the indirect piezoelectric effect, used during signal generation.

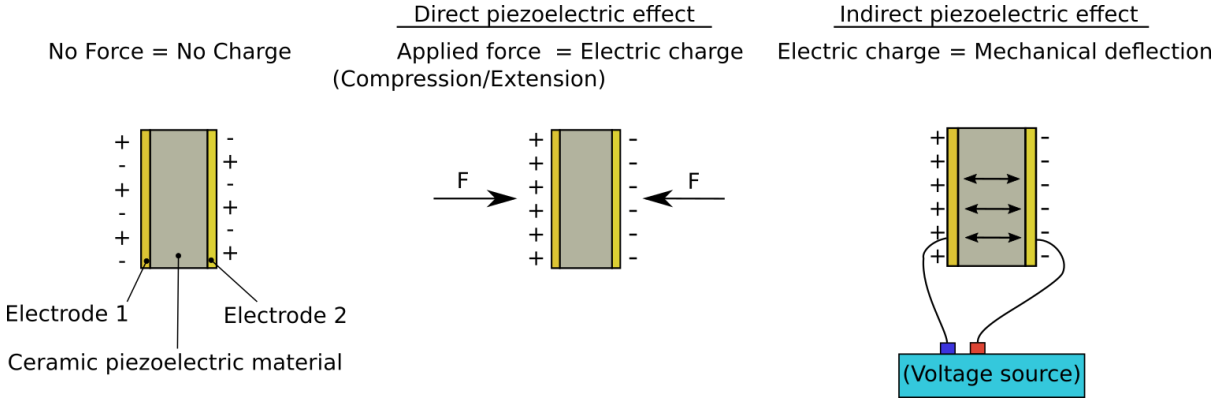

Figure 2-18: The piezoelectric effect.

It is this behaviour that permits the production of mechanical pressures, deformations and oscillations, along with the acquisition, of ultrasonic waves (Krautkrämer & Krautkrämer 1968). Piezoelectric crystals are both sensing elements and transducers as they permit the exchange of energy from one form into another, i.e. electrical to mechanical and vice versa. Ultrasonic waves are high frequency pressure pulses which can be produced when a piezoelectric material deflects in contact with a substrate in which the sound wave can propagate through. The effect can be seen in a number of materials, although the most commonly used piezoelectric material for ultrasonic applications is Lead-Zirconate Titanate (PZT) ($Pb(Zr_{0.52}Ti_{0.48})O_3$), a perovskite ceramic which has optimal ferroelectric properties.

The perovskite structure of the piezoelectric material permits the production of ultrasound from piezoelectric materials. The perovskite structure is composed of a Body Centred Cubic (BCC) lattice formation of cathodes and anodes. The ion in the centre of the BCC when considering PZT, is a titanium atom with a 4+ charge, this is surrounded in a cubic formation by oxygen atoms which have a 2- charge, which in turn is encased in lead atoms with a 2+ charge, as seen in Figure 2-19.

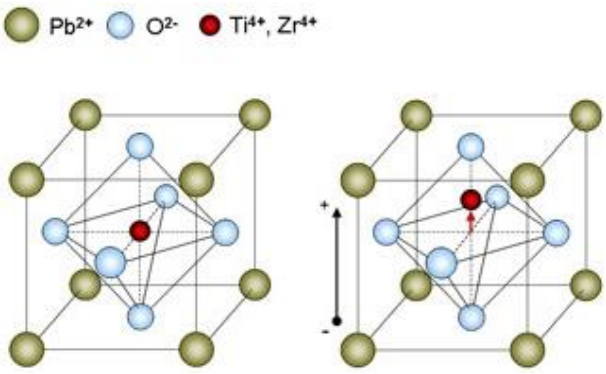

Figure 2-19: Perovskite structure of a piezoelectric PZT. Image adapted from:(YTC America Inc 2008)

Two plates permit the electrification of the piezoelectric and thus the polarization of the ceramic which in turn produces a deflection due to the polarisation and movement of the centre titanium atom. Piezoelectric transducers comprise a dielectric composition, in which two electrically conductive plates sandwich a capacitor in the form of the PZT ceramic. When the accumulative effect of many units is considered, a physical mechanical deflection of the material is produced in response to an electric field applied to the electrodes. It is the periodicity of the alternating current which is used to define the frequency of the deflection, and such, of the ultrasonic wave.

Expansion or contraction of a PZT can be controlled by the application of an electric field via the use of an Arbitrary Function Generator (AFG). This apparatus can be used to apply a voltage to a piezoelectric material in order to produce a deflection of the crystal, high frequency voltage pulses from an AFG are therefore used to generate ultrasonic signals. In order to capture ultrasonic signals, the voltage produced by a PZT in response to a deflection must be digitised, this is the function of the oscilloscope.

2.4.2. Piezoelectric Transducers

Many types of commercial transducers are readily available which have been optimised for a particular application, such as crack detection, or acoustic emission, produced with particular bandwidth, and frequencies tailored to their proposed application. Commercial transducers contain piezoelectric materials which are backed with acoustically dampening material in order to reduce the natural resonant oscillation which continues to vibrate after the applied voltage. This helps to reduce low frequency noise from the element, while also acting to secure the electrical connection between the piezoelectric element and wires. Commercial transducers are multiple use as they are coupled to the specimen using a solid or liquid couplant in order to permit ultrasonic transmission into the material. Many configurations of commercial transducers are available, capable of producing different polarities and waves, such as standard bulk shear and longitudinal waves or surface waves.

Most commercial transducers are often susceptible to damage at high temperatures, thus are only suitable for applications at room temperature. Real engineering components may reach hundreds of degrees centigrade during operation, so specialised transducers are required for

high temperature systems. Work in this report involves the use of bare piezoelectric transducers as viscosity measurements often require a demonstration of measurement feasibility at a large range of temperatures.

Bare elements are those which consist of only the piezoelectric crystal, often with a conductive coating. The transducers are versatile, small and robust if instrumented correctly, and so are used throughout this work. The transducers are available in a range of piezoelectric materials, principally categorised into 'soft' and 'hard', and are available in a variety of shapes and polarities. Operating limits of transducers are governed by the curie temperature of the piezoelectric element. At this point, the electrical polling of the material becomes unstable making signal generation difficult, however for ceramic based elements this point can exceed a few hundred degrees Celsius. Figure 2-20a emphasises the small size of the transducers and ease of instrumentation which can be achieved using these bare piezoelectric elements shown in Figure 2-20b and c. Transducer instrumentation will be covered in Section 3.3.2.

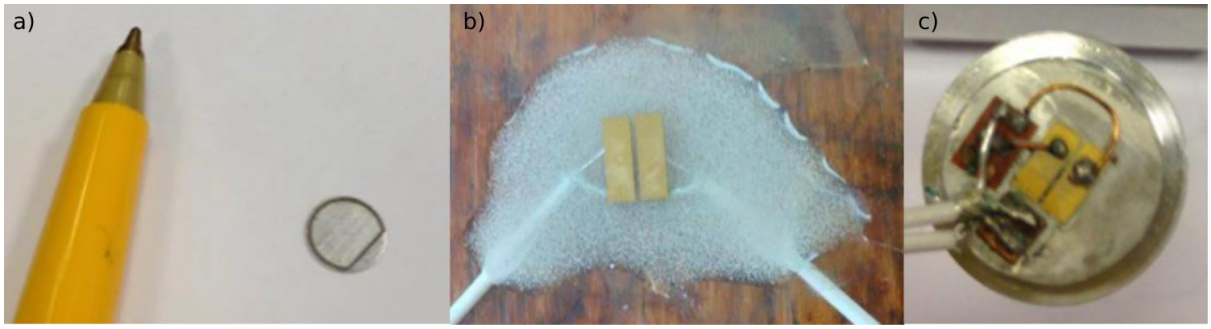

Figure 2-20: Bare piezoelectric materials showing a) a longitudinal transducer b) a pair of shear transducers covered in epoxy, and c) an instrumented aluminium component with two shear transducers.

It is the thickness and shape of the piezoelectric which principally governs the operational frequency of the transducer. The aspect ratio is a ratio of the width to the height of a geometry. The aspect ratio of transducers which operate in the shear mode is often around 1:2.5, (the length is 2.5 times the height of the transducer) although it mainly the material thickness which determines the resonant frequency of the element.

2.4.3. Reflection Coefficient

When an ultrasonic wave meets a boundary between two components a proportion of the wave is reflected, and a portion of the wave continues to travel in the same direction through into the next material. This mechanism is however only possible when the interface is perpendicular to the propagating wave. This action can be seen in Figure 2-21a where the wave initially travels from point (A) to point (B) at the perfectly bonded interface where some of the wave is reflected back in the same direction of the incident wave to point (A), and some propagates into the connected interface to point (C). When this is normalised to the incident wave amplitude, the proportion reflected is known as the reflection coefficient, R. The reflection coefficient is dependent on the acoustic impedance, z, difference between the materials either side of the

interface. z, is a quantity used to define how easily an ultrasonic wave can travel from one material to another.

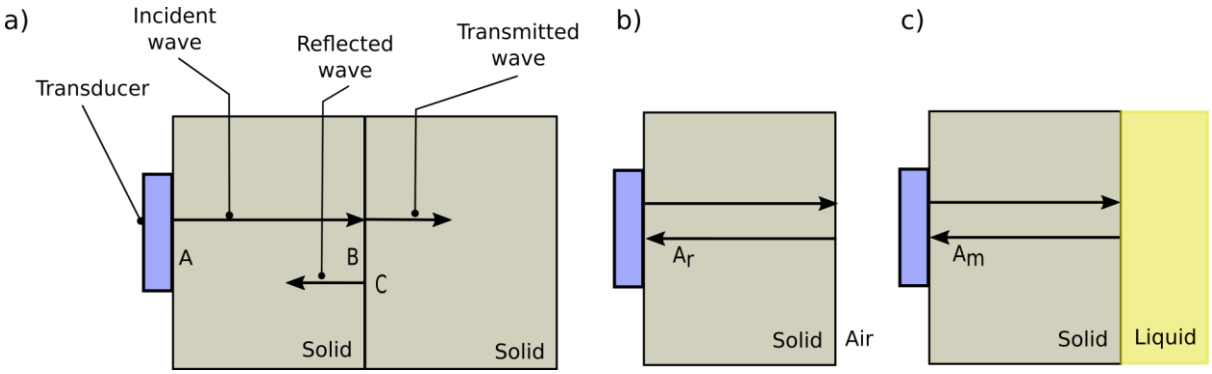

Figure 2-21: a) Wave propagation and reflection paths at an interface. b) Reference condition, c) Measurement condition.

The reflection coefficient can be expressed by Equation 2-13 for R between component 1 and 2 in a perfectly bonded case. Where z_2 is the acoustic impedance of the second material in which the wave becomes incident, and z_1 the acoustic impedance of the first material in which the wave propagates through.

$$R = \frac{z_2 - z_1}{z_2 + z_1} \qquad \text{Equation 2-13}$$

It is therefore evident that R remains between values of 1 and 0. The physical nature of this interaction is seen in the amplitude of the 'measurement' and 'reference' signals, hence the reflection coefficient can also be defined by,

$$R = \frac{A_m}{A_r} \qquad \text{Equation 2-14}$$

where A_m is the amplitude of the solid-liquid (measurement) signal, and A_r the solid-air (reference) signal, as shown in Figure 2-21 b and c. When an ultrasonic shear wave meets a solid liquid boundary and the wave is reflected back towards the transducer, the angle at which it does so is determined by Snell's law of reflection shown in Equation 2-15.

$$\frac{c_i}{c_{r/t}} = \frac{sin\theta_i}{sin\theta_{r/t}} \qquad \text{Equation 2-15}$$

This is where c_i is the speed of sound of the incident wave, $c_{r/t}$ is the speed of sound in the media in which transmission or reflection occurs, $sin\theta_i$ is the sine of the angle of incidence and $sin\theta_{r/t}$ is the angle at which transmission or reflection occurs. The reflection coefficient, and phase (which will be addressed later in this chapter) will be determined, as shown in Equation 2-13 and Equation 2-15 by the difference between the acoustic properties of the materials.

2.4.4. Speed of Sound

The stiffness of inter-particle electrostatic bonds within a solid will determine the rate of propagation of an ultrasonic bulk wave. Speed of sound reduces with increasing temperature, this has a much greater influence in liquids and gasses as the variation is much lower in solids. Pressure also influences speed of sound, while much less so in solids, pressure changes in liquids can affect the speed of sound considerably. In order to experimentally determine speed of sound, a 'time-of-flight' method can be used for a material of a known thickness. By observation of the time, t taken for a sound wave to propagate through the body, the speed of sound c can be determined by the following velocity equation. When a pulse echo measurement is assumed, twice the material length, L must be considered as the ultrasonic wave must travel firstly through the material and then back to the ultrasonic emitter receiver.

$$c = \frac{2L}{t} \qquad \text{Equation 2-16}$$

The speed of sound then permits the calculation of ultrasonic wavelength, λ at a given frequency, f.

$$\lambda = \frac{c}{f} \qquad \text{Equation 2-17}$$

The speed of sound is a function of a materials elastic properties, specifically the bulk modulus, B and the density of the material, ρ. Intermolecular bond stiffness of a solid determines bulk modulus, which is effectively a measure of how quickly particles return to a state of equilibrium once strained. Sound waves can therefore travel faster through materials which can return to equilibrium quicker, thus the speed of sound in a solid with a higher elastic modulus, such as steel can travel faster than a sound wave in rubber, which has a lower elastic modulus, the relationship of which is shown in Equation 2-18 (Krautkrämer & Krautkrämer 1968).

$$c = \sqrt{\frac{B}{\rho}} \qquad \text{Equation 2-18}$$

Materials with larger molecules transmit sound slower as mechanical wave propagation requires more energy to vibrate the atoms. As temperature influences the speed of sound, the acoustic impedance is also affected, an influence which will be considered in Section 7.3.2.

2.4.5. Solid Acoustic Impedance

Acoustic impedance of a solid z_s is by definition the product of the density ρ and speed of sound c, of a material. The acoustic impedance is a relative value, with units of Rayl, or Pa.s/m^{-3}. This physical parameter determines how ultrasonic waves behave at an interface. The acoustic impedance of solid materials, z_s (z_{PZT} Piezoelectric acoustic impedance, and z_{Al} aluminium acoustic impedance) are calculated using the shear speed of sound in the solid, c_s m/s and density, ρ_s kg/m^3 of the respective material using Equation 2-19.

$$z_s = c_s \rho_s \qquad \text{Equation 2-19}$$

The acoustic impedance of solid materials is a complex due to acoustic losses, however for the purposes of this work, the quantity will be defined by real quantities only. If two materials have similar acoustic impedance, sound can transmit easily between them. If the materials show acoustic differences, they pose an obstruction to the sound wave at the boundary, reducing the proportion of sound which may be transmitted.

2.4.6. Liquid Acoustic Impedance

Unlike solid acoustic impedance, the acoustic impedance of a liquid, z_l is a complex quantity dependent on the complex shear modulus of the liquid, G where ρ_l is the density of oil.

$$z_l = \sqrt{\rho_l G} \qquad \text{Equation 2-20}$$

G is a complex variable, where G' is the real part known as the storage modulus and, G'' is the complex part known as the loss modulus:

$$G = G' + iG''. \qquad \text{Equation 2-21}$$

For a Newtonian liquid, relaxation effects are negligible, thus the storage modulus is zero, $(G' = 0)$ and the loss modulus is the product of the angular frequency, ω $(\omega = 2\pi f)$ and viscosity, η of the liquid $(G'' = \omega\eta)$. The acoustic impedance of a Newtonian fluid can then be expressed by Equation 2-22 for frequencies used here (Franco et al. 2010).

$$z_l = \sqrt{i\rho_l\omega\eta} \qquad \text{Equation 2-22}$$

z_l is therefore a function of frequency, as seen in Figure 2-22 below using Equation 2-22. The acoustic impedance of the liquid can be used to relate viscosity to the ultrasonic response.

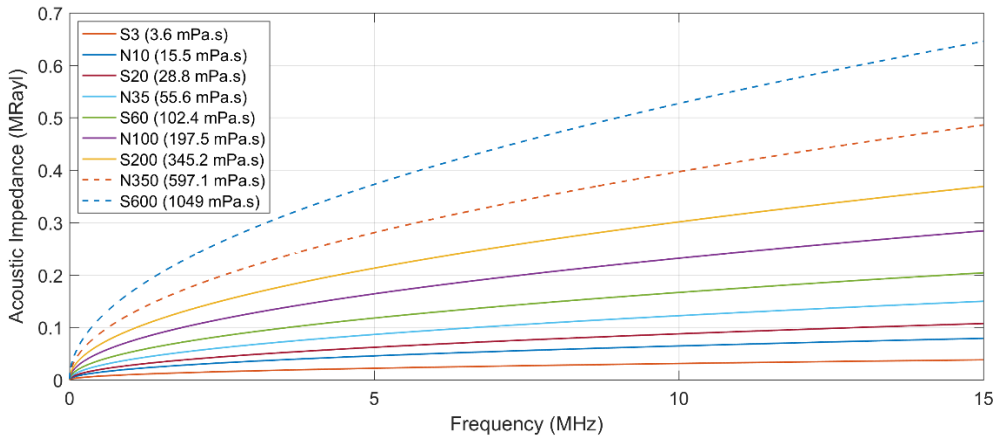

Figure 2-22: Acoustic impedance of different viscosity liquid variation with frequency.

2.4.7. Attenuation

As an ultrasonic wave passes through a material, it will be attenuated as the distance travelled increases, ultimately decaying exponentially to zero amplitude. There are two types of attenuation, the first is vis-absorption, this is the attenuation due to anisotropy within the material resulting in wave scattering and splitting at grain boundaries. The second type of

attenuation is pure attenuation which is the direct conversion of sound energy into heat (Krautkrämer & Krautkrämer 1968).

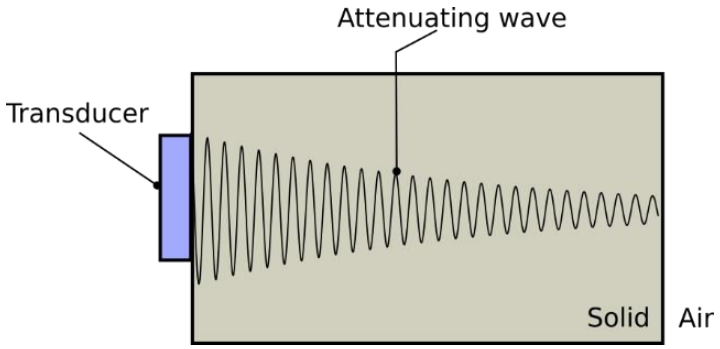

Figure 2-23: Schematic illustration of an ultrasonic wave attenuating within a component.

Higher frequency ultrasonic waves attenuate more readily than low frequency ultrasonic waves as rapid oscillations seen at higher frequencies lose more energy than low frequency oscillations. The attenuation coefficient, α is a material property expressed in terms of Nepers per meter (Np/m), however a more commonly used unit is dB, for which the relationship can be seen in Equation 2-23.

$$1Np = 20/\ln 10\ dB \qquad \text{Equation 2-23}$$

The attenuation coefficient of a material determines the difference between the initial amplitude, A_0, and the amplitude of the wave after travelling through a material of length L, this relationship is shown in Equation 2-24.

$$A = A_0 e^{-\alpha L} \qquad \text{Equation 2-24}$$

2.4.8. Phase

The phase shift of a wave refers to the cycle shift of the reflected wave in comparison to the incident wave. If the phase shift at an interface is zero or π, the reflected wave will be in phase with the incident wave. A phase shift at a value which is not a multiple of π would produce a reflected wave which is out of phase with the incident wave. Figure 2-24 shows a schematic of an incident wave and reflected wave which undergoes a phase shift of $\frac{\pi}{2}$ at the solid-air interface.

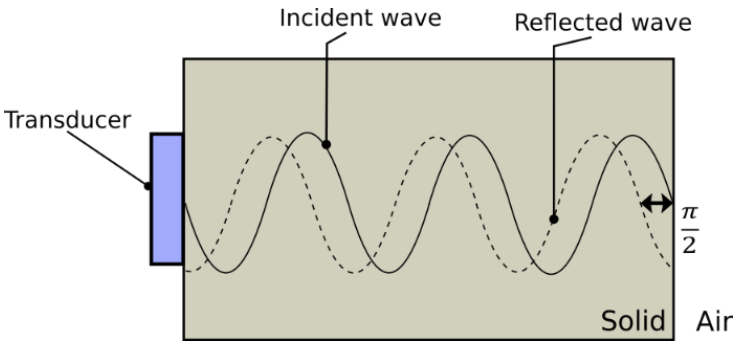

Figure 2-24: Schematic illustration of the effect of phase shift.

The phase, ϕ and magnitude R of a wave are intrinsically linked, demonstrated in Equation 2-25 where R^* is the complex reflection coefficient.

$$R^* = |R|e^{i\phi} = |R|\cos(\phi) + isin(\phi) \qquad \text{Equation 2-25}$$

The phase at the solid-liquid interface can be calculated using Equation 2-26 if R of the wave is known (Schirru & Dwyer-Joyce 2015).

$$\phi = 0.5\, acos\left(1 - \frac{(1 - R^2)}{(2 + R^2)}\right) \qquad \text{Equation 2-26}$$

When considering a shear wave reflection between a solid-liquid interface, the acoustic mismatch is great, meaning the effect of viscosity is insignificant compared to that of the difference between the solid-liquid acoustic impedance differences. The phase of the wave at the solid-transducer interface, ϕ' can be calculated using Equation 2-27, where R' is the reflection coefficient at the transducer interface (Schirru & Dwyer-Joyce 2015).

$$\phi' = 0.5\, acos\left(1 - \frac{(1 - R'^2)}{(2 + R'^2)}\right) \qquad \text{Equation 2-27}$$

As liquids cannot sustain mechanical shear waves, little phase shift is expected at a solid-liquid boundary, however if a layer of intermediate acoustic impedance material was to be placed between the solid and liquid, a phase shift would be expected.

2.4.9. Ultrasonic Viscosity Measurement Principles

As previously discussed, R^* is dependent on the conditions at the interface when an ultrasonic pulsed (pulsed ultrasonic methods use the reflection from a single sound wave to produce a measurement) method is adopted. This is described in Equation 2-28 when an ultrasonic wave is propagating from a solid into a liquid interface.

$$R^* = \frac{z_l - z_s}{z_l + z_s} \qquad \text{Equation 2-28}$$

The influence of viscosity on the real and complex reflection coefficient is calculated through the determination of the acoustic impedance of the liquid. Thus by substituting Equation

2-19and Equation 2-22 into Equation 2-28 the viscosity can be found from the R^* assuming the liquid is an infinite entity and of entirely Newtonian behaviour.

$$R^* = \frac{\sqrt{i\rho_l\omega\eta} - \rho_s c_s}{\sqrt{i\rho_l\omega\eta} + \rho_s c_s} \qquad \text{Equation 2-29}$$

Viscosity measurement is also dependent on the solid component, higher values of z_s lead to reduced viscosity measurement capability. The acoustic impedance of steel, aluminium and acrylic are 25.1, 8.1, and 1.3 MRayl respectively; by comparing the expected R from each of these materials using Equation 2-29 (where $R = |R^*|$) the hinderance of acoustic mismatch between the solid and liquid is demonstrated, as seen in Figure 2-25. As frequency increases R tends to zero, however the rate at which this does so is dependent on z_s.

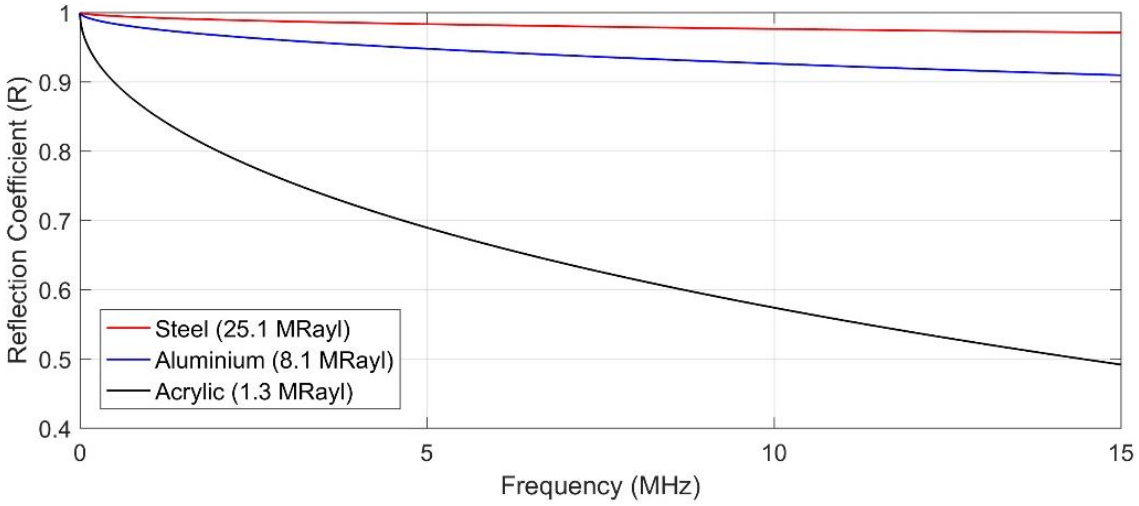

Figure 2-25: Mathematical prediction of R expected from an S200 (345.2 mPa.s) oil at 25℃.

The acoustic impedance of liquids is frequency dependent, hence producing a frequency dependent reflection coefficient for all materials. The acoustic impedance of the S200 oil used here is 0.00095 MRayl at 100 Hz and 0.36 MRayl at 15 MHz. The greater the difference between the liquid and solid acoustic impedance, the higher the reflection coefficient remains.

2.5. Ultrasonic Rheology Review

2.5.1. Ultrasonic Viscosity Measurement

Ultrasonic viscosity measurement has been in use since the 1950's and many developments to improve the performance of such techniques have been successful. Mason et al. (Mason et al. 1949) was the first to highlight the relationship between the shear impedance of liquid and the phase change of ultrasonic reflections. The technique required a PZT ceramic to be in direct contact with the liquid in order to deduce liquid measurements. Since then, ultrasonic viscometry developments have focussed on a number of areas, all of which have individually contributed to making in-situ measurement more accessible and useful as an engineering tool.

Following the pioneering work of Mason et al. (Mason et al. 1949), Rich and Roth (Roth & Rich 1953), and Woodward et al. (Woodward 1953) instrumented components with sensors,

being the first to produce viscosity measurements from a counter surface. However the technique still required liquid immersion of the device. The longitudinal pulsed wave Doppler effect was first developed in 1947 by Carl Eckart, (Eckart 1948), but the technique was not used for viscosity measurement of a liquid inside an enclosed chamber until 1991 by Hertz et al (Hertz et al. 1991). The technique uses liquid velocity and density measurement to predict the viscosity of dynamic liquids.

In order to improve viscosity measurement, both longitudinal and shear polarised ultrasonic waves were used in series through a Perspex wedge to create surface waves. Ultrasonic shear waves incident upon a fluid at oblique angles induce plane wave conversion to surface waves (Sheen et al. 1997).Ultrasonic wave guides (Turton et al. 2005) have also been developed to enhance the effect of surface waves. Viscosity measurement using surface waves increases the contact area between the ultrasonic wave and the fluid, where traditional pulsed techniques permit only a few microns of penetration into the fluid at a single contact point. This technique would be suitable for large volume viscosity measurements, where the viscosity over the surface area of the wave guide is uniform.

Several surface wave modes exist although the two most widely known are Rayleigh (Rayleigh 1885) and Lamb waves (Lamb 1917). Rayleigh waves travel along the surface of a component in a similar fashion to longitudinal waves, where particle motion is produced in elliptical displacement in the vertical plane parallel to the direction of propagation. Whereas Lamb waves create elliptical particle displacement horizontal to that of the direction of propagation. Kiełczyński et al. used Bleustein-gulyaev (B-G) surface waves to measure viscosity of fluids at high pressures above 1 GPa (Kiełczynski et al. 2008). The technique required the immersion of a piezoelectric ceramic waveguide with a transducer attached to a plane face to produce the surface waves. This permitted multiple reflections between opposite surfaces. This work demonstrated how liquid sensitivity can be improved by the use of surface shear horizontal waves although the technique still required direct contact between the piezoelectric and the liquid.

Love mode surface waves can be used to measure the density viscosity product, using a polyimide ML as a wave guide through which the ultrasonic wave propagates (Turton et al. 2005). Further developments such as the measurement of multiple reflections (Greenwood et al. 2006) from the measurement surface to more recently, the use of a chirp (Schirru et al. 2015) to excite the resonance of the component have also contributed to increasing interest in ultrasonic viscometry devices. A summary of key ultrasonic viscosity studies can be found in Table 2-3.

Table 2-3: A chronological Table of key advances in ultrasonic viscosity measurement.

Date and Author Reference	**Ultrasonic wave mode and method**	**Technique**	**Ultrasonic Frequency**	**Viscosity Range (mPa.s)**
(Mason et al. 1949)	Longitudinal Pulsed	Piezoelectric direct contact- Shear reflectance	4.5-60 MHz	55 to 160,000
(Barlow & Lamb 1959)	Shear Pulsed	Piezoelectric direct contact.	6-78 MHz	300 to 26100
(Woodward 1953)	Shear Pulsed	Vibrating plate-plate immersion within liquid.	800 Hz	0.1 to 100,000
(Roth & Rich 1953)	Shear Pulsed	Magnetostrictive strip-Resonance.	10-150 kHz	0 to 50,000
(Hertz et al. 1991)	Longitudinal Pulsed	Doppler shift velocity measurement.	10.4 MHz	1 to 1200
(Sheen et al. 1997)	Longitudinal and Shear Pulsed	Perspex wedge, incident angle.	1-10 MHz	1 to 30
(Turton et al. 2005)	Love Mode Surface Waves Pulsed	Polyimide wave guided Love-mode surface wave.	121-124.5 MHz	0 to 7
(Greenwood et al. 2006)	Shear Pulsed	Fused single wedge-multiple reflection measurement.	14 MHz	1 to 934
(Kiełczynski et al. 2008)	Shear horizontal surface waves Pulsed	Wave guide-Normalised viscosity is measured while the actual viscosity is unknown.	2 MHz	0 to 25,000
(Waszczuk et al. 2011)	Longitudinal Pulsed	Tuning fork placed in liquid.	25 to 32 kHz	5 to 16
(Rabani et al. 2011)	Shear Pulse	Torsional waveguide probe.	525-725 kHz	0.9 to 1000
(Schirru et al. 2015) (Schirru & Dwyer-Joyce 2015)	Shear Pulsed	Polyimide ML. Acoustic resonant layer between metal and liquid.	1-15 MHz	0.01 to 1500
(Franco & Buiochi 2019)	Longitudinal wave mode conversion to Shear pulsed	Aluminium wedge wave guide.	0.1-10 MHz	10-1400

Ultrasonic techniques to measure viscosity in-situ have been demonstrated by a number of authors using a variety of ultrasonic methods which each present a measurable range of viscosity values. A typical automotive engine oil ranges between 80 and 5 mPa.s from a cold engine to fully warmed up. Schirru et al. (Schirru et al. 2015) demonstrated successful ultrasonic viscosity measurement in a journal bearing using a pulsed method. While Greenwood et al. (Greenwood et al. 2006) uses a multiple reflection method to increase viscosity measurement sensitivity. While many techniques use a pulsed method, little progress on the use of continuous waves for ultrasonic viscosity measurement have been reported.

This literature review will now be directed towards the use of standing waves, multiple reflections and matching layers to gain a deeper understating into their function within ultrasonic viscometry.

2.5.2. Standing Waves

While many ultrasonic techniques use a more conventional pulsed method, whereby single ultrasonic reflections are analysed, a standing wave is proposed as a measurement method when using a continuous wave. A standing wave is a vibration of a material, in which some points remain stationary, known as nodes in between points which fluctuate between a maximum and minima, known as antinodes. These waves can be explained via the mechanisms of both construction and destruction of ultrasonic waves. By considering sound as a sine wave, Figure 2-26 illustrates the relative position of waves which construct and those which destruct within a solid component.

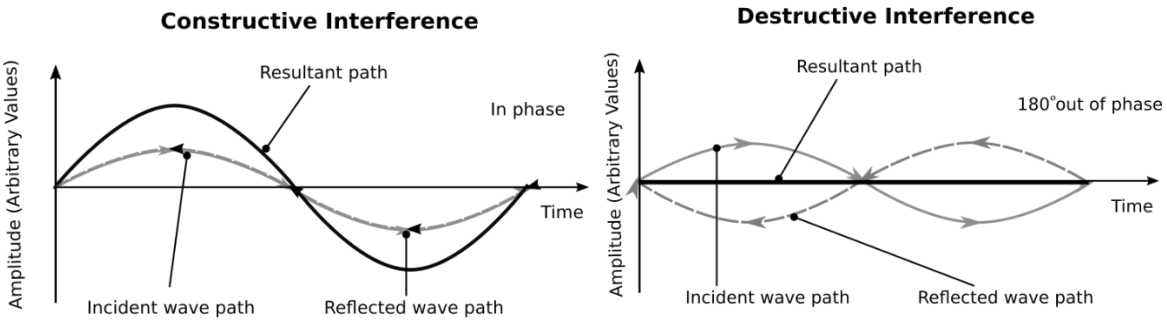

Figure 2-26: Schematic illustrations of constructive and destructive interference.

It is evident that if the reflected wave path travels in the same phase as the incident wave, the two waves constructively interfere. The resulting wave amplitude is the sum of the incident and reflected wave amplitudes. If the incident wave at this frequency is continuously generated, a standing wave is produced. Alternatively, if the reflected wave undergoes a 180° phase change, the wave is reflected in the opposite phase to the incident wave and so destruct, resulting in no resultant wave amplitude.

Standing waves with mixed frequencies in the literature have been named pseudo-standing waves, but the wave mode can also be described as a ‘quasi-static’ standing wave. By considering the movement of a single particle in a structure which has two waves of different

amplitude, frequency and direction of propagation, the simultaneous action of both waves can be observed, shown in Figure 2-27.

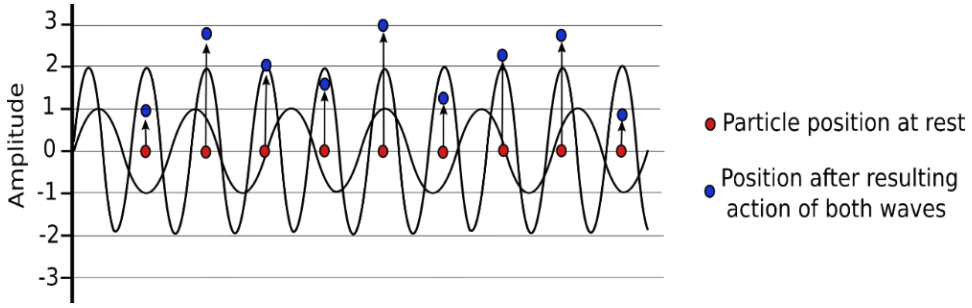

Figure 2-27: The effect of particle displacement from different frequency, amplitude and phase ultrasonic waves.

Assuming the combined stress of the two waves does not exceed the elastic limit of the solid, the motions of the waves can be added vectorially so the resulting action on the particle is composed of the sum of motions which the particle would experience by each wave alone. The waves of different frequencies are unchanged by the presence of each other, so their frequency amplitude and phase do not alter as a result of their interaction.

By simply replicating this wave arrangement with two waves of identical frequency and amplitude, but opposite direction of propagation; superposition of the waves creates a standing wave particle oscillation. In Figure 2-28 the waves travelling in opposite directions combine to form one wave where the amplitude is the sum of wave 1 (red) and 2 (blue). By considering five conditions of the same frequency wave propagating in opposite directions travelling a progressively shorter distance, or time, the degree of construction or destruction can be visualised using a schematic diagram in Figure 2-28. The resulting behaviour shown in Figure 2-28f can only form if both waves are however continuously generated at their source point.

Figure 2-28f indicates the motion of a standing wave as a series of nodes, which are points in the structure which remain at a constant state of rest, and antinodes, which have a maximum constant amplitude located between the nodes which fluctuate between extreme values. The standing wave amplitude varies as a function of the degree of interference, i.e. the waves which are fully constructive have a larger standing wave amplitude, such as Figure 2-28a and e, than those which show partial construction, Figure 2-28b and d.

The amplitude of the waves which half construct have half the standing wave amplitude than those which completely destruct. Waves which are 180° out of phase show complete destructive behaviour, such as those seen in Figure 2-28c, and thus result in point 3 in Figure 2-28f.

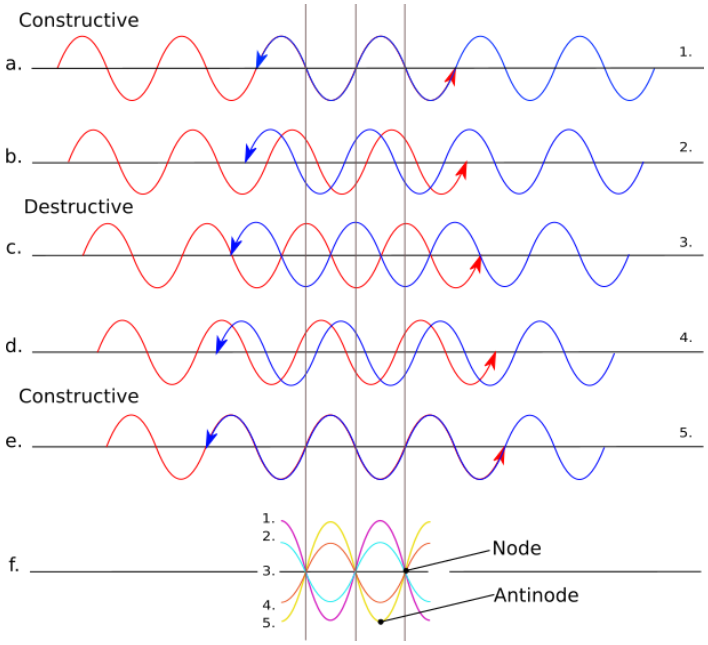

Figure 2-28: a-e) Interference of two waves to form a standing wave. f) Resulting standing wave amplitude comparison of conditions a-e.

The resonance method has been quoted as 'the oldest of all non-destructive methods' being an established practice for crack detection (Krautkrämer & Krautkrämer 1968). Thus it has long been known that very efficient comparable measurements can be made by the analysis of a resonant frequency before the application of a liquid, and again after.

Frequencies which construct to form standing waves are known as harmonics, or resonant frequencies, f_s, of the component. The amplitude of the standing wave produced within the component is dependent on the material properties, the component geometry and also the resonant frequency of the transducer, f_t. The maximum amplitude of the standing wave is present when the resonant frequencies of the transducer and component are identical.

$$f_t = f_s \qquad \text{Equation 2-30}$$

The lowest frequency at which this occurs is known as the fundamental or first harmonic, occurring where the length (L) of the component is equal to half the wavelength of the frequency, possessing the following definition in Equation 2-31.

$$2L = \lambda \qquad \text{Equation 2-31}$$

The first harmonic therefore occurs when:

$$f_s = \frac{nc_s}{2L}. \qquad \text{Equation 2-32}$$

If the driving frequency deviates from f_s, the amplitude of the standing wave will not be at a maxima, however when the driving frequency is a multiple of f_s, the waves in the component will again undergo constructive interference and a maximum will be present, shown in Figure 2-29.

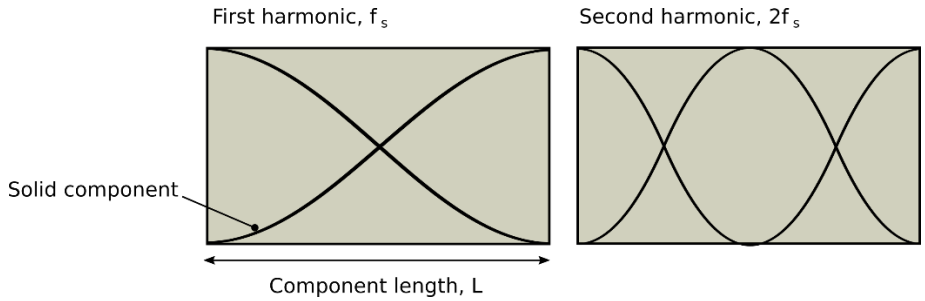

Figure 2-29: Harmonic frequencies within a solid component of the same length.

Each resonant frequency within the component will therefore be separated by the lowest resonant frequency increment at a constant rate. High frequency waves decay faster than low frequency waves, due to higher particle velocity and hence greater damping, as described in Section 2.4.7.

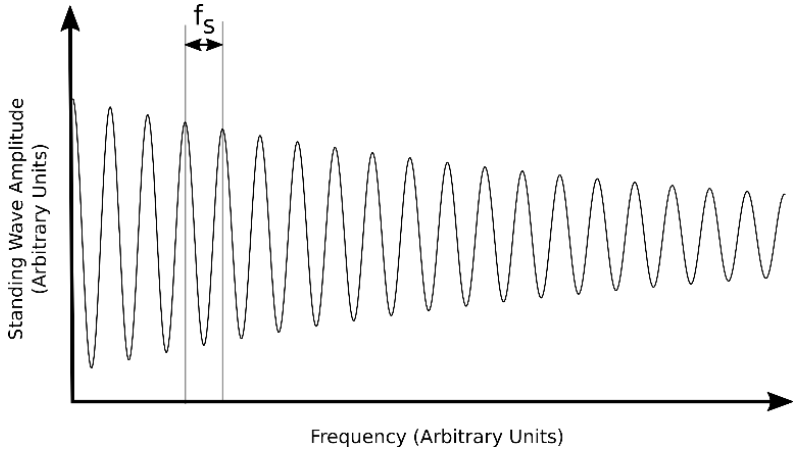

Figure 2-30: Standing wave amplitude as frequency increases.

If a transducer is directly bonded to a component, the conditions at the transducer interface would remain constant, making any changes in the resonance a result of the component geometry and boundary conditions only.

The resonance method was traditionally used for thickness measurements of metals using a device named the 'automatic sonigague' and was later used to determine mechanical properties of materials. The technique measured the influence of thickness and material properties resonant frequencies (Erwin & Rassweiler 1947). Initial measurements demonstrated the effect of the thickness of a steel rod on the resonance. The method was reported to have 'greater sensitivity, convenience and speed' compared to conventional pulsed methods. Some uncertainty surrounding the influence of continuously arriving varying frequency waves on the oscillator and the relative phase of these were expressed, although measurements were deemed highly sensitive.

Woodward et al. in 1953 was the first to use resonance as a liquid measurement method. The measurement concerned the damping effect from a vibrating plate excited by a resonating piezoelectric transducer immersed within the fluid, as a method to measure liquid properties. In the same year Rich and Roth developed a magnetostrictive strip or cylindrical rod driven by

a transducer to measure viscosity (Woodward 1953; Roth & Rich 1953). Both of these techniques compared the resonance of the plate or rod when immersed in the liquid to that when in air. These methods demonstrate the use of resonance at a single frequency to measure liquid properties. These techniques importantly paved the way for fluid measurements to be taken from the counter surface of a component, rather than direct contact between the transducer and the liquid. The method was however unsuitable for measuring viscosity of oil in-situ due to the geometry of the plate or rod, seen in Figure 2-31.

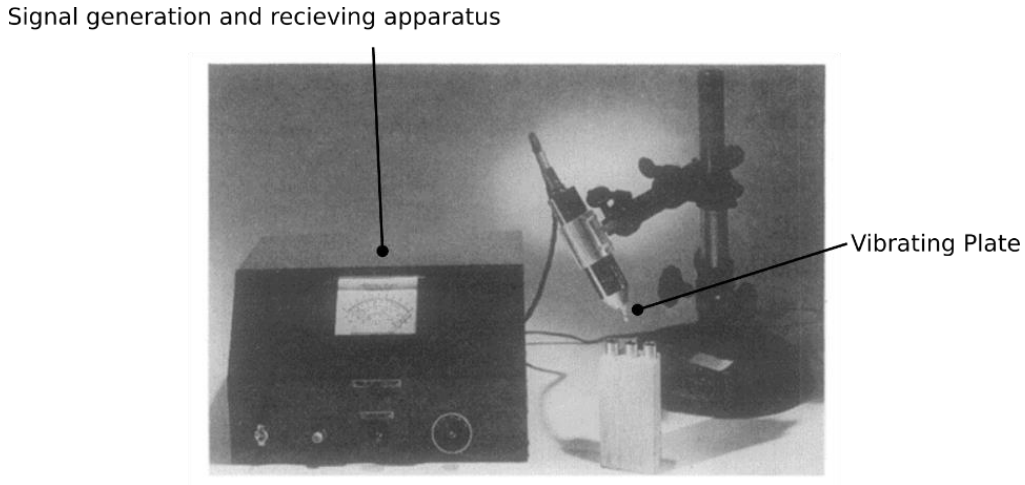

Figure 2-31: Vibrating Plate viscometer, image adapted from (Woodward 1953).

Through the correct frequency selection, permitting the construction of an incident wave with a reflected wave, a resonance in the form of a standing wave can be produced which not only has more energy than the individual input signal, but also encompasses the reflection coefficient from many reflections.

Standing waves have been used for the manipulation, accumulation and separation of particles within liquids. This application has proven to be important in the medical field for analysis and clinical diagnosis. Use of a third harmonic within micro-fluidic channels have been investigated, using two excitation frequencies at differing amplitudes and distributions. The number and position of nodes can be tuned to control the number of particles and their position within the liquid.

Acoustic methods are suitable for on-chip particle manipulation as unlike other techniques, such as optical, electrical and magnetic tweezers, acoustic waves do not interfere with the electrical or biological state in a detrimental manner (Sriphutkiat & Zhou 2017). Fine tuning of the wavelength has been used to separate cells of different sizes, achieving 100% separation efficiencies, demonstrated by (Petersson et al. 2005) who separated fat cells from red blood cells within arteries using the relative cell size differences under laminar flow.

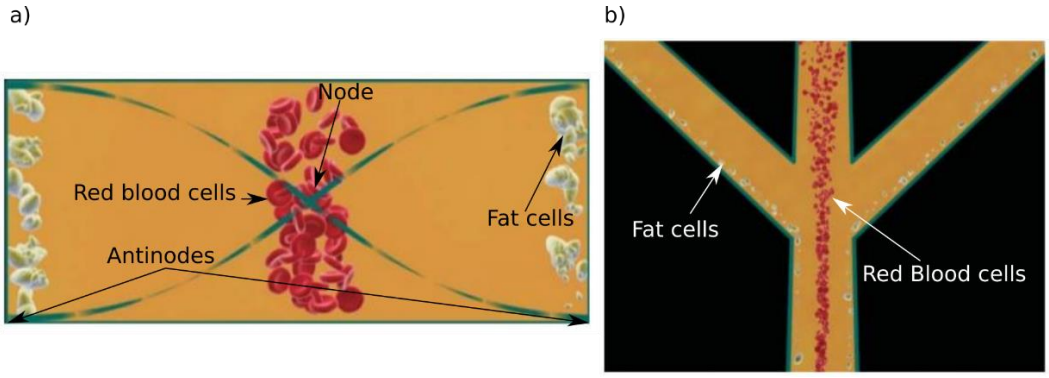

Figure 2-32: a) A cross sectional illustration of a channel with red blood cells and fat particles, separated by ultrasonic pressure. b) Particles are collected into different channels if the main channel is split into three outlets. Images adapted from (Petersson et al. 2005).

A substantial amount of research has been conducted into calculating the acoustic radiation force which could be generated using a standing wave, beginning with the experiments of (Kundt 1868). Kundt placed a cork ring on a glass tube observing the cork's movement when the tube was vibrated with a standing wave. Webber then observed cork filings move from the end to the middle of a glass tube when the tube was held horizontally and rubbed. Following this, (King 1934) first studied the force on an incompressible sphere in an inviscid liquid under the influence of a standing wave, developing highly regarded analytical solutions to this behaviour. Doinikov et al. later analysed the influence of viscosity of a liquid on the acoustic radiation force(Doinikov 1994). Viscosity is not the principal measurement parameter hence no viscosity is stated, although it is stated that the penetration depth of the wave is affected by viscosity.

2.5.3. Multiple Reflections

Several authors have documented the use of multiple reflection techniques to increase the sensitivity of ultrasonic measurements. To increase the range of measureable viscosities a multiple reflection technique was adopted by (Greenwood & Bamberger 2002). This method had a measurable viscosity range between 1 and 934 mPa.s. All reflection coefficients in this study are > 0.79, demonstrating promise for the technique as conventional single pulsed methods may produce $R > 0.9$ for this range of measurements (Greenwood & Bamberger 2002).

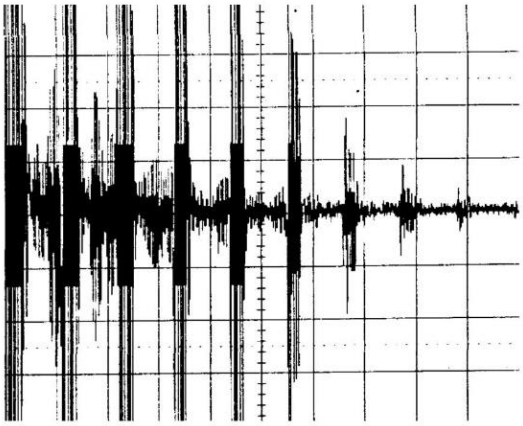

Figure 2-33: A trace taken from an oscilloscope of multiple reflections of a 2.25 MHz 10 cycle tone burst. Units in the horizontal scale are $10\mu s$ per division (Time), and 200 mV in the vertical scale per division (Amplitude). Image taken from (Greenwood & Bamberger 2002)

Following this, Greenwood analysed lubricants through a fused silica wedge (Greenwood et al. 2006), measuring 'light fluids' with viscosities ranging from 1.3 to 143 mPa.s, the technique could successfully identify the difference between solutions. The method involved measuring 28 echoes of a single shear horizontal pulse to observe multiple reflections of a single burst wave. In order to generate the power to receive each reflection, a square pulse of 80 V was used to excite the transducer, a voltage deemed reasonable in the field of NDT as many widely available ultrasonic measurement apparatus have 100 V capabilities. The number of measurable reflections reported differs between authors, Gasparoux et al. (Gasparoux et al. 2008) uses up to 10 reflections, hence the definitive number of reflections which is deemed useful has been shown to be specific to the apparatus in question.

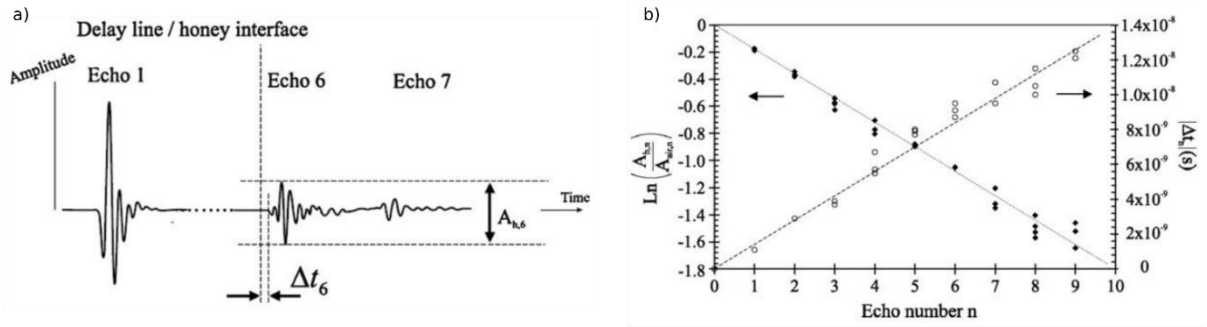

Figure 2-34: a) Echo 1, 6 and 7 amplitude reduction as the number of reflections increase, echo's 6 and 7 are magnified 6 times in this image from (Gasparoux et al. 2008). b) An example of experimental points obtained when considering the amplitude phase, expressed as a change in temporal shift with the number of reflections, image from (Gasparoux et al. 2008).

The number of reflections has been shown to increase the effect on the amplitude of the wave, although the change in temporal phase shift Δt, defined as:

$$\Delta t = -\frac{\Delta \phi}{\omega}, \qquad \text{Equation 2-33}$$

between reflections has been shown to reduce with the number of reflections, reducing from 14 ns at one reflection to 2 ns at 9, indicating a dependency on the amplitude of the wave or reduced capability to detect phase change from small amplitudes. Multiple reflections were also the adopted technique by (Camara et al. 2010), who evaluated the use of the technique with bulk shear waves with a combination of substrate materials, concluding improved results from the material with the lowest acoustic impedance. In summary, by capturing multiple reflections from a solid liquid interface, the effect of the interface is amplified increasing the sensitivity of the measurement.

2.5.4. Matching Layer

A quarter wavelength matching layer (ML) can be used to increase the influence of viscosity on the reflection coefficient (Schirru et al. 2015). The ML provides an acoustically less dense layer between the solid and liquid, improving the proportion of wave energy incident on the liquid. The ML can also be selected to create destructive interference of waves in the component, acting to enhance the influence of the liquid on the signal using the ¼ wavelength theory. A schematic illustration of a metallic component with and without the ML is shown in Figure 2-35.

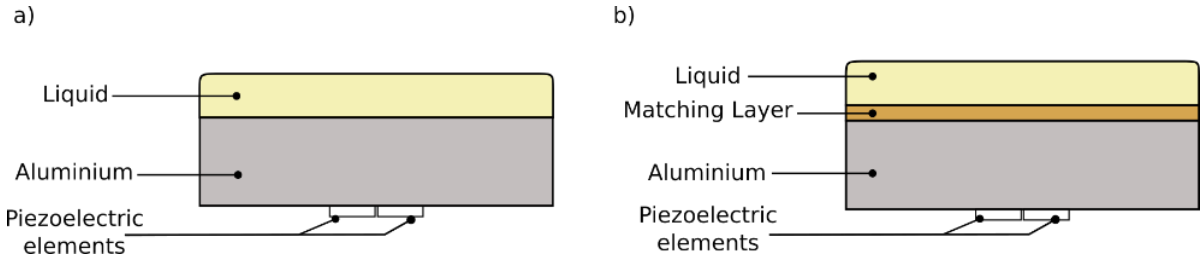

Figure 2-35: A schematic illustration of an aluminium component in the measurement condition, a) without a ML, and b) with a ML.

The ideal acoustic impedance of the layer is defined by (Schirru et al. 2015) as:

$$z_m = \sqrt{z_l z_s}. \qquad \text{Equation 2-34}$$

The density of the ML, $\rho_m$and speed of sound in the ML c_m are used to find a material with the optimum properties for a specific combination of a solid-liquid arrangement. The ML thickness is chosen to be one quarter wavelength of the resonant frequency of the transducer. Frequencies which destruct within the solid become highly susceptible to changes at the ML-liquid interface, making measurement of liquid viscosity more sensitive. For example a 5 MHz centre frequency transducer would require a 50 µm thick ML with c_m equal to 1000 m/s, as shown by:

$$t_m = \frac{Nc_m}{4f}, \qquad \text{Equation 2-35}$$

where N is a natural integer and t_m is the matching layer thickness. Destructive interference of frequencies which match a quarter wavelength is produced through simple wave destruction, schematically represented in Figure 2-36.

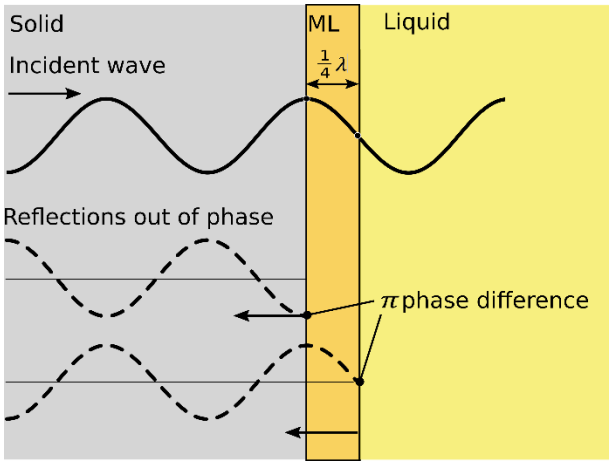

Figure 2-36: A schematic diagram of the behaviour of a wave within a layer ¼ wavelength thick ML.

There are two interfaces present when a ML is added to the component, that between the component and the ML, and that between the ML and the liquid. A reflection from both of these interfaces in produced in this case. If these waves are out of phase they destruct. If the layer is a quarter wavelength thick, the reflection difference between the first and second reflected wave is 180 degrees out of phase and so produce complete destruction. It is this destruction and the improved acoustic properties between the liquid and ML material to enhance the effect of viscosity on the ultrasonic signal.

By implementation of the ML, measurement of a liquid therefore becomes a three layered system. For a solid-ML-air condition the complex reflection coefficient in a three-layered system is given by Equation 3-23 (Kinsler et al. 2000)(Haines et al. 1978).

$$R^* = \frac{\left(1 - \frac{z_s}{z_a}\right)\cos\left(\frac{\omega t_m}{c_m}\right) + i\left(\frac{z_m}{z_a} - \frac{z_s}{z_m}\right)\sin\left(\frac{\omega t_m}{c_m}\right)}{\left(1 + \frac{z_s}{z_a}\right)\cos\left(\frac{\omega t_m}{c_m}\right) + i\left(\frac{z_m}{z_a} + \frac{z_s}{z_m}\right)\sin\left(\frac{\omega t_m}{c_m}\right)} \qquad \text{Equation 2-36}$$

This is where z_a is the acoustic impedance of air, z_m is the ML acoustic impedance and t_m is the ML thickness. For a measurement condition, where a solid-ML-liquid configuration is present, z_a is replaced by z_l, as shown in Equation 3-24.

$$R^* = \frac{\left(1 - \frac{z_s}{z_l}\right)\cos\left(\frac{\omega t_m}{c_m}\right) + i\left(\frac{z_m}{z_l} - \frac{z_s}{z_m}\right)\sin\left(\frac{\omega t_m}{c_m}\right)}{\left(1 + \frac{z_s}{z_l}\right)\cos\left(\frac{\omega t_m}{c_m}\right) + i\left(\frac{z_m}{z_l} + \frac{z_s}{z_m}\right)\sin\left(\frac{\omega t_m}{c_m}\right)} \qquad \text{Equation 2-37}$$

The complex shear acoustic impedance of a liquid is viscosity dependent, (see Section 2.4.6), so measurement is possible by the analysis of the relative signal differences between the solid-air and solid-liquid signals (Buckin & Kudryashov 2001). The influence of the ML on the amplitude of a signal at different frequencies is shown in Figure 2-37.

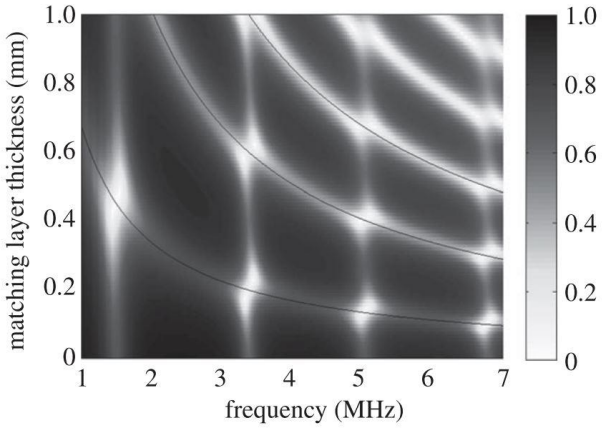

Figure 2-37: Reflection coefficient colour bar graph as a function of frequency and ML thickness. Image from (Courtney et al. 2012).

Clearly, each ML thickness has multiple frequencies which produce an increased sensitivity, shown by the *R* reduction, and frequencies which do not correspond to the thickness which show a higher reflection coefficient. Figure 2-37 highlights the importance of the quarter wavelength theory to improve viscosity sensitivity, demonstrating how several frequencies can be influenced by the same ML. The ML approach therefore provides a great deal of versatility for practical applications as the material properties of the layer, and thickness can be tuned for a particular transducer resonant frequency and metallic component properties.

Implementation of a ML for ultrasonic applications was achieved by (Desilets et al. 1978) using theory taken from electronic systems developed to ultimately improve the efficiency of electrical transmission from one material to another. The technique aimed to produce transducers with ‘large bandwidths, good sensitivity and good impulse response’. Research into the use of quarter wave length ML’s had been conducted by (Kossoff 1966), with the aim to couple longitudinal transducers with water for increased transmission into a solid for flaw detection within a water bath, the response of several materials is shown in Figure 2-38.

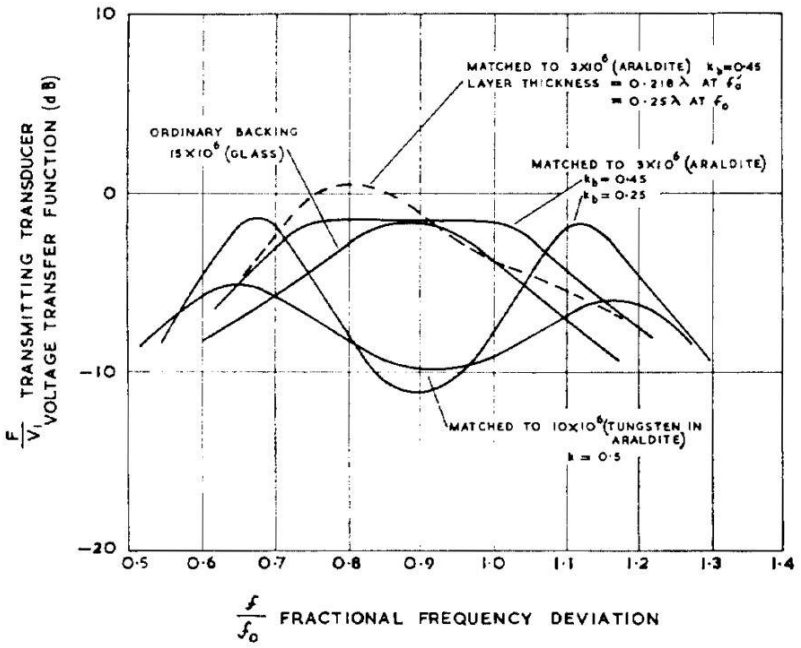

Figure 2-38: Voltage transfer function vs frequency for a series of ML thicknesses and materials. Image from (Kossoff 1966).

Desilets research produced several transducers with ML's composed of epoxy, light borosilicate glass with epoxy and a high gloss high impedance tungsten-loaded epoxy in order to tune the technique for the greatest overall response following the electrical transmission model (Leedom et al. 1971).

Since then many materials have been developed to act as a ML between the transducer and liquid (or tissue in the medical field), with the general aim to improve longitudinal wave propagation into the substrate. Nanocomposites composed of cerium oxide particles, or aluminium oxide particles with variable densities were produced by hydrolytic condensation and polymerisation, where the layers were deposited directly onto the PZT (Tiefensee et al. 2010). Silicone micromachining technology borrowed from the micro-electrical-mechanical industry has also been used to create multi-layered ML's for the ultrasonic medical imaging industry, where again the ML is bonded directly to the PZT (Manh et al. 2014).

The multi-layered system was developed based on (Desilets et al. 1978) optimal criteria for the outer, inner and intermediate acoustic impedance of the layer, these being 24.9, 7.6 and 2.3 MRayl respectively. The intermediate layer was composed of a composite of the materials used for the first and third layers to create a material with intermediate properties. A schematic image of the triple layered system is shown in Figure 2-39.

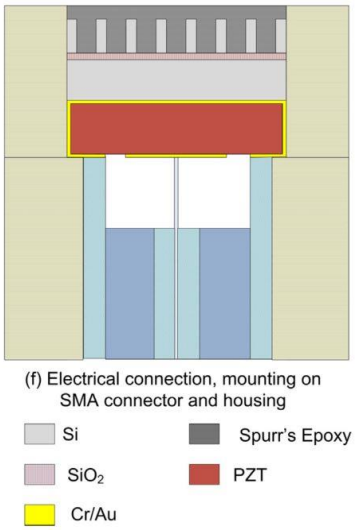

Figure 2-39: Schematic illustration of the multiple micro-machined ultrasonic transducer. Image from (Manh et al. 2014).

In each case where ML's have been used to improve ultrasonic transmission, the ML has been directly bonded to the PZT element. Schirru et al. applied this principle to ultrasonic viscometry with an applications based approach (Schirru et al. 2015). Rather than placing the layer directly onto the PZT, the ML was used to improve the transmission of ultrasonic shear waves from metallic surfaces to liquids. Similarities between transmission losses experienced between the high acoustic impedance transducer to water occur between a metallic and liquid media, hence by placing the ML on the measurement surface of a metallic bearing, using bare element piezoelectrics, the engineering part itself can act as the measurement device.

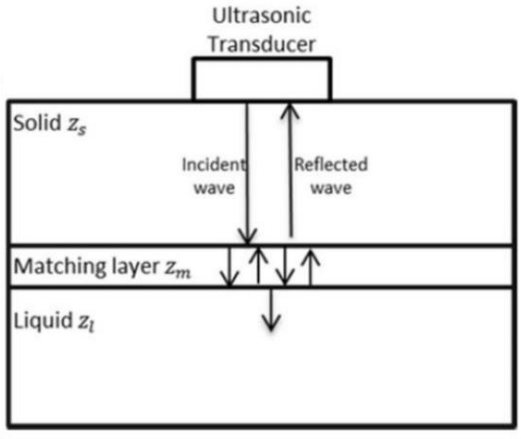

Figure 2-40: Shear ultrasonic transmission and reflection from a solid–ML–liquid system. Image from (Schirru et al. 2015).

For an aluminium substrate, a polyimide ML was chosen, possessing an acoustic impedance of 1.4 MRayl and a thickness of 50 μm. The layer thickness was chosen based on the quarter wavelength theory to further improve the sensitivity of the device (Schirru et al. 2015) using Equation 2-35. For the application of engineering lubricant applications a polyimide ML, which is a polymeric chemically inert flexible film was shown to be suitable for applications within a journal bearing, with the author demonstrating a viable in-situ viscosity measurement

technique in real time from an operational bearing (Schirru 2016). Figure 2-41 demonstrates the application of the ultrasonic technique to a journal bearing.

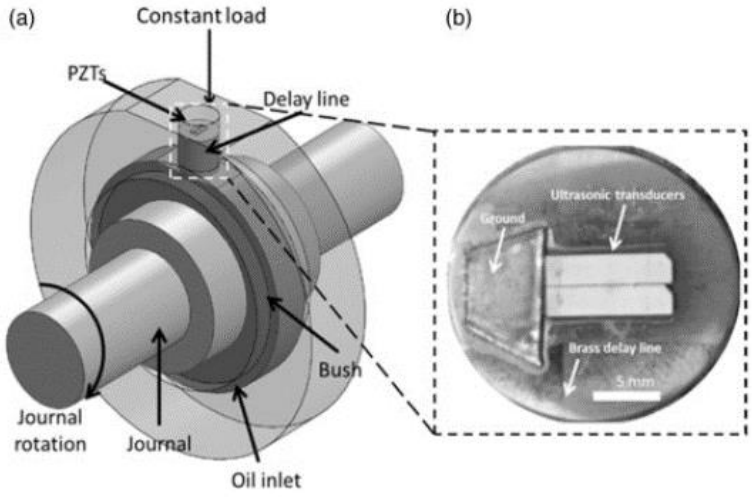

Figure 2-41: Journal bearing test rig used in Schirru et al (2015): (a) schematic of the journal and bush with the transducer location identified, (b) photograph of the piezoelectric transducer and brass delay line. Image adapted from (Schirru & Dwyer-Joyce 2015).

Reflection coefficients <0.25 were achieved in a calibration procedure for PAO 100 which has a high shear viscosity of 1.4 Pa.s, revealing a high level of sensitivity of the technique. Ultrasonic instrumentation of the component was completed on a removable component, labelled the delay line in Figure 2-41 to permit ML and PZT bonding, revealing a potential limitation of this technique as access to the measurement interface was required pre-test.

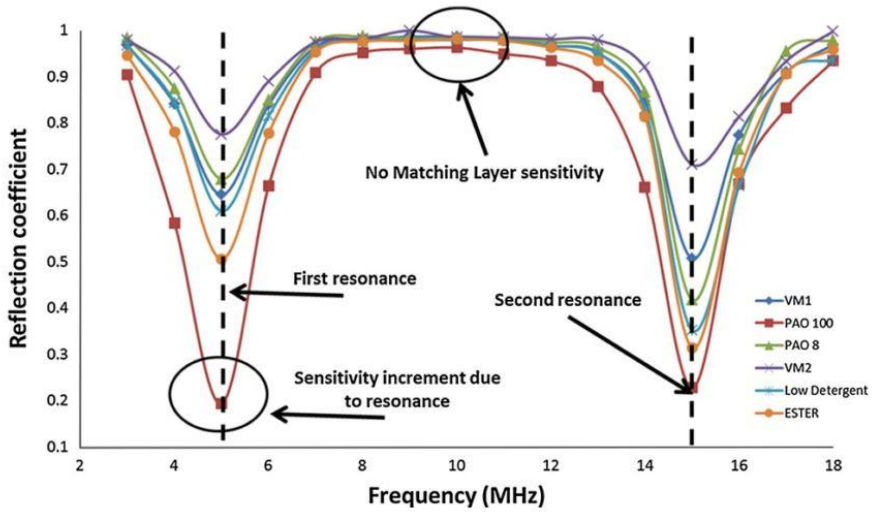

Figure 2-42: The frequency sensitivity dependence produced by the ML. Image from (Schirru et al. 2015)

The study demonstrates superior viscosity sensitivity than the techniques addressed within this review, increasing the sensitivity of numerous resonances within a component to produce

characteristic resonant dips in the reflection coefficient in the frequency domain, as shown in Figure 2-42.

2.5.5. Steady and Oscillatory Shear Behaviour

There remains some debate on the relationship between viscosity measured by continuous shear in a conventional steady shear viscometer to that measured by small amplitude high frequency oscillations (Bair et al. 2014). Generally for simple structural liquids up to a few kHz the methods are in agreement (Wen et al. 2004), whilst for more complex molecular structural liquids and high oscillatory frequencies (such as in the MHz range) there is uncertainty.

A number of empirical models have been developed to understand the relationship between steady shear and oscillatory shear, The Cox-Merz rule (Merz & Cox 1958) is a widely accepted means of relating the dynamic viscosity to the viscosity in steady shear flow. The relationship demonstrates that mechanically induced shear rate from a conventional rotational viscometer is the same as that produced by the equivalent vibrational angular frequency as shown in Equation 2-38.

$$\eta(\omega) = \eta(\gamma)\,, \qquad \text{Equation 2-38}$$

Cox and Merz were able to prove this for low shear rates between 10 and $10^4 s^{-1}$ for polymer melt solutions. Bair (Bair et al. 2014) then used this rule to show oscillatory and steady shear agreement with the Carreau model, a shear thinning model. Figure 2-43 demonstrates how the Carreau model can be used to compare fluid viscosity during steady and oscillatory shear as a function of shear rate or angular frequency in the transition zone of squalane.

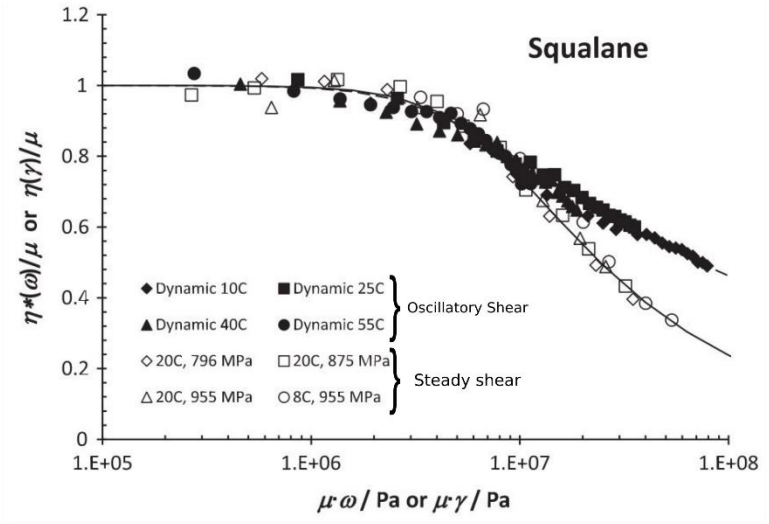

Figure 2-43: Oscillatory shear, denoted by solid points, and steady shear denoted by open points at the given pressures. Extracted from (Bair et al. 2014).

For purely Newtonain liquids, Bair demonstrated agreement between high rotational frequencies, in the region of MHz. A comparison between steady and oscillatory shear indicates agreement up to 10^7 s^{-1}, as shown in Figure 2-43.

The relative viscosity values of static and dynamic viscosity are plotted against the product of shear rate and low shear viscosity for steady shear, and the product of angular frequency and low shear viscosity for dynamic data, where η is given in Pa.s. This was calculated using a shifting rule which predicts viscosity at arbitrary temperatures and pressures, permitting comparison of results which were produced in different conditions to directly compare static and dynamic data (Bair et al. 2014). At shear rates above 10^7 s^{-1}, measurement data deviate, though this is thought to be due to the non-Newtonian nature of squalene. Further work by Bair et al. (Bair et al. 2017), demonstrated that by using a modified Carreau model, (see Equation 2-39), the frequency of an oscillation in Hz, is required to compare the steady shear rate to oscillatory shear, rather than the angular frequency.

$$\eta = \mu_2 + (\mu - \mu_2)\left[1 + \left(\frac{\tau}{G}\right)^2\right]^{\frac{1-\frac{1}{n}}{2}} \qquad \text{Equation 2-39}$$

Where μ is the limiting low shear first Newtonian viscosity, μ_2 a parameter representing the limit to the viscosity at infinite shear rate, and G the liquid shear modulus associated with rotational relaxation time (Habchi et al. 2013, Bair et al. 2017). Hence Equation 2-38 can be modified to:

$$\eta(\gamma) = n(f), \quad y = f \qquad \text{Equation 2-40}$$

Agreement is clearly shown in Figure 2-44, by a comparison of experimental data and the modified Carreau model.

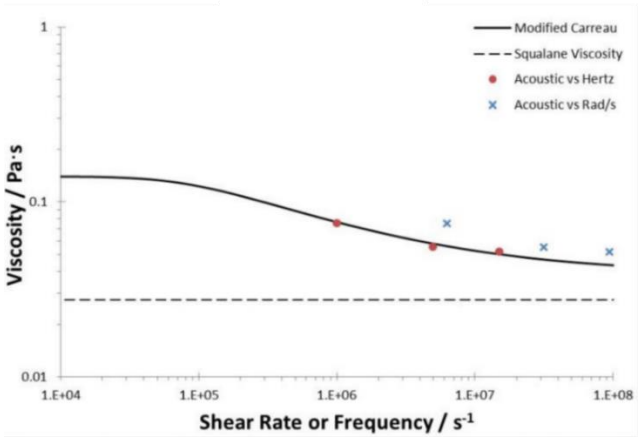

Figure 2-44: Viscosity as a function of frequency measured at 24℃ at ambient pressure, and viscosity calculated using the modified Carreau equation as a function of frequency. Image extracted from (Bair et al. 2017)

These findings collectively demonstrate that by using the modified Carreau model, ultrasonic viscosity measurements can be directly related to steady shear measurements at the same viscosity. Furthermore, steady shear viscometers are generally unable to generate shear rates above 10^6 without causing cavitation within the fluid, however ultrasonic measurements can produce oscillatory shear thinning without generating shear stress, this permits high shear rate viscosity measurements at levels un-achievable by steady shear viscometers (Bair et al. 2017) which can then be converted to steady state viscosity using the model.

2.6. Summary

Lubricants are required to enable machinery to perform efficiently, preventing seizure by forming a lubricating layer between two solid contacts. Selection of the optimal grade for each application allows a fluid film to form between the contacts, in turn reducing friction. If the lubricant is sufficiently viscous at the operating parameters of the tribosystem, the lubricant film is able to push two sliding surfaces apart through the pressure generated within the contact, however if the viscosity of the lubricant deviates from this, friction between the contact increases either due to asperity contact between the surfaces or due to viscous drag generated when the lubricant layer is too thick. The viscosity of the lubricant can therefore define the efficiency of a contact, and so the study of its behaviour is highly important for many industries.

The operating conditions in which a lubricant must perform are considered in detail before the introduction of a lubricant as the temperature, pressure and shear rate all influence viscosity. The Society of Automotive Engineers and the International Organisation for Standardisation are commonly used in the automotive industry, to provide information regarding numerous standard viscosity grade oils. The viscosity of an oil within a contact is difficult to determine in-situ due to the usually small size of the contacts. Conventional techniques use bespoke pieces of equipment to measure viscosity, and while these machines can be highly accurate many remain incapable of real-time non-invasive viscosity measurement. The majority of devices require an articulating mechanism to be partially or fully submerged within the liquid, so measurement during operation is inaccessible in many instances. This disadvantage further prevents condition monitoring of a lubricant, as a gold standard viscosity measurement would be taken when of the oil when it resides in the contact.

Ultrasonic techniques to measure viscosity in-situ have been demonstrated by a number of authors, but many are incapable of producing measurements through a metallic substrate. A typical automotive engine oil ranges between 80 and 5 mPa.s from a cold engine to fully warmed up, hence relatively low viscosity measurements are required in many applications. Acoustic mis-match between metals and liquids presents difficulties to ultrasonic techniques at these viscosities, therefore technologies to overcome acoustic mis-match are required.

A matching layer can be used to reduce the impact of acoustic mis-match. The method has been shown to improve viscosity measurement sensitivity, although the technique requires the installation of an additional material into the measurement apparatus. The layer can be produced from a variety of materials at a range of thicknesses, adding to the versatility of the method and possible reverse engineering of an ultrasonic system. The advantages of multiple reflections are evident in the literature, amplifying the effect of viscosity, expressed by a greater reduction in reflection coefficient due to the influence of phase and amplitude amplification. However this principle has not yet been attempted via the use of standing waves. While standing waves have previously been used for crack detection using the principles of resonance, their use is more profound in the field of particle manipulation, rather than measurement applications of liquids. Thus, the use of standing waves to enhance viscosity measurement capability through a metallic substrate is a novel method which is yet to be investigated.

3. The Standing Wave Method

The standing wave method is a novel ultrasonic viscosity measurement technique which produces a multiple frequency standing wave within the component. Mechanisms which govern standing waves may allow measurement of a wider range of viscosities than when using pulsed methods. The method is known as the standing wave measurement of interfaces and layers (STAMINA) but within this thesis the method will be referred to as the Standing Wave method (SW) to shorten the term (Mills et al. 2017). The method is presented qualitatively with accompanying elementary signals to aid explanation in this chapter.

The first section presents the standing wave methodology, and the second section of this chapter presents the apparatus, hardware and signal processing methods, also covering the test oils used herein. The standing wave methodology describes the requirements in order to generate and acquire the signal, also covering factors which are known to influence the standing wave profile.

3.1. Standing Wave Methodology Outline

The SW methodology has been developed using the principals of standing waves and resonance (Mills et al. 2017). A standing wave is produced using a continuously repeating frequency sweep, centred on the resonant frequency of the transducer. The method produces a standing wave within the component which can be used to measure interfacial conditions, the focus here is on the measurement of Newtonian viscosity at the interface, measured by analysing the standing wave signal, an example of which is shown in Figure 3-1.

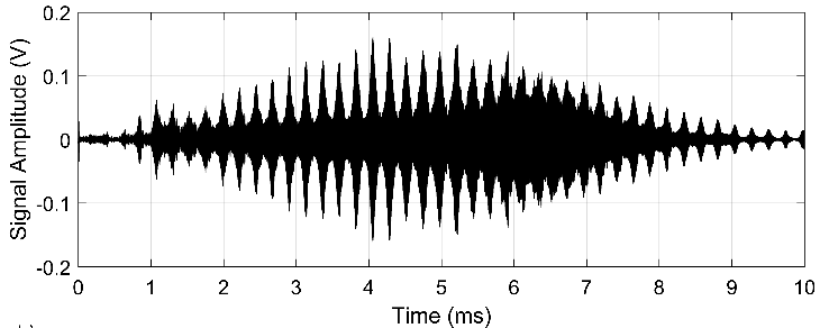

Figure 3-1: A SW signal.

Generation of the SW signal will be the focus of this section, as measurement using the full frequency sweep has multiple advantages. The full sweep enables the possibility for auto-calibration, where the requirement for a solid-air signal could be eliminated, as a resonant frequency peak which is not influenced by viscosity is selected as the reference. The method also has the potential to produce viscosity measurements at a range of frequencies simultaneously, possibly creating a novel measurement device for the effect of shear rate on viscosity.

3.2. Standing Wave Generation

In order to create a multiple frequency standing wave, a continuous chirp is generated. The continuous nature of the signal requires the piezoelectric transducer to be arranged in a pitch-catch orientation when bonded to a component. Thus the method requires one transducer to generate the standing wave, and the other to acquire the signal. In order to understand the interference mechanisms which contribute to the SW, multiple reflections of a single frequency continuously generated within a bounded structure are firstly considered.

The first wave propagates through the solid component, reflecting at the solid-air interface and returning towards the source of the wave. The returning wave interferes with the subsequent incident wave at the same frequency produced by the wave source. This process continues to create a standing wave within the component due to the continuous nature of generation signal. If subsequent waves are generated within the component at a greater rate than that at which the waves decay, a standing wave is produced. A schematic illustration of a single frequency standing wave within a solid is shown in Figure 3-2.

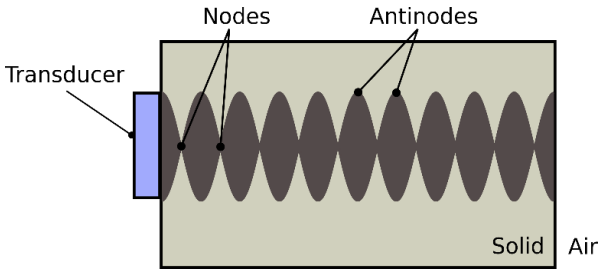

Figure 3-2: Schematic diagram of a single frequency standing wave within a solid component.

To experimentally produce a multiple frequency standing wave within a component, a number of parameters must first be gathered, these parameters relate to the component and transducer used to generate the signal, and consist of the centre frequency, the frequency span, and the sweep time. Figure 3-3 indicates the relevance of each of these in the formation of the SW signal.

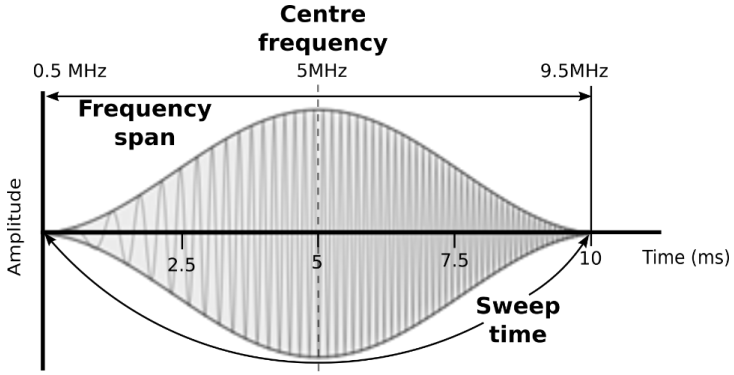

Figure 3-3: Standing wave parameters.

Each parameter will now be discussed in greater detail with experimental reasoning for parameter selection.

3.2.1. Excitation Frequency Selection

The continuous frequency sweep is selected based on the capabilities of the transducer. The resonant frequency of the transducer is chosen to be the centre frequency of the sweep, and the frequency sweep span is chosen to encompass the operational bandwidth of the transducer. Table 3-1 shows a typical set of input parameters required to produce the SW.

Table 3-1: Test parameters defined for a 5MHz transducer with a 7.38mm aluminium component.

Parameter	**Set Value**
Centre Frequency	5 MHz
Frequency Span	9 MHz
Sweep duration	10 ms
Voltage	10 Vpk-pk

A representative schematic of the repeating continuous frequency sweep for the parameters in Table 3-1 is shown in Figure 3-4.

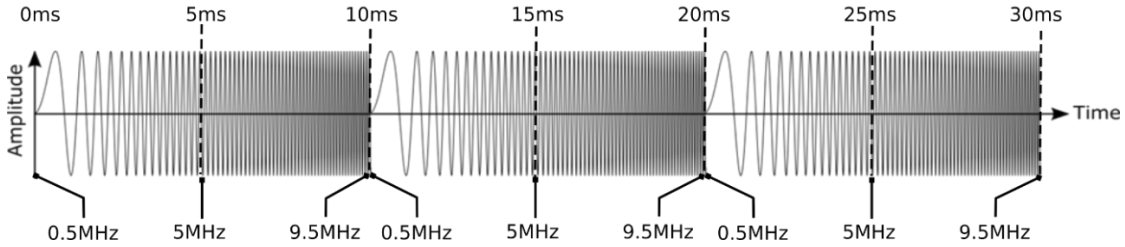

Figure 3-4: A schematic representation of the excitation signal applied to the generating transducer.

The schematic significantly simplifies the sweep, however demonstrates the repetitive nature. The start frequency for this set of parameters is 0.5 MHz, and the stop frequency 9.5 MHz while the frequency sweep is given a repetition time of 10 ms.

3.2.2. Duration of the Excitation Frequency Sweep

The duration of the frequency sweep must be considered to enable the formation of the SW within the component. The rate of change of frequency of the sweep must be small enough to permit the assumption that, at a given point in the sweep, the change in frequency content of the superimposed reflections that form the standing wave is sufficiently small to allow it to be considered a single frequency. Figure 3-5 shows this behaviour schematically.

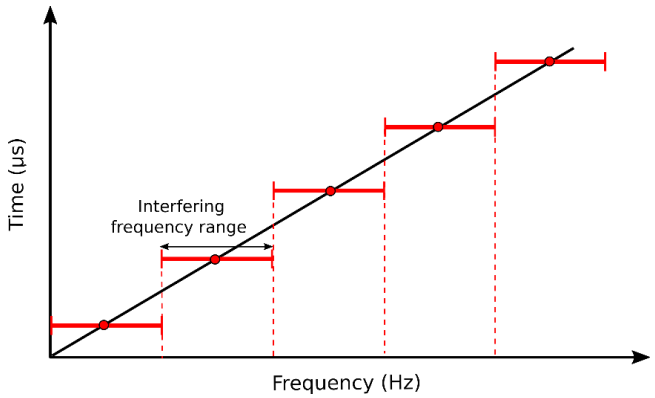

Figure 3-5: A schematic illustration of the frequency input (black), and frequencies which are considered as the same frequency in the sweep (red).

For the set of parameters outlined in Table 3-1, the time (t) it takes for one reflection of a wave to travel from the transducer, to the measurement interface and back to the transducer interface again is calculated to be 4.85 μs, if the length of the component is 7.38 mm and $c_s = 3040$ m/s, according to Equation 3-1.

$$\frac{2L(\mathrm{m})}{c(\mathrm{m/s})} = t(\mathrm{s}) \qquad \text{Equation 3-1}$$

If a linear frequency sweep with a time duration of 10 ms is used with a 9 MHz frequency span, the output frequency of the transducer would change by 4.36 kHz in the time it takes for a wave to make one reflection, (if the speed of sound is 3040 m/s). As frequencies here are in the MHz range, this would account for a frequency change of 0.43% of a 1 MHz frequency, reducing to 0.087% change at 5 MHz. Hence each subsequent frequency is $< 1\%$ different, to the previous frequency at frequencies over 0.42 MHz. This relationship is shown in Figure 3-6.

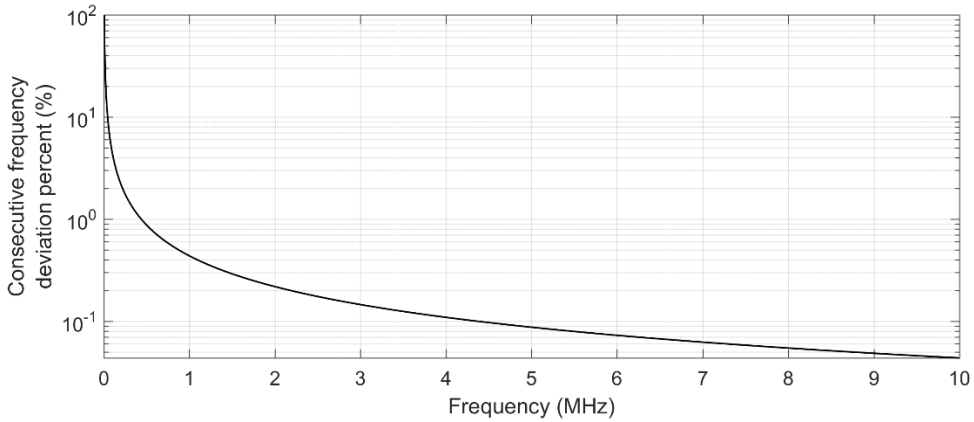

Figure 3-6: Consecutive frequency deviation expressed as a percent of the previous frequency produced by the frequency sweep for parameters given in Table 3-1.

The sweep time duration is defined by finding the time which is sufficient to permit the SW to form the maximum amplitude. The duration of the frequency sweep is a variable input as it is effected by the length of the frequency sweep and component geometry. If the time given to the sweep too short the standing wave produced will not have fully formed to reach the waves

steady state. If it is too long, the signal is generated inefficiently as the standing wave can be fully formed in a shorter time.

3.2.3. Composition of the Standing Wave

The standing wave is the sum of multiple reflections at each frequency within the sweep forming a single symmetric wave profile about 0 V. The data acquired is in the form shown in Figure 3-1a, however to gain a clearer understanding of this signal, and its composition, Figure 3-7 shows a sequence of increasingly magnified images of the signal.

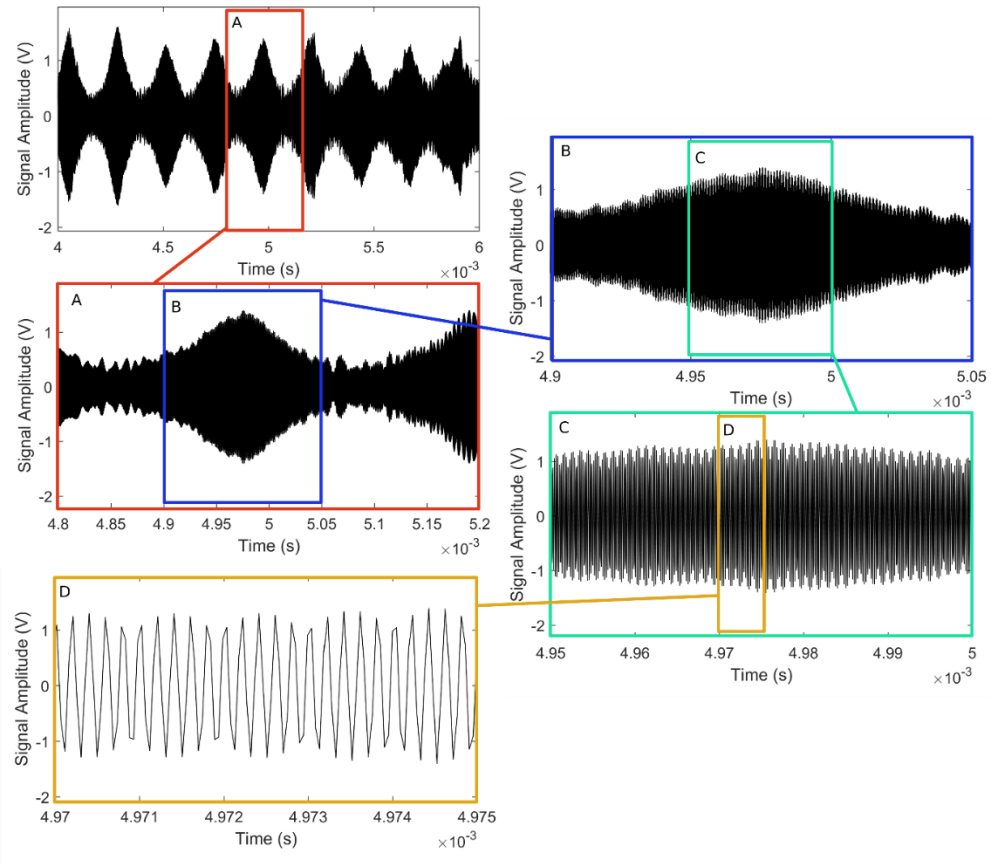

Figure 3-7: A sequence of standing wave profiles to show the typical stamina profile composition. Magnification increases from A to D. Corresponding colour boxes show the selected region of magnification.

As shown in Figure 3-7 the standing wave is composed of many discrete points, each representing the resulting amplitude of multiple waves within the component. While mixed frequency ultrasonic waves interfere to create the standing wave due to the effect of the sweep time discussed earlier in Section 3.2.2, the amplitude of the standing wave is also the result of multiple reflections of each frequency within the material. Wave reflections continue until the amplitude of the wave decays to zero as the number of reflections and attenuation act on the wave transmission.

The amplitude of the standing wave is defined by the degree of interference, which in turn is defined by the frequency of the wave and length of the component. A repeating linear

frequency sweep, also known as a chirp identifies the resonant frequencies shared by the transducer and component, in the form of antinodes.

Initially the bandwidth of the transducer modulates the signal input from the generator shown in Figure 3-4, producing a profile similar to that of Figure 3-8a. As the signal propagates through the component, reflecting within it, some frequencies destruct, creating nodes, and antinodes, resulting in a profile similar to that shown in Figure 3-8b.

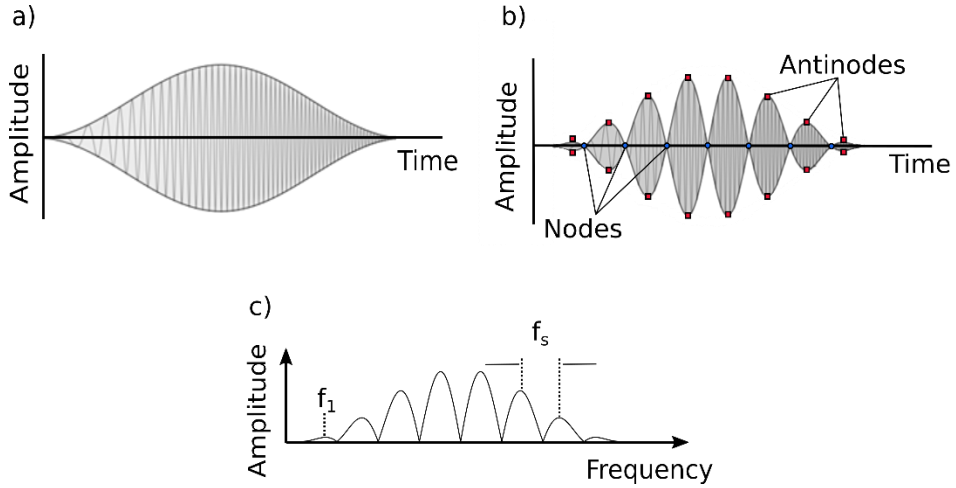

Figure 3-8: A schematic representation of the a) modulating effect of the transducer on the excitation frequency sweep. b) modulating effect of the component and transducer on the signal. c) fast fourier transform of the time domain signal in b) first harmonic f_1, the resonant frequency f_s.

The location of nodes and antinodes appear stationary if the acquisition window time matches the sweep duration. Frequencies between nodes and antinodes of the standing wave do not fully construct or destruct, but show an intermediate response indicated by their relative amplitude and deviation in frequency from resonant peaks. By taking a Fast Fourier Transform (FFT) of the time domain signal, the frequencies which form resonant peaks (antinodes in the frequency domain) can be identified (Figure 3-8c). An FFT of the signal in Figure 3-1 is shown in Figure 3-9.

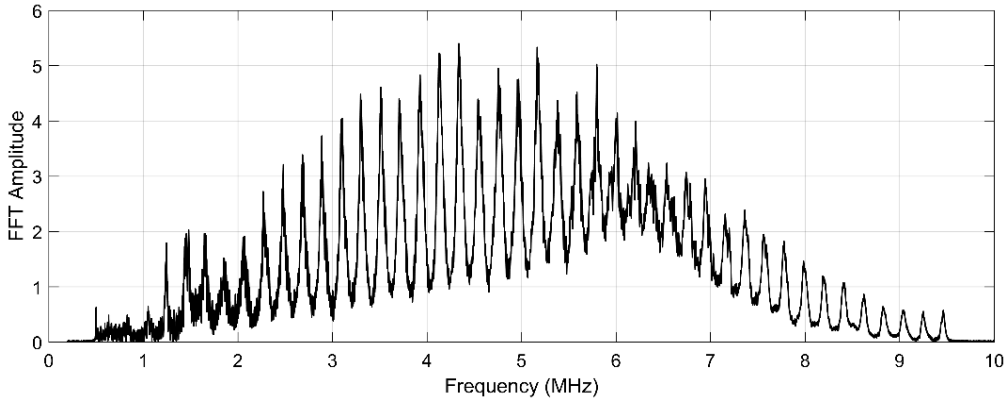

Figure 3-9: An FFT of the SW signal.

Due to window time matching of the time domain signal, the captured signal shows great similarity to the frequency domain signal, demonstrated by the similarity of the maximum profile of Figure 3-1 and Figure 3-9. Figure 3-10 is a spectrogram of the time domain signal acquired showing the linear response of the SW amplitude with frequency over the sweep time.

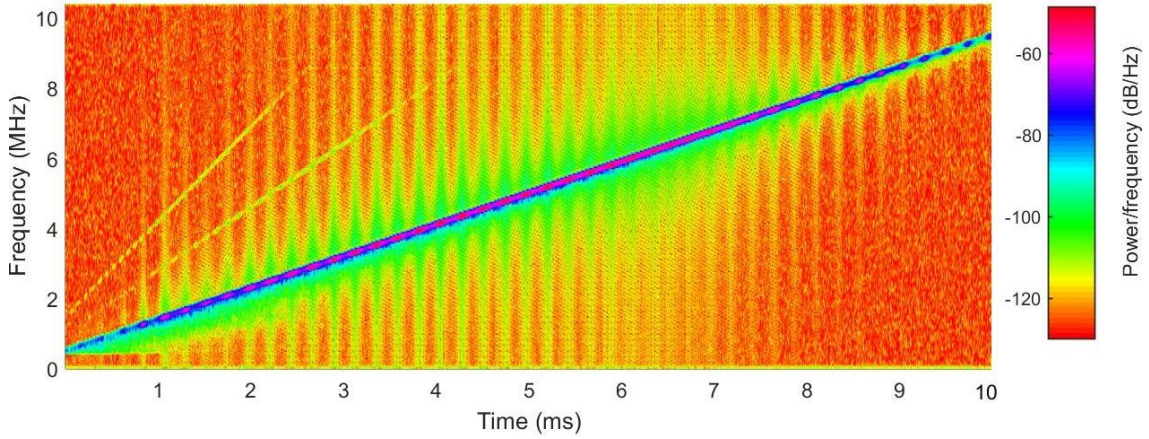

Figure 3-10: A spectrogram of a measurement signal using the SW method, created by the input of a continuously repeating chirp ($0.5 - 9.5$ MHz frequency sweep with a 10 ms sweep time). The spectrum shows the standing wave generated within an aluminium component and the variation in amplitude of the standing wave as the time and frequency increase.

The striations in Figure 3-10 indicate that multiple frequencies exist within the signal at times which correspond to a single frequency input, confirming that the input frequencies resonate within the component. The most prominent frequencies are those which lie above -60dB/Hz shown by the colour bar, seen as small red dots in the centre of the blue linear stripe, these are the antinodes of the standing wave.

3.2.4. Measurement Parameter for the Standing Wave Method

The technique presented here uses the anti-node peak frequencies as measurement locations, however this selection is completed post analysis. The SW reflection coefficient is termed, S for the full frequency span of the signal, consisting of the division of the wave amplitude in the measurement condition, A_m, by that of the wave in the reference condition, A_r, as shown in Equation 3-2 (which is the SW equivalent of Equation 2-14). At the dips in the S profile this is referred to as, $S_{(pk)}$ and is therefore defined by Equation 3-3. This is where $A_{m(pk)}$ is the peak anti-node amplitude in the solid-liquid condition and $A_{r(pk)}$ the peak amplitude of the same anti-node peak in the solid-air condition. This essentially represents the equivalent form of R, only for a SW peak measurement.

$$S = \frac{A_m}{A_r} \qquad \text{Equation 3-2}$$

$$S_{(pk)} = \frac{A_{m(pk)}}{A_{r(pk)}} \qquad \text{Equation 3-3}$$

This effect is particularly evident when considering a SW profile in the presence of a ML at the measurement surface. A clear increased sensitivity at frequencies which correspond to the antinodes of the reference and measurement signal is indicated by the greatest reduction in the

S spectrum at these frequencies in Figure 3-11, although this effect will be discussed in greater detail in Chapter 6, 7 and 8.

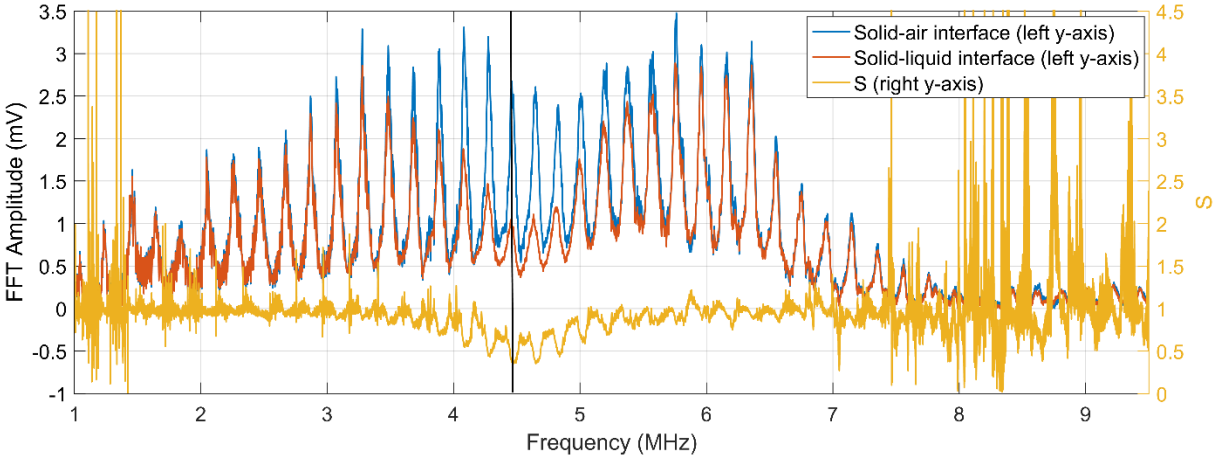

Figure 3-11: A_r, reference, A_m, measurement and S spectrum in the frequency domain.

3.2.5. Factors which Influence the Standing Wave

Many factors influence the profile of the SW method, in brief, being the reflection coefficient at the measurement interface, specifically defined as R, and at the transducer interface, R', the phase at the measurement interface, ϕ and at the transducer interface ϕ'. The attenuation coefficient of the component material α may also influence the SW, as will the length of the component L. These factors essentially influence the number of reflections n, which have an amplitude greater than that of the parasitic noise within the system. The location of each of these parameters in an experimental arrangement is shown in Figure 3-12.

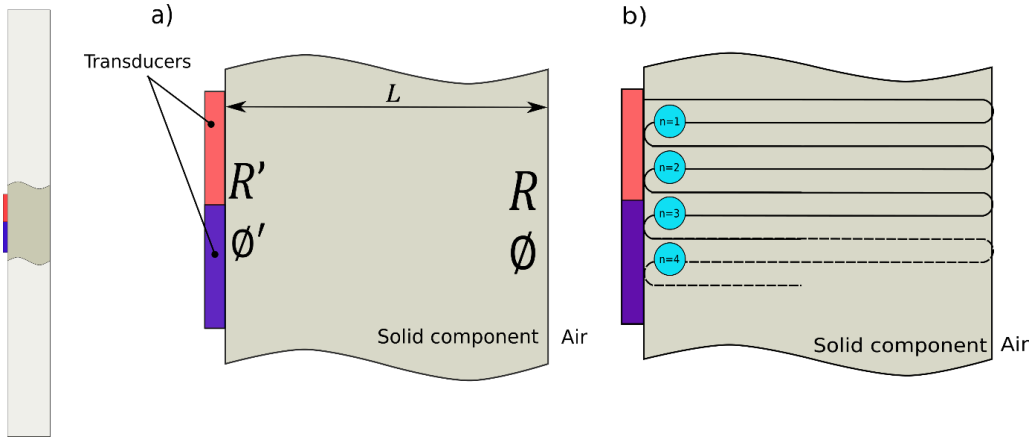

Figure 3-12: A schematic indicating the location of parameters.

R' plays a major role in the maintenance of the reflecting waves. By considering a solid-air interface where $R = 1$ the effect of R' can be seen in Figure 3-13 as n increases. This is calculated as the cumulative effect of R' on an initial amplitude of 1 for the range of R' values given in Figure 3-13 after n reflections.

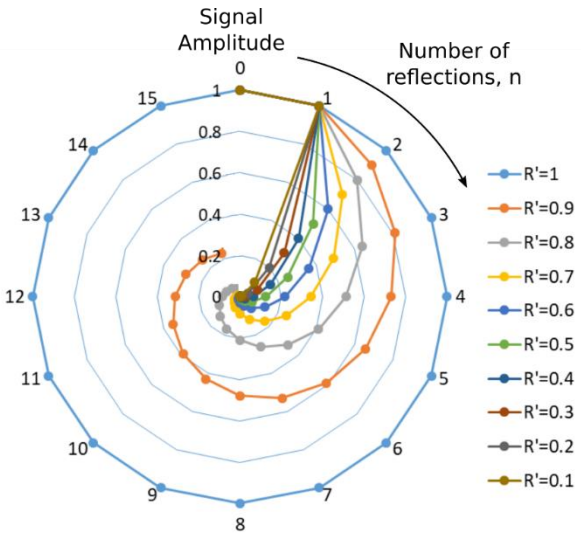

Figure 3-13: A plot to show how the amplitude of a single frequency wave decays at each reflection, n, with varying R'.

Lower reflection coefficients cause the amplitude of the wave to decay more rapidly than those with higher values of R'. As the phase and amplitude of the wave are influenced by liquid at the interface, a maximum number of distinguishable reflections is preferable as the effect of phase and amplitude increases cumulatively with the number of reflections.

3.3. Ultrasonic Apparatus

This paragraph begins the second section of this chapter, covering typical ultrasonic apparatus which can be used to generate the SW and typical component instrumentation.

3.3.1. Measurement Rig

To evaluate the SW method, a component was designed to permit a comparison of the technique with and without a ML, with the capability of generating a pulsed sine wave as a further comparison. An aluminium component was chosen as the test material as the material is metallic and so enables demonstration of the ultrasonic technique with a commonly used engineering material. A single component was therefore instrumented with two arrangements. The first was a pitch-catch arrangement of 5 MHz transducers where the liquid measurement surface was aluminium (Side A in Figure 3-14), and the second was identical to the first only with the addition of a 50 μm polyimide ML (Side B in Figure 3-14). This arrangement was chosen to achieve a similar wave interference in both conditions as transducers were placed an equal distance from the edges of the component.

The test apparatus chosen for consideration was a single 7.5 × 10.2 cm by 7.38 mm thick aluminium plate. Figure 3-14 shows a schematic diagram of a typical transducer-component arrangement used when taking a measurement using the SW method.

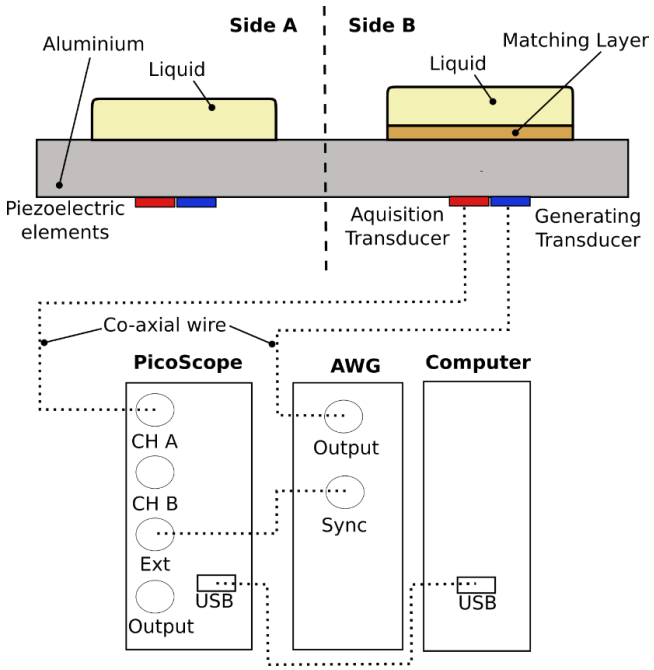

Figure 3-14: A diagram of the aluminium plate and signal generation and acquisition hardware used for SW measurements, where only Side B is electrically connected.

Further details regarding signal generation and acquisition hardware will be discussed in Section 3.6. Figure 3-15 shows an image of the instrumented plate, plate legs were used ensure a level surface for oil measurement, and to maintain consistent contact with the plate and desk. This was completed as edge effects have the potential to affect the measurement when using a the SW method.

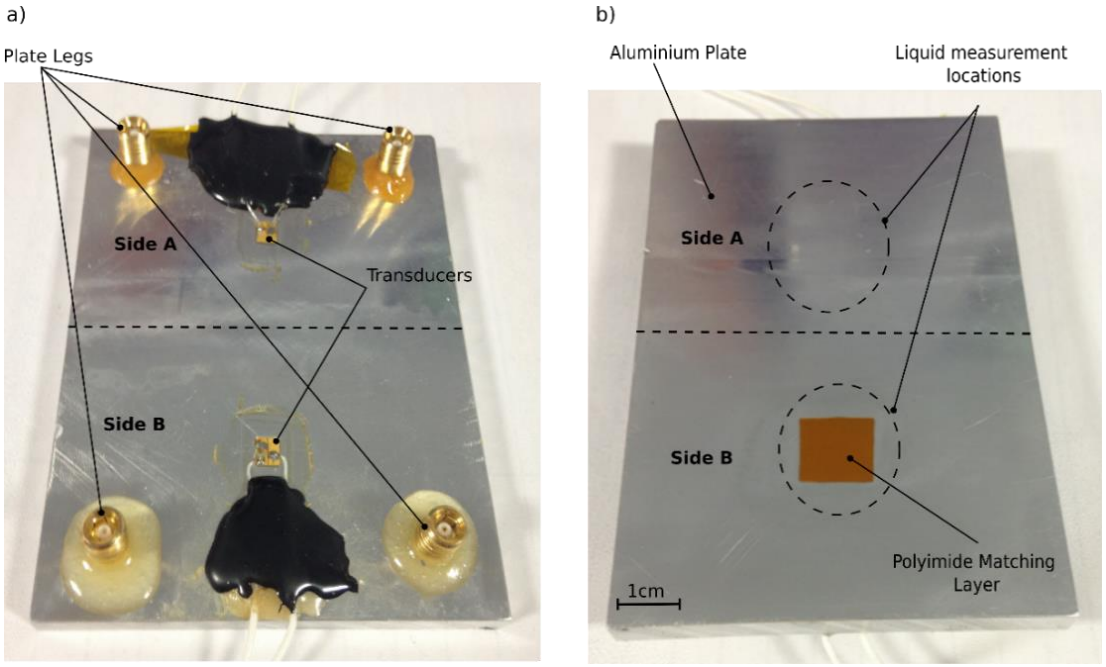

Figure 3-15: The instrumented aluminium test plate, a) the underside with bonded transducers, and b) the measurement interface with and without the ML.

3.3.2. Transducer and Matching Layer Instrumentation

Four 5 MHz chrome-gold plated shear polarised PZT-5A transducers (DeL Piezo Specialties LLC) were used to generate the SW signal. Figure 3-16 is an image of two PZT-5A transducers bonded onto an aluminium surface. PZT-5A is stable at the temperatures used for ultrasonic measurement within this thesis ($20 - 120℃$) and the Curie temperature of these transducers is 350℃, making them capable of withstanding the temperatures required for transducer bonding and soldering.

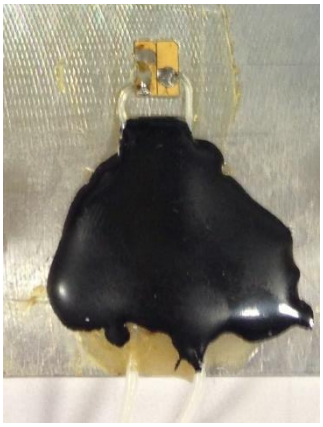

Figure 3-16: An image of two 5 MHz transducers on an aluminium plate.

The transducers are directly bonded to the aluminium plate using a strain gauge adhesive. The adhesive used was M-Bond 600, an epoxy-phenolic adhesive for high-performance applications which creates a void free, very thin glue layer between the transducer and component. Once fully cured at 150℃ for three hours, and after post curing at 200℃ (50℃ above the maximum operating temperature), the glue forms a creep resistant layer permitting electrode-aluminium electrical connection through asperity contact.

As the SW method requires continuous wave generation, one transducer was continuously excited by the Arbitrary Wave Generator (AWG) (TTI TG5011), while the acquisition transducer was used only when a measurement was required. In order for the strongest signal to be captured, the transducers were placed in close proximity to one another in the same polarisation direction. As both transducers have the same polarisation, the resonant direction of the generating transducer will produce an ultrasonic shear wave in the long plane of the rectangular transducer, and hence the acquisition transducer is the most receptive to the signal in the same orientation. The transducers were therefore placed parallel to one another, with a small gap to prevent electrical connection. Figure 3-17 shows a schematic diagram of the transducer bonding arrangement.

In this thesis, isolated electrode transducers were used. The use of Kapton tape between two layers of copper sheet prevented high thermal conduction through the copper element which was electrically connected to the metallic component. This allowed soldering indirectly onto the metallic surface to electrically connect the base of the transducer with a co-axial wire. This technique is used to create a grounding bond when the transducer does not have a wrap-around configuration. Alternatively a silver epoxy conductive adhesive can be used to ground the

transducers. Figure 3-17 shows a schematic diagram of a copper wrap and an isolated electrode shear transducer.

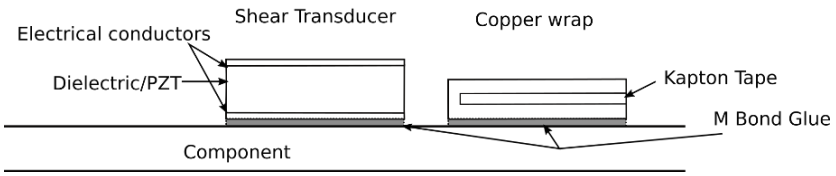

Figure 3-17: Schematic arrangement of transducers and coupling materials bonded to a surface.

In order to secure the wires connected to the copper wrap to the plate, a thermally stable epoxy was used, as seen in Figure 3-16 as the black agent coating the wires, this acts to reduce stress on the transducer-cable connection.

3.3.3. Cables

A 1.2 mm coaxial cable connects the transducers to a Sub-Miniature version B (SMB) connector, which in turn connects to a Bayonet Neill–Concelman (BNC) connector. The BNC connectors were then attached to the AWG and PicoScope. The coaxial cable has a braided outer sheath which connects to the negative terminal of the transducer, and a polymer shielded single core wire which connects to the positive electrode. The flexible wire is essential due to the fragility of the electrodes, and also heat resistant up to 350°C producing a low signal attenuation (2.3 dB/m at 1 GHz).

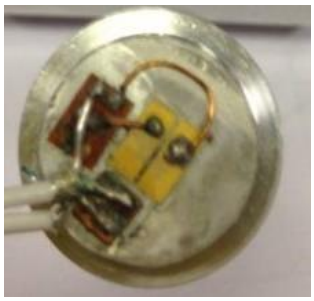

Figure 3-18: An image to show the soldered connection of coaxial wires to transducers.

3.3.4. Thermocouples

The temperature of the component and test oil were measured using K-type thermocouples. The test oil temperature was recorded by the immersion of the thermocouples active region into the liquid, and the component measured by connection with the centre of the aluminium plate. These thermocouples were deemed to be of a suitable accuracy, this being ±0.5°C, and were consistently used for each measurement. Previous work has demonstrated no hysteresis and good agreement of the K-type thermocouple with the most accurate thermocouple device, an RTD thermocouple (Schirru 2016).

3.4. Matching Layer Instrumentation

The ML used here was composed of polyimide (DuPont), a chemically inert polymer which maintains this property at high temperatures. The material is available in a variety of thicknesses, ranging from 10's to 100's of microns in a flexible adherent film. The ML was bonded onto the surface of the aluminium component using the same method used to bond transducers with an additional step of ensuring a bubble free glue layer underneath the ML, possible by visual inspection due to the translucent nature of the film.

3.5. Test Oils

3.5.1. Standard Viscosity Oils

Table 3-2 gives the viscosity and density of a range of standard oils tested in this thesis. The samples are Newtonian mineral hydrocarbon base oils which have been certified by the NIST (National Institute of Standards and Technology) and produced by Cannon Instrument Company®.

Table 3-2: Corresponding density and viscosity of Cannon^{TM} standard oils at 25ºC.

Cannon^{TM} standard oil name	**Density (kg/m^3)**	**Tabulated viscosity, Cannon Instrument Company® (mPa.s)**
S3	865.1	3.6
S20	855.2	28.8
S60	850.9	102.4
S200	857.5	345.2
S600	863.6	1049.0
N10	867.7	15.5
N35	840.4	55.56
N100	836.9	197.5
N350	843.5	597.1

These oils are commonly used to calibrate commercially available viscometers due to their viscosity stability within their shelf life.

3.5.2. Blended Oils

In order to test the experimental capability of the SW method blended oils were made using a mixture of two Cannon^{TM} standard oils. The samples were blended by initial mechanical stirring, followed by placement in an ultrasonic bath for 20 minutes at room temperature. At least 48 hours between initial mixture and measurement was left to ensure full homogeneity of the samples. The uniformity of each blended oil was assessed by its visual appearance to ensure no difference in colour or layer could be seen within the blend. Details of the blended oils can be found in Table 3-3.

Table 3-3: S600:S200 and S600:S3 blended Cannon^{TM} standard Newtonian viscosity oils.

High Viscosity Band			**Low Viscosity Band**		
Oil Blend	% Volume S600	% Volume S200	Oil Blend	% Volume S600	% Volume S3
1	92.9	7.1	11	57.1	42.9
2	85.7	14.3	12	50	50
3	78.6	21.4	13	42.9	57.1
4	71.4	28.6	14	35.7	64.3
5	64.3	35.7	15	28.6	71.4
6	57.1	42.9	16	21.4	78.6
7	50	50	17	14.3	85.7
8	42.9	57.1			
9	35.7	64.3			
10	28.6	71.4			

3.6. Ultrasonic Hardware and Software

3.6.1. Arbitrary Wave Generator

The AWG was used to produce the ultrasonic wave. When considering a single pulsed wave, the AWG produces a short duration alternating current voltage difference between the positive and negative terminal on the transducer through the co-axial wire which was connected to the output. This created a charge between the electrodes of the transducer, in turn creating a polarisation and hence a mechanical deflection of the piezoelectric material resulting in the production of an ultrasonic wave in the component which the transducer was bonded to.

The frequency of the wave is the inverse of the period of excitation chirp, which was programmed using the AWG. The voltage of the signal determines the initial amplitude of the wave produced by the AWG. By increasing the voltage, and hence the amplitude of a signal, the signal to noise ratio is improved. Voltages between 1 to 100 V are commonly used within industry, however the voltage capabilities of devices do vary. The voltage of a signal can be controlled using either the AWG or by the introduction of an amplifier connected between the AWG and transducer.

3.6.2. Oscilloscopes and PicoScopes

An oscilloscope in the form of the PicoScope 5000a series (PicoTechnologies) was used throughout this work to digitise the ultrasonic signal from the acquisition transducer. PicoScopes are Universal Serial Bus (USB) powered devices which also have the capability of an AWG, having a maximum output voltage of 2 V. When a measurement is required, a Personal Computer (PC) is used to trigger the PicoScope which digitises and records the signal in real time via the USB connection.

The sampling rate is the capacity of the PicoScope 5000a to resolve a signal in a number of discrete points. The sample rate must therefore be sufficiently larger than the highest frequency signal generated, in general this is 5 to 10 times greater. Without a sufficient sampling rate, information contained in the signal may be lost due to aliasing, schematically shown in Figure 3-19.

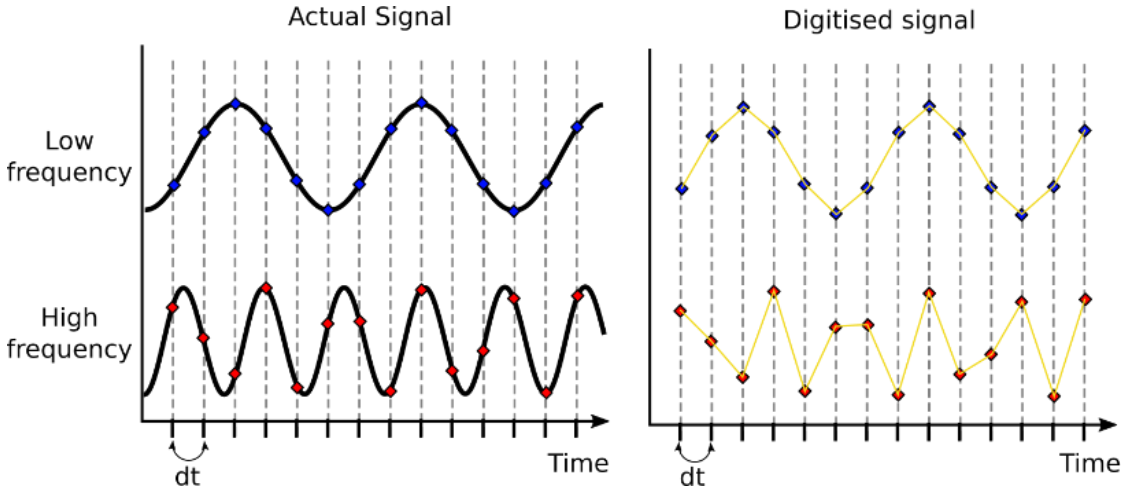

Figure 3-19: A schematic illustration of the sampling rate influence on the digital signal.

The sampling rate of the PicoScope is 1 GS/s, an ample rate for frequencies in the MHz range used here. When using the SW method the sampling window was significantly larger (10 ms) than the acquisition window used when using pulsed or burst techniques (often 40 μs for the size of component used here). The standing wave envelope is the only requirement for a measurement to be made using the SW method, hence a lower sample rate can be used to adequately resolve the signal. Unlike pulsed methods, the digitisation rate of the acquisition is controlled by the sweep time rather than the frequency of the standing wave, making it possible to reduce the sample rate to 100's or even 10's of kHz, permitting simplification of the acquisition hardware significantly.

3.6.3. Viscosity Measurement Test Protocol

Before each test, the solid (aluminium or ML)-air interface was cleaned with isopropanol, left to dry then the reference signal recorded. The test oil was then deposited on the surface and the ultrasonic signal and temperature acquired for the sample. The test sample was deposited onto the measurement surface using a pipette, covering an area of 1.5 cm^2 (the same area of the ML in Figure 3-14b) in each measurement case, care was taken to ensure the sample remained within the marked area. Measurements conducted for each condition were completed individually to eliminate the possibility of ultrasonic interference from the counter set of transducers i.e. the set of transducers taking measurements using the ML were disconnected while measurements from the condition without a ML were taken and vice versa.

For pulsed wave measurements, the transducer was driven by the AWG, which generated a series of short duration voltage pulses. One such pulse is acquired when a measurement is taken using the second transducer in the pitch-catch arrangement. An FFT is completed on this signal

and the relative amplitude of the reference and measurement signals used to find the reflection coefficient. Input parameters used to generate the pulsed signal can be found in Table 4-1.

Error bars for all data presented herein are calculated from the standard deviation of five independently repeated experiments, where in each instance three repeats were taken to account for signal fluctuations, producing fifteen measurement signals for each liquid in total (unless otherwise specified). Fifteen reference signals were captured in between each oil measurement to provide individual reference data for each oil sample.

3.7. Standing Wave Signal Processing

A PC was used to store the digitised signal produced by the PicoScope. A bespoke programme written in Labview was used to trigger the PicoScope and determine the acquisition settings, such as the sample rate and number of captures. The samples were then processed using a Matlab® function by completing the following steps for each sample.

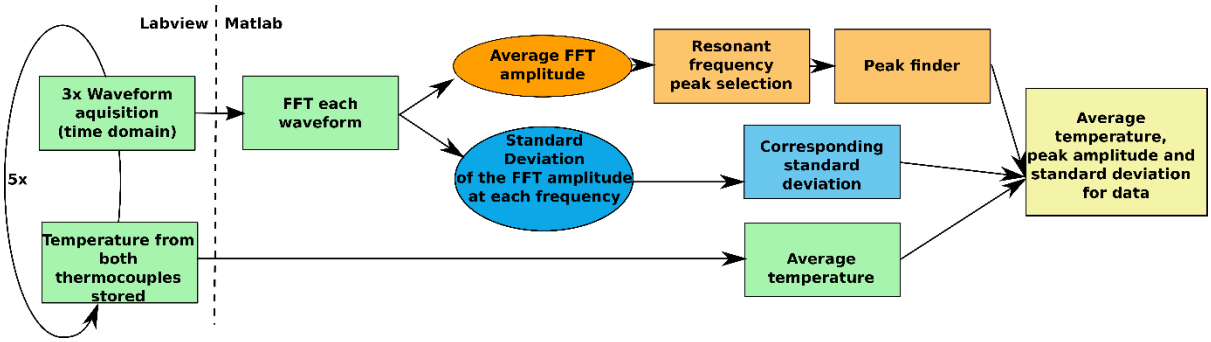

Figure 3-20: Signal processing steps completed by Labview and Matlab®.

The process shown in Figure 3-20 was completed for the solid-air and solid-liquid measurement conditions to acquire the average peak amplitude of each data set. The standard viscosity oils were firstly measured using the process in Figure 3-20, to produce a viscosity calibration curve. The calibration curve was then produced by calculation of S_{pk} for each known viscosity oil measured.

3.7.1. Auto-Referencing Method

One disadvantage of the previous signal analysis method is the requirement for a reference signal, hence an alternative method which uses only the measurement signal to find the viscosity can be used. This was completed by using a peak in the same signal which is unaffected by viscosity as the reference amplitude. All peaks in the SW signal are influenced by a change in temperature, due to changes in physical properties of the materials which will be discussed in Section 7.3.2. However each antinode is affected by viscosity to a varying extent when using the SW method. It could be feasible to use a peak which is unaffected by viscosity as the reference amplitude, if the behaviour of the signal in the reference condition is known for a range of temperatures.

In order to evaluate this method, two alternative signal processing methodologies have been investigated:

- Individual peak selection
- Fixed frequency

Figure 3-21a and Figure 3-22a show the individual peak selection method which requires peak finding for each averaged measurement signal, whereas Figure 3-21b and Figure 3-22b show the fixed frequency method, where one frequency is chosen and the amplitude of the signal at this frequency consistently used for each measurement.

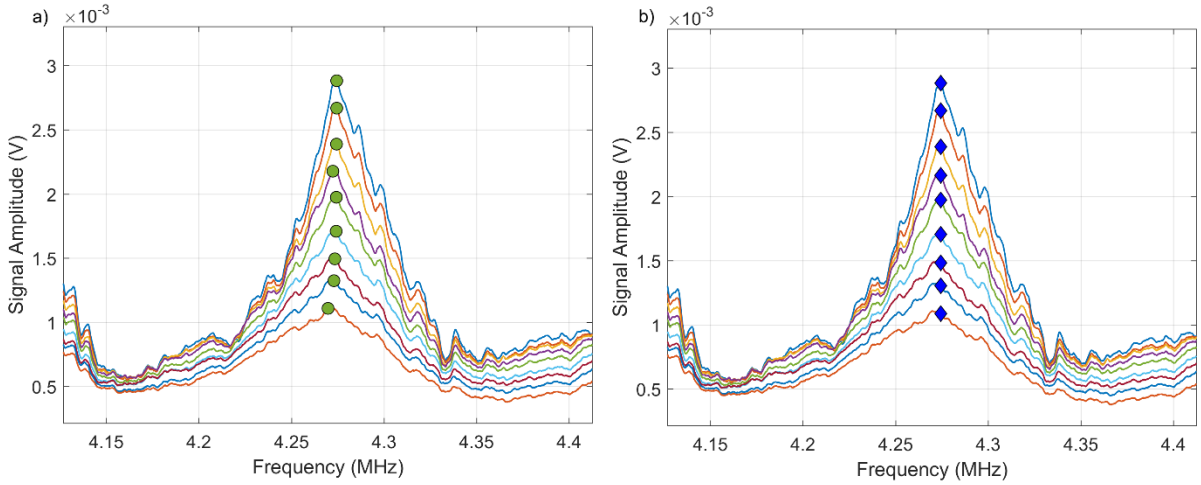

Figure 3-21: Measurement amplitude selection (Peak 19 in Figure 4-17); a) using the individual peak selection method and b) peak selection using the fixed frequency selection method.

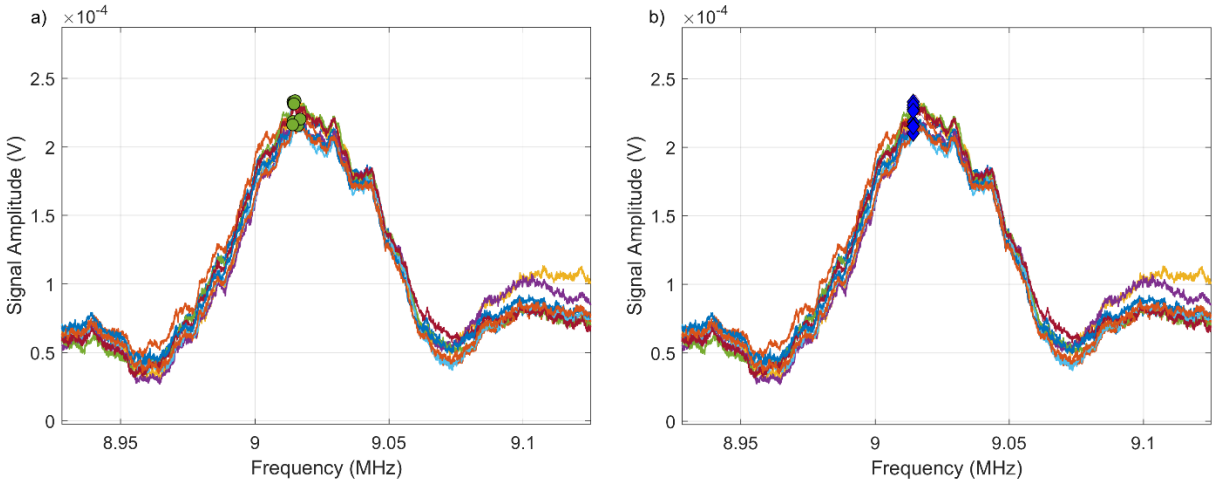

Figure 3-22: Reference amplitude selection (Peak 42 in Figure 4-17); a) using individual peak selection b) peak selection using the fixed frequency selection method.

3.7.2. Peak Finding Analysis

The amplitude of the reference and measurement peak was defined using a peak finder function in Matlab®, using the ratio of amplitude of the reference to measurement peak. This produces the Auto-referencing standing wave reflection coefficient 'S_A'. This value was then used to

produce an auto-calibration curve by assigning the known viscosity of the oils tested, from Table 3-2, to the S_A value. S_A values were obtained from the measurement data only.

Peak selection technique: the peak finder function in Matlab® was used to identify the individual location and amplitude of the peak at 4.27 and 9.014 MHz, the amplitude of these peaks were then used to find S_A.

Fixed frequency technique: an array of the average profile of all oil measurements was composed, with the addition of frequency as the first column in the array. The array was then indexed at the frequency of the peak amplitude defined from the first peak selection then corresponding values of S_A could be calculated for each oil.

Signal processing for both methods of auto-referencing was completed using the same protocol outlined in Figure 3-20, but for two peaks in the same data set for solid-oil conditions only. To find the viscosity of a liquid which was unknown, the liquid sample was measured, as per the protocol outlined in Section 3.6.3, but no reference signal was required. This technique can be used for a single temperature if the relative amplitude of the reference and measurement peak are known independently for temperature and viscosity previously. The response of these peaks are used to find the calibration curves, which can then be used for subsequent liquid measurements.

3.7.3. Peak Frequency Temperature Determination

The temperature of the metallic component will influence the ultrasonic signal due to a change in the transducer response and thermal expansion of the component in which the wave travels. As temperature increases and the propagation length increases, larger wavelengths, and thus lower frequencies within the material resonate, seen as a peak shift in the frequency domain. A SW profile shift to lower frequencies is intensified by a reduction of c_s, and also deviation of α, which all accumulate to produce the unique response of each system to temperature, therefore an individual calibration for each component must be made.

Temperature will influence the maximum amplitude of the signal produced by the transducer, and also the resonant peak frequency, as shown in Figure 3-23. Because of this the SW peak frequency can be used to determine the temperature of a component as the peak frequency changes with temperature. This could be useful for applications where the temperature of the measurement surface is likely to differ from the location in which temperature is measured.

The frequency of the resonant peak in the measurement condition can therefore be used to determine the temperature of the component at the time of the measurement if a prior temperature calibration has been completed. A calibration is completed by acquiring the reference signal at a range of temperatures to determine how the peak amplitude changes. To complete a temperature calibration, the device can be placed into an oven, heated to a temperature above the maximum operating temperature then slowly allowed to cool. Reference signals at a range of temperatures can therefore be captured periodically as the device cools.

This signal then acts as a temperature indication for the measurement signal as peak frequencies of the measurement and reference signals will align if the temperature which they were taken is the same. The influence of temperature on a reference signal is shown in Figure 3-23.

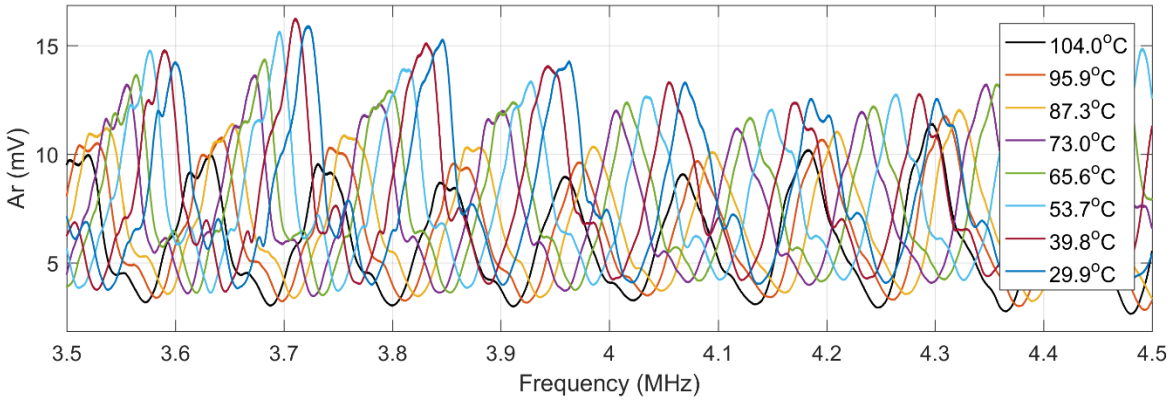

Figure 3-23: The influence of temperature on the SW profile.

This procedure will be used in Chapter 9 for viscosity measurement at varying temperatures.

3.7.4. Summary

In summary, standard ultrasonic hardware can be used to generate a standing wave signal. Parameters which define the standing wave, such as frequency selection of the sweep span and centre frequency as well as the sweep time are defined by the experimental arrangement, and so initial evaluation is required to determine sufficient resolution of the signal. When capturing the standing wave signal the full frequency content is acquired, although this requirement could be reduced to only the envelope of the signal, acting to reduce the resolution of the hardware required, in turn reducing costs.

The method has been implemented using bare element piezoelectric transducers onto an aluminium plate to simulate an engineering part, as many engineering components are metallic. Implementation of a matching layer with the technique has also been produced in order to define the synergistic effect of both techniques of improving ultrasonic viscosity measurement, and thus the procedures sensitivity will be evaluated. The test rig was evaluated using a series of Newtonian standard viscosity oils which are commonly used to calibrate viscometers as they are supplied with a certificate of analysis which details the $\eta - T$ relationship. The standing wave method offers the opportunity for auto-referencing, and so methodologies which use a standard solid-air reference signal and alternative methods have been detailed.

4. Newtonian Viscosity Measurement using the Standing Wave Method.

In this chapter the standing wave method is evaluated against a pulsed ultrasonic technique for Newtonian viscosity measurement to compare viscosity measurement sensitivity and accuracy. The methods are evaluated in two physical component arrangements, the first with a ML at the oil interface, and the second without a ML. The four following ultrasonic viscosity methods are compared and referred to as follows from herein: Pulsed Wave no ML (PW); Standing Wave no ML (SW); Pulsed Wave with a ML (PW ML); Standing Wave with a ML (SW ML) unless explicitly stated.

The relationship between R or S with η was found for each technique, by initial measurement of nine standard Newtonian viscosity oils. The tabulated viscosity values for each oil were used to initially define this relationship, which were then validated using a Couette viscometer. A number of blended oils formulated using a mixture of two standard oils were produced to assess the capability of each ultrasonic method. Test data was first analysed in a standard sequence, where the reflection from a solid-air interface is required for each solid-liquid measurement, then an auto-referencing technique will be evaluated against this result to test the feasibility of this approach for referencing when using the SW method. Furthermore a clear comparison between two data analysis techniques, fixed frequency and peak selection, was completed.

4.1. Test Parameters and Initial Observations

The viscosity calibration was performed using the operating parameters previously defined in Table 3-1 for the SW method. The peak observed to have the greatest sensitivity in the ML and no ML arrangements was selected for the PW method. The signal generation parameters for each ML and no ML conditions are outlined in Table 4-1.

Measurements were recorded at room temperature, which remained within $\pm 1℃$ for the full duration of the test and so may be considered isothermal. The SW signal differs with and without the addition of the ML, resulting in different measurement frequency selection for each method as the frequency identified as the most sensitive was chosen from tests carried out using the calibration oils using the SW method. The corresponding frequency of the resonance from the SW method was then used for the PW method to permit ML comparability. Figure 3-15 shows an image of the test piece used to evaluate the four ultrasonic viscosity measurement methodologies.

Table 4-1: PW and SW Test parameters

Signal Type	Generation Parameters	Sample rate (Mega Samples per Second)	ML
SW	Centre Frequency: 5 MHz Frequency Span: 9 MHz Sweep time: 10 ms Voltage: 10 Vpk-pk	31.25	No ML
SW ML	Centre Frequency: 5 MHz Frequency Span: 9 MHz Sweep time: 10 ms Voltage: 10 Vpk-pk	31.25	$50\mu m$ Polyimide
PW	Frequency: 3.1 MHz 10 cycle burst Voltage: 10 Vpk-pk	500	No ML
PW ML	Frequency: 4.45 MHz 10 cycle burst Voltage: 10 Vpk-pk	500	$50\mu m$ Polyimide

4.1.1. Conventional Measurement of Sample Viscosity.

In order to validate the ultrasonic measurement technique using the tabulated viscosity values given in Table 3-2 for each oil a DV1 digital Couette viscometer (Brookfield^{TM}) was used to measure the viscosity of each standard oil at 20, 25 and 30℃. Viscosity values were then compared to the documented standards (provided by the Cannon® Instrument Company (Cannon Instrument Company 2018)) at the same temperature measured using the viscometer to provide multiple measurements at different temperatures. The results showed good agreement as shown in (Figure 4-1).

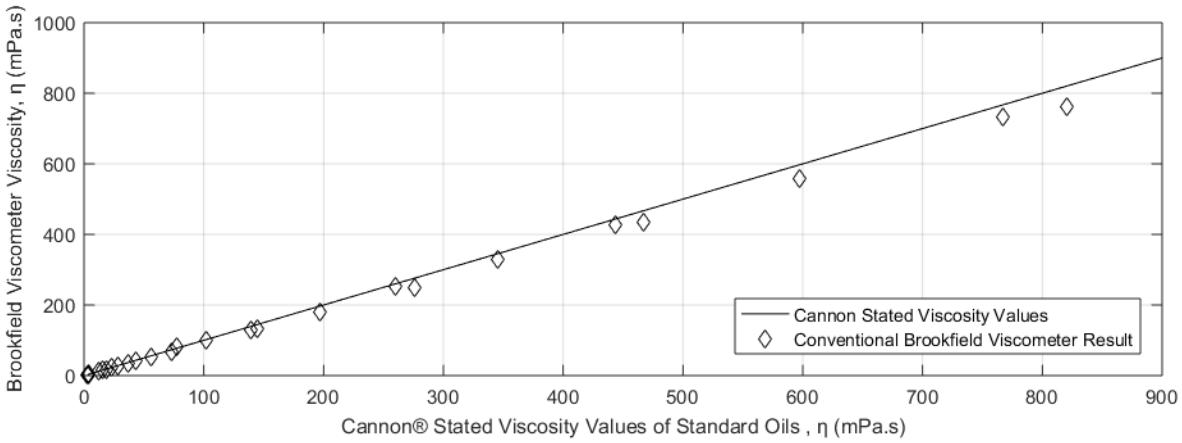

Figure 4-1: A graph to show the comparison between Cannon® stated values and conventional Brookfield viscosity results.

The results of the 25℃ Couette measurement of each standard can be seen in Table 4-2 alongside values from the tabulated viscosity values. This step was completed to validate the

Couette measurements of the blended oils for comparison with ultrasonic results. Couette measurements of the blended oils are shown in Table 4-3, details of the blended oils can be found in Section 3.5.2. The Vogel equation (Equation 2-5) was then used to determine the viscosity of the oils at the same temperature as the ultrasonic measurements.

Table 4-2: Corresponding density and viscosity of Cannon^{TM} standard oils at 25ºC.

Cannon^{TM} standard oil	**Density (kg/m^3)**	**Tabulated viscosity, Cannon Instrument Company® (mPas)**	**Couette η (mPa.s)**
S3	865.1	3.6	3.5
S20	850.9	28.8	26.8
S60	863.6	102.4	98.4
S200	836.9	345.2	330.5
S600	843.5	1049.0	993.3
N10	855.2	15.5	14.7
N35	857.5	55.56	51.8
N100	867.7	197.5	179.8
N350	840.4	597.1	558.2

Table 4-3: S600:S200 and S600:S3 blended Cannon^{TM} standard Newtonian viscosity oil Couette measurement at 24ºC.

High η band		**Low η band**	
S200 percent volume (%)	**Couette η (mPa.s)**	**S3 percent volume (%)**	**Couette η (mPa.s)**
7.1	1080.1 $\pm$ 10.80	42.9	65.1 $\pm$ 0.65
14.3	930.1 $\pm$ 9.30	50.0	42.0 $\pm$ 0.42
21.4	980.2 $\pm$ 9.80	57.1	28.3 $\pm$ 0.28
28.6	787.4 $\pm$ 7.87	64.3	19.4 $\pm$ 0.19
35.7	736.0 $\pm$ 7.36	71.4	13.5 $\pm$ 0.14
42.9	665.0 $\pm$ 6.65	78.6	9.3 $\pm$ 0.09
50.0	661.1 $\pm$ 6.61	85.7	6.7 $\pm$ 0.07
57.1	534.9 $\pm$ 5.35	-	-
64.3	559.8 $\pm$ 5.60	-	-
71.4	468.0 $\pm$ 4.68	-	-

4.1.2. The Influence of the Matching Layer on the Standing Wave and Pulsed Wave Signals

While the effects of liquid viscosity on an ultrasonic wave are well studied, the influence of viscosity on the amplitude of a shear standing wave have not, at the time of writing, been documented. Through initial observation of the SW method, a single frequency measurement

was selected to be used in the PW method, corresponding to the peak frequency of the measurement antinode in the SW. In order assess the behaviour of the SW method, the influence of Newtonian test oils was measured and the amplitude of the FFT evaluated using the procedure detailed in Section 3.7. Figure 4-2 shows the SW response to S200 oil. The presence of liquid at the solid interface reduces the amplitude of the SW both with and without the presence of the ML to differing extents.

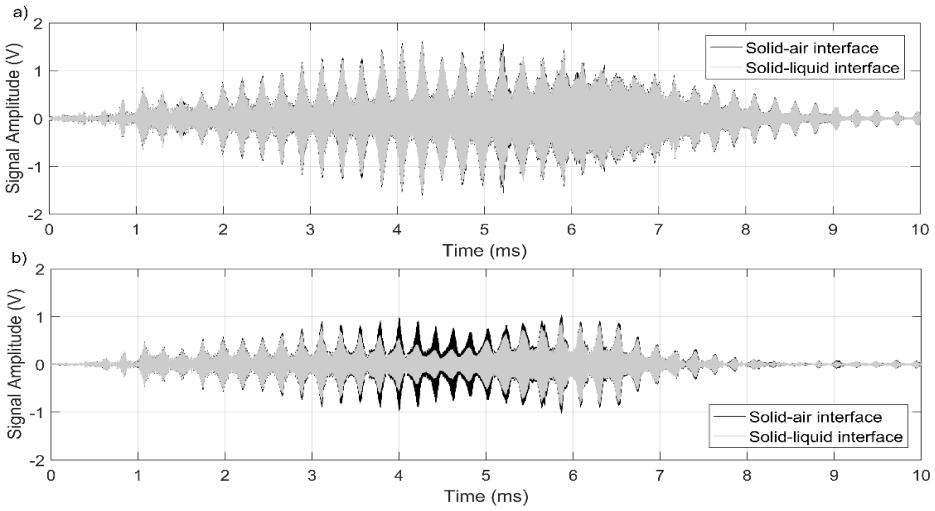

Figure 4-2: The influence of viscosity on the signal amplitude (a) without a ML and (b) with a 50 µm polyimide ML. Measurement was made using the S200 Cannon^{TM} standard oil (345.2 mPa.s).

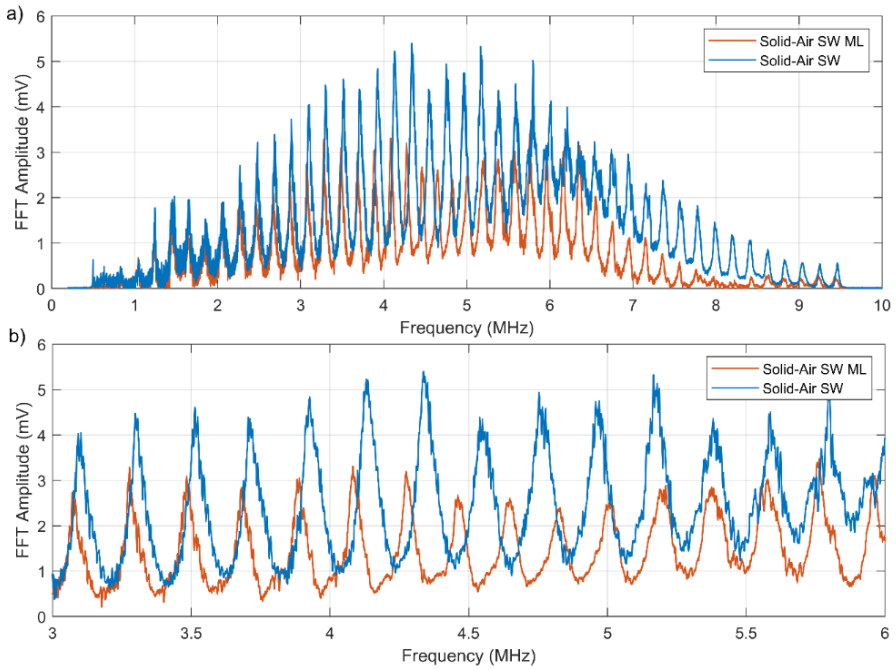

Figure 4-3: FFT of Solid- air reference SW signals with and without a ML, a) full profile, and b) magnified section.

Figure 4-3a shows the FFT of the solid-air interface with and without the ML, while Figure 4-3b is a magnified image of the same signals in Figure 4-3a to show the deviation of the signals at the frequencies most affected by the addition of the ML. Multiple antinodes and nodes are influenced by the addition of the ML, shown in Figure 4-3a and b as the shift in resonant peaks between the two profiles. The entire signal amplitude reduces, although the amplitude of the signal around 4.5 MHz appears to reduce the most. This may be explained by the extra material in the form of the ML which the ultrasonic wave must propagate, and also the number of interfaces it may incur. Within the centre of the sweep, the signal from the ML configuration shows a dip, characteristic of a resonant dip, although many peaks are influenced. The FFT of the solid-(ML)-air and solid-(ML)-liquid interfaces are shown in Figure 4-4 to highlight the sensitivity of each wave profile when measuring the same viscosity oil.

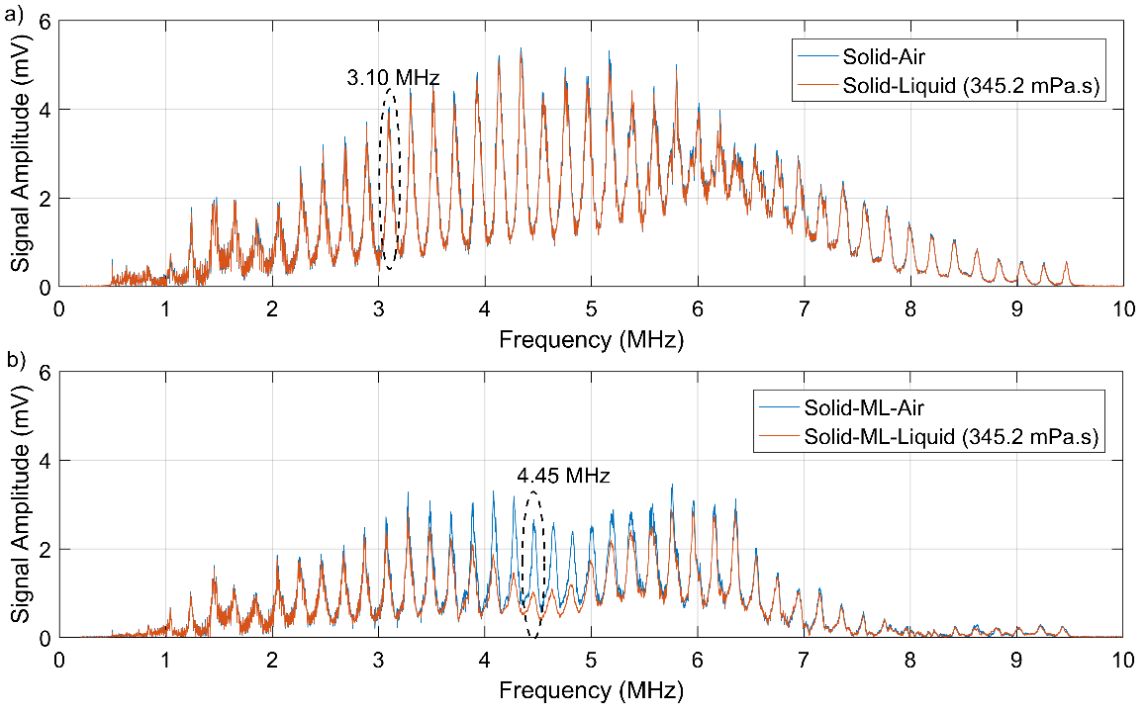

Figure 4-4: (a) An FFT profile of Figure 4-2(a), a SW signal with no ML and (b) the FFT profile of Figure 4-2(b) a SW signal with the presence of a ML.

The amplitude of the SW signal in the solid-liquid measurement condition, shows a uniform reduction in amplitude in comparison to the reference signal. The SW ML signal peaks closest to the resonance of the ML show the greatest amplitude reduction, although sensitivity is seen to reduce as the peak frequency deviates from this value.

With the ML, greatest sensitivity is expected at the peak closest to the frequency which corresponds to the quarter wavelength of 50 μm, in the case of the ML used here, this is 4.25 MHz, calculated after the re-arrangement of Equation 2-35. The highest sensitivity is experimentally seen at 4.45 MHz, highlighted in Figure 4-4b. This frequency deviation may be due to the additional glue layer added as a consequence of the additional ML.

The greatest sensitivity using the SW method without the ML was found to be 3.1 MHz, highlighted in Figure 4-4a by an elliptical marker. The most sensitive peak frequencies

identified using the SW approaches were then used to create corresponding PW method measurements. The PW pulses and FFT results are shown in Figure 4-5.

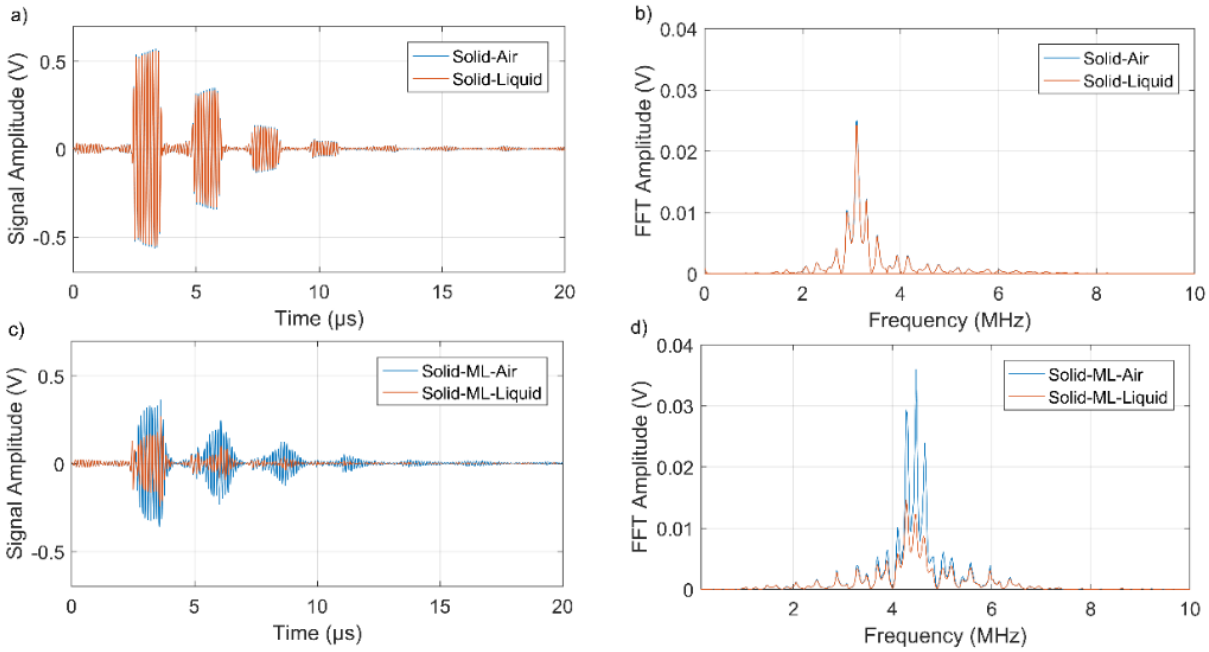

Figure 4-5: A reference reflection against air, and measurement signal against S200 oil (345.2 mPa.s) using a 3.1 MHz 10 cycle burst sine wave, a) without a ML, and c) with the ML. b) and d) show the FFT of the time domain signal respectively.

The addition of the ML, produces a greater sensitivity of the PW signal, shown by a greater reduction of the measurement amplitude in Figure 4-5c and d. This ultrasonic technique has been evaluated previously (Schirru et al. 2015; Schirru & Dwyer-Joyce 2015) and so will be used as a successful comparative method.

4.1.3. Standing Wave Viscosity Calibration Results

a) Without a ML

The influence of viscosity on the SW method without the ML is shown in Figure 4-6 by the S spectrum. The spectrum illustrates the requirement for resonant peak selection, as S fluctuates with frequency at differing extents throughout the signal.

Frequencies which constructively interfere within the component show a greater sensitivity to η, indicated by a negative correlation between η and S. The amplitude of the peaks observed in the S-f plots are generated by the excitation frequencies that constructively interfere within the component. As previously demonstrated by the multiple reflection method by Greenwood et al. (Greenwood et al. 2006), this acts to increase the influence of the solid-liquid interface on the signal. The amplitude of frequencies which correspond to nodes show little relation to viscosity, possibly as these frequencies lie within the noise of the signal. This fluctuation of S over the f span indicates the importance of peak selection when using the SW method, but also the heightened sensitivity at the peak locations.

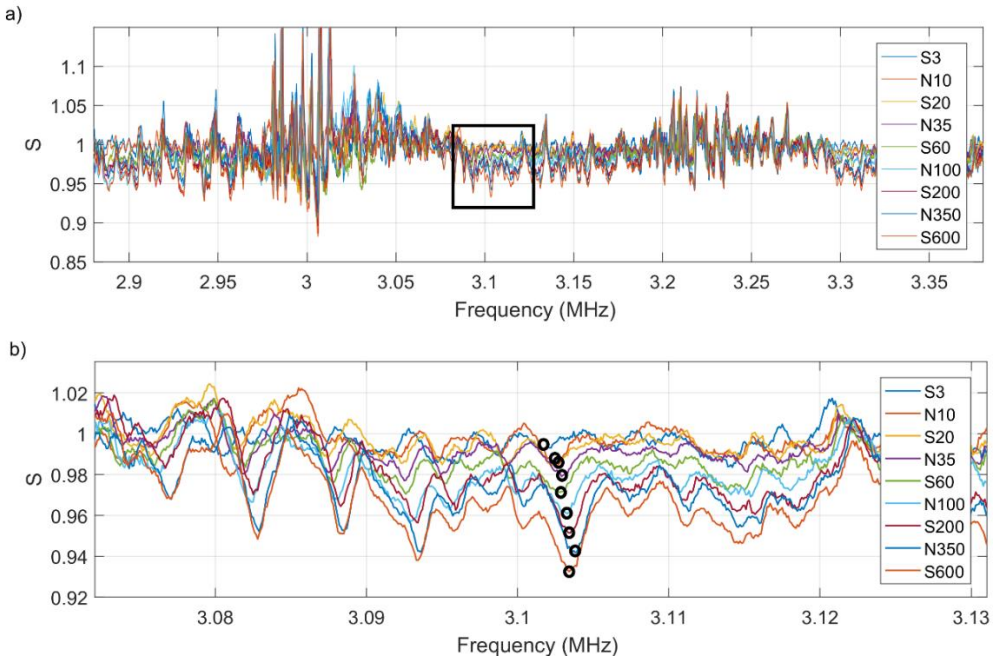

Figure 4-6: a) The influence of η on S, and b) Peak selection highlighted by the black circles when using the SW method without the ML for a magnified portion of the signal.

When a frequency which resonates within the component is selected at each measurement condition, the relationship between η and S can be found, as shown in Figure 4-6b. The value of S here reduces with increasing η, also resulting in a slight change in frequency increasing with incremental η measurement. Newtonian fluids may exhibit non-Newtonain behaviour at high viscosities, even though at the frequencies used here, liquids are thought to reside in the second Newtonian plateau (Schirru et al. 2018) due to the order of shear rate used. Thus a better reasoning may be given by a temperature fluctuation between measurements, which would result in a frequency deviation of the signal. The influence of phase at the measurement interface may also account for this, however this will be further analysed in Chapter 6, by the comparison of the phase of a measurement and reference signal.

Without the ML when a liquid is measured directly at the aluminium interface using the SW method, viscosity is seen to predominantly influence the amplitude of frequencies at resonant peaks only, showing a narrow frequency susceptibility in comparison to the SW method when a ML is present.

b) With a ML

With the addition of the ML the effect of viscosity on the SW signal is enhanced as shown in Figure 6-7. The signal processing steps detailed in Section 3.7 are shown in the form of experimental results using the SW ML method in Figure 6-7. The FFT of the solid-air and solid-liquid reflection data shown in Figure 6-7b was calculated from the time domain signal (Figure 6-7a), then S was calculated by a direct division of signals to produce the S profile for each measurement, shown in Figure 6-7c. Peak detection was then used to find the average and standard deviation of the amplitude of each oil measurement, ultimately producing calibration curves for each frequency, shown in Figure 6-7d and e.

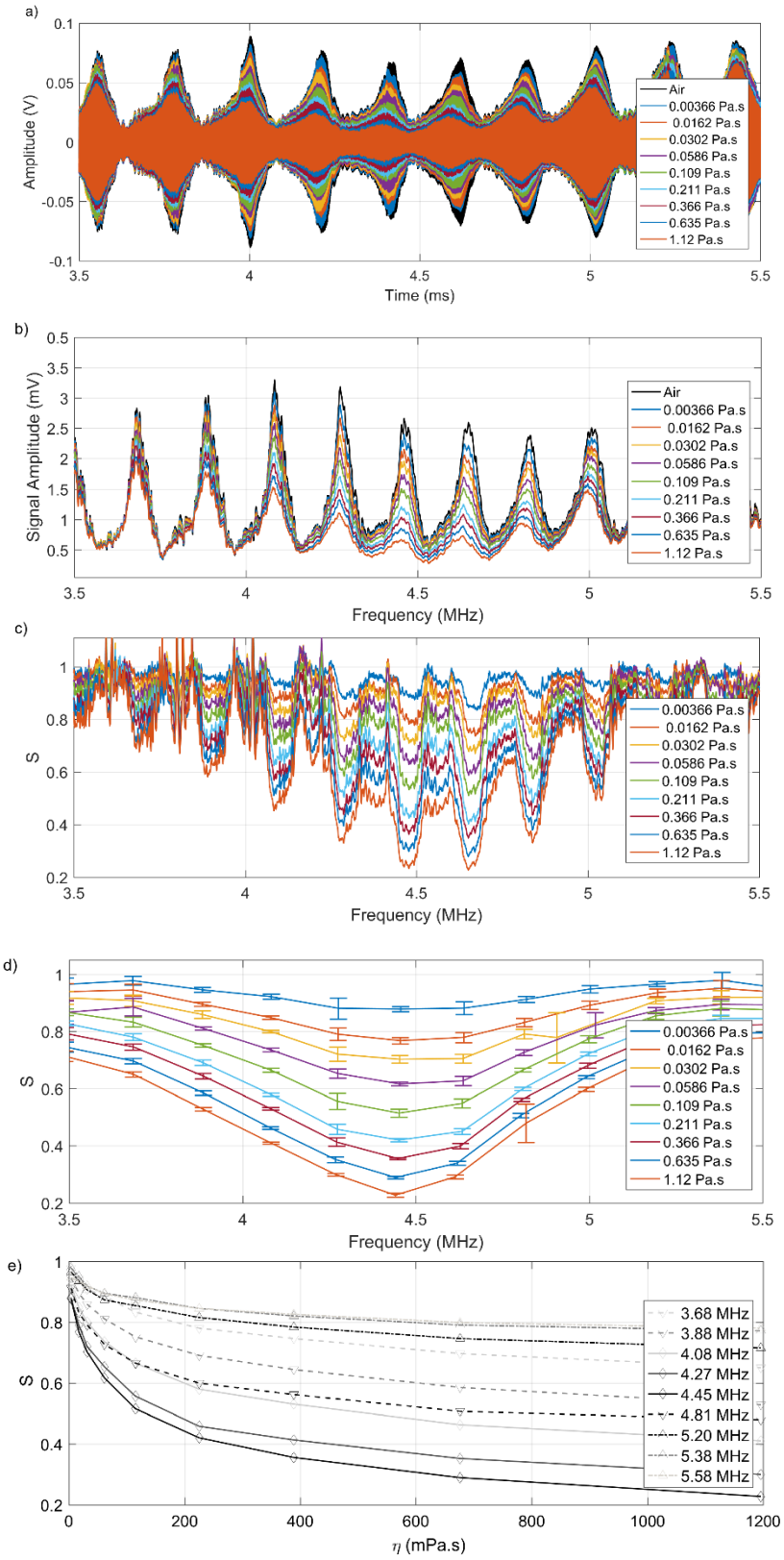

Figure 4-7: The influence of η on the SW with ML arrangement on a), the amplitude of the measurement signal, b) the amplitude of the FFT c) the S profile, d) the S profile at the peak frequencies, and e) the frequency peak selection on the S-η relationship.

When using a ML configuration, a large frequency range of the SW profile was shown to be influenced by viscosity, including the amplitude of nodes. Resonant frequencies show the greatest sensitivity, with the highest found at the centre of the resonant dip; produced by the combination of the ML, material geometry and transducer resonant frequency. This behaviour was reflected in the S profile, as higher viscosities produce a greater reduction in S at frequencies which correspond to resonant peaks.

c) S-η Calibration Relationship

The viscosity of the Cannon^{TM} standard oil at the same temperature as the experimental data was calculated using the Vogel equation (Crouch & Cameron 1961) using data provided by the Cannon Instrument Company. This was then used to create an $S-\eta$ curve for several peak frequencies around the centre of the span (Figure 6-7d).

The response at 4.08 MHz is seen to produce the smallest standard deviation (Figure 4-7d), indicated by the magnitude of the error bars. The 4.45 MHz peak was however selected as measurements at this frequency show the greatest change in S over the range of η, seen as the lowest curve in Figure 4-7e for the SW method with the ML. After completion of this procedure for both the SW and SW with ML condition, the results can be directly compared (Figure 4-8).

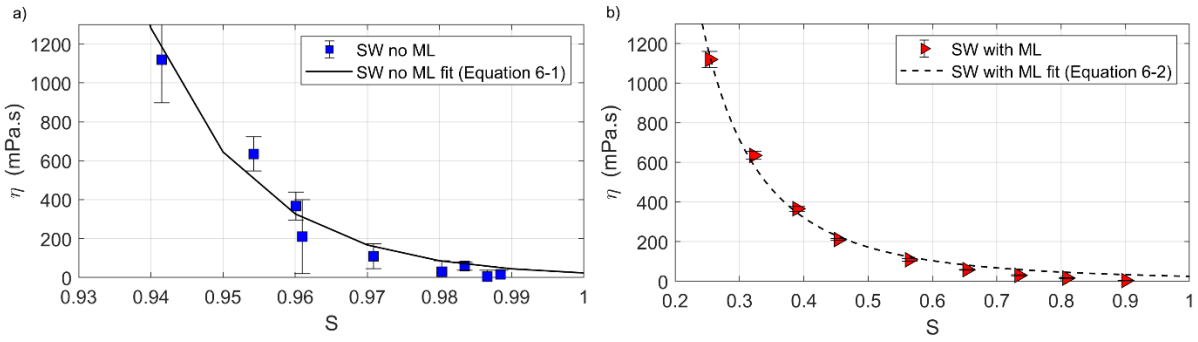

Figure 4-8: S-η calibration curves, SW with ML at 4.45 MHz, SW with no ML at 3.1 MHz.

Calibration curves for each method were produced with a Coefficient of Determination (COD) of 0.9607 and 0.9939 for the SW method without and with the ML respectively. Equation 4-1 was produced for data without the ML at 3.1 MHz, and Equation 4-2 with the ML at 4.45 MHz. The calibration curves are first order power equations which have been chosen as they follow the mathematical relationship outlined in Section 2.4.6, between liquid acoustic impedance and viscosity.

$$\eta = 23.06\, S^{(-64.94)} \quad |f = 3.10\ MHz \qquad \text{Equation 4-1}$$

$$\eta = 25.13\, S^{(-2.781)} \quad |f = 4.45\ MHz \qquad \text{Equation 4-2}$$

The relationships outlined for each method here are valid only for the peak frequency in which they have been calculated from. Although the acoustic impedance of the liquid is frequency dependent, a direct f match between the ML and no ML profiles was not possible due to a discrepancy in the peak location in each signal. The frequencies here are thought to be of a

suitable similarity however, as they both reside in the MHz range. As previous research suggests, the shear rates subjected to the oils from each method are similar enough to permit a comparison of method capability (Schirru et al. 2018).

4.1.4. Pulsed Wave Viscosity Calibration Results

The SW method has been shown to be capable of viscosity measurement with and without the ML, repetition of the calibration experiment was then completed using the PW method. These results are summarised in Figure 4-9 where the presence of the ML again is shown to improve the capability of the ultrasonic technique, a response documented by Schirru et al (Schirru 2016; Schirru et al. 2015; Schirru & Dwyer-Joyce 2015).

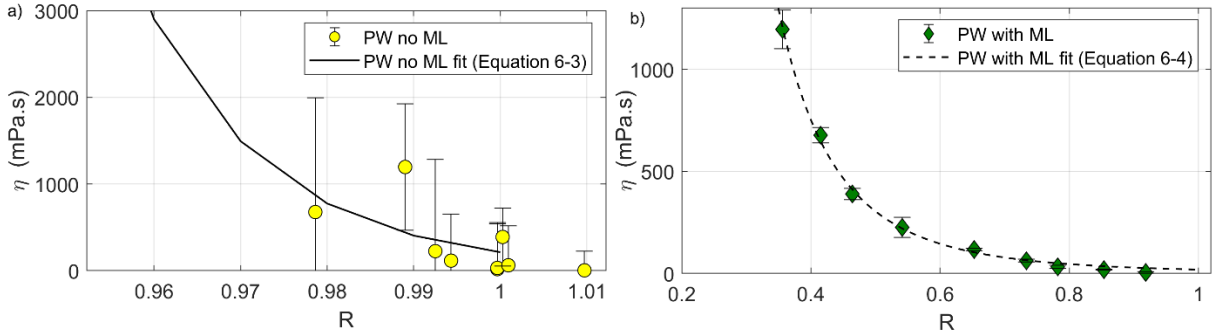

Figure 4-9: R-η calibration curves, for a) PW with no ML at 3.1 MHz, and b) PW with ML at 4.45 MHz.

The calibration curve produced for the PW method without the ML is shown in Equation 4-3 and with the ML in Equation 4-4. Corresponding coefficients of determination of 0.3769 and 0.9979 respectively.

$$\eta = 212.5\, R^{(-64.01)} \quad |f = 3.10\, MHz \qquad \text{Equation 4-3}$$

$$\eta = 18.13\, R^{(-4.063)} \quad |f = 4.45\, MHz \qquad \text{Equation 4-4}$$

4.2. Blended Oil Ultrasonic Viscosity Measurement

The blended oils, detailed in Table 4-3 were measured by each ultrasonic technique individually to produce a value of S and R for each oil at the frequency used for the calibration, 3.10 and 4.45 MHz for PW and SW respectively. The corresponding calibration curves in the previous section were then used to determine the viscosity of the blended oils. Figure 4-10 and Figure 4-11 show the viscosity measured using the four ultrasonic techniques, compared to data acquired from the Couette viscometer. Error bars were calculated from the standard deviation of 5 independently repeated experiments, in each instance three repeats were taken to account for signal fluctuations, producing 15 measurement signals for each oil in total.

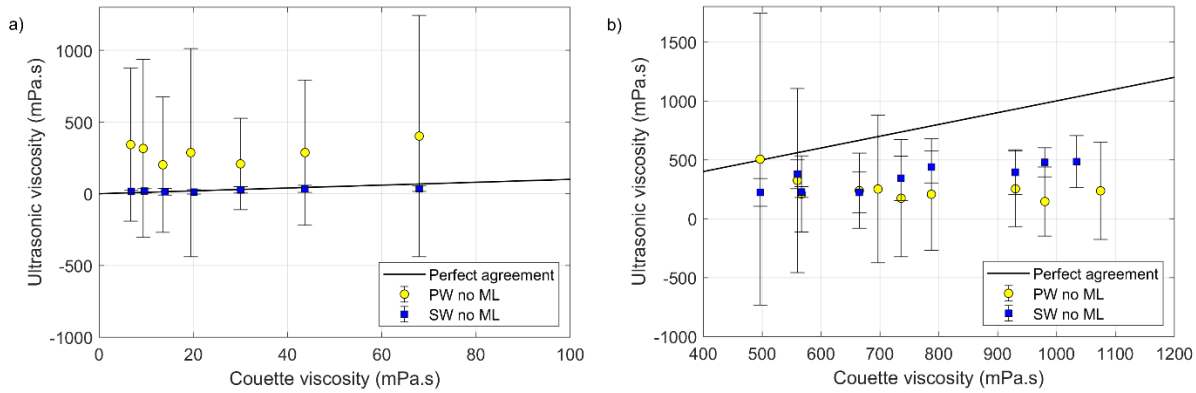

Figure 4-10: A figure to show the comparison of ultrasonic viscosity measurement using the PW and SW methods without a ML at a) low η, and b) high η.

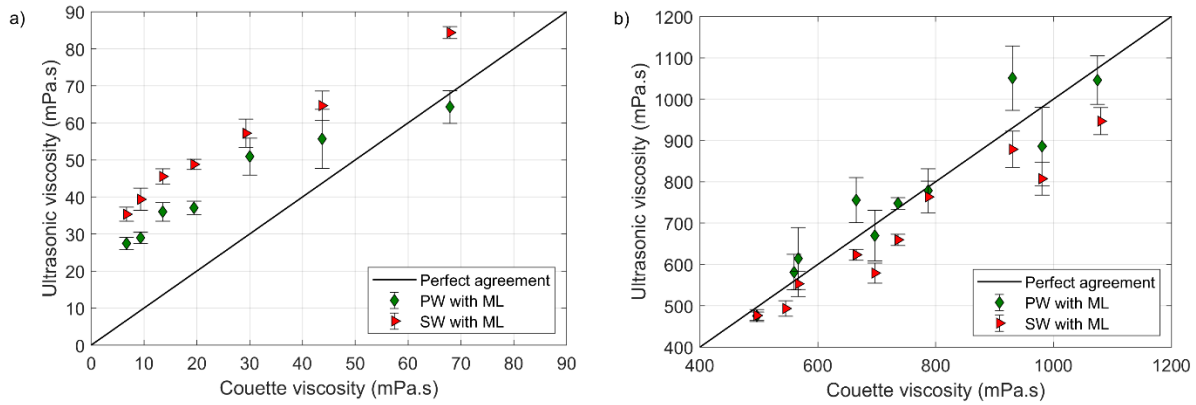

Figure 4-11: A figure to show the comparison of ultrasonic viscosity measurement using the PW and SW methods with a ML at a) low η, and b) high η.

In Figure 4-10 results indicate that the PW method is incapable of viscosity measurement over the full range of frequencies measured here. Little difference can be seen in R with the presence of the Cannon^{TM} standard oils for the PW method without the ML. Only a small difference is shown between 0 and 200 mPas tending to 1 in all cases. The change in R between 200 and 1200 mPa.s fluctuates with a large standard deviation, making viscosity measurement in this range difficult to distinguish from noise in the signal.

Although viscosity measurement using the SW method is conducted using the same apparatus, greater capability is achieved. Figure 4-10a and b show a significant reduction of error bars associated with the SW method in comparison to the PW method, and also greater agreement between ultrasonic SW and Couette viscosity.

When measurements are taken in the arrangement with the ML, better agreement between ultrasonic and Couette measurements were achieved. Clear agreement between both methods with the ML and with Couette measurements is shown in Figure 4-11a and b, while smaller errors seem to be associated with the SW method if the full range of viscosity values are taken into consideration.

4.3. Ultrasonic Viscosity Measurement Accuracy and Sensitivity

Errors associated with each technique from the Cannon^{TM} oil calibration data have been collated to find the accuracy at each viscosity expressed as percentage error of viscosity in Figure 4-12. The errors associated with each measurement have been calculated by the conversion of the standard deviation from the amplitude of the signals to viscosity for an indication of viscosity error within each technique for each oil measured.

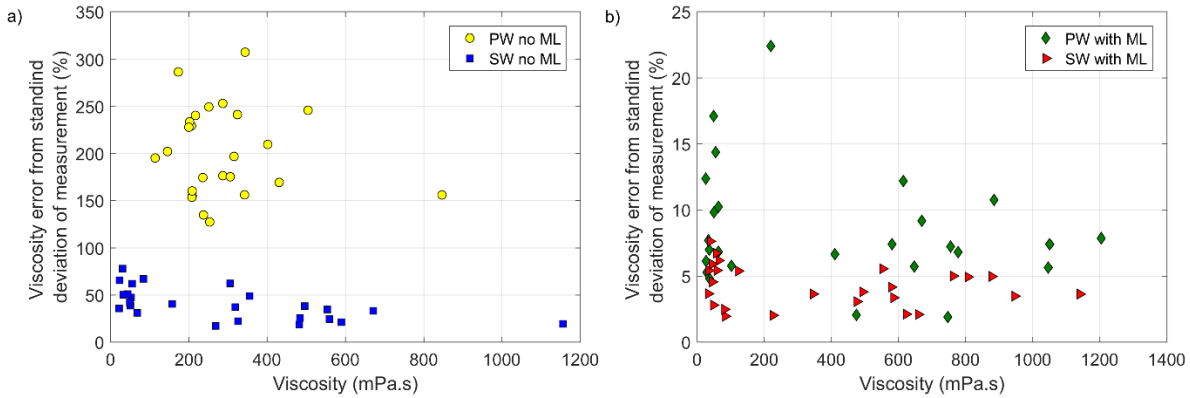

Figure 4-12: Ultrasonic viscosity error expressed in viscosity for SW and PW methods with and without the ML.

The lowest errors and thus highest accuracies are achieved using the SW ML method, closely followed by the PW ML method. Figure 4-12a shows the SW has lower viscosity errors than the PW method by an order of magnitude along the full range of viscosities investigated here without the ML. The SW method without the ML had significantly lower errors than the PW method without the ML, when a two tailed paired t-test was completed (P=0.027). While errors may seem large, shear wave viscosity measurement through a metallic component, as previously discussed is fundamentally challenging due to acoustic mis-match. The SW method has been found to partly overcome this limitation, shown clearly in Figure 4-10 as a direct comparison between the PW and SW methods. With the addition of the ML, a substantial difference was found between the errors produced by each technique, where P=0.092, although errors here are lower than those produced when using the SW method without the ML.

Figure 4-13 shows ultrasonic deviation from the expected viscosity value measured by the Couette viscometer for each ultrasonic technique. Results highlight how the SW method improves upon the PW method without the ML for 90% of the data. The improvement is particularly prominent in the lower viscosity band, expected due to the almost complete inability to measure viscosity in this range using the PW method without a ML at a metallic surface. Figure 4-13 also shows the similarity between errors produced from the PW and SW method with the ML.

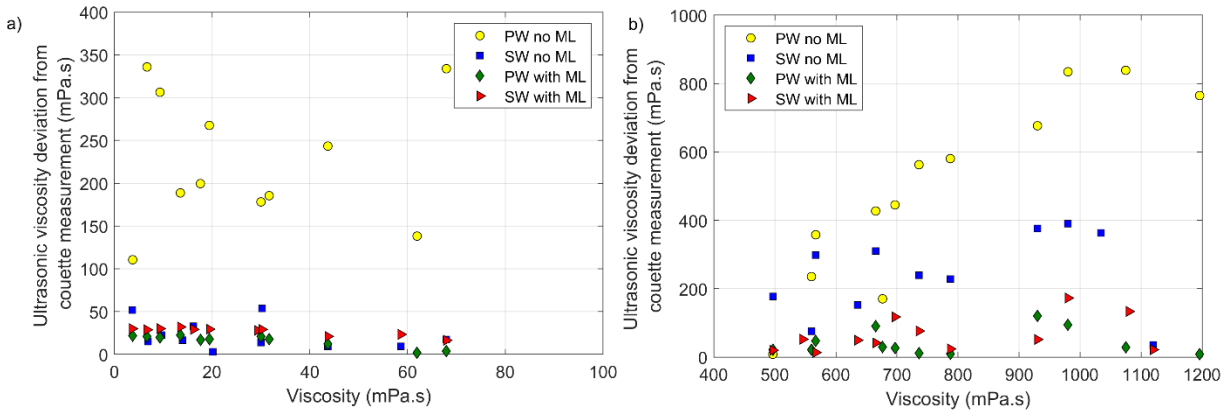

Figure 4-13: a) low band and b) high band, viscosity ultrasonic deviation from Couette measurement of the blended oil sample.

To evaluate each technique fully, a value of R or S was calculated for 1000 mPa.s for each technique by re-arranging the calibration equations (Equation 4-1, Equation 4-2, Equation 4-3, Equation 4-4). The response of each technique was then directly compared, as shown in Figure 4-14 to investigate the potential sensitivity of each method. The greater the reflection value range the greater the sensitivity of the technique. The addition of the ML, as outlined by Schirru et al. (2015) significantly improves in-situ liquid measurements through a metallic substrate using the PW and SW methods. When using the PW method, R is almost 25 times greater with the ML, while for the SW method S is 13 times greater with the addition of a ML. The ML is therefore shown to increase the sensitivity of ultrasonic viscosity measurements as there is a larger number of measurable increments for a given change in viscosity. Increasing sensitivity in this manner improves the precision of the measurement allowing greater accuracy to be achieved in viscosity measurement.

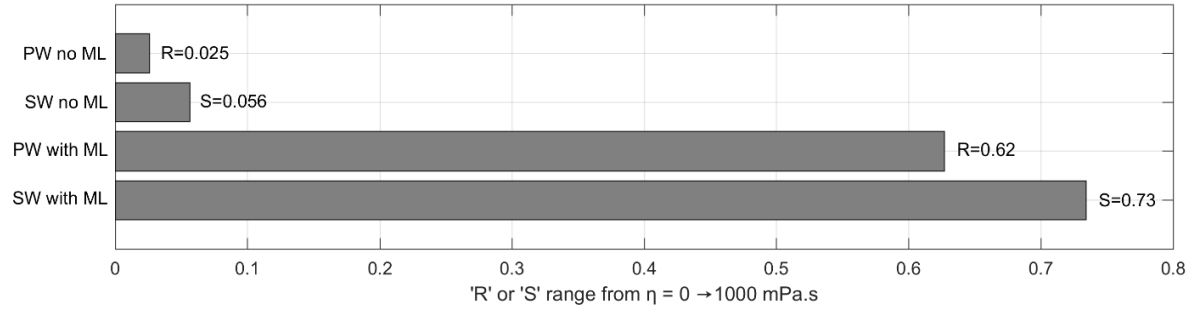

Figure 4-14: A bar chart to show the measurement range of S and R of each technique.

It is clear that ML improves viscosity measurement when using both ultrasonic methods; though the SW method shows greater sensitivity than the PW method in each arrangement. In the absence of the ML the PW method reflection range is more than doubled by using the SW method, from $R = 0.025$ to $S = 0.056$, and in the presence of the ML the reflection range from the PW method increases by 17% by using the SW method. The value of S reaches 0.94 at 1.12 Pa.s, giving the technique a greater sensitivity to liquid viscosity in comparison to R when using the PW method which reduces to only 0.98, therefore doubling the sensitivity of viscosity measurement at a metallic interface.

The addition of a ML when using the PW technique gives a clear reduction in R and associated errors for all oils measured. It is clear that the ML acts to greatly improve ultrasonic sensitivity to liquid viscosity; while the SW method acts to further improve the response of S, also reducing associated error. The sensitivity of each technique at each viscosity band was then determined by the calculation of a change in S for individual viscosity bands, the results of which are shown in Figure 4-15.

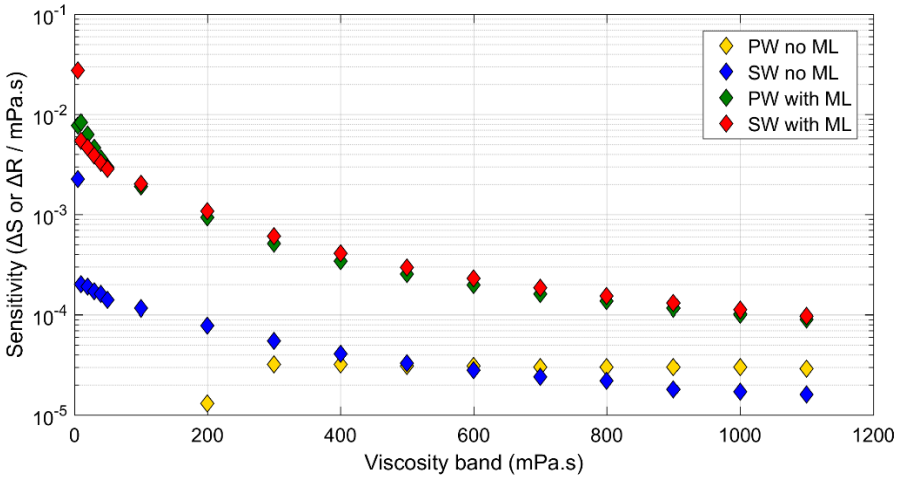

Figure 4-15: Comparison of the sensitivity of each method.

Figure 4-15 shows the change in S per mPa.s for a range of viscosities for each technique. The 'Viscosity band' value represents the band between the value itself and the previous value. i.e. data at 400 mPa.s represents the 350 to 400 mPa.s. The sensitivity of the PW method without the ML was calculated to have no sensitivity between 5 and 200 mPa.s. This was shown through a reflection coefficient of 1 and hence no measurable ultrasonic response to viscosity in this range was possible. The SW method without the ML however shows some sensitivity to viscosity measurement within 5-200 mPa.s. While the sensitivity is a few orders of magnitude lower than that achieved with a ML, the relationship between viscosity measurement ability and viscosity, is seen to follow the same trend as that shown by the ML techniques.

By combining the SW method with the ML approach a resonant peak of the highest sensitivity could be achieved at the frequency which is completely constructive within the component, and completely destructive within the ML. The most sensitive peak was found to be that which was located near the centre of the resonant dip produced by the ML, indicating the ML importance here.

4.4. Auto-Referencing Analysis

The auto-referencing analysis method uses antinodes of the SW signal which are not sensitive to the presence of oil but still sensitive to temperature and transducer output as references. This removes the need for solid-air reference signals at each temperature a measurement is made, and so increases the applicability of the method as features of the measurement signal itself are sufficient to produce a measureable viscosity value. This is completed by selection of a peak

which is affected by T but not η as the reference peak, and one which is affected by both T and η as the measurement peak.

Standard referencing and auto-referencing was used to analyse the same data set previously reported in this chapter. The resonant frequencies used as the measurement and reference peaks were first selected based on the procedure previously outlined in Section 3.7.1. The auto-reference procedure was evaluated on the SW method with the ML technique as this technique was deemed the most sensitive, with smallest errors in previous analysis to allow a direct comparison of analysis technique.

The relationship between the S value calculated using the auto referencing technique, (S_A) and η is determined for viscosity measurements between 3 to 1200 mPa.s to produce the auto-reference calibration curve. Zones of the SW signal which are affected by temperature, and those which are influenced by viscosity are highlighted in Figure 4-16. Figure 4-16a, shows how a solid-ML-air signal changes when the component is heated in an oven. The signal was periodically captured at a range of temperatures. It is evident that there is a relationship between frequency and temperature, however all peaks change in response to temperature. The data in Figure 4-16b was captured for a range of different viscosity oils at the same temperature.

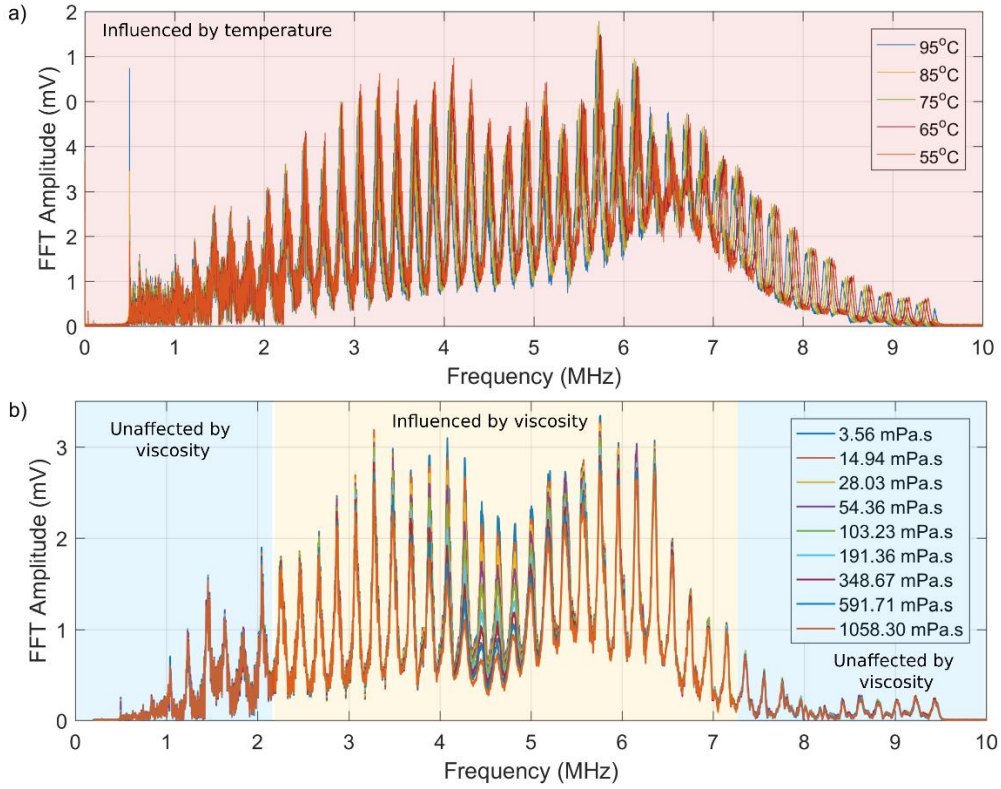

Figure 4-16: a) The influence of temperature on the SW profile, b) The influence of viscosity on the SW profile.

To complete auto-referencing, the reference and measurement peak must firstly be identified. As temperature variation influences the full spectrum of peak locations and amplitudes, it is the identification of peaks which are the most and least influenced by viscosity that are selected. The standard deviation of all viscosity measurement signals was calculated for the full range

of frequencies shown in Figure 4-16b. The peak with the lowest standard deviation, shown in Figure 4-17, was set as the reference peak (Peak 42), i.e. the peak which shows the smallest response to viscosity. The peak with the highest standard deviation in Figure 4-17 is selected to be the measurement peak (Peak 19), as it is this frequency which shows the greatest change in response to liquid viscosity.

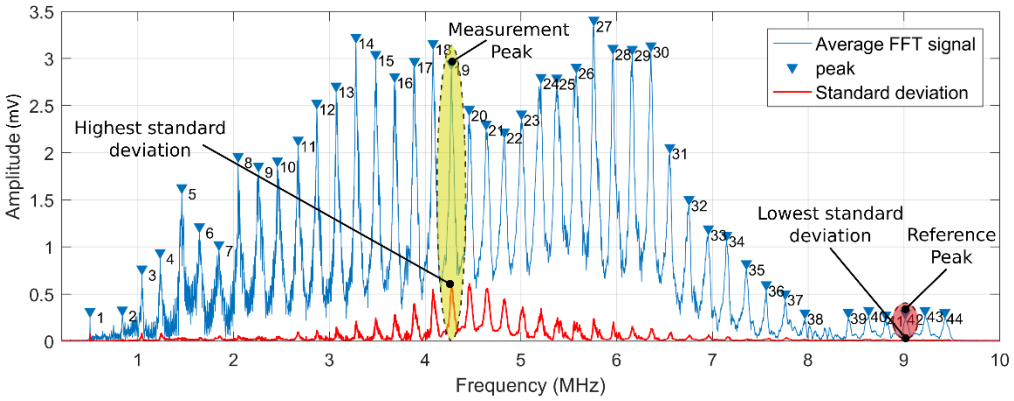

Figure 4-17: A figure to show the average FFT signal of all the measurement signals, and the standard deviation of this in the frequency domain.

The highest standard deviation was found when $f = 4.275$ MHz, Peak 19 in Figure 4-17, and the lowest standard deviation when $f = 9.014$ MHz, Peak 42 in Figure 4-17. Although the reference peak lies outside the bandwidth of the transducer, the stability of the peak amplitude was found to be sufficient to produce a measurement using these peaks. The ratio of peak 19 (measurement) and peak 42 (reference) was then calculated for each measurement signal using two methods. The fixed frequency method involves first selecting the peak frequency of the initial signal, then the amplitude of all other measurements at this same frequency (which may not be at the highest amplitude of that resonance for all other measurements) is used.

The frequency selection method involves finding the peak amplitude of the peak for each measurement signal, which may therefore occur at a slightly different frequencies. Results from both the individual peak selection and fixed frequency methods are shown in Figure 4-18.

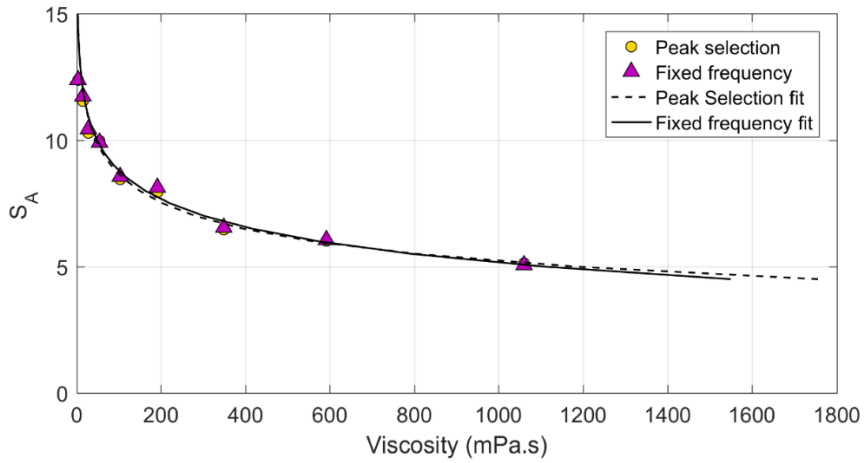

Figure 4-18: Calibration curve comparison of alternative auto-referencing methods. The COD was 0.9935 for the fixed frequency selection, and 0.9937 for peak selection.

This data was used to create a calibration curve for each technique. The calibration curve for the fixed frequency is given by Equation 4-5, and the individual peak selection method, Equation 4-6.

$$\eta = 13840e^{(-0.5723 \times S_A)} + 30130e^{(-0.9127 \times S_A)} \quad \text{Equation 4-5}$$

$$\eta = 9635e^{(-0.5402 \times S_A)} + 114100e^{(-1.074 \times S_A)} \quad \text{Equation 4-6}$$

When using the auto-referencing technique, the value of S_A has no physical meaning as it is a relative value for the specific measurement apparatus.

4.4.1. Auto-Referencing Analysis Technique Comparison to Standard Referencing.

The blended oil measurement signals were then analysed using the auto-referencing procedure and the viscosity was calculated for each technique using Equation 4-5 and Equation 4-6. A comparison of the results from each technique is outlined in Figure 4-19.

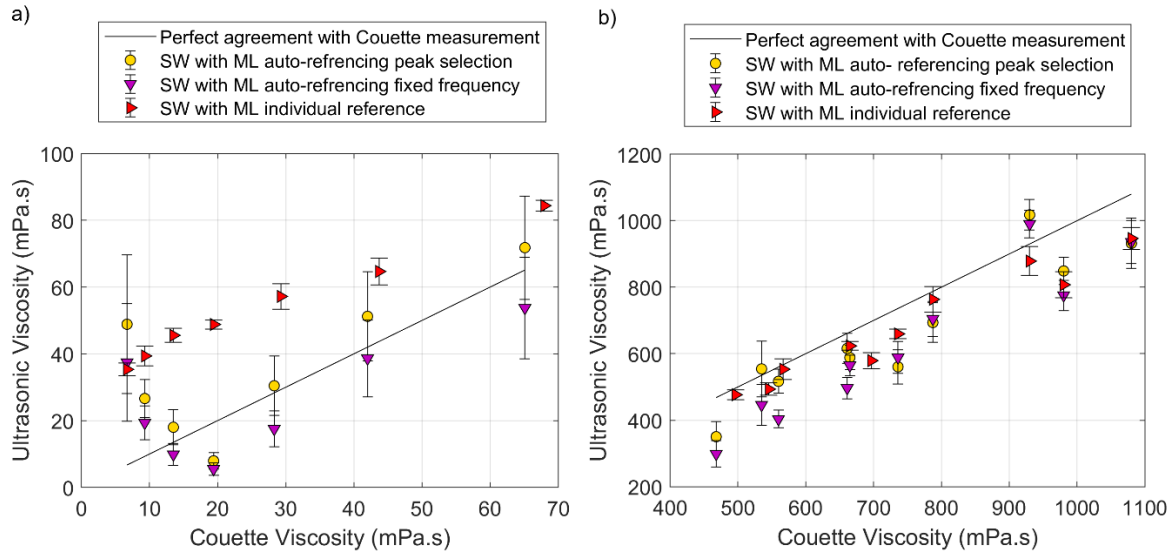

Figure 4-19: Auto-calibration peak selection method blended oil results.

Both auto-referencing techniques show a good agreement with the conventional technique without the need for a reference signal. This presents a favourable feature of the SW method as in some practical applications a solid-air interface may not be accessible and so not possible to acquire. The peak selection method produces viscosity values closest to the Couette measurement for the auto-referencing techniques, and while auto-referencing results do not provide accuracies as high as the individual referencing method, a two tailed paired t-test revealed no significant difference between the auto-referenced and individually referenced results, with a P value of 0.485.

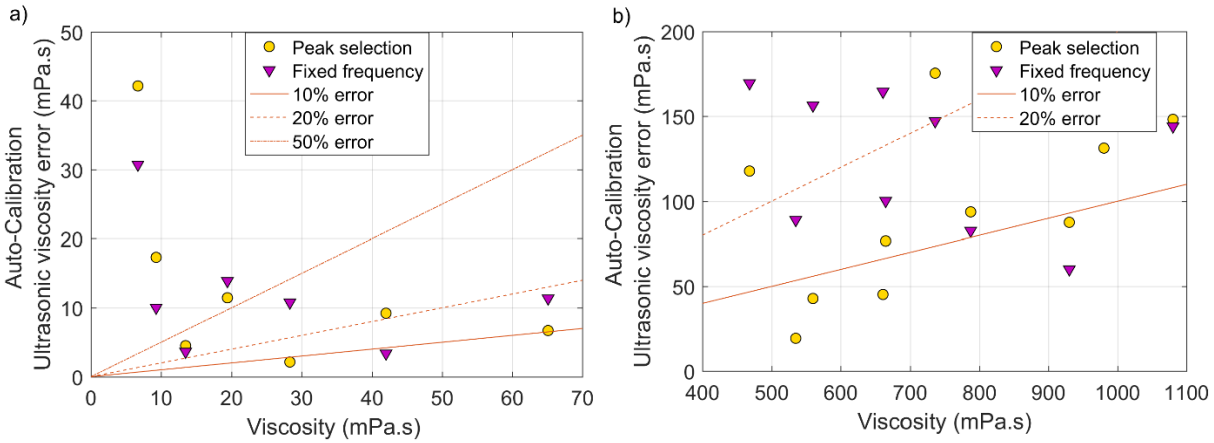

Figure 4-20: The viscosity error in mPa.s for each auto-calibration technique.

Figure 4-20 demonstrates how the error with each technique fluctuates over the range of viscosities measured here. The error here is that between individual referencing and the auto-referencing techniques. Although the relationships between viscosity and auto-referencing errors are similar, the peak selection method produces the lowest error, being an overall error of 1031.8 mPa.s in comparison to the fixed frequency cumulative error, which is 1402.3 mPa.s.

4.5. Discussion

The SW method uses the principles of interference to create a quasi-static standing wave composed of mixed frequency interference. Standing waves have previously been shown to improve sensitivity (Krautkrämer & Krautkrämer 1968), although the use of a mixed frequency signal is yet to be utilised for viscosity measurement. Within the non-destructive testing field, the use of standing waves has previously been isolated to component thickness as quote 'in other cases they may cause considerable confusion and should be avoided'(Krautkrämer & Krautkrämer 1968). However in practice the standing wave responds to conditions at an interface with greater sensitivity than the pulsed method for viscosity measurement, clearly shown in Figure 4-10a so demonstrating the potential of this method.

The standing wave reflection coefficient, S, achieved using the SW method are equivalent to the reflection coefficient, R when using the pulsed method. A smaller R or S value for a given viscosity indicates a greater ultrasonic sensitivity (the number of measurable points for a given change in viscosity) and so enables the technique to measure lower viscosity values. Viscosity measurements taken using the SW technique produce comparable values to those found by Greenwood et al. who reports a R of 0.9711 for a 107 ± 11 mPa.s liquid measurement at 14 MHz (Greenwood et al. 2006); where the SW method gives S=0.9708 for a 108 ± 10.8 mPa.s liquid at 3.1 MHz without the ML. From the relation shown in Figure 2-25 (for liquid acoustic impedance and frequency), measurement at a higher frequency results in a greater reduction of R so while R and S are similar for a liquid around 108 mPa.s using the multiple reflection technique, if materials used as the substrate were identical, the SW method would produce the highest sensitivity measurement.

Through further considering Figure 2-25, and noting that results presented in Greenwood are a result of measurement through a fused silica wedge with an acoustic impedance of 1.9 MRayl, one may conclude that a greater acoustic mismatch is experienced between liquid and aluminium and so the SW method with no ML is a more capable method than that presented by Greenwood. Errors associated with the SW method with no ML are large however these may be reduced through optimisation on the technique.

SW results found with the ML were compared to those reported by Schirru et al. (Schirru 2016). Schirru et al used a chirped sine wave to excite resonance with a polyimide ML, showing R=0.7 for η =1000 mPa.s at 4.5 MHz when measuring Newtonian standard oils, like those used for the calibration here. At 1000 mPa.s the SW method gives S=0.265 at 4.5 MHz hence the use of the SW ultrasonic method has greater resolution when using the same hardware for viscosity measurement.

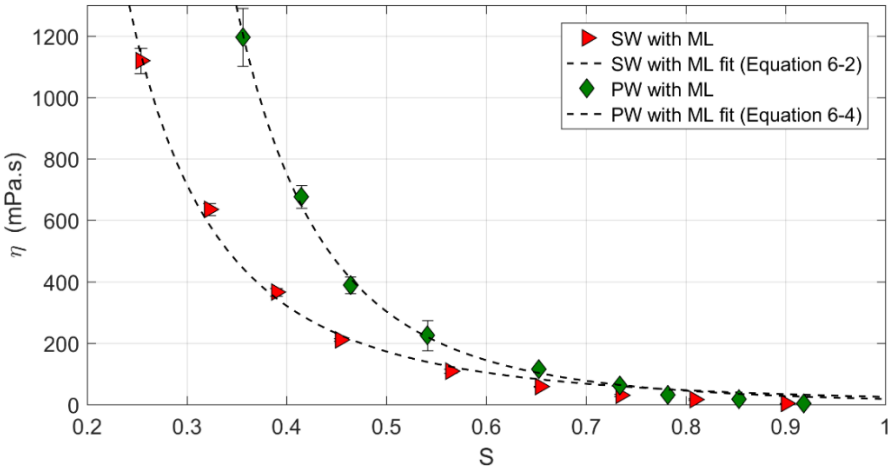

Figure 4-21: ML calibration curves for the PW and SW methods.

By now considering the PW method presented here, Figure 4-15 shows the sensitivity of the SW method is higher after 100 mPa.s, an effect highlighted by a direct comparison of the calibration curves for each technique, shown in Figure 4-21. This indicates that the SW method is preferable for viscosities above 100 mPa.s, in all measurements the SW method produces substantially lower errors (P=0.092) when compared to the PW method.

4.6. Conclusion

Evaluation of four ultrasonic viscometry techniques was completed by adopting a practical pre-calibration procedure to establish the capabilities of each technique individually. Nine Newtonain standard calibrations oils were used as the calibration test oils to define the relationship between R or S and η when measurement is made directly through an aluminium component, and also with the addition of a ML between the aluminium component and liquid sample. Calibration curves for each technique were established between 3 and 1200 mPa.s and the sensitivity of each method defined after validation of tabulated viscosity values using a Couette viscometer. 17 unknown viscosity oil samples were blended from a mixture of three cannon standard Newtonian oils between 3 and 1200 mPa.s. Blended oils were then measured ultrasonically and also with a Couette viscometer for validation, with variable agreement between the ultrasonic techniques and conventional viscosity. The calibration curves produced are specific to each component in which the measurements are taken from. Each component which is instrumented will produce a unique calibration curve as the physical position of the transducers, materials and environmental conditions of the component are unique to each system.

The SW method was capable of viscosity measurements without a ML at an aluminium-liquid interface, doubling the overall sensitivity of the PW method, while significantly reducing associated errors. ML implementation was found to be as effective at improving viscosity measurement when using the SW method, as it is when using the PW method, while the sensitivity of the SW method was found to have improved by more than an order of magnitude by the addition of a ML.

Thus when considering practical applications, the optimum ML thickness would be ¼ wavelength of the highest amplitude resonant peak in a component before the addition of a ML. In addition to this an alternative processing method was evaluated against traditional A_m: A_r ratio determination by auto-referencing. The method reduces the accuracy of viscosity measurement at the low viscosity band, however this analysis procedure eliminates the requirement for a solid-air reference signal for each measurement.

5. Standing Wave Mathematical Model

The previous chapter demonstrated the ability of the SW method to experimentally measure viscosity. This chapter describes the development of an analytical model to simulate the SW. Development of the model was completed through consideration of principle parameters known to influence ultrasonic waves. The aim of the model was to predict the viscosity of a liquid from the value of S, determined using the mathematical principles of the SW, through an understanding of interference mechanisms and wave behaviour within a bounded structure. A mathematical explanation of the SW model will be detailed firstly, taken from (Mills et al. 2017), followed by the adaptation of the model to incorporate the ML using the three layer reflection coefficient.

5.1. Mathematical Explanation of the Standing Wave Method

In order to define the interfacial mechanisms which contribute to the formation of a standing wave at a single frequency, the trajectory of single frequency continuous waves as discrete entities were initially considered. A standing wave of a single frequency was firstly considered mathematically. Wave formation within the transducer and between the transducer and component interface are assumed to be perfect, so the behaviour of the transducer in this respect was not incorporated into the model. The first consideration of the wave was upon entering the solid. The influence of the bonding agent between the transducer and component are deemed negligible as the layer is adequately thin compared to the wavelengths under consideration here, and were not included within this model.

The relationship between the initial amplitude, A_o and A, the amplitude of the wave once it has travelled a length, L, is described Equation 5-1. The wave decays as a function of the length and attenuation coefficient, α, expressed in the exponential form.

$$A = A_0 e^{L\alpha} \qquad \text{Equation 5-1}$$

Figure 5-1b shows a schematic diagram of a single wave passing through a solid from a transducer, where the wave reflects from both the transducer and measurement interfaces. The model was based on a solid with a finite length perpendicular to the transducer but an infinite length adjacent to the transducer (see Figure 5-1c), hence no edge effects are included within this consideration as the model assumes a linear trajectory only through the body of the component. The SW equations were built by considering the form of the wave at a series of circled number locations within the component, shown in Figure 5-1b.

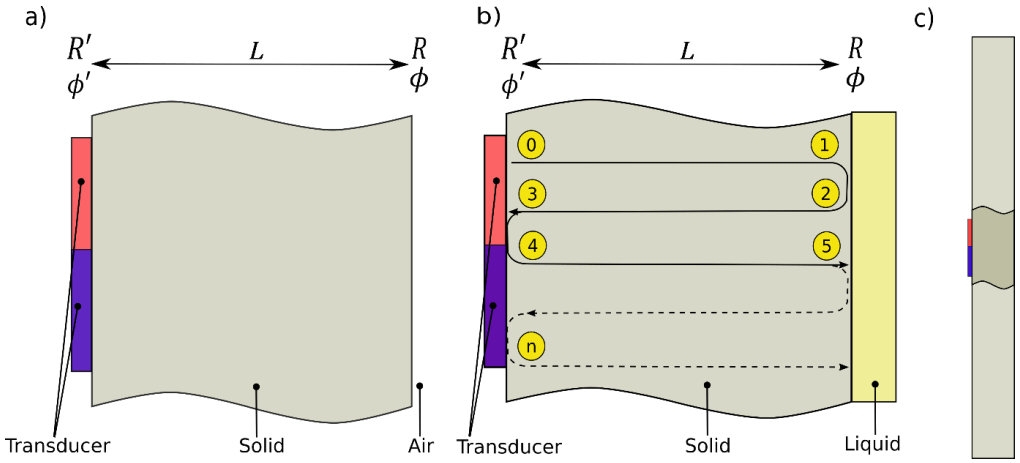

Figure 5-1: a) The physical location at which ultrasonic parameters will influence the wave in the solid-air condition b) Wave position diagram in the solid-liquid condition and c) the position of the solid within the system.

By considering an initial wave at the first resonant frequency, it is possible to describe the wave using a number of phyiscal properties. If we denote the emitter function (i.e. at location 0 in Figure 5-1) by the phasor below.

$$f(t) = A_0 e^{i\omega t} \qquad \text{Equation 5-2}$$

At location 1, just before the first reflection, the wave has been attenuated according to Equation 5-3 where *c* is the speed of sound in the solid.

$$A_1 = A_0 e^{i\omega(\frac{L}{c}-t)} e^{L\alpha} \qquad \text{Equation 5-3}$$

Immediately after the first reflection the amplitude is given by, location 2 in Figure 5-1:

$$A_2 = A_0 e^{i\omega(\frac{L}{c}-t)} e^{L\alpha} R e^{-i\phi} \qquad \text{Equation 5-4}$$

where R and ϕ are the reflection coefficient and phase change respectively at the measurement boundary. The wave then passes back through the material and immediately before the reflection at the transducer location (location 3) has an amplitude of:

$$A_3 = A_0 e^{i\omega(\frac{2L}{c}-t)} e^{2L\alpha} R e^{-i\phi} \qquad \text{Equation 5-5}$$

The amplitude immediately after the reflection at the solid to transducer interface (location 4) is given by:

$$A_4 = A_0 e^{i\omega(\frac{2L}{c}-t)} e^{2L\alpha} R e^{-i\phi} R' e^{-i\phi'} \qquad \text{Equation 5-6}$$

where R' and ϕ' are the reflection coefficient and phase change respectively at the transducer boundary. The wave then passes back through the solid where the amplitude reduces further due to attenuation (location 5). After another passage of the wave through the material, inclusive of reflection and attenuation, the amplitude is:

$$A_5 = A_0 e^{i(\omega(\frac{4L}{c}-t)-2\phi-\phi')} e^{4L\alpha} R^2 R' \qquad \text{Equation 5-7}$$

The R is raised to a power related to the number of passages through the material as it is the proportion of the wave that is lost which determines the amplitude of the subsequent wave, whereas the ϕ is a summation as this has an accumulative effect on the wave. After n passages through the structure (where a passage consists of travelling from the transducer to the measurement interface and back again), the amplitude of the wave is:

$$A_0 e^{i[\omega(\frac{2nL}{c}-t)-n\phi-(n-1)\phi']} e^{2nL\alpha} R^n R'^{(n-1)} \qquad \text{Equation 5-8}$$

The influence of n can be visualised using a polar plot (Figure 5-2) where the amplitude and phase are considered at each reflection from both the reference and measurement interface for a single frequency wave. Wave attenuation is not considered here as this is a demonstration of the effect of R and ϕ only so is normalised to the incident wave.

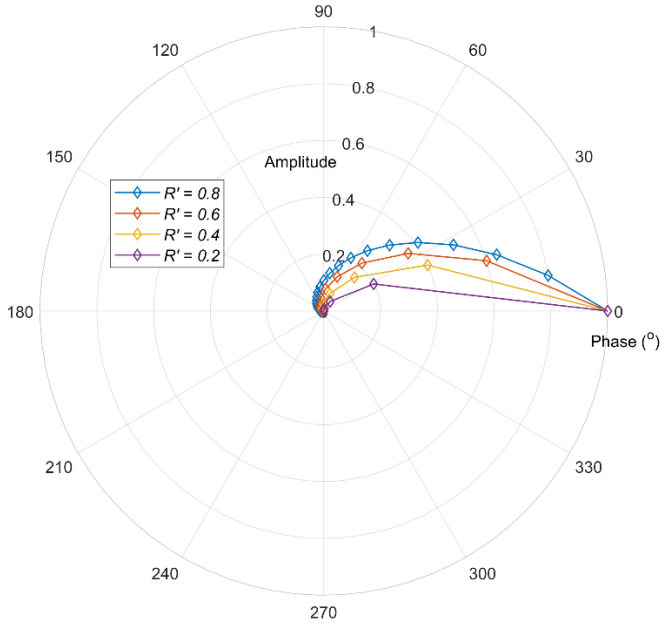

Figure 5-2. A polar plot to show how the amplitude and phase of a single frequency wave changes as n increases. Results are calculated when R=1, and phase is calculated for R and R' values using Equation 2-26 and Equation 2-27.

In the reference condition where R = 1, the amplitude of the wave as it reflects within the component is a function of R'. The data points in Figure 5-2 denote the amplitude of a wave after each reflection, hence the wave at R' = 0.2 decays more rapidly than the R' = 0.8 wave which completes 7 reflections (shown as consecutive data points on the curve) before the amplitude of the wave reduces to 0.2. In order to increase the proportion of incident energy on the measurement interface, the number of reflections which are of a sufficient amplitude to be distinguished from noise must be maximised; to achieve this R' should be as close to 1 as possible.

As the reflected waves superimpose, the wave amplitude detected by the transducer is then:

$$A_m = A_0 \sum_{n=1}^{\infty} e^{i[\omega(\frac{2nL}{c}-t)-n\phi-(n-1)\phi']} R^n R'^{(n-1)} e^{2nL\alpha} \qquad \text{Equation 5-9}$$

where A_m is the amplitude of the wave in the measurement condition. Equation 5-9 characterises the measurement condition when the reflection coefficient at the measurement interface is < 1 for a single frequency wave. This allows the maximum amplitude at a particular frequency to be found after *n* reflections within a material, including the influence of interference of the wave within a component of a given length, given the material properties which are contained within *R* and *R'*.Furthermore, Equation 5-10 gives the reference amplitude when $R = 1$ in the condition where a solid-air interface is present, so A_r is the amplitude of the wave in the reference condition.

$$A_r = A_0 \sum_{n=1}^{\infty} e^{i[\omega(\frac{2nL}{c}-t)-(n-1)\phi']} R'^{(n-1)} e^{2nL\alpha} \qquad \text{Equation 5-10}$$

If we denote the standing wave reflection coefficient, *S* as the proportion of the superimposed incident wave that is reflected back, it is determined as follows in the form of Equation 3-3.

$$S(t) = \frac{\sum_{n=1}^{\infty} e^{i[\omega(\frac{2nL}{c}-t)-n\phi-(n-1)\phi']} R^n R'^{(n-1)} e^{2nL\alpha}}{\sum_{n=1}^{\infty} e^{i[\omega(\frac{2nL}{c}-t)-(n-1)\phi']} R'^{(n-1)} e^{2nL\alpha}} \qquad \text{Equation 5-11}$$

This mathematical explanation will produce the maximum amplitude of the standing wave at a series of discrete frequencies, contained within the model as ω. Thus the profile of the solid-air, and solid-liquid wave can be simulated using these equations.

5.2. Explanation of Components Forming the Standing Wave Equations

Observation of Equation 5-9 shows the mechanisms which govern the SW and which features of the wave they influence. The SW equation can be split into two portions, the first describing the wave position and phase, and the second governing the amplitude due to interaction with an interface and attenuation. These sections are shown in Figure 5-3 as waveform, and amplitude.

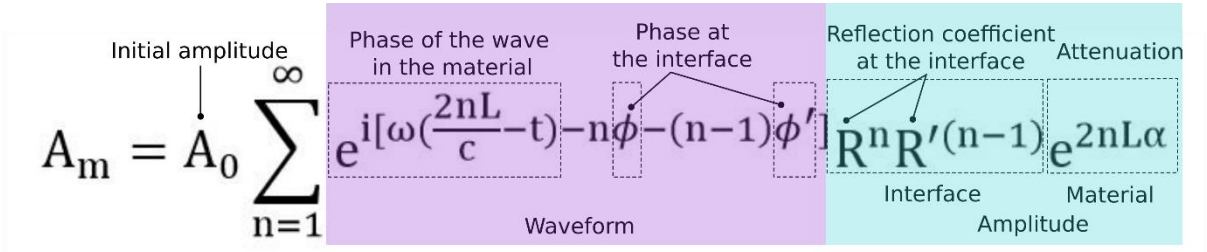

Figure 5-3: A visual explanation of
Equation 5-9 split into principal components which govern the SW.

The first portion of the equation describes the waveform, specifically at the transducer interface, as this is the signal which is captured as a measurement response. The angular frequency and time function, describe the position of the wave in relation to the length of the component. Phase values relate to the phase change as a result of an interaction with an interface.

R and R' also influence the amplitude of the wave, and are determined using Equation 2-13 at the transducer interface, and Equation 2-29 at a liquid measurement interface. The viscosity of the liquid is contained within z_l which is used to find the reflection coefficient. The attenuation will also cause the amplitude of the wave to reduce progressively with the distance the wave travels within the solid. The influence of these parameters will be addressed later, however the composition and sequence of the model will firstly be detailed.

5.3. Model Inputs and Structure

5.3.1. Mathematical Model Outline

In order to test the validity and accuracy of the relationships outlined in Equation 5-9 and Equation 5-10, a script was written in Matlab®, which can be found in Appendix 1. The model was made to simulate the response of the standing wave within the aluminium test plate used in Section 4. The analytical model consists of three sections, the first composes the SW reference signal (Equation 5-9) the second composes the SW measurement signal (Equation 5-10), and the third combines these functions to produce S (Equation 5-11). The model has been produced to calculate the envelope of the signal in the frequency domain, thus a single maximum profile of the wave is displayed. As measurements with this technique are made from the peak amplitude of the wave, sufficient data from the model can be acquired to make a good comparison to practical data by consideration of the maximum envelope only.

5.3.2. Model Input

Table 5-1 lists the values and relationships used to define each term in the measurement function, (A_m), and the reference function, (A_r). These values have been taken from the literature to give a first indication of the accuracy of the model. In addition to these inputs for each function, global variables are also required in the form of vectors, such as viscosity (η) density (ρ) frequency (f), and number of reflections (n), typical values of which are shown in Table 5-2. Each of these inputs can be varied to determine their effect on S.

Table 5-1: Input parameter values.

Function Inputs		A_r **– Reference**	A_m **– Measurement**
A_0	Initial Amplitude	1	
α	Attenuation coefficient	-0.4 Np/m	
L	Component length	0.00738 m	
ω	Angular Frequency	$2\pi f$	
z_T	Acoustic impedance of the transducer	16.86×10^6 Pa.s/m^3 (NDT Resource Centre n.d.)	
z_{Al}	Acoustic impedance of solid (Aluminium)	8.21×10^6 Pa.s/m^3 (ONDA n.d.)	
η	Liquid viscosity	N/A	0.00365 to 1.1196 Pa.s
ρ_l	Liquid density	N/A	865.9 to 844.1 kg/m^3(Cannon Instrument Company 2018)
z_L	Acoustic impedance of liquid	N/A	0-0.7 MRayl (Cannon Instrument Company 2018)
R'	Reflection coefficient at the transducer interface	$\frac{z_{PZT}-z_{Al}}{z_{PZT}+z_{Al}}$	
R	Reflection coefficient at the measurement interface	Air = 1	Liquid= $\frac{z_l-z_{Al}}{z_l+z_{Al}}$
c_{Al}	Velocity of sound in aluminium	3040 m/s	
t	Time vector	$0:((\frac{2L}{c_{Al}})/1000):\frac{2L}{c}$	
ϕ	Phase change at the measurement interface	$0.5\ acos\left(1-\frac{(1-R^2)}{(2+R^2)}\right)$	
ϕ'	Phase change at the reference interface	$0.5\ acos\left(1-\frac{(1-R'^2)}{(2+R'^2)}\right)$	

Table 5-2: Global variables.

Global Variable		**Typical values**
n	Number of full reflections	1:50
f	Frequency	0 : 50 kHz :10 MHz
ρ	Density	865.7 to 844.1 kg/m^3
η	Viscosity	0.00365 to 1.1196 Pa.s

5.3.3. Model Structure

Three loops operate within the script, (see Appendix 1.1) these will be described in the order of their position within the code in terms of operations. Hence the first loop calculates the

amplitude of A_r and A_m at each value of n, using the A_r and A_m Equations, (Equation 5-10 and Equation 5-9). This is followed by the second loop which calculates the sum of $A_r(n)$ and $A_m(n)$ at each frequency, also calculating S at each frequency. The third loop calculates $A_r(n,f)$, $A_m(n,f)$ and $S(n,f)$ for a range of corresponding η and ρ_l values to give the relationship between S and η at a range of frequencies. The amplitude of A_m, is now a function of n, f, η and ρ. A flow chart of the model is shown in Figure 5-4. The coded model can be found in Appendix 1.1.

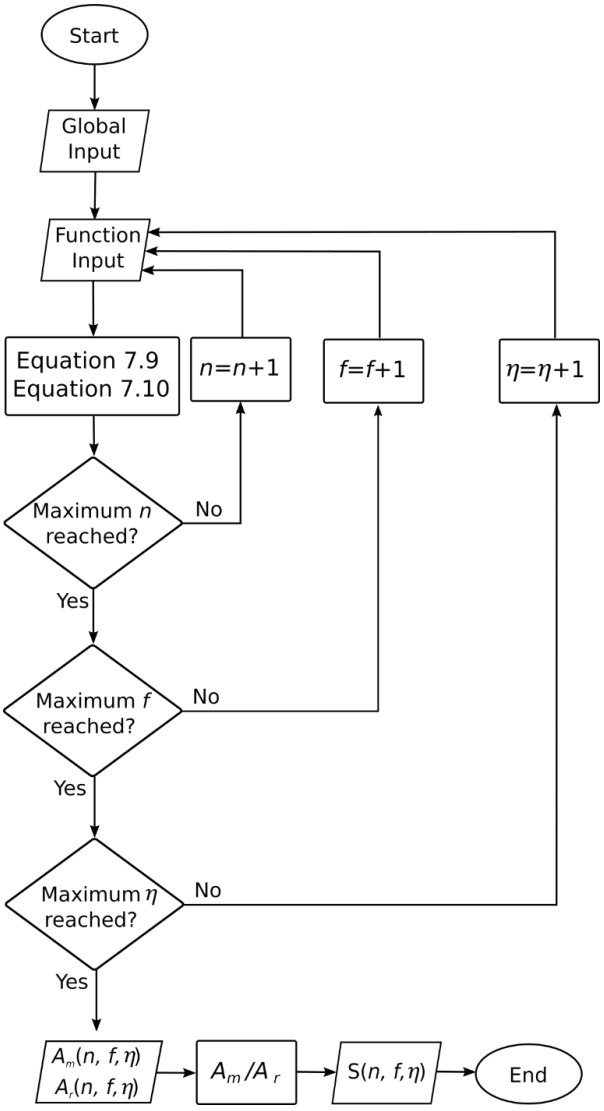

Figure 5-4: A flow chart to show the order of the Matlab® code script to produce A_r and A_m.

5.3.4. Model Output

To compare the wave equation derived in Equation 5-10 (A_r), to the experimental signal, the reference signal was firstly simulated. As the first loop iterates, (that which concerns, *n*, the number of reflections) the standing wave at a single frequency is calculated. Figure 5-6 shows both the constituent waves from n= 1 to 7 alongside the sum of such waves. When the reflection of a wave is out of phase with the incident wave (Figure 5-5), the amplitude of the sum of the waves is lower than if the waves reflect in phase (Figure 5-6).

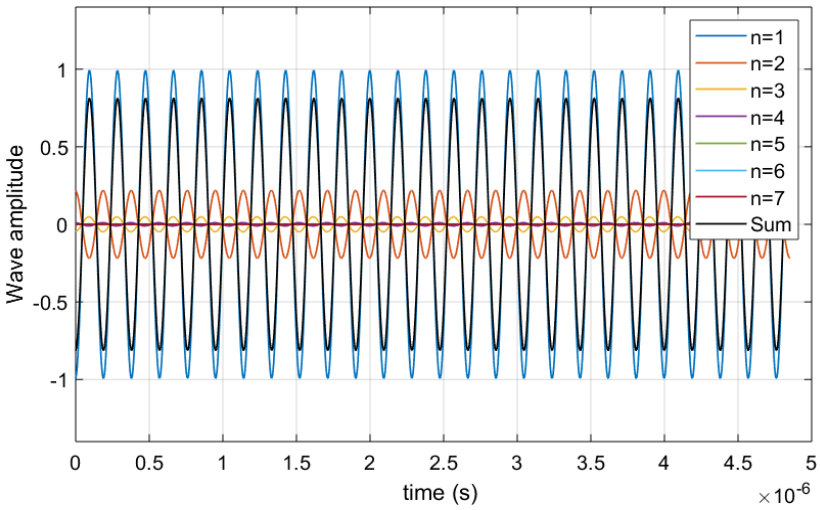

Figure 5-5: Wave amplitude of individual waves from n = 1 to 7 and the sum of these waves, for 5.25 MHz when L = 7.38 mm.

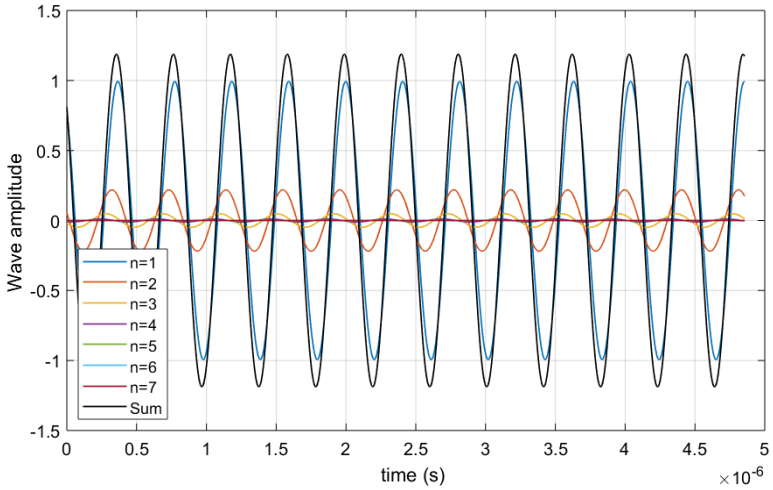

Figure 5-6: Wave amplitude of individual waves from n = 1 to 7 and the sum of these waves, for 2.45 MHz when L = 7.38 mm.

Each frequency wave amplitude and phase is considered within the length of the component, then finally the sum of these waves is calculated to provide the amplitude of the wave at the transducer interface. It is the maximum amplitude of the sum which is the output of this operation at this point within the model.

The model calculates the maximum amplitude of the summated wave for each frequency, as this is equivalent to the profile which is measured when using the SW technique. The wave in Figure 5-7 is modelled at an air interface, where $R = 1$, the model shows the response of the wave at a range of frequencies, highlighting the resonances within the length of material given.

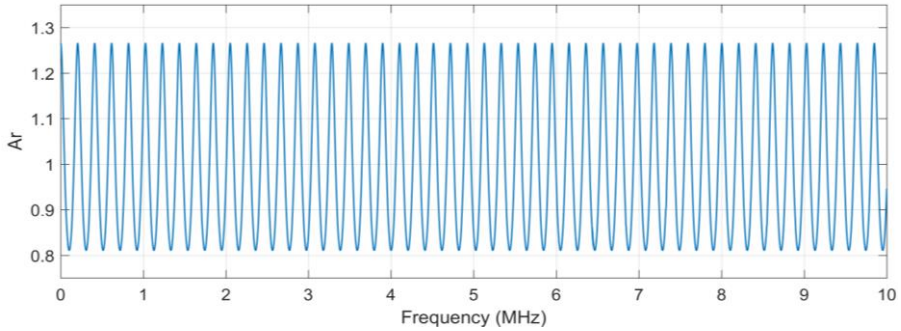

Figure 5-7: Mathematical simulation of the reference signal, A_r.

The profile shows a series of peaks and troughs, each with a uniform maximum amplitude over the range of frequencies. This behaviour is expected as the model does not incorporate the operational bandwidth of the transducer, so all frequencies which interfere within a material of this length do so at their maximum. The peaks are spaced at a constant interval across the range of frequencies, much like the expected response from a standing wave. The SW reference signal is therefore able to provide information about the resonant frequency, f_s.

The model was then used to predict how this wave behaves in the measurement condition, to show how A_m is affected by viscosity. When the viscosity in the model is set to zero, the model produces the same profile for A_m as A_r. The effect of η on the SW is incorporated into the model via the R and ϕ at the measurement interface. Values of viscosity between 0 and 1.2 Pa.s with corresponding ρ_l values were used to calculate the maximum amplitude of the standing wave in the frequency domain. The influence of η on A_m is shown in Figure 5-8.

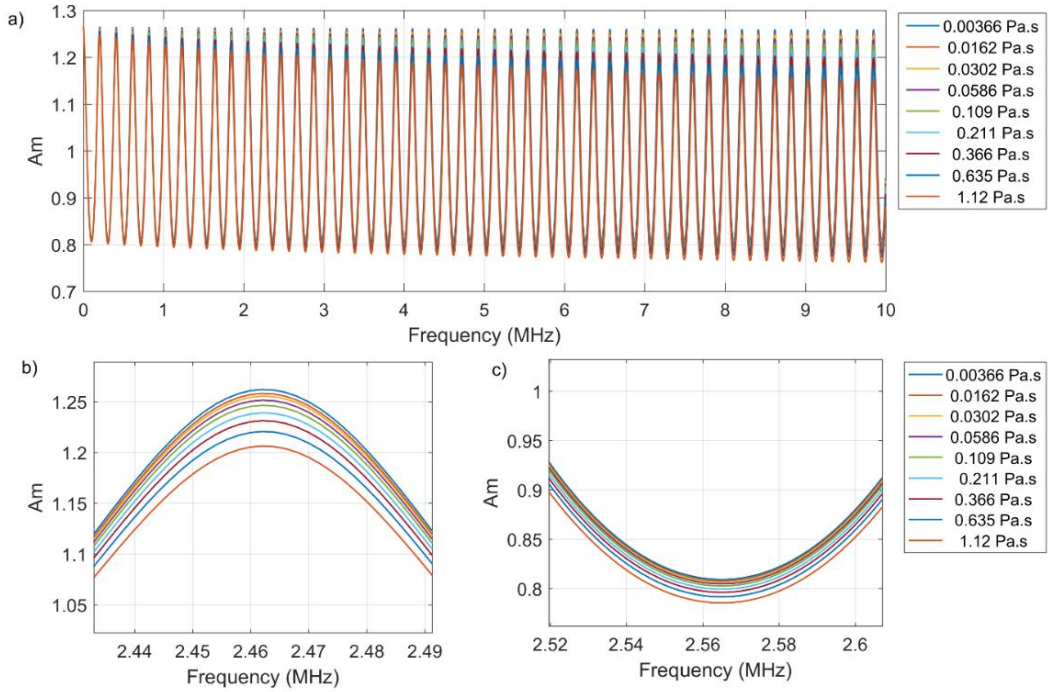

Figure 5-8: a) Mathematical simulation of the measurement signal, A_m, for a range of viscosities. b) magnification of a peak, c) magnification of a trough.

Although the full frequency span is influenced by η, the greatest deviation in amplitude due to the effect of viscosity is seen at the peaks of the signal. This can be seen more clearly in Figure 5-8b as the peaks of the wave change with increasing viscosity more than the troughs of the signal, shown in Figure 5-8c. A negative correlation between the wave amplitude and frequency is seen in Figure 5-8 as viscosity increases. The effect of viscosity becomes more prominent in the signal at higher frequencies, resulting from the incorporation of Equation 2-22 into the model which outlines the effect of angular frequency, and so frequency on z_l.

The outputs A_r and A_m, are then used to find S, using Equation 3-2 within the script. This is calculated from A_m at each viscosity shown in Figure 5-8, the result of which are shown in Figure 5-9.

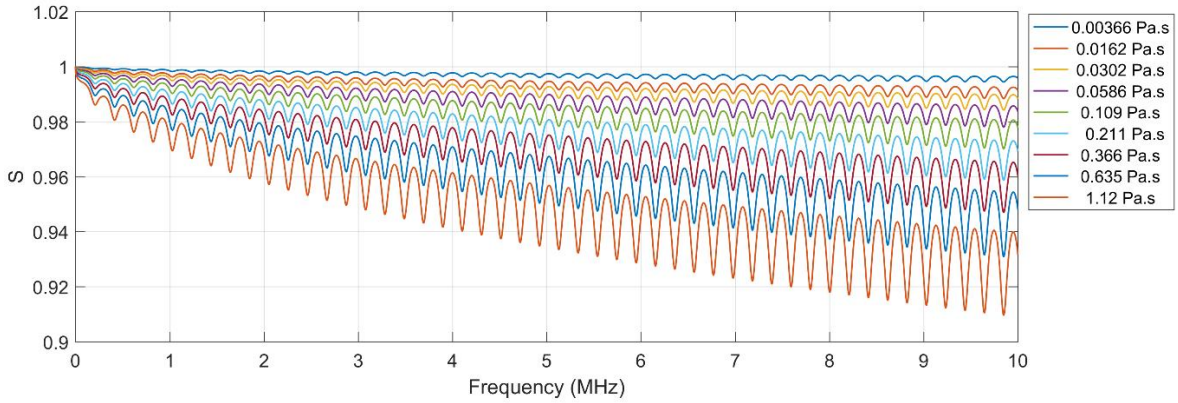

Figure 5-9: Model output in the frequency domain of S at a range of viscosities.

With increased viscosity, the overall amplitude of S decreases. Dips in S indicate a greater sensitivity to viscosity at the peak frequencies in A_m, this affect is shown in Figure 5-10 by a lower value of S at the peak frequencies of A_m. Model outputs shown in Figure 5-9 are similar to those found experimentally, previously demonstrated in Figure 4-7c, however differences in the sensitivity of S exist due to the bandwidth of the transducer in experimental results which have not been included in the model.

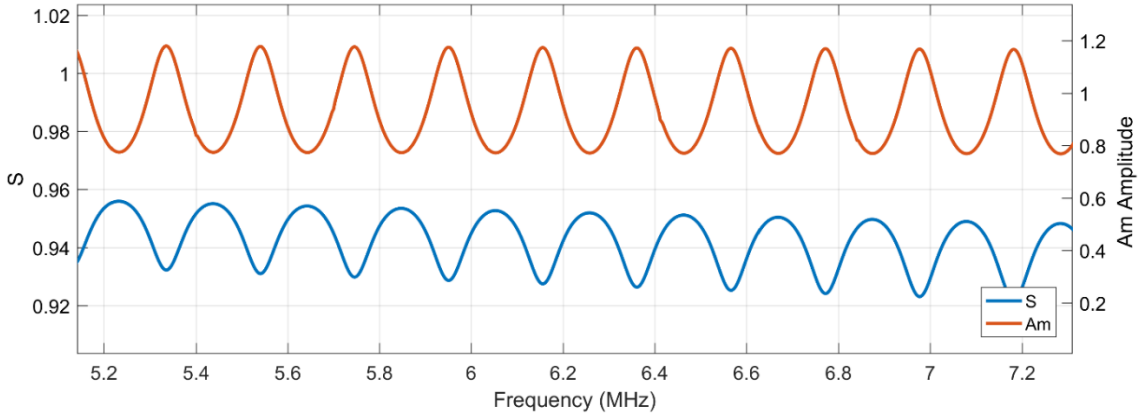

Figure 5-10: S and A_m for 1.12 Pa.s.

The behaviour of the model with respect to L, η, n and f agrees with the expected relationship for a single wave outlined in Chapter 3 as the SW profile shows a similar trend. The influence

of n on the sensitivity of the model provides a demonstration of the effect of the SW method in comparison to the PW method when only one reflection is used. These results for each viscosity are shown in Figure 5-11. The value of R is calculated at n=1 in the model, and n=7 to calculate S, however all other parameters within this simulation are identical.

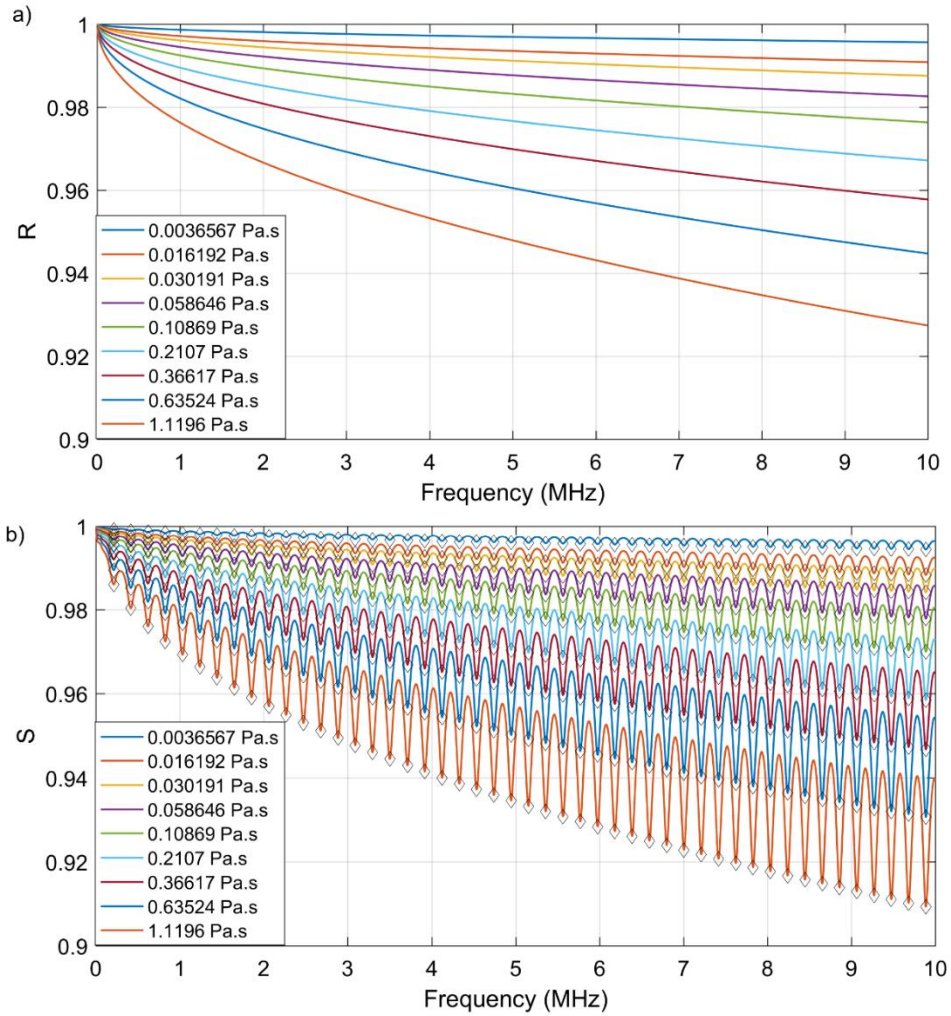

Figure 5-11: The relationship between viscosity, frequency and a) R, and b) S.

Due to the frequency dependency on viscosity measurement, R and S are evaluated at the dips in the S profile when investigating the SW method, identified by grey markers in Figure 5-11b. At 9.26 MHz in Figure 5-11a, R=0.93 while at 9.26 MHz in Figure 5-11b S=0.91 at 1.1196 Pa.s. This demonstrates that mechanisms of the standing wave may improve the sensitivity of viscosity measurement at a metallic interface when using the SW method.

A summary of assumptions made by the model are shown in Table 5-3. The assumptions may account for a number of differences between the analytical results and those shown experimentally, which will be evaluated in Chapter 8.

Table 5-3: A table of assumptions used to produce the analytical model.

Interface assumptions	• R=1 when an air interface is present. • A perfect bond between the transducer and component is present, the effect of the adhesive between the solid component and transducer is negligible. • The transducer and measurement interfaces are perfectly parallel to one another.
Reflections	• S is calculated at each frequency, no mixed frequency interference is considered, i.e. the behaviour of the previous frequency does not influence that of the next.

While these assumptions may be able to account for differences between the model and experimental results, the way in which they contribute to this may be further investigated by analysing the influence of inputs into the model such as, the number of reflections which significantly contribute to the sum of the wave. Several inputs into the model will now be considered in greater detail to address the selection of such parameters within the model.

5.4. Factors Influencing Model

5.4.1. Quasi Static Nature and the Number of Reflections

The SW method experimentally is considered to be a quasi-static standing wave, meaning multiple frequency waves do not interfere to produce a standing wave, as previously discussed in Section 3.2.2. While this occurs experimentally, the model calculates the maximum amplitude achieved by the interference of single frequencies, hence mixed frequency wave interference is not considered by the model. To determine whether single frequency consideration is an acceptable practise, a calculation of the change of input frequency after a significant number of reflections was determined. A single frequency wave was considered to determine the significance of frequency when calculating the amplitude of the wave.

The number of reflections is denoted as n, within the boundaries of the solid. The standing wave amplitude is the sum of n reflections calculated in the first loop of the model. While in practise the number of reflections from all boundaries of the solid is vast, a single trajectory of the wave is considered within the model, being that directly opposite the transducer interface.

Figure 5-6 and Figure 5-5 show the wave profile of two single frequency waves in terms of the amplitude and phase as the number of reflections, n increases, calculated using the model. The contribution of each wave to the sum of the wave amplitude for all frequencies is constant for

all frequencies, hence the contribution of n to the amplitude of a resonance was selected, results of which are shown in Figure 5-12.

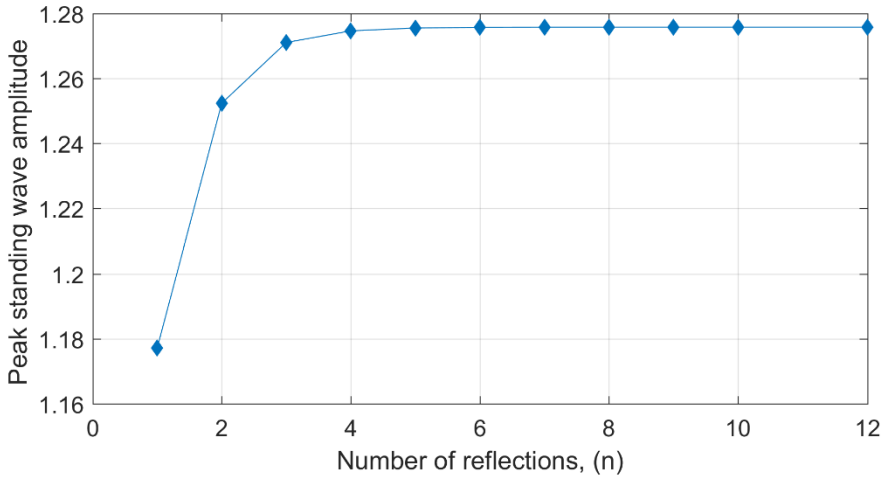

Figure 5-12: The influence of the cumulative number of n on the standing wave amplitude at a single frequency.

The peak amplitude of the standing wave sharply rises before reaching a maximum. In order to define the number of reflections which make a significant difference to the amplitude of the signal, Table 5-4 gives the amplitude of the standing waves for several values of n.

Table 5-4: The cumulative amplitude of the reference signal as n increases.

n	A_r	Percent of n=12 A_r (%)
1	1.1772	92.2798
2	1.2524	98.1692
3	1.2710	99.6323
4	1.2746	99.9130
5	1.2755	99.9825
6	1.2757	99.9959
7	1.2757	99.9992
8	1.2757	99.9998
9	1.2757	100.0000
10	1.2757	100.0000
12	1.2757	100.0000

For the purposes of this model $n = 7$ will be considered to be the minimum required number of reflections as this value achieves 100% of the maximum amplitude to 4 significant figures. A deviation smaller than 4 significant figures would result in a viscosity change too small to be deemed significant by the measurement amplitude. A change in amplitude of 0.0001 corresponds to a variation of viscosity of 0.25 mPa.s, a sensitivity too high to be deemed practical when noise within the experimental signal is considered. Note this calculation is

subject to the length of the solid, and so only applies to the solid component modelled here. The resonant frequency of the 7.38 mm solid component is $205.96\ kHz$ where c=3040 m/s and n=1 according to Equation 2-32.

The minimum number of reflections thought to significantly contribute to the amplitude of the standing wave has been considered to be 7 for this length. The time required to complete 7 reflections is then given by:

$$\frac{2 \times 7 \times 0.00738\ \mathrm{m}}{3040\ \mathrm{m/s}} = 3.39 \times 10^{-5}\mathrm{s} \qquad \text{Equation 5-12}$$

$\Delta f/s$ was then calculated for an experimental arrangement where the duration of the excitation frequency sweep of 9 MHz is 10 ms.

$$\frac{9 \times 10^{6}\mathrm{Hz}}{10 \times 10^{-3}\mathrm{s}} = 9 \times 10^{8}\mathrm{Hz/s} \qquad \text{Equation 5-13}$$

The change in frequency in the time it takes for seven reflections to occur experimentally was then found to be:

$$3.39e^{-5}\mathrm{s} \times 9 \times \frac{10^{8}\mathrm{Hz}}{s} = 30588.16\ \mathrm{Hz} = 30.6\ \mathrm{kHz} \qquad \text{Equation 5-14}$$

This represents a 14.85% change from the resonant frequency (205.96kHz) to the next corresponding frequency. In reality, measurements are made around 5 MHz, hence the change in frequency per unit of time for seven reflections is 4.3697kHz, a change of 0.61%. This change is sufficiently small to permit the assumption of a quasi-static standing wave. This finding indicates that the deviation between the frequency output is <1% hence permitting single frequency interference to be sufficient to describe the wave profile using the model.

5.4.2. Component Length

The magnitude and number of resonant frequencies depends on the path length, and thus the size of the component. A positive correlation between path length and number of anti-nodes of the wave envelope is produced by the model. This behaviour agrees with that outlined in the theory, as a greater number of frequencies can resonate within a larger path length of a given set of frequencies. This behaviour is shown in the model, and demonstrated in Figure 5-13.

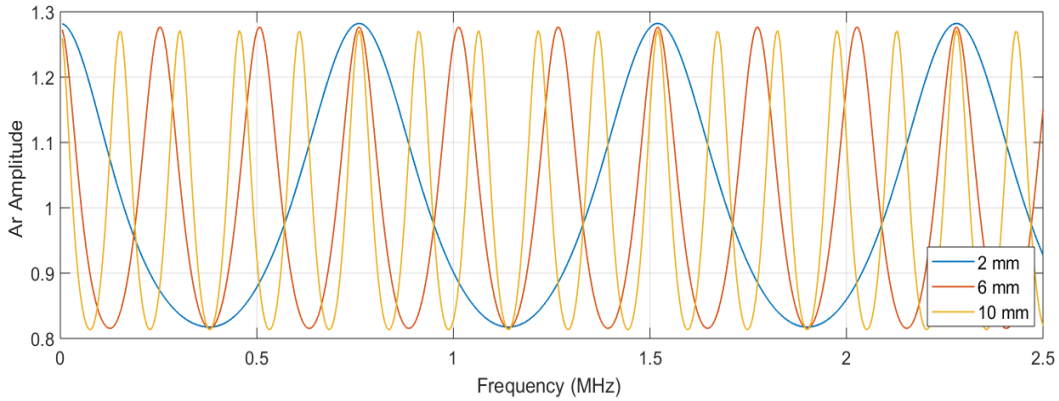

Figure 5-13: The effect of component length on fs.

The amplitude of the SW in Figure 5-13 has a slightly greater amplitude at shorter component lengths due to reduced attenuation.

5.4.3. Attenuation Coefficient

The value of attenuation coefficient was increased in steps of 0.4 Np/m. The specific value of the shear wave attenuation coefficient was not determined as its use within the model serves no significance when considering viscosity measurement as the effect of attenuation in the solid is removed due to the division of A_m and A_r, leaving only the effect of the liquid as a measurable variable. The value of S for a given viscosity was not found to change if the attenuation coefficient of the solid in the reference and measurement conditions are equal, regardless of their value. Figure 5-14 shows the linear behaviour of A_r with the attenuation coefficient.

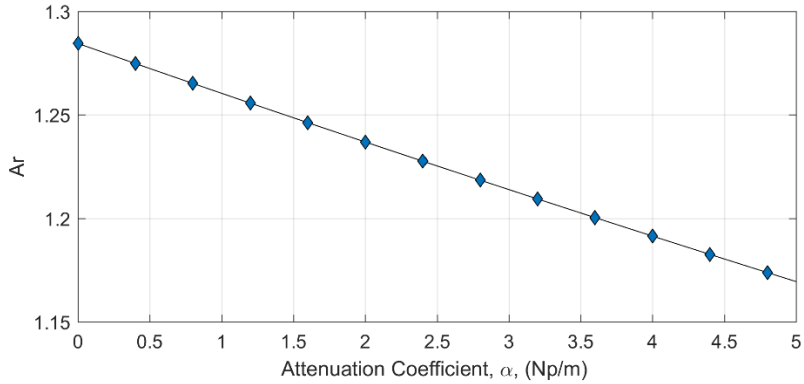

Figure 5-14: Amplitude of the reference function relation to attenuation coefficient.

5.4.4. Angular Frequency

A positive non-linear correlation between f and z_l has been shown graphically previously in Figure 2-22.The peaks of the measurement signal reduce with increasing frequency, as z_l is frequency dependent, shown in (Figure 5-15).

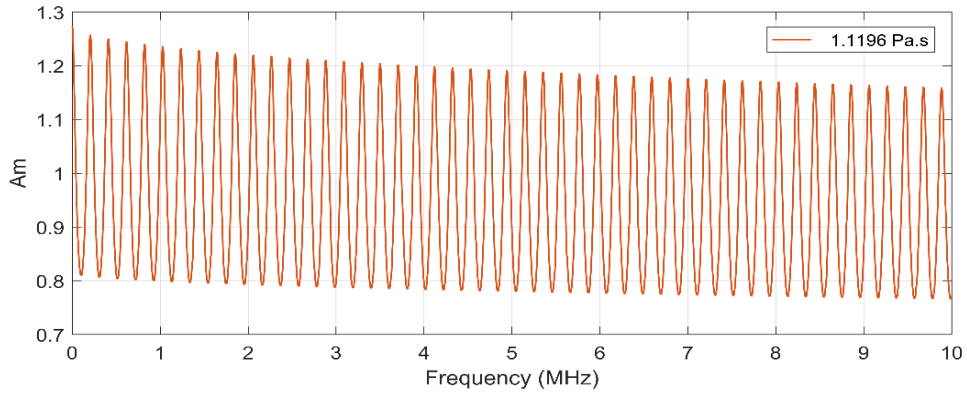

Figure 5-15: A graph to show how the measurement peak amplitude reduces with increased frequency when using the model.

As frequency increases, the value of z_l also increases shown previously in Equation 2-22. This relationship causes A_m to reduce with increasing frequency as z_l is larger at higher frequencies, meaning a lower reflection coefficient is produced. The features of this graph correspond to those produced by a pulsed wave, such as the relationship shown in Figure 5-11a. While this result is mathematically correct, the relationship is not seen in theoretical data due to the operational bandwidth of the transducer, which overrides the effect of z_l on frequency.

As each parameter relating to the standing wave analytical model output has now been addressed and their relative effect on the model individually considered, the influence of the ML on the SW can now be considered analytically.

5.5. Standing Wave Model with a Matching Layer

In order to incorporate the ML into the model, R at the solid-ML-liquid interface was considered. The code for the model can be found in Appendix 1.2. In the reference and measurement condition, (Equation 5-9) is used where $Re^{-i\phi}$, is replaced with the three layer reflection equations Equation 2-36 and Equation 2-37 as shown in Equation 5-15 and Equation 5-16.

$$A_m = A_0 \sum_{n=1}^{\infty} e^{i[\omega(\frac{2nL}{c})-(n-1)\phi']} \left(\frac{\left(1-\frac{z_s}{z_a}\right)\cos\left(\frac{\omega t_m}{c_m}\right) + i\left(\frac{z_m}{z_a}-\frac{z_s}{z_m}\right)\sin\left(\frac{\omega t_m}{c_m}\right)}{\left(1+\frac{z_s}{z_a}\right)\cos\left(\frac{\omega t_m}{c_m}\right) + i\left(\frac{z_m}{z_a}+\frac{z_s}{z_m}\right)\sin\left(\frac{\omega t_m}{c_m}\right)} \right)^n R'^{(n-1)} e^{2nL\alpha} \qquad \text{Equation 5-15}$$

$$A_m = A_0 \sum_{n=1}^{\infty} e^{i[\omega(\frac{2nL}{c})-(n-1)\phi']} \left(\frac{\left(1-\frac{z_s}{z_l}\right)\cos\left(\frac{\omega t_m}{c_m}\right) + i\left(\frac{z_m}{z_l}-\frac{z_s}{z_m}\right)\sin\left(\frac{\omega t_m}{c_m}\right)}{\left(1+\frac{z_s}{z_l}\right)\cos\left(\frac{\omega t_m}{c_m}\right) + i\left(\frac{z_m}{z_l}+\frac{z_s}{z_m}\right)\sin\left(\frac{\omega t_m}{c_m}\right)} \right)^n R'^{(n-1)} e^{2nL\alpha} \qquad \text{Equation 5-16}$$

Table 5-5 details additional inputs to the model required for the incorporation of the ML.

Table 5-5: Input parameter values

Function Inputs		Input Value
z_a	Acoustic impedance of air	$\sqrt{i\omega\rho_{air}\eta_{air}}$
ρ_{air}	Air density	1.225 kg/m^3
η_{air}	Air viscosity	2×10^{-5} Pa.s
z_m	Acoustic impedance of the ML	1.4×10^6 Pa.s/m^3 (Schirru et al. 2015)
c_m	Velocity of sound in the ML (polyimide)	850 m/s (Schirru et al. 2018)
t_m	Thickness of the ML	$\frac{nc_m}{4f}$

Figure 5-16a shows the effect of the three layer reflection coefficient on the SW model, through the comparison of the model with and without the ML. Input parameters relating to frequency and material properties are the same as those for the model without the ML previously reported in Section 5.3.2. The model was based on a 5 MHz transducer, with a ML thickness of 42.5μm. The influence of the ML on A_r is shown in Figure 5-16.

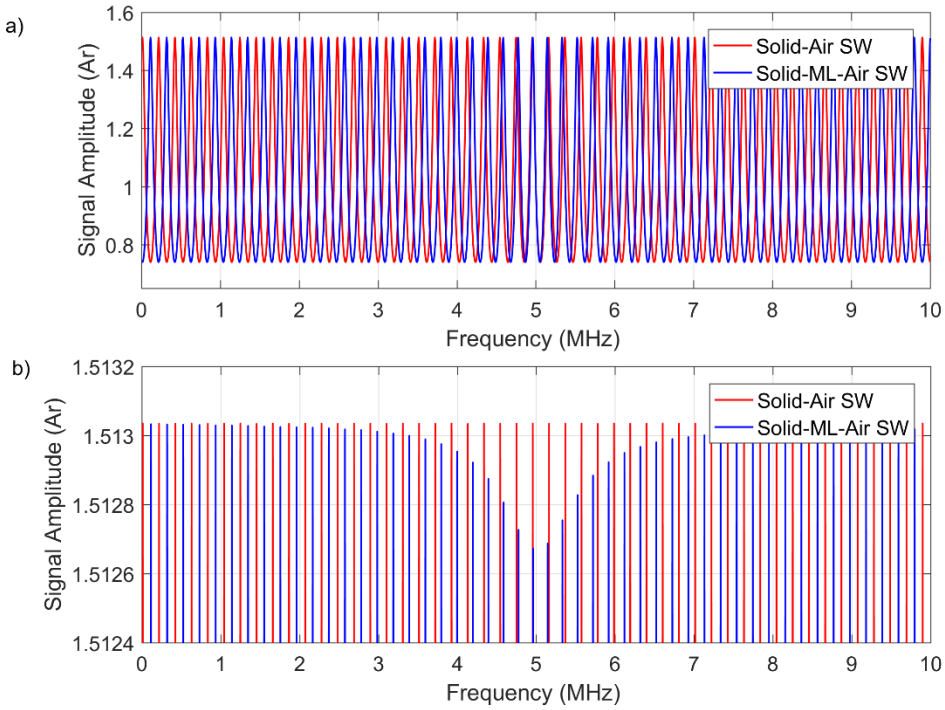

Figure 5-16: a) Mathematical simulation of the SW method with the ML in the solid-ML-Air condition, b) magnified image of a.

The addition of the ML to the model results in a small amplitude change in A_r, shown by the magnified image of the signal in Figure 5-16b however a shift is seen in the position of the peaks, centred around 5 MHz, where the position of the peaks agree. The shift is caused by the phase difference introduced by the ML which causes different frequencies to constructively interfere.

Figure 5-17 shows how the amplitude of the measurement signal changes with viscosity. With the addition of the three layer equation into the SW model, greater sensitivity to viscosity around 5 MHz was found.

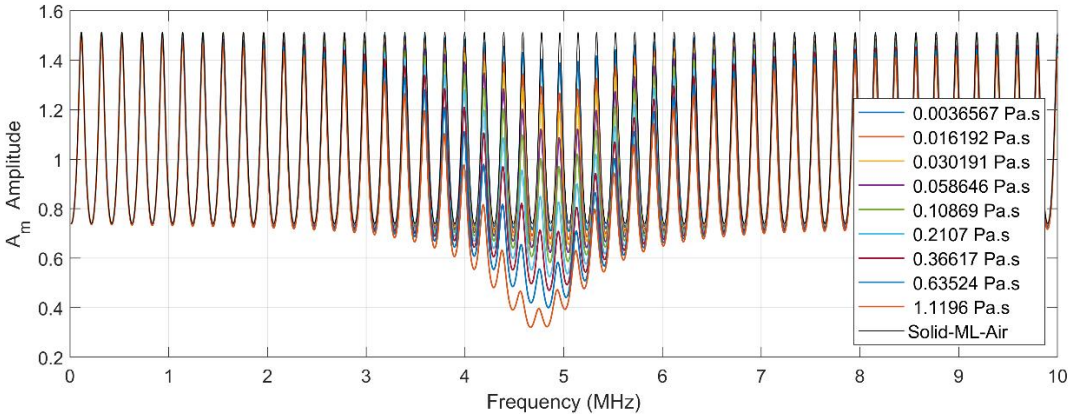

Figure 5-17: Mathematical simulation of the SW ML method showing the solid-ML-air and solid-ML-liquid wave profiles at a series of viscosities using a 42.5µm ML.

The behaviour shown in Figure 5-17 was similar to that found experimentally in Figure 4-7b, although the amplitude of the nodes are shown to also reduce with increasing viscosity to a greater extent to that shown experimentally. The greatest sensitivity was shown at the antinode frequencies however the full frequency span is influenced by η. The $S-\eta$ relationship produced by the model was then produced using Equation 3-2, shown in Figure 5-18.

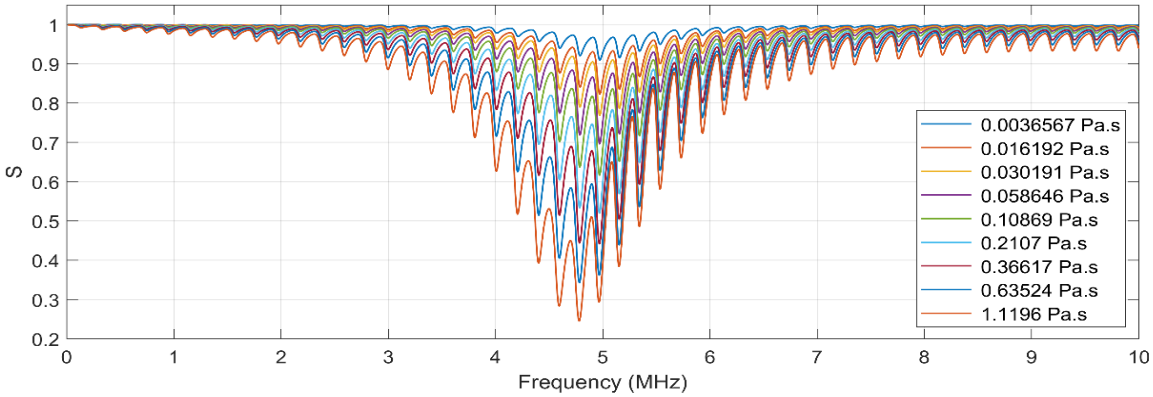

Figure 5-18: Mathematical simulation of S vs frequency for the SW method with a 42.5µm ML at a series of viscosities.

5.6. Using the Standing Wave Analytical Model to Predict Viscosity

In order to find η from S using the model, the relationship was firstly defined for the frequency peak selected, and the component geometry used as an input within the model. This requires both prior input of the acoustic properties of the materials and subsequent inputs such as global variables, and the value of S produced from experimental measurement. A list of the prior input values is detailed in Table 5-1. While this may seem extensive, if this methodology was to be repeatedly used, values regarding transducer properties would be standard, and simple

ultrasonic measurement of the velocity of sound in the material and length could be conducted by the generation of the SW and physical length measurement initially.

The model was used to find the relationship between viscosity and S, for the full range of frequencies. The relationship for a frequency closest to that seen experimentally can then be chosen and the results compared. Figure 5-19a shows yellow markers at the frequencies which could be selected, and Figure 5-19b shows the relationship between viscosity and S at one selected frequency. The curve fitted to this equation shown in Figure 5-19c, can be used to find viscosity from a given value of S.

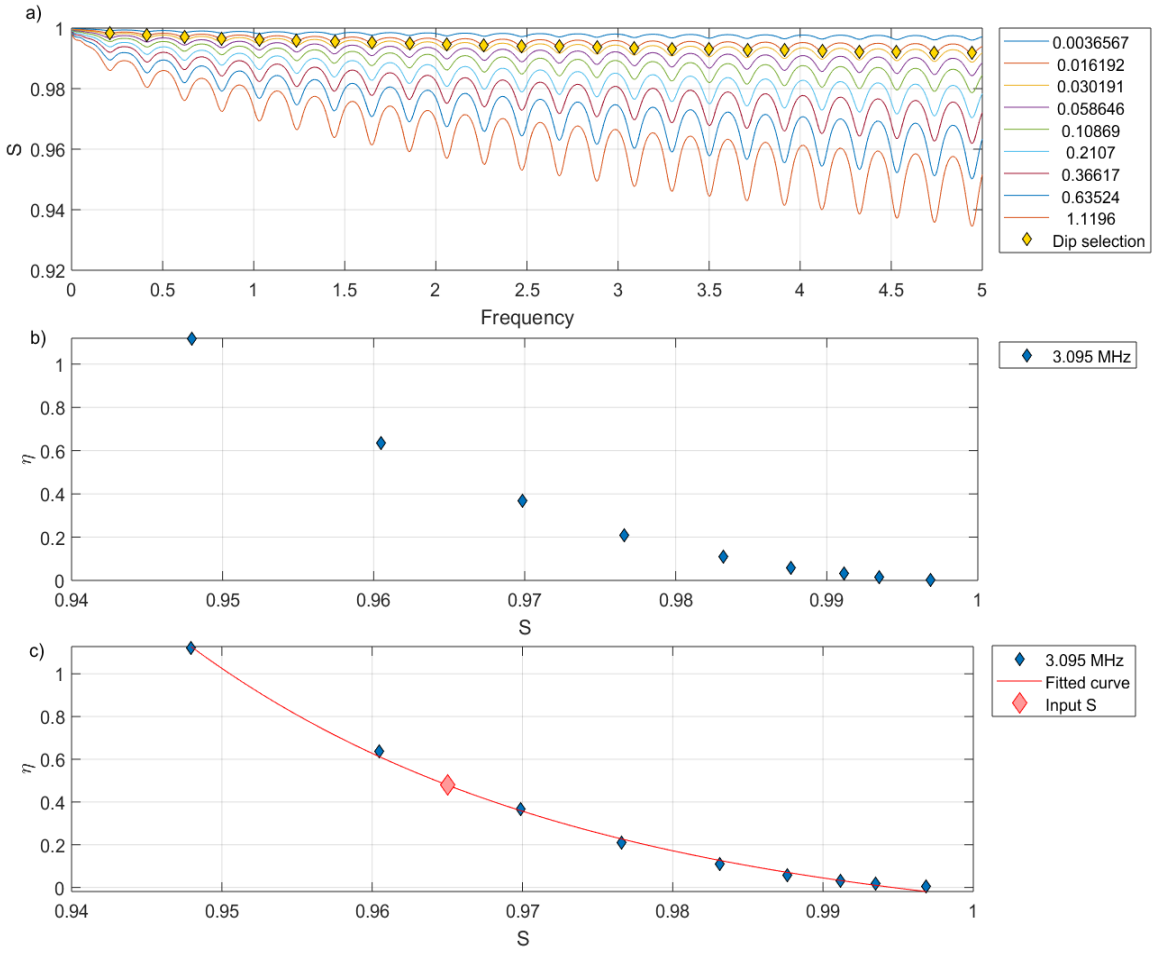

Figure 5-19: The output of the model, a) after initial inputs the S-η relationship is found, followed by an identification of the minima in the S profile (Dip Selection). b) the $\eta - S$ relationship for the given frequency c) Curve fitting used to produce the value of η from the experimental value of S.

The model frequency, and experimental S value for the given frequency from experimental data can be added to the model via prompts once the model has completed finding the $S - \eta$ relationship for each peak frequency identified by troughs in the $S - f$ profile. The value of viscosity for the input S value is therefore given by the model. This serves only as an example of the capability of the model to find η from S, which should not be considered the limit of the models capabilities. A full calibration curve for each resonant frequency can be easily

produced, while the input parameters can be inserted directly into the code, therefore completing the objectives of this chapter.

5.7. Discussion

While interference of multiple frequency waves is important for formation of the SW in theory, this factor is not encapsulated within the model, as the maximum amplitude at each frequency is determined by consideration of multiple reflections of that individual frequency alone. While the model fails to replicate this phenomenon, it is the ratio of the measurement and reference standing waves which governs S. Consequently a deviation of the SW amplitude simulated by the model in response to viscosity change in principal describes the ratio difference between the waves, hence this proportion should simulate that which is present in reality.

The influence of the reflection coefficient at the transducer interface on the maintenance of signal amplitude was reviewed. This highlighted the impact of the number of reflections within a component which are sufficiently large to remain outside the noise level of the signal when considering an experimental signal. Additionally the contribution of the number of reflections to the amplitude of the SW was assessed, and it was concluded that seven reflections were required to attain 100% of the maximum amplitude to four decimal places for the SW model without the ML. The influence of length of the component on the number of resonant frequencies found by the model was them demonstrated, while the effect of frequency on the amplitude of A_m was shown to have a favourable effect. Furthermore, the influence of viscosity on S was found for a range of resonant frequencies. A comparison of the SW response was made to that of a single reflection using the model, achieved by fixing n=1 to demonstrate the sensitivity increase produced through using the SW method.

The model was then further developed to assist in processing experimental data by automatic determination of η from the resonant frequency and S input, a capability which is fully adaptable to improve the versatility of the model. The model can only be used as a comparison with frequencies which show a maximum amplitude from experimental implementation as the bandwidth of the transducer is not included in the model. As detailed in Chapter 3 and 4, the bandwidth is transducer dependent so to prevent a reduction of the applicability of the model to multiple transducer component arrangements this has not been incorporated into the model. Incorporation of the quarter wavelength theory and a three layer model in a solid-solid-liquid arrangement also demonstrates a favourable output when experimental results are considered.

5.8. Conclusion

The standing wave equations outlined in (Mills et al. 2017) were used to produce an analytical model to simulate the SW response to viscosity. This was completed through consideration of physical and ultrasonic parameters which influence to the formation of the wave. The importance of the reflection coefficient on at the transducer interface was highlighted as a factor which could influence the sensitivity of the method if sensitivity is a factor of n.

The model was found to show relationships similar to those found experimentally in response to viscosity and the length of the solid component, while also following principle ultrasonic

relationships. The magnitude of S in response to viscosity was demonstrated, however the agreement of this to experimental results must still be evaluated to validate the model.

Incorporation of the three layer reflection coefficient results in greater sensitivity to viscosity at peak frequencies which relate to a quarter wavelength of the matching layer thickness. The capability of the model to predict viscosity when given the frequency and S of a component in response to viscosity must be evaluated before the model can be validated.

6. Experimental Validation of the Mathematical Model

Chapter 6 and 7 detailed experimental and analytical results of the SW method. This chapter aims to validate the analytical model using experimental results. Along with the influence of viscosity, the effect of several physical parameters were addressed in order to determine whether the model could be used as an alternative method to determine viscosity from a SW signal.

6.1. Comparison of Experimental and Modelled Results

To produce a direct comparison of the experimental results, a series of prior input parameters were required, previously summarised in Table 5-1, Table 5-2 and Table 5-5. Analysis of the model was first completed with tabulated ultrasonic and material properties followed by experimental measurement of these parameters where possible.

6.1.1. Standing Wave Method without a Matching Layer

The wave was modelled using the values of viscosity and density of standard Newtonian oils measured in Chapter 6 to reveal the SW response expected for each oil. Figure 6-1a and b show the reference and measurement signals for the SW method without the ML generated by the model. The model was produced using parameters outlined in Table 5-1 and Table 5-2, which were applicable to the arrangement without the ML.

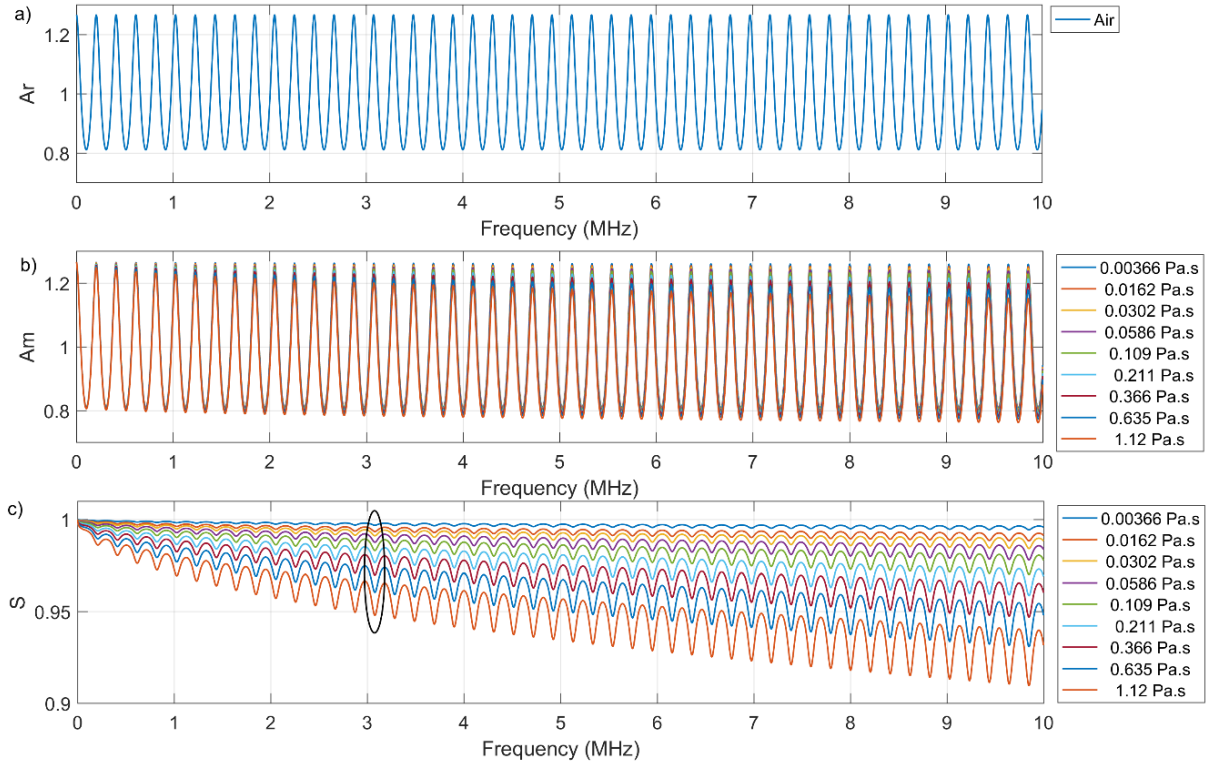

Figure 6-1: SW profile produced using the mathematical simulation for a) A_r, b) A_m and c) S in the frequency domain. f_s = 0.002 and n = 12.

A direct comparison of experimental and modelled reference signals is shown in Figure 6-2. The amplitude of the modelled signal has a uniform distribution in the reference condition, unlike that shown experimentally. The bandwidth of the transducer produces greater signal amplitudes at frequencies which surround the resonant frequency of the transducer in the experimental arrangement. As the model does not incorporate the bandwidth of the transducer, the curved amplitude of the reference peaks is not present in the modelled signal. Peaks and troughs are present in both experimental and modelled signals as the effect of component length influences both.

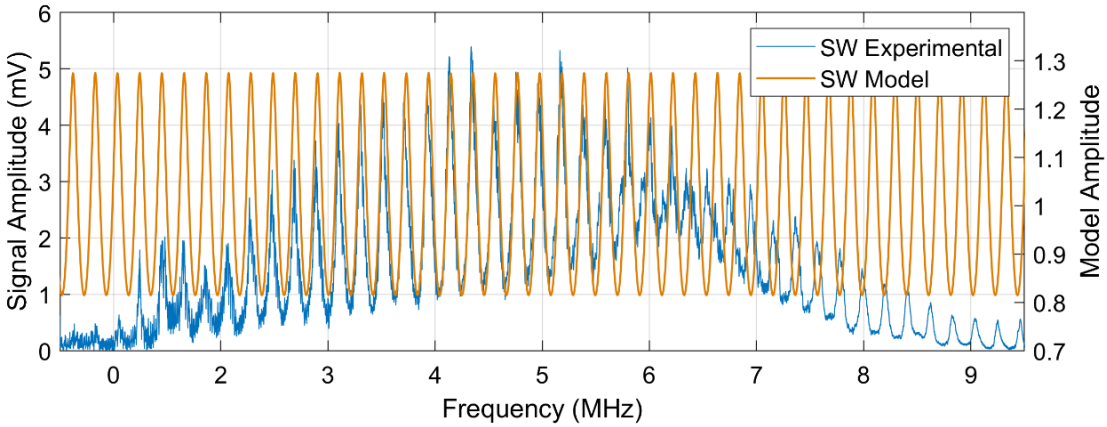

Figure 6-2: An experimental and modelled reference signal of the SW.

The peaks in the modelled data are in the same location to those in the experimental data until 6.4 MHz in Figure 6-2. The resonant frequency of the signal is determined by the velocity of the shear wave and the length of the component. The length of the component was measured using digital callipers with an accuracy of $0.5\mu m$ which may be a sufficient error to produce a deviation of the experimental result to that found using the model.

An additional path length may be produced experimentally due to the small spacing between the excitation and acquisition transducer due to the pitch-catch arrangement. The resonant peaks agree at the frequency primarily under investigation here (3.1 MHz). This frequency was used in Chapter 6 to determine viscosity using the SW with no ML, and so no greater investigation into this deviation will be made as the model is sufficiently accurate for the purposes of this comparison.

Figure 6-3 shows the $S - \eta$ relationship from the model at 3.11 MHz and experimental data at 3.1 MHz. The model produces a relationship and values similar to those found in experimental results. The equation of the fitted curve to the modelled data is shown in Equation 6-1. The experimental data here is taken from Chapter 6 and the frequency of the model was selected using the approach outlined in Section 5.6 to be the closest resonant frequency. Modelled data shown in Figure 6-3 is taken from the dips in S highlighted in Figure 6-1c by a black ellipse, hence the value of S was found for a given viscosity. Equation 6-1is the fitted curve to the modelled data shown in Figure 6-3.

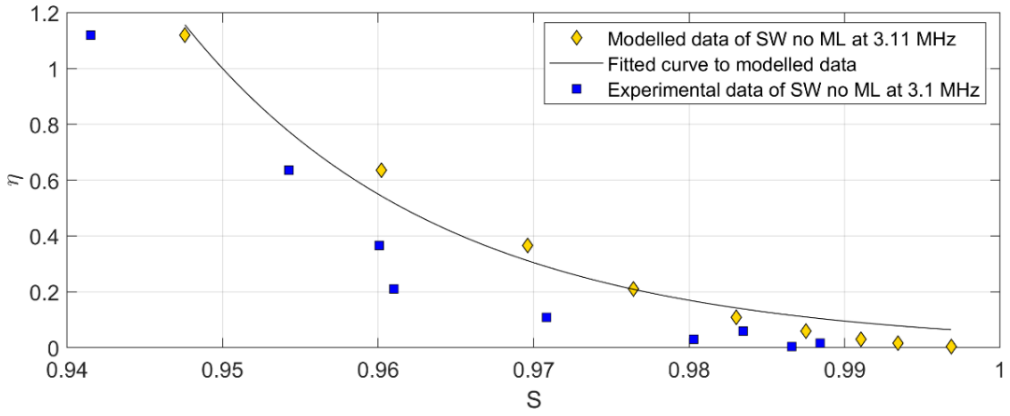

Figure 6-3: The relationship between viscosity and S using the model, at the 3.11 MHz resonant peak and 3.1 MHz peak in experimental data.

$$\eta = 0.05348\, S^{-57.08} \qquad \text{Equation 6-1}$$

Fair agreement between modelled and experimental viscosity was found however the model predicts higher values of S for all viscosities shown here. The average difference in S between analytical and experimental values for corresponding viscosities shown in Figure 6-3 deviates by 0.00882. This difference equates to 19% of the span of the experimental S results. The model assumes exact parameters of the physical arrangement, however a number of physical factors may interfere with the wave to produce an overestimation of η in experimental results. Lower S values found experimentally may be a result of the interaction of the wave with a large contact area with the liquid.

Figure 6-4 shows the predicted viscosity using the analytical model from experimental S values found in Chapter 6 of the blended oils. The analytical model also predicts a higher viscosity for most blended oils. The values were calculated from the model using the experimental value of S at 3.11 MHz using Equation 6-1.

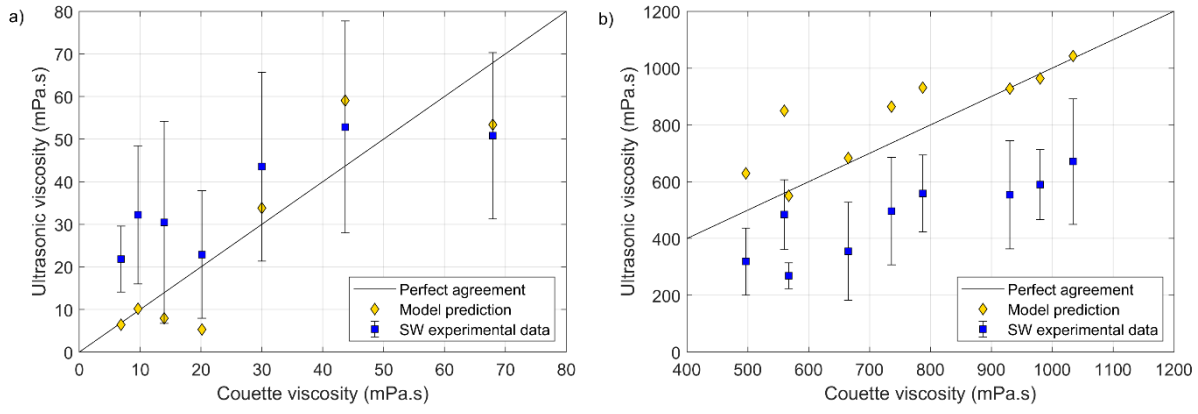

Figure 6-4: Modelled viscosity values from experimental S value a) low viscosity range and b) high viscosity range.

The model underestimates viscosity at low viscosities (0-30 mPa.s), but then overestimates viscosities at higher viscosities (40-1200 mPa.s). The magnitude of the error associated with experimental measurements reduces the pertinence of the data points, however the model predicts viscosities outside the standard deviation of the results for 75% of the data shown in Figure 6-4.

6.1.2. Standing Wave Method with the Matching Layer

The analytical model for the SW method with the ML was achieved by the incorporation of the three layer reflection model at the measurement interface detailed in Section 5.5. Figure 6-5 shows the reference, measurement and S profiles of the SW method with the ML.

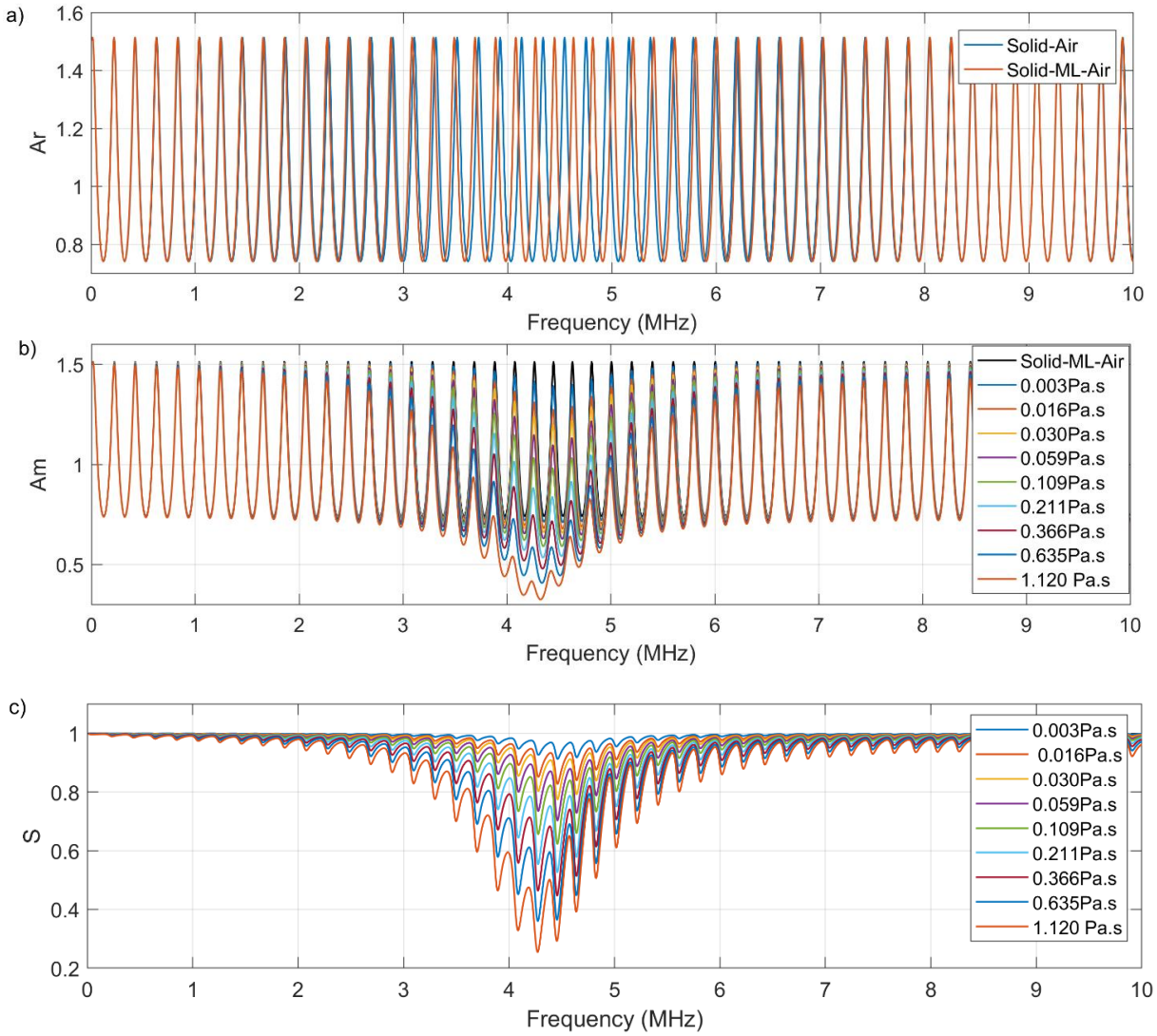

Figure 6-5: Analytical simulation of the SW method with a 50 µm ML for the a) solid-ML-air condition, A_r in comparison to no ML, b) measurement amplitude, A_m at a range of viscosities, and c) S at a range of viscosities.

The use of the three layer model changes the resonant position of the peaks, resulting in a gradual deviation between the two responses of the SW model with and without the ML shown in Figure 6-5a. This effect is shown experimentally in Chapter 6, Figure 4-3.

The amplitude of the SW profile experimentally shows a reduction of the profile amplitude around 5 MHz corresponding to the $\frac{1}{4}\lambda$ of the ML thickness in the reference condition. This effect is also seen in the modelled reference signal, however to a much lesser extent as shown in Figure 5-16b. The influence of the ML on the SW in the reference condition does not affect S as it is the change in viscosity which creates the deviation of S. The profile of the reference wave simulated with the ML is unimportant here, as it is the relative amplitude difference produced by the liquid viscosity which is the relationship of interest.

Figure 6-5b shows how the amplitude of the measurement signal, A_m, changes with respect to viscosity. The model replicates the behaviour shown experimentally in Figure 4-7b. As η increases, the amplitude of the peaks reduces to the greatest extent at antinodes which correspond to the ML resonant frequency of 5 MHz. Each signal is composed of peaks and troughs, which both reduce with increasing viscosity in the region of the signal influenced by the ML.

Results in Figure 4-7b show that a reduction in trough amplitude found experimentally is not as prevalent as that achieved using the model, as shown in Figure 6-5c. The trough amplitude in experimental results is in the region of noise within the signal, a feature which is not present within the model. The amplitude of the peaks in the model reduce by a greater proportion than that of the troughs, reiterating enhanced sensitivity at the peaks, a behaviour of the SW previously documented in Chapter 6. A direct comparison of experimental and modelled reference signals with the ML is shown in Figure 6-6.

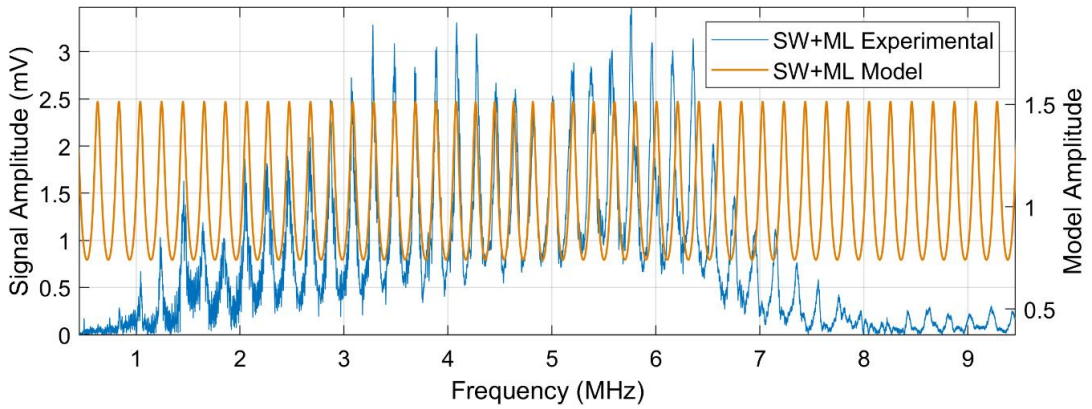

Figure 6-6: An experimental and modelled reference signal of the SW with the ML.

The modelled reference wave shows good agreement with experimental reference data until around 6.4 MHz, similar to that of the SW without the ML discussed previously. For validation of the model, the comparison will be made at 4.45 MHz, a frequency which is in complete agreement, as demonstrated in Figure 6-6. Results produced using the experimental and analytical approaches at 4.45 and 4.449 MHz respectively are compared in Figure 6-7.

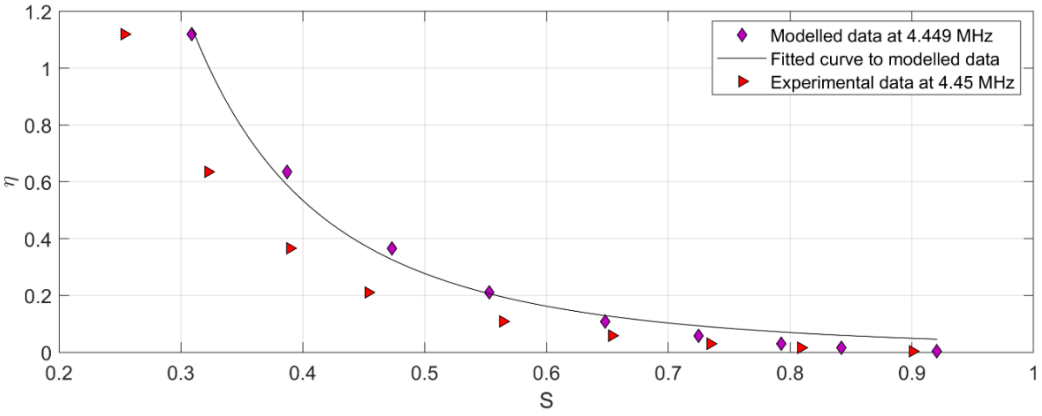

Figure 6-7: The relationship between η and S using the three layer model for a 50 µm ML at the 4.36 MHz resonant peak and 4.44 MHz peak in experimental data.

$$\eta = 0.03616\, S^{-2.941} \qquad \text{Equation 6-2}$$

Equation 6-2 is the equation which is fitted to the modelled data in Figure 6-7 at 4.44 MHz. This equation only stands for measurements taken at 4.44 MHz only, and only when measurements are made using this specific component-transducer arrangement. In a similar way to the SW analytical response, the modelled data predicts a higher viscosity than the experimental data. The average deviation in S is 0.06, representing 9.8 % if the span of experimental results indicating a closer agreement between modelled data for the SW ML model than that of the SW alone, although the reason for this is unclear. Figure 6-8 shows the viscosity of the blended oils calculated from Equation 6-2 using values of S from experimental results in Chapter 4.

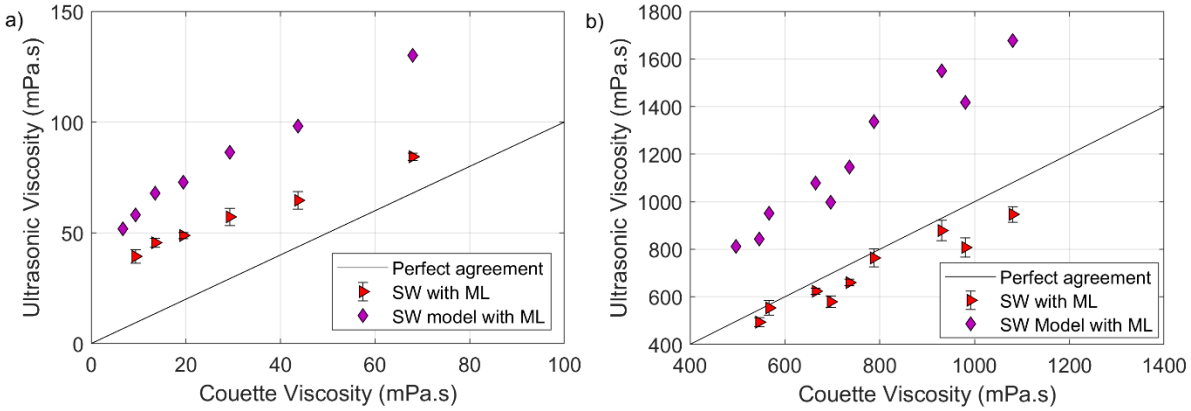

Figure 6-8: Blended oil viscosity measurement compared to that predicted from experimental S value using the analytical model for a 50 µm polyimide ML.

The model again produces higher η values than experimental results. This result was increasingly likely in the SW with the ML model, as the addition of a ML to the surface of the solid adds additional interfaces, such as the glue layer between the component and ML and so additional complexities to the SW response.

6.2. Tuning of Parameters Based on Experimental Results

6.2.1. Phase Shift and Reflection Coefficient at the Transducer Interface

Conditions at the transducer to component interface have a significant influence on the amplitude of the SW. R' and ϕ' influence the amplitude of the wave, and thus define the number of waves which contribute to the final SW amplitude. Experimentally, if R' is low, only a few reflections of the wave within the component may sustain a sufficient amplitude to deviate significantly from signal noise. However if most of the ultrasonic energy is reflected, the wave can complete a larger number of trajectories through the component outside the noise region. Increasing the number of reflections acts to increase the sensitivity of the method, as previously documented by (Greenwood et al. 2006). In this section the reflection coefficient and furthermore the phase at the transducer are investigated.

In order to experimentally measure R' and ϕ' an immersion scanning probe was used in a water bath to scan a simple aluminium plate, as shown in Figure 6-9a. The plate was instrumented with two longitudinal transducers, one of which had been potted in tungsten packed epoxy, and the other left with a free surface, shown in Figure 6-9b.

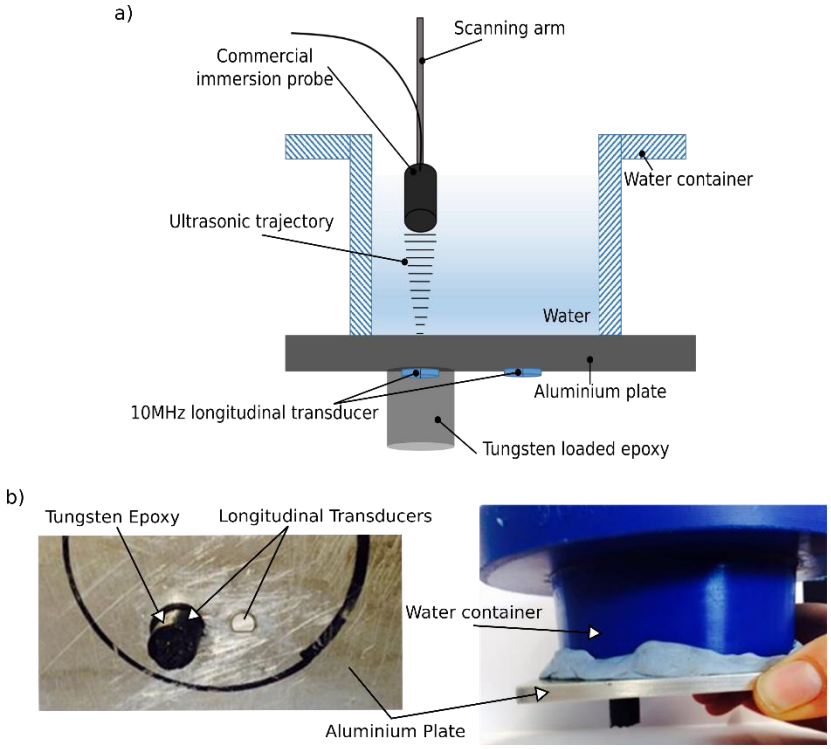

Figure 6-9: a) Schematic diagram of the immersion probe and metal plate arrangement. b) images of the aluminium plate instrumented with 10 MHz longitudinal transducers, showing one transducer potted in tungsten loaded epoxy, and the other with a free surface.

Longitudinal transducers were bonded to the aluminium interface, and a longitudinal water immersion probe used to scan the plate. As shear waves are incapable of propagation through liquids, measurement of shear transducers bonded to the aluminium component using a shear wave was impractical without direct coupling to the plate, which would prevent a scan of the

surface. The system thus reproduces ultrasonic reflections from the transducer interface experienced within the component for a longitudinal system to gain a clearer understanding of this interaction.

The plate was placed into the water bath and the probe immersed into the liquid. The probe position was controlled using a mechanical arm in order to correlate ultrasonic measurements to the position of the plate. Labview software was then used to extract the phase and amplitude from the data. An area of 29×15 mm was scanned, with a lateral resolution of 0.5mmin the 'x' direction, (see Figure 6-11), covering both transducers. A 10 MHz immersion probe was used and the FFT profile of a single reflection can be seen in Figure 6-10.

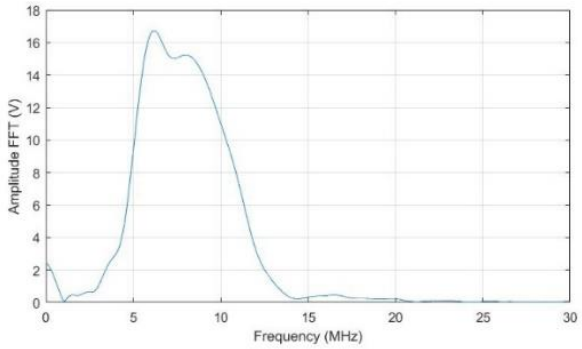

Figure 6-10: FFT of a single measurement through the aluminium plate using the immersion probe.

6.2.1.1. Phase Shift

The amplitude and phase extracted from the scan is shown in Figure 6-11 at each point in the scan.

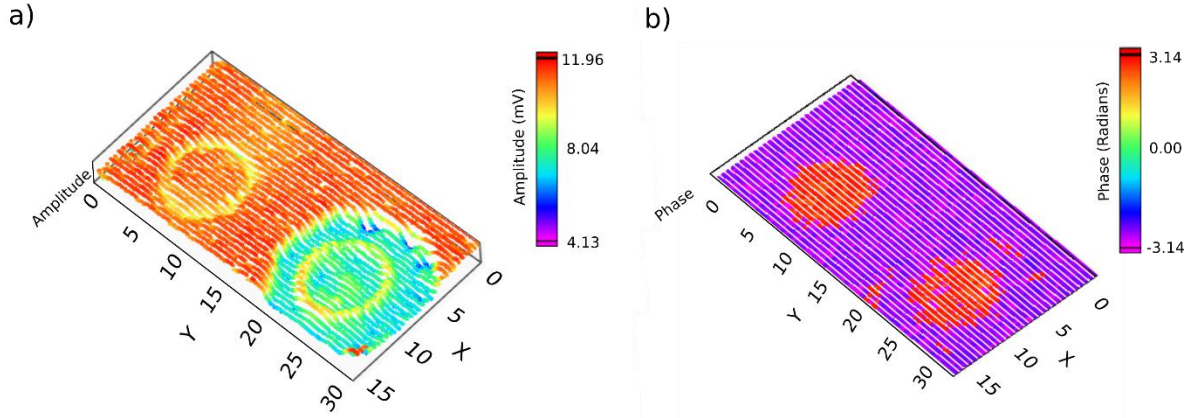

Figure 6-11 : A 3D plot in the X and Y direction from the aluminium plate of (a) the amplitude of the FFT, and (b) the phase of the scan.

The amplitude of the FFT shown in Figure 6-11a reveals the profile and location of the transducers and the potting compound. When these scans are compared to the images of the plate measured in Figure 6-9b, the similarities are revealed. Ultrasonic measurement reveals the location of both transducer bonded to the aluminium plate side by side, however only one can be seen in Figure 6-9b as the other has been enclosed in epoxy. The difference between the

phase at the component surface and that at the transducer is 2π, shown in Figure 6-11b, as the phase at the surface is -3.14 and the phase at the location of the transducer is 3.14.

In reality the influence of the transducer interface may be a combination of the phase at the transducer, and the solid-air interface surrounding the transducer. The ultrasonic wave trajectory is unlikely to remain solely linear through the component. When ultrasound is generated by a transducer bonded to a solid component, it projects as lobes over 180° of the flat surface. Consequently the SW signal may be predominantly a result of waves which propagate perpendicular to the measurement interface, however oblique wave reflections may also be detected from the solid-air interface. Although this study was completed with longitudinal transducers, the same behaviour is assumed to occur when using shear waves, so the value of ϕ' was subsequently set to 2π, showing the following behavior of the model, seen in Figure 6-12.

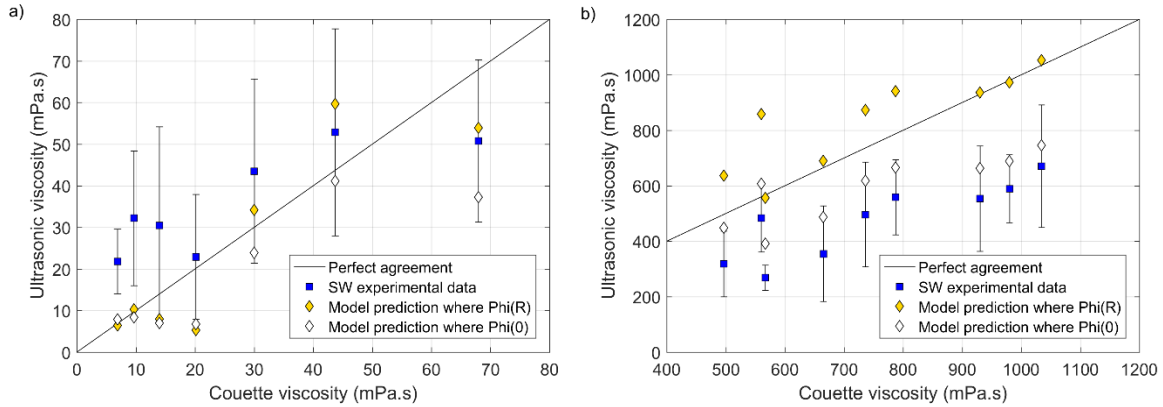

Figure 6-12: Modelled viscosity values from experimental S value a) low viscosity range and b) high viscosity range. Experimental results taken at 3.1 MHZ and experimentally modelled at 3.11 MHz.

The agreement of the model with ultrasonic viscosity was selected as the aim of the analytical technique is to predict the ultrasonic response, as an alternative to prior viscosity calibration. Agreement between the modelled viscosity and experimental data is improved in the higher viscosity band as 88.9% of the modified model lies within the error of the experimental data, improving agreement as 0% previously were within this region. At lower viscosities, Figure 6-12a, no clear relationship is shown. This modification to the model improves agreement to experimental data for the higher viscosity band, improving agreement of the model by on average 52%. This was calculated by representing the modelled viscosity as a percentage of the experimental data then finding the difference between these values for each model. While these results are interesting, no clear indication of improvement was found for the full range of viscosities and so the phase change at the transducer interface will be calculated using conventional relations in the model for the SW with no ML.

The phase change was then applied to the ML model, however an inconsistent trend was found, as the model deviated further from experimental results at lower frequencies by on average 4%, however grew closer to experimental data in the higher frequency band by 9%.

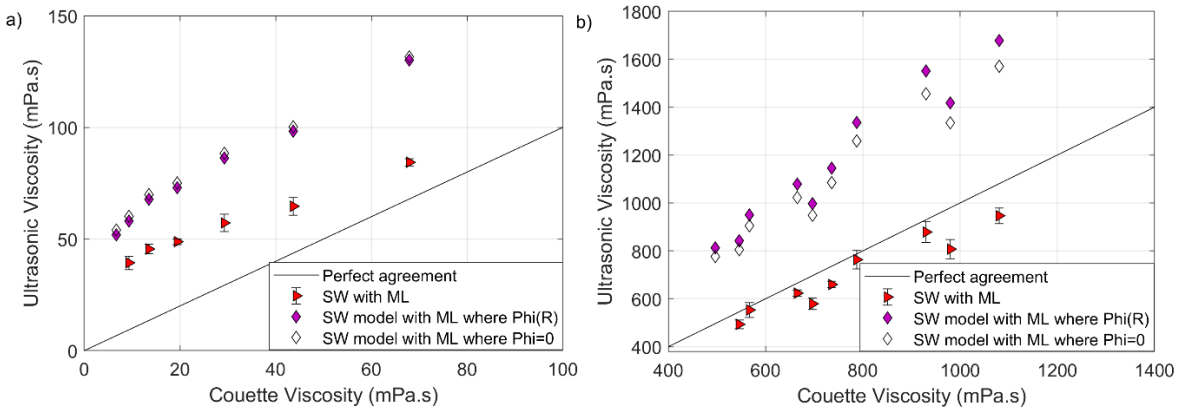

Figure 6-13: The effect of $\phi' = 0$ on the analytical model agreement to experimental and pre-existing values.

Due to this inconsistency, the phase change at the transducer interface for the SW model with the ML will remain calculated using the conventional equations, shown previously in Equation 2-27.

6.2.1.2. Reflection Coefficient

Figure 6-14 shows R' at the transducer interface, this was calculated using the maximum amplitude of the FFT signal as the reference value.

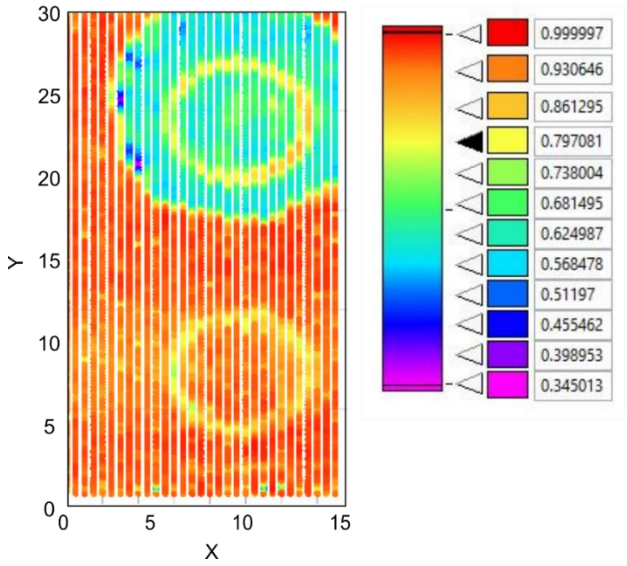

Figure 6-14: Scanning tank data converted to the R', shown using a colour bar graph.

R' measured at the surface of the plate is on average 1 when an air interface is present. Around each transducer this drops to R'= 0.79, as the wave scatters at the edges of the transducer. The area covered by tungsten packed epoxy is mostly between R = 0.56 and 0.73, although R' at the edge of transducer is around 0.79 again. Potting transducers is conventionally thought to stabilise the ultrasonic signal when a pulsed method is considered, acting to reduce the influence of surface waves which may contribute to higher levels of noise.

The reflection coefficient in the centre of the un-potted transducer is between 0.93 and 0.99, indicating a greater proportion of ultrasonic energy is maintained within the system without potting, hence preferential results are achieved using the SW without the addition of a potting media. This finding is key when considering the SW method as R' has a greater influence on the measurement capability than when using a pulsed technique. The analytical model was then used to simulate the effect of R' on the reference amplitude for a series of reflections, represented in the model as n. This data is shown in Figure 6-14.

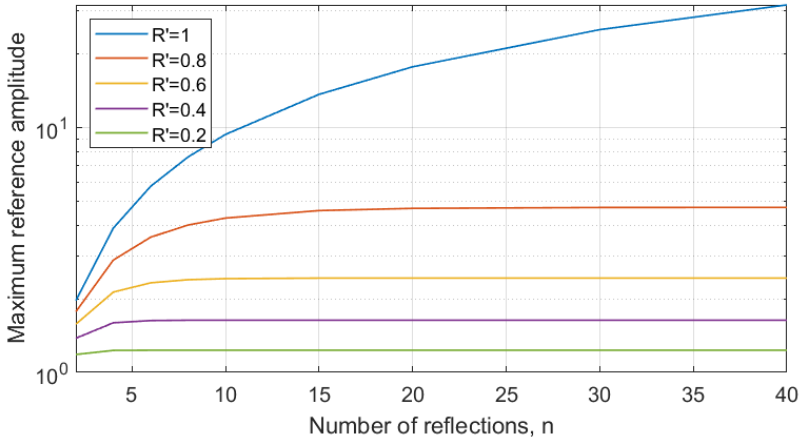

Figure 6-15: Maximum amplitude of the SW between 0 and 5 MHz as the number of reflections increases for a range of R' values, where the amplitude is in the log scale.

Increasing R' in the model presents some interesting relations. The first is the obvious increasing amplitude of the signal, a feature which could be present experimentally if R' was increased through optimal materials selection. The second regards n, Figure 6-15 shows the maximum amplitude of the signal is met after a greater number of reflections with increasing values of R'.

The R' value used initially in the model was calculated using Equation 2-13, to be 0.345. Experimentally, the maximum amplitude of the reference signal will continue to increase with n if both R' and R equal 1. The influence of R' was modelled using n=20. When a viscosity of 1.1196 Pa.s was simulated at the 3.11 MHz resonance; when R'= 0.345, S= 0.93, while when R'=1, S=0.67. A higher R' value is therefore shown to improve the sensitivity of the SW method using the model. The scanning tank measurements indicate that R' is close to 1, and so the number of reflections of the signal, capable of lying outside the noise in the signal, would influence signal saturation.

In practice the number of reflections of a wave within the bounded structure is not a factor which is controlled, as the wave continues to reflect within the component until it decays to zero naturally. Experimentally, we consider the amplitude of the wave to be at a minima when it lies within the noise of the signal. When simulating the wave however, n must be changed accordingly with R' in order to permit the maximum amplitude to be found. This parameter may be a factor to consider when tuning the sensitivity of the model to that of experimental results, however fair agreement with standard conventional values is found and so this parameter will not be changed in the model.

6.2.2. Phase Shift Measurement of the Standing Wave Method

While the phase shift at the transducer interface can be measured experimentally, the effect of the phase at the measurement interface can be extracted from the SW by comparison of the phase of a solid-air and solid-liquid signal. The phase was calculated using an FFT of A_r and A_m. The phase of a reference signal alone is shown in Figure 6-16. On closer inspection a saw tooth behaviour is shown, Figure 6-16b.

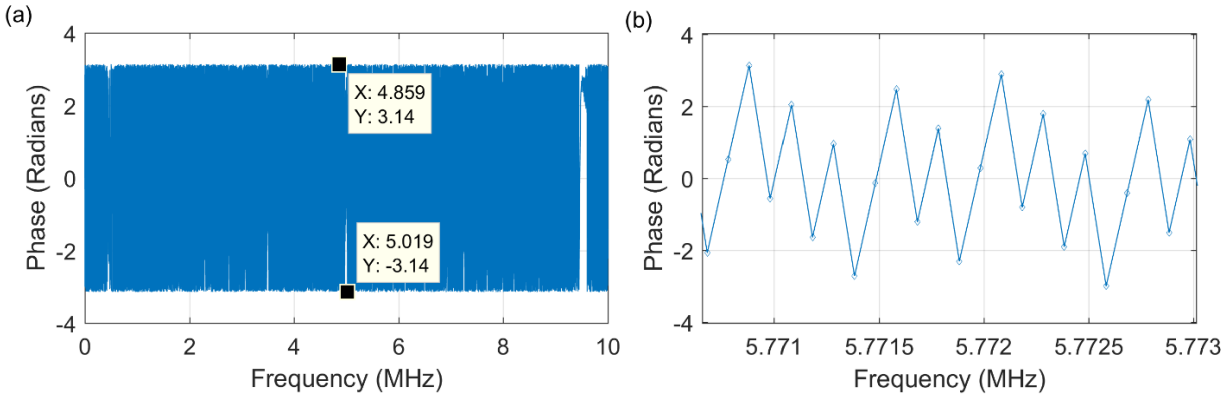

Figure 6-16: The phase of a SW reference signal with no ML. a) Full frequency sweep behaviour, b) magnification of a).

The saw tooth nature of the phase profile is due to the continual phase change in frequency. The phase spectrum further highlights the reason for nodes and antinodes within the SW signal. This saw tooth effect is seen in both the reference and measurement phase spectra from the data analysed here and is an effect documented in work by (Reddyhoff et al. 2005). This behaviour is known to be associated with frequencies within the vicinity of harmonics (Haines et al. 1978) and so would be expected from a standing wave signal of this type. A typical reference and measurement FFT signal amplitude, and phase difference between the signals is shown in Figure 6-17 for the SW with and without the ML.

To isolate the influence of liquid at the measurement interface, the reference phase was subtracted from the measurement phase, the results of which is shown in Figure 6-17 as the phase difference. For the SW method, the data which lies within in the operational frequency bandwidth of the transducer is shown to be largely independent of frequency, only fluctuating slightly, within the region of noise when considering the SW with no ML. Figure 6-17b, shows phase difference data from the SW with the ML, producing the greatest difference in phase at frequencies which correspond to the resonant peaks of the signal.

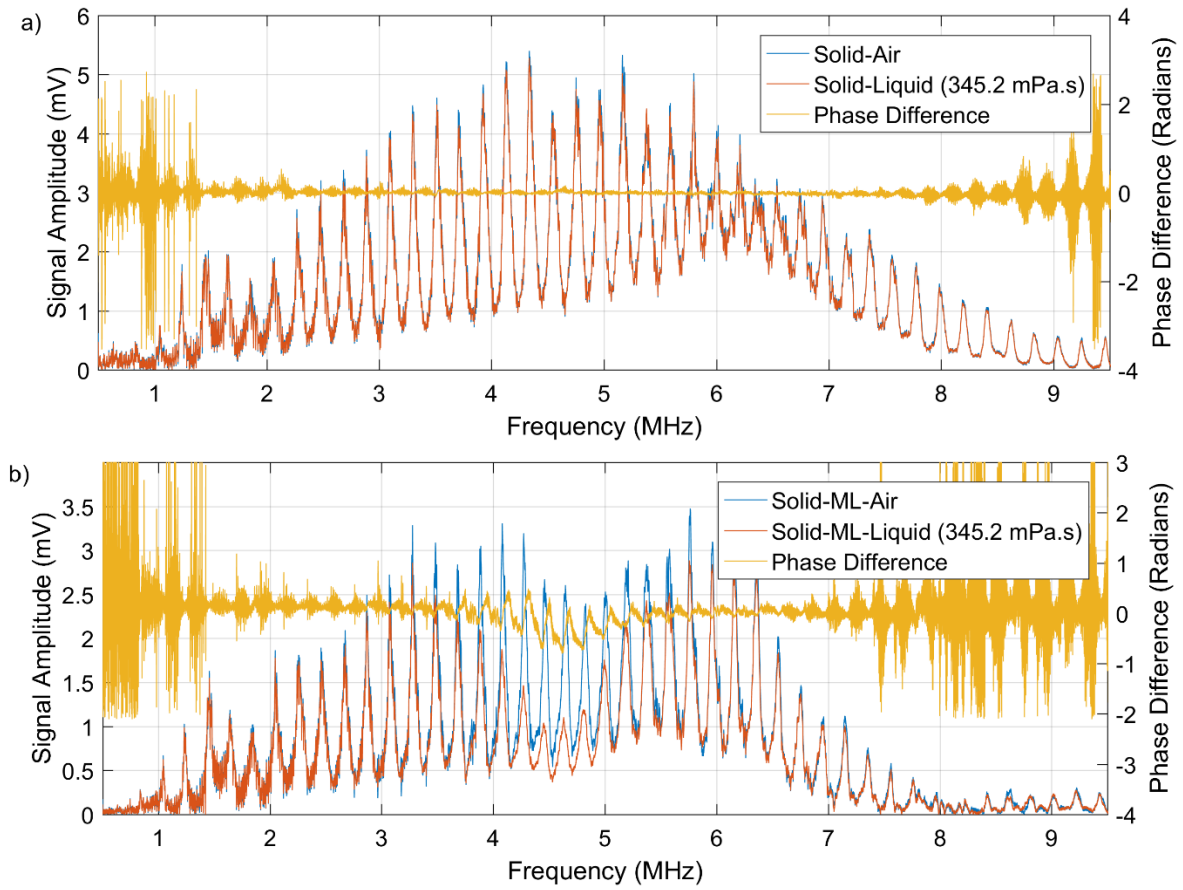

Figure 6-17: The FFT amplitude of a reference and measurement signal with corresponding phase difference between the two signals for a), the SW with no ML, and b) SW with the ML.

Figure 6-18 shows the phase difference between each liquid viscosity calculated using data from Chapter 6 for SW data with and without the ML. No distinguishable deviation of the phase indicates that liquid viscosity does not influence the phase of the SW signal to an extent which overcomes the noise of the signal in Figure 6-18a. Thus without the ML differences between each individual phase difference could not be related to viscosity.

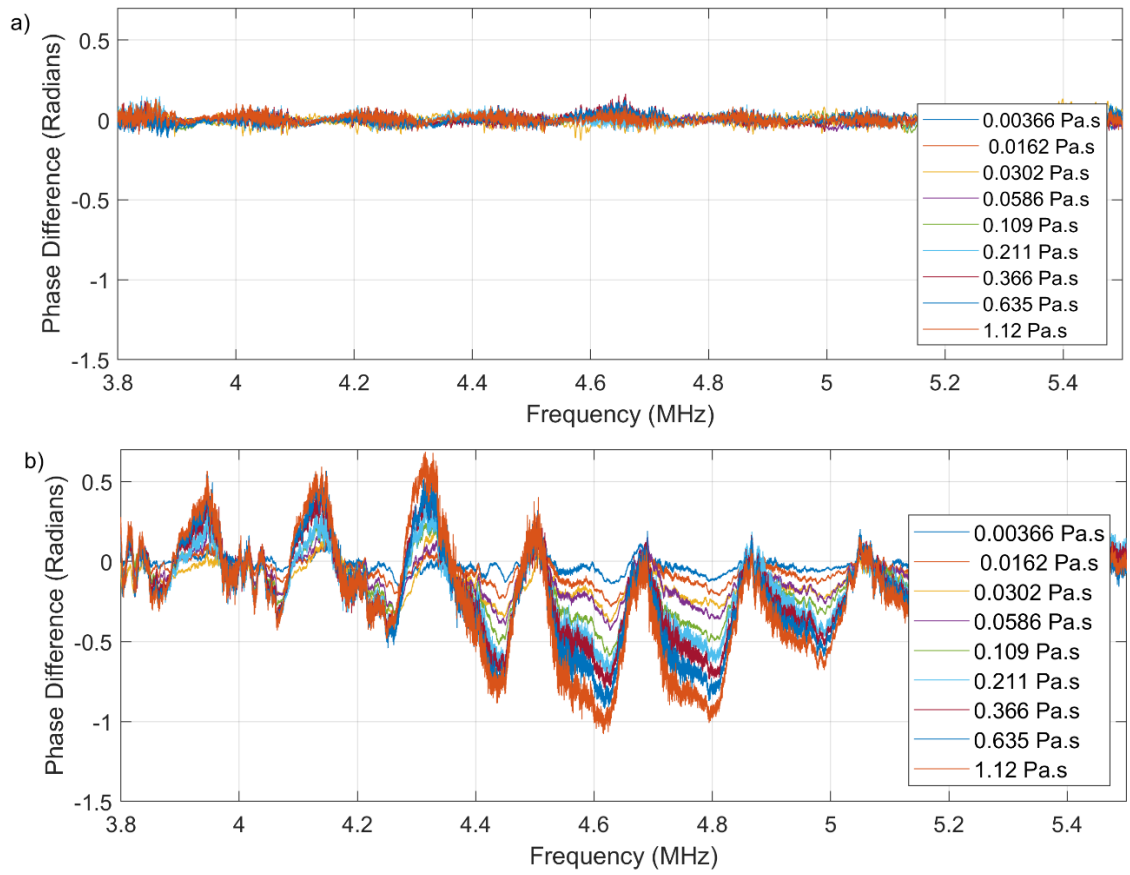

Figure 6-18: A figure to show the phase difference between reference and measurement signals for each liquid viscosity for a) the SW method with no ML, and b) the SW method with the ML.

Phase differences from the SW method with the ML correspond to liquid viscosity. Figure 6-18 shows how phase differences increase with increasing viscosity, while further demonstrating the influence of frequency on phase. The phase difference is the greatest at frequencies which lie in the most viscosity sensitive region of the sweep, and thus correspond to ML thickness and also resonant frequency position.

6.2.3. Comparing Analytical and Experimental Phase Data.

The experimental phase difference found between measurements of liquid viscosities was then simulated using the SW model. As the SW with no ML produced no measureable phase experimental results, the SW model with the ML only will be considered. The cumulative phase of the SW with the ML was calculated from the final A_r and A_m signals produced. The model produces comparable phase differences with experimental results, as shown in Figure 6-19.

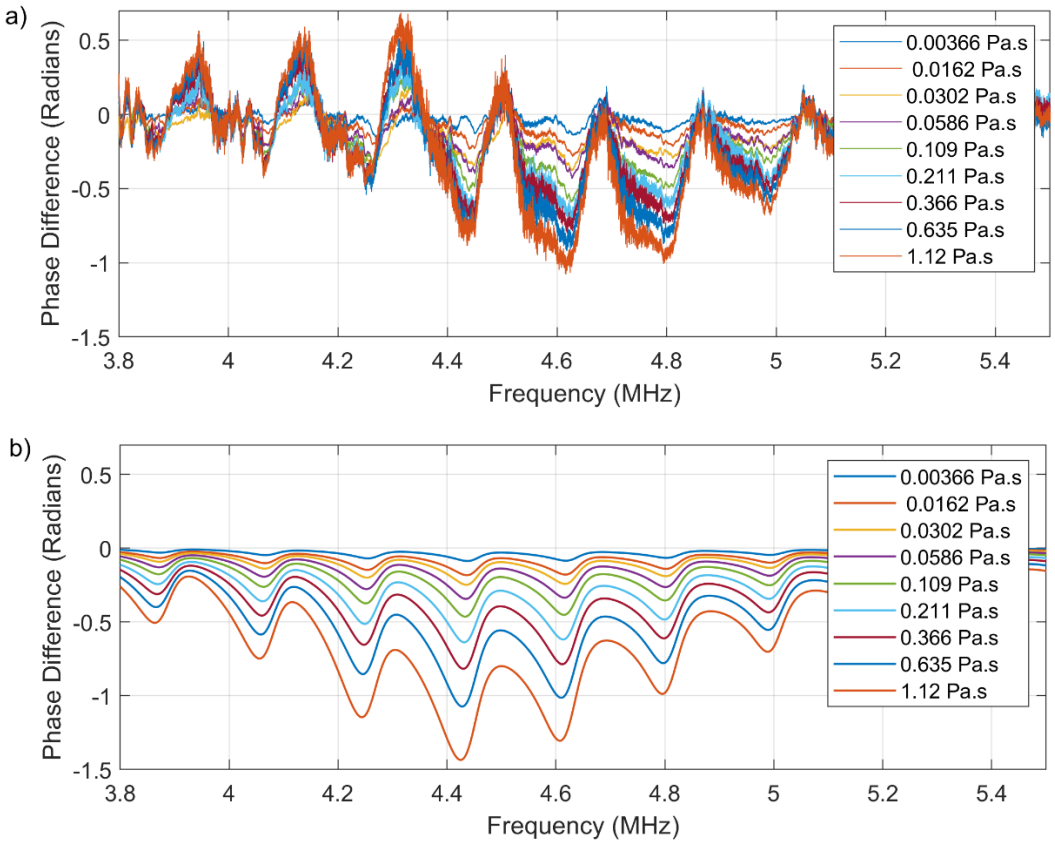

Figure 6-19: Phase difference between reference and measurement signals, a) experimentally and b) using the SW ML analytical model.

Similar phase behaviour is shown between modelled and experimental results, however the model predicts a greater phase change. The greatest change in phase is shown at 4.618 and 4.426 MHz for the experimental and modelled phase change respectively. A direct comparison of the phase change seen experimentally and that produced by the model is shown in Figure 6-20.

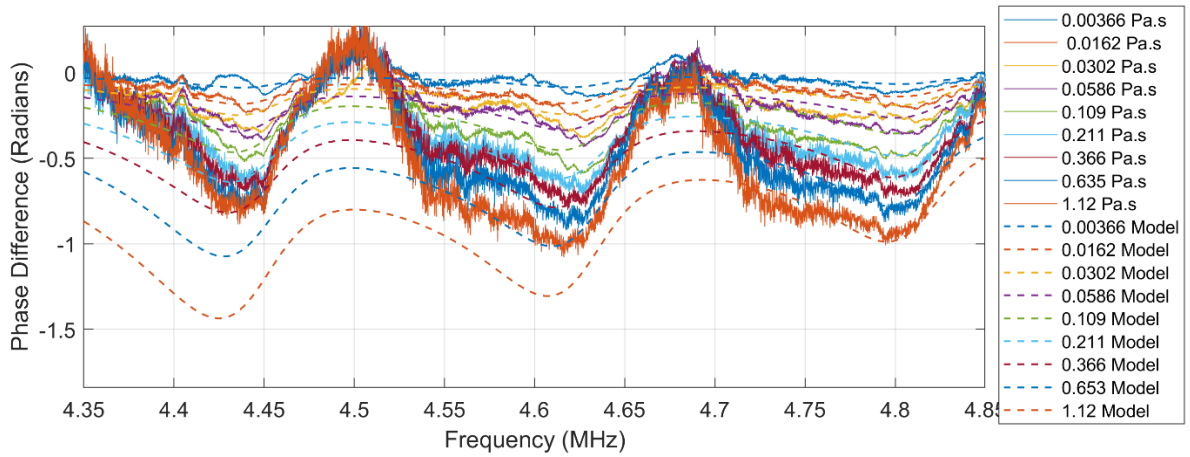

Figure 6-20: Phase change between reference and measurement signal for experimental data shown as solid lines, and modelled results shown as dashed lines.

The agreement shown here can be seen as validation for the SW ML model, as purely analytical predictions match closely with those of experimental results. Experimental and analytical results shown in Figure 6-20 show better agreement with lower viscosity data than high viscosity data. As the use of the amplitude to determine viscosity using the SW method with the ML is in less agreement, the use of phase difference to determine viscosity could be seen as an alternative approach to the viscosity measurement. The maximum phase difference shown at 4.442 MHz using the model is 1.432 Radians, however the experimental equivalent only amounts to 53% of this, at 0.769 Radians. At 4.8 MHz however greater agreement is shown, as the analytical results produce a similar shaped response to that shown experimentally, and experimental results cover 95% of the analytical data.

6.3. Discussion

A good overall agreement between analytical and experimental results was found. The signal profiles of each method agree sufficiently with analytical results to allow a reasonable comparison to be made. The model overestimates viscosity for both methods, as the values of S found experimentally are smaller than what analytical results suggest for the same viscosity. This could be attributed to the mechanisms of the model which consider only a one dimensional linear path of the wave, hence the actual influential solid-liquid surface in which the experimental standing wave contacts could be greater and so cause a greater amplitude reduction.

The inclusion of the three layer reflection coefficient into the model was found to influence the distribution of resonant peaks at frequencies which have experimentally been found to be affected by the presence of the matching layer. The amplitude of the measurement signal simulated by the model had a greater sensitivity at the same frequencies as experimental results, and so a robust comparison between viscosity results could then be made.

Practical measurement of the phase shift at the transducer interface was found to be zero, although this adaptation to the model produced mixed results. No clear result was found at the low viscosity band for the SW model, however results were found to worsen in the SW ML model. In the high viscosity band investigated, replacing $\emptyset'$ with zero improved the model agreement with experimental results by 52% without the ML and 9% with the ML. As implementation of the ML does not affect the conditions at the transducer interface practically, this result suggests a variability in $\emptyset'$ between the two experimental arrangements as consistent trend between phase change and agreement of the model was found. As transducers for each method were bonded individually, differences between the qualities of the bond and also glue layer thickness could account for this variability however further investigation would be required to determine this.

Measurements of R' indicated a favourable result when the transducer was in the un-potted assembly. Increasing R' could improve the sensitivity of the SW method experimentally, as indicated by the model. When R' is greater, a larger number of reflections, n in the model, is required to achieve the saturated amplitude of the wave. This finding presents two uses, the first regards the consideration of n within the model for variable values of R' to ensure signal

saturation is achieved, and the second regards the practical selection of transducer materials to optimise R' to improve method sensitivity.

Analysis of the experimental phase shift from SW results in Chapter 6, indicated no measureable phase differences, although a clear trend was found between η and phase difference from SW results with the ML. The greatest phase difference was shown at 4.63 MHz, although the greatest change was anticipated to be at 4.45 MHz as it is at this frequency where the greatest amplitude reduction, and so sensitivity to viscosity is found experimentally. Negative phase changes are shown at frequencies which correspond to peak amplitudes of the experimental signals however positive phase changes are also found at frequencies which correspond to troughs. The reasoning for this is unclear as a direct subtraction of measurement and reference phase was used to produce these findings. However the SW ML model produces the greatest phase change at 4,45 MHz, the most sensitive peaks in the measurement condition, perhaps indicating erroneous results shown by experimental data.

6.4. Conclusion

The model overestimates viscosity for both methods however this could be attributed to the fitting of the curve which is completed within the model in order to find viscosity. Further investigation and refinement of this trend may therefore improve agreement. Implementation of the three layer reflection coefficient shows agreeable results to experimental data, indicating that the behaviour of a single wave at the interface can also be used to describe that which is present for a standing wave when using the SW model. Favourable agreement of phase also indicates good validity of the model as the shape of the phase behaviour with respect to frequency is well replicated by the model. Further refinement of physical parameters such as speed of sound, thickness of component and acoustic impedance values could all contribute towards better agreement of the model to experimental results if the system was to be used to predict viscosity, while the practice of potting a transducer should be avoided if possible when aiming to use the SW method.

7. In-situ Measurement of Marine Diesel Engine Oil Viscosity.

This chapter provides an application of the SW method as a condition monitoring technique for marine engine lubricant oil viscosity. The aim was to determine whether the SW method can be used to perform in-line viscosity measurement in real time without the need to take samples from a real engineering system. To do so an in-line ultrasonic viscometer was developed. Iterations of the device development are detailed, followed by experimental calibration prior to a field test on a common rail lubricant system of a test engine (RTX-6) at WinG&D, Winterthur. The capabilities and limitations of using the SW method are then addressed.

7.1. Marine Diesel Industry Background

Lubricating oil is used within the marine diesel industry to lubricate the cylinder liners of the engines which can have in excess of 14 cylinders each (WinG&D 2018). These cylinders can have a bore diameter up to 9.60 m and a stroke of 2.5 m (Wärtsilä 96C), for this reason large volumes of oil are required to lubricate the various contacts between the cylinder and piston. A common rail lubricant system is adopted as the oil is used not only as a lubricant but also as a means of neutralising acidic compounds in the fuel which can lead to significant corrosion on the inner bore of the liner. Fresh lubricant is therefore circulated around the engine to neutralise the acidity, however the properties of the lubricants can vary significantly during the running of the engine.

Figure 7-1 shows images of a cylinder liner as well as the position of the common rail system and its connection to the injectors which are inserted through the cylinder. The lubricant that is injected into the cylinder liner on start-up will operate at lower initial temperatures than that of the lubricant injected when the engine is in full operation, influencing engine operation. The viscosity of the oil may also be affected by varying the TBN; a measure of alkalinity of the oil, which is controlled to neutralise the sulphuric acid that is yielded during the combustion of the diesel fuel. A fuel with a higher percent of sulphur requires a lubricant with a higher base number, hence fine tuning the properties of the lubricants during operation is essential. Many marine fuels used in practice are subject to less refinement; such as desulphurisation, than other higher value fuels (such as petrol and diesel). The control of the resulting sulphur combustion products is therefore crucial to the longevity of the engine.

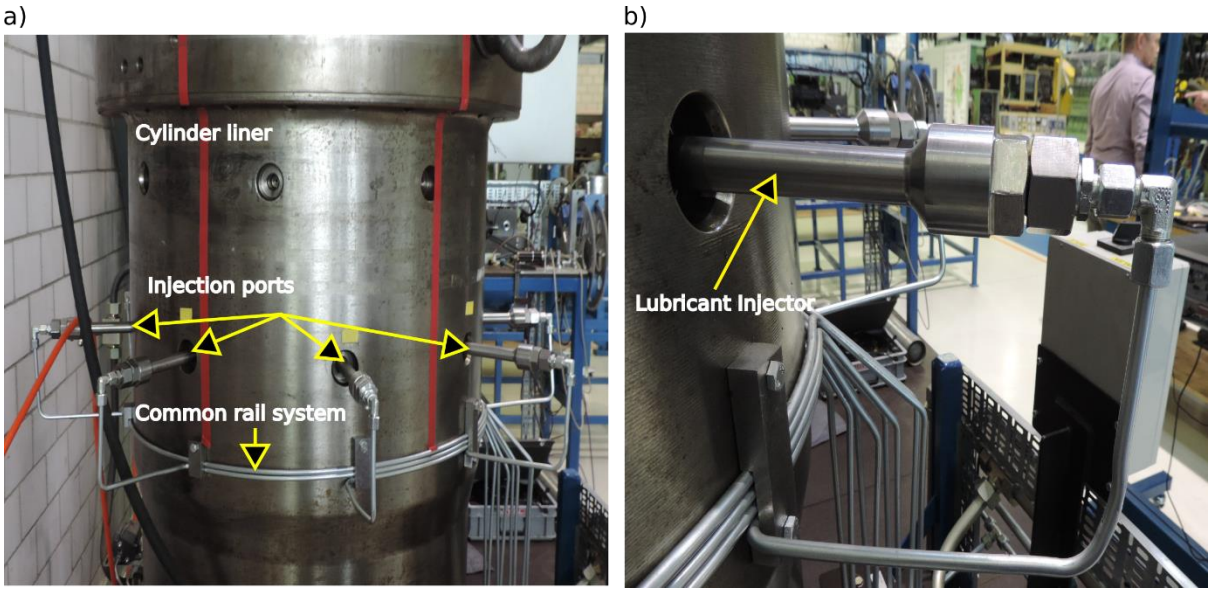

Figure 7-1: a) Lubricant oil lines on a common rail system, five injector sites are shown in the image. b) Lubricant line leading to injector.

This presents an opportunity for ultrasonic viscosity measurement for applications at the research and development sector at WinG&D.

7.2. Development of the Engine Lubricant Viscometer

The decision to create a device rather than to directly instrument an existing component on the engine was made to ease the calibration process and to permit a more time efficient flexible installation process. To directly instrument existing components, they must ideally have two opposing parallel surfaces, one used to mount the transducer, the other acting as the measurement interface. While potentially possible, an aim of the project was to take a minimally invasive approach to measure viscosity in-line with minimal disruption to the operation of the engine.

The final design selected is shown in Figure 7-2 as a CAD drawing and an image of the assembled Engine Lubricant Viscometer (ELV). The ELV was composed of three main components;

1. The housing: produced in steel, provides a channel through which the lubricant can flow, accompanied by threaded ports to accommodate the pipework.

2. The puck: composed of an aluminium cylinder instrumented with two 5 MHz shear transducers. Cable protection and strain relief were achieved using a steel guarded cable wrap. The puck had a 50 µm polyimide ML bonded to the surface adjacent to the transducers to achieve the highest measurement sensitivity.

3. Puck enclosure; the steel puck enclosure accommodated the puck via a push fitting, with a threaded outer rim to join to the housing. The puck enclosure holds the puck measurement surface in the path of the lubricant.

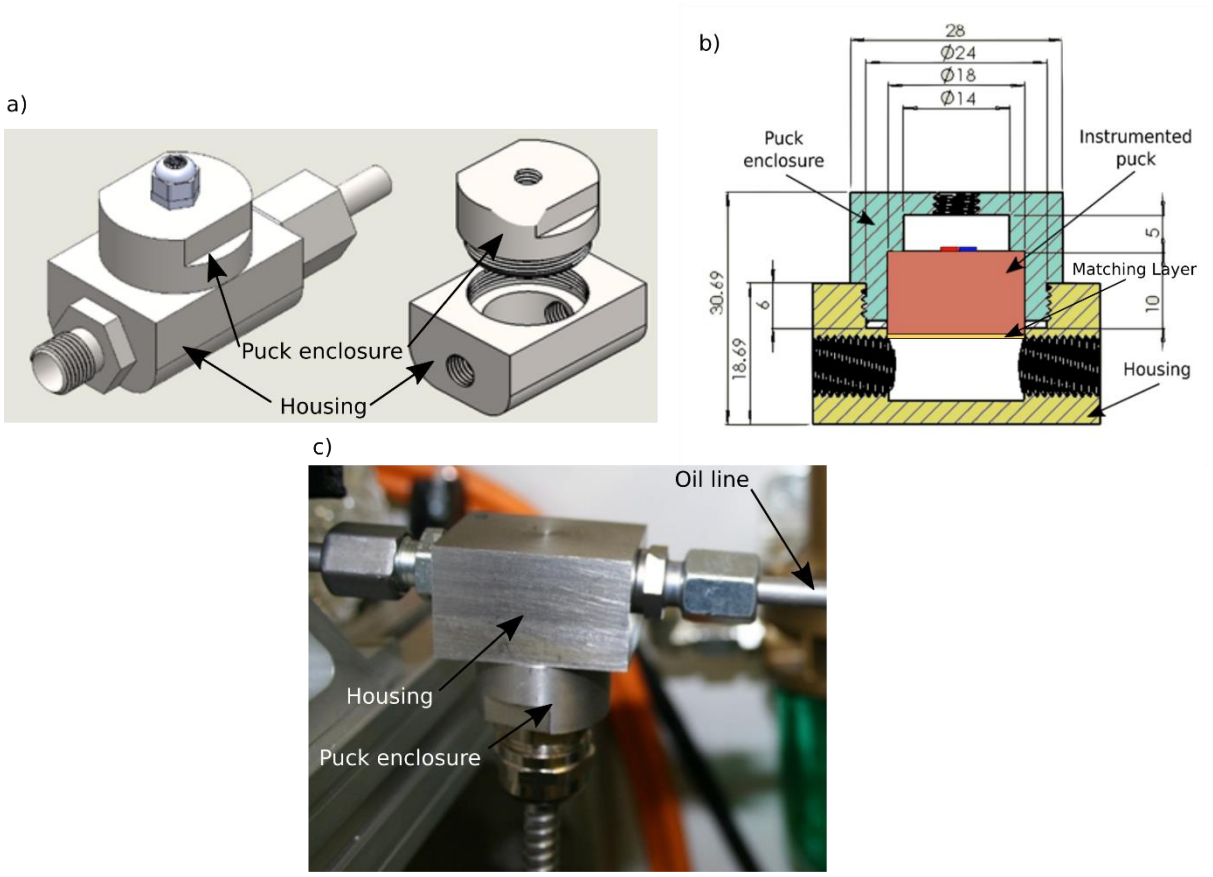

Figure 7-2: a) CAD ELV design, b) CAD side view of ELV, c) Image of ELV installed in oil line.

The ELV was designed as a modular component to enable replacement of the sensors if necessary, and to also permit ease of ultrasonic instrumentation for clamping locations when bonding transducers and the ML, because pressure could be applied from a parallel surface. The size of the ELV was small enough to enable ease of installation on the common rail while the production in steel provided a robust containment for the puck. An experimental set-up of the puck in use is shown in Figure 7-7 and Figure 7-20.

7.3. ELV Calibration Procedures

7.3.1. The Influence of Fluid Flow and Volume on SW Measurement.

The volume of liquid measured has previously been assumed to be irrelevant as shear ultrasonic waves can only travel a few microns into liquids. Hence the thickness of the oil is not considered for previous measurements. In the ELV application, the oil measured will flow through the chamber and so a constant volume of liquid will be measured by the device. In order to demonstrate that the SW is not influenced by the thickness of liquid, or flow of the liquid simple tests were conducted using the aluminium test plate documented previously in Chapter 6 where liquids were contained on the surface of the plate, and use of the ELV to investigate liquid flow. The following signal parameters shown in Table 7-1 were used for all measurements with the ELV.

Table 7-1: SW parameters for calibration tests.

Parameter	Aluminium plate values	ELV values
Voltage	2 V	2 V
Frequency sweep	9 MHz	6 MHz
Centre Frequency	5 MHz	4.5 MHz
Sweep Duration	10 ms	10 ms

7.3.1.1. Liquid Thickness

A reference signal was captured, with the attachment of a temporary enclosure surrounding the measurement area of the plate, followed by the acquisition of a measurement signal once liquid had been placed onto the measurement surface. 1 ml of S200 oil was placed onto the measurement interface, followed by the addition of another 1 ml of liquid and a second measurement acquired. Figure 7-3 shows an image of the plate with oil in the containment used for this test.

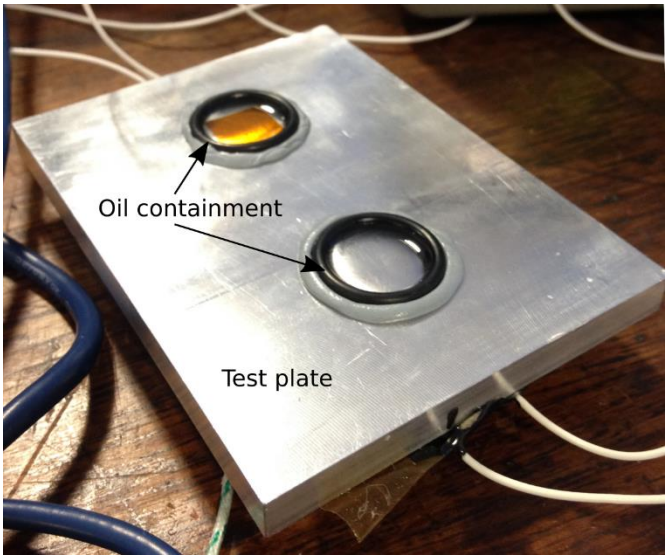

Figure 7-3: Image of the test plate used to conduct liquid thickness tests.

Reference and measurement signals are shown in Figure 7-4 for the SW method and Figure 7-5 for the SW ML method. Each figure also shows the *S* result in the frequency domain from each test. Increasing the fluid layer thickness has negligible effect on the SW amplitude, the deviation seen is in the order of noise within the signal, and thus this effect was deemed negligible for results taken with or without the addition of the ML.

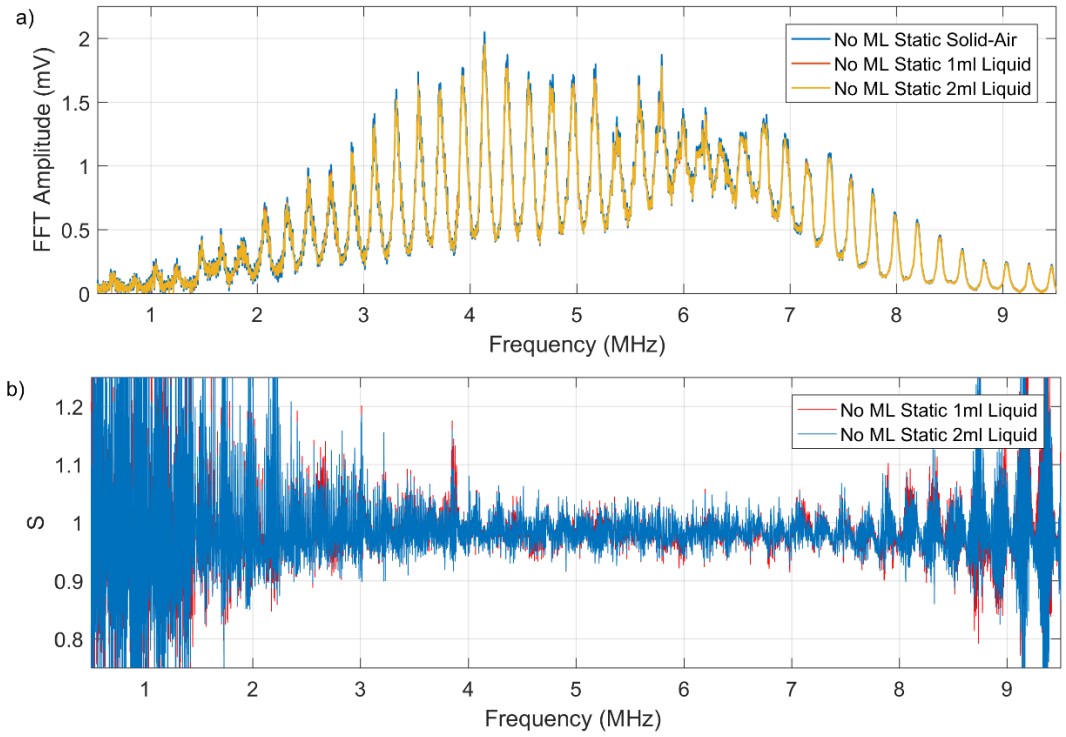

Figure 7-4: Liquid measurement comparison using the SW method without the ML.

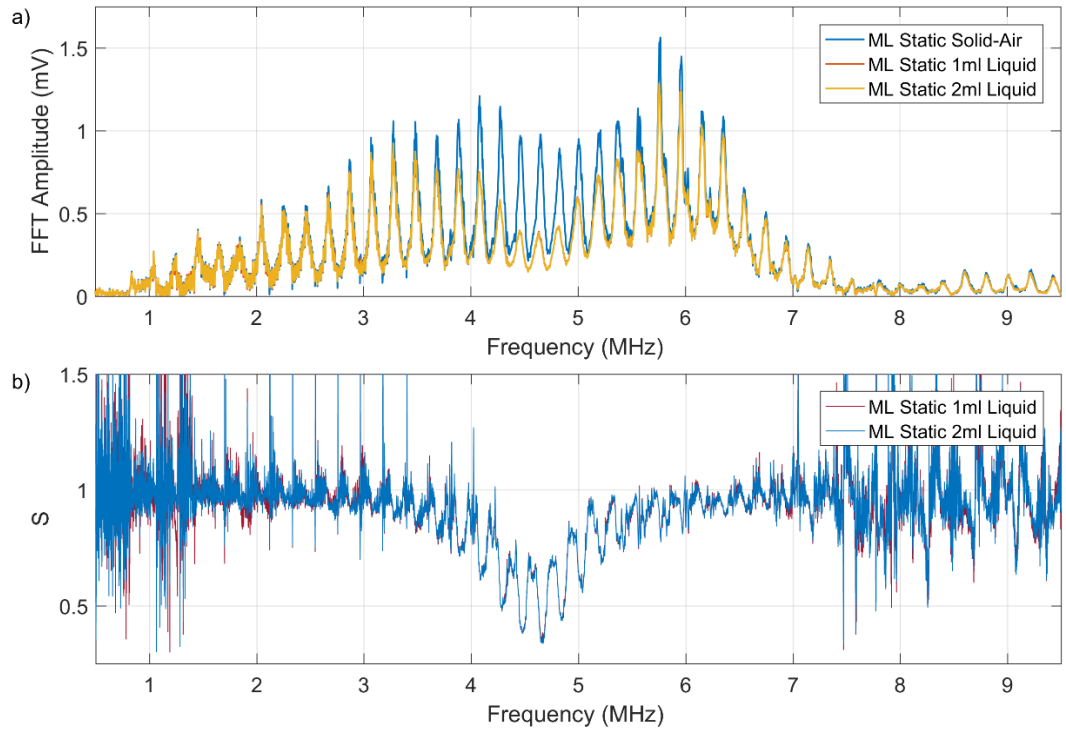

Figure 7-5: Liquid measurement comparison using the SW method with a ML.

7.3.1.2. Fluid flow

The influence of liquid flow on the signal was then investigated. Firstly the measurement of a static fluid on the surface of the plate was performed, followed by the acquisition of the SW signal when 2 ml of S200 oil was running over the surface. This second case produced a dynamic measurement, the results of which are compared in Figure 7-6.

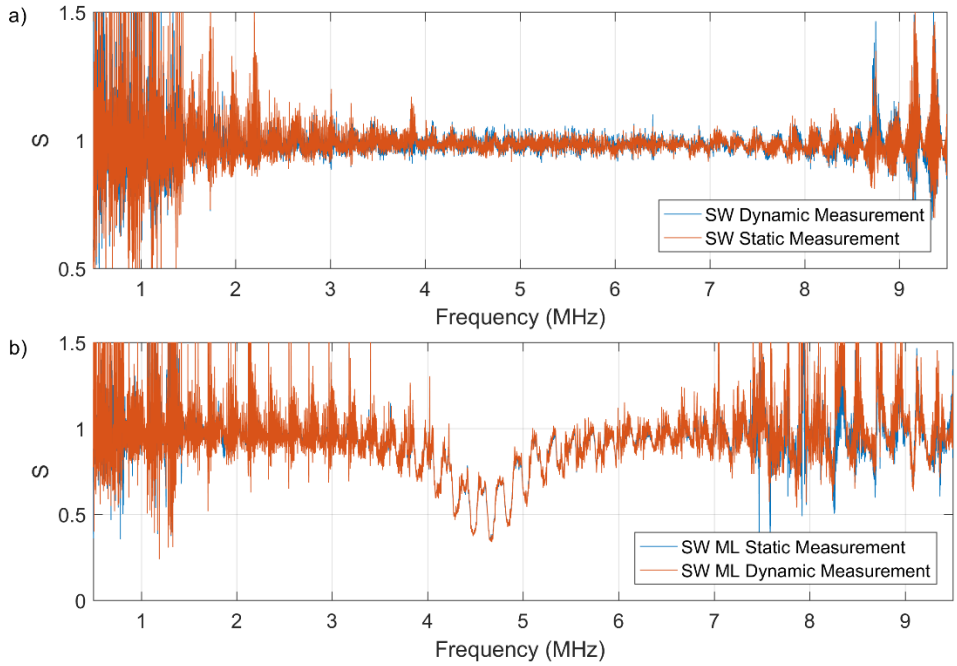

Figure 7-6: A comparison of static and dynamic oil measurements using the aluminium plate with S200 oil using the SW method a) without the ML and b) with the ML.

A second dynamic measurement was then made with the ELV in the arrangement show in Figure 7-7 to prove static calibration and dynamic field measurements with the ELV can be related.

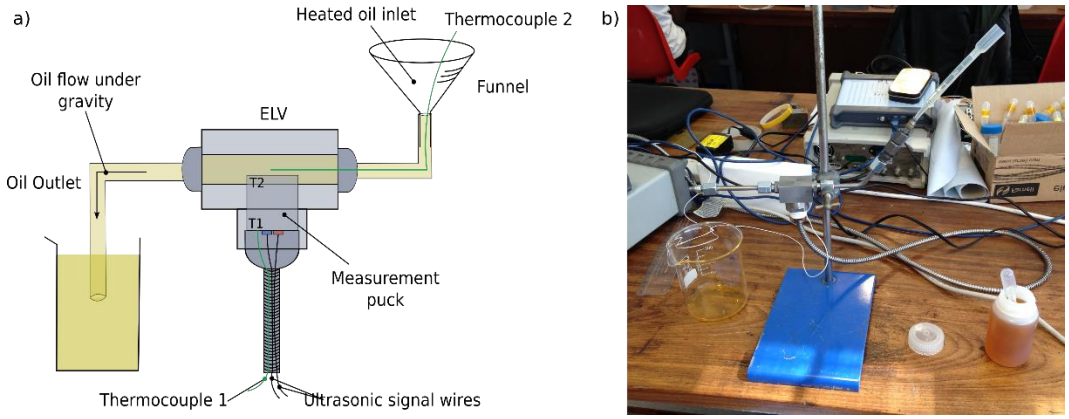

Figure 7-7:a) A schematic illustration of the dynamic oil measurement arrangement. b) An image of the apparatus.

The ELV was connected to an inlet and outlet, and S200 oil fed into the funnel, the oil then travelled through the ELV, flowing under gravity, and fell into a beaker at the outlet. Dynamic measurements were taken as the oil was flowing through the ELV and the static measurement was captured when the outlet line was blocked. Figure 7-8 shows the result of these measurements.

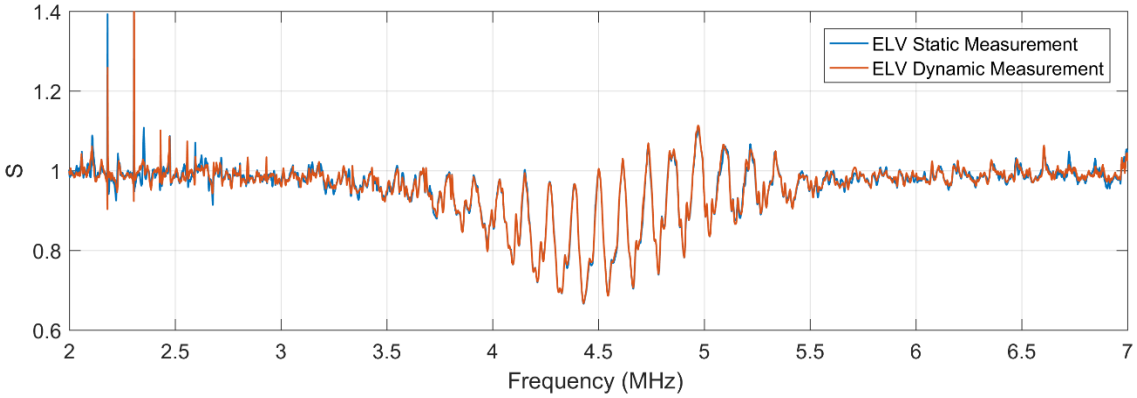

Figure 7-8: *S* profile of measurements of S200 in the dynamic and static flow conditions, using the ELV.

Again no difference between static and dynamic measurements was observed. Indicating that ultrasonic viscosity measurement using the SW method is independent of liquid flow at the velocity investigated here. The velocity of the oil measured here is expected to be greater than that subject to the oil within the ELV. It is because of the great difference in speed that ultrasonic measurements are unaffected by oil velocity. Additionally, the boundary layer measured ultrasonically lies at the perimeter of the vessel, and due to the velocity curve of fluid flowing through the device, the oil at the surfaces is essentially stationary. The penetration depth of shear ultrasonic waves is in the region of nm hence the measurement will be unaffected by flow.

7.3.2. Temperature Calibration

The effect of temperature on the ELV was then investigated to clarify the response of the SW method. The speed of sound in a solid reduces with temperature. If the length change of the material was neglected, and only the speed of sound considered, the influence on the SW is demonstrated in Figure 7-9, simulated by the model produced in Chapter 7.

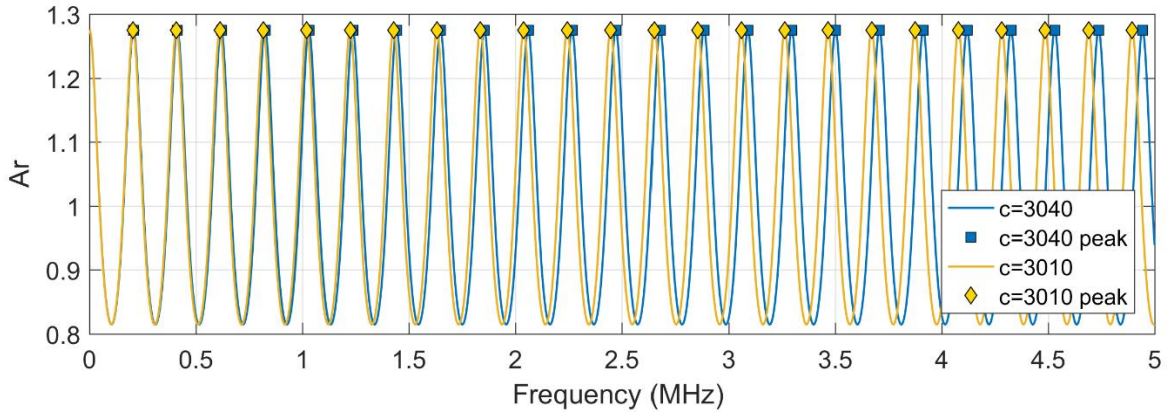

Figure 7-9: The effect of speed of sound only on the SW profile simulated using the analytical model.

The value of f_s changes from 0.206 to 0.204 MHz, with a change in speed of sound from 3040 to 3010 m/s. A 1% reduction of speed of sound, results in a 1% change of resonant frequency. While the speed of sound is expected to change the SW profile, the component length is also expected to change. As the temperature of a component increases, the path in which a wave must travel increases due to thermal expansion. The component changes in area and volume. Due to the nature of the SW method, the whole geometry of the component influences the SW profile. Thus a thermal expansion of the material, may not only increase the length of the component in the direction of propagation, but in other directions also.

A temperature calibration of the device was performed to acquire the SW profile for a range of temperatures, this procedure was outlined in Section 3.7.3. As measurements made using the ELV in line will have a varying temperature, a calibration of the device is essential if a standard solid-air interface is used as the reference profile. To thermally calibrate the ELV's the devices were heated to 100℃ and slowly left to cool, while reference signals were captured in order to define the reference profile at each temperature.

Figure 7-10 shows that thermal expansion of the component causes a reduction in the resonant peak amplitude, however this effect is not uniform over the entire profile, and does not show a purely linear behaviour. This could be due to the thermal performance characteristics of the transducers, for which between 30 and 100℃ undergo a non-linear increase in the dielectric constant, which refers to the ability of a substance to store electrical energy. A LabVIEW program was written to analyse the data, no envelope or windowing functions were used and a simple FFT transform on the signal was completed.

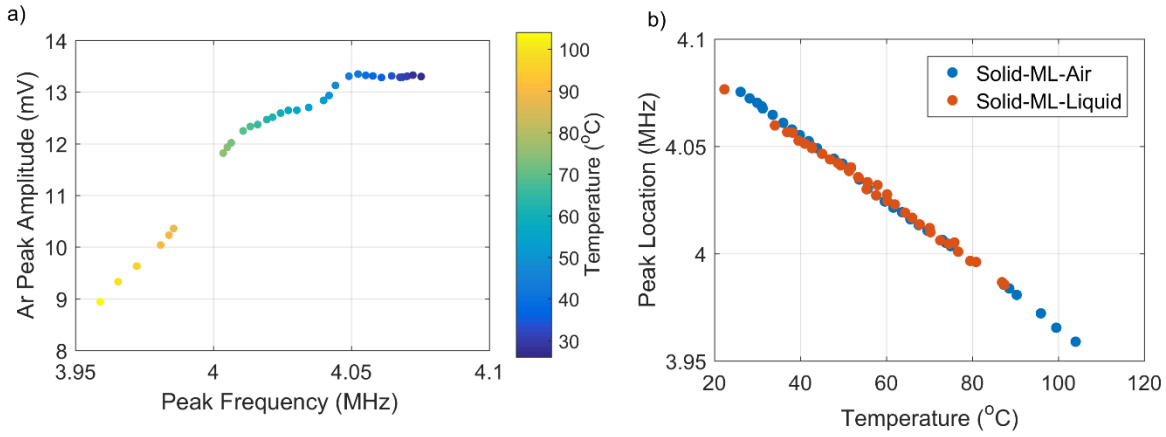

Figure 7-10: a) Reference peak amplitude behaviour with temperature. b) Peak location for solid-air and solid-liquid calibration with temperature.

A linear relationship between temperature and resonant peak location can be clearly seen Figure 7-10b. The measurement signal shown here is that of the data acquired when measuring the oil used in an engine test system at a range of temperatures at ambient pressure. Due to the complex behaviour of the SW with temperature, a solid-air signal was used to determine S for all measurements taken using the ELV. The temperature of the device was measured using K-type thermocouples located at the transducer interface adjacent to the transducers.

The peak frequency was used to define the temperature of the puck for each measurement, in order to select the correct reference value with the matched temperature. Selection of the correct temperature reference signal to use was an essential part of the analysis technique, as a false reference amplitude subsequently produces an incorrect reading of η. Figure 7-11 shows the temperature difference between that measured using the thermocouple embedded at the surface of the transducer within the ELV, and the temperature of the puck calculated using the peak position of the SW signal as the ultrasonic predicted temperature.

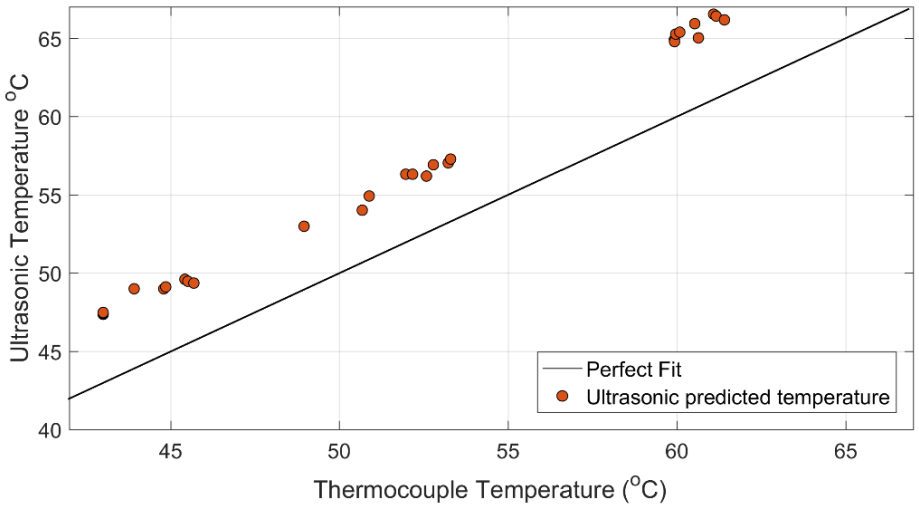

Figure 7-11: A figure to show the temperature difference between that measured using the thermocouple and that predicted using the peak location of the SW.

The temperature calculated by the peak location is on average 4℃ higher than that measured using the thermocouple, an observation that was expected due to the distance of the thermocouple from the oil. The temperature at the transducer interface is expected to be lower as this point is located 10 mm away from the heated oil. Although the temperature of the oil was set to a constant, the temperature of the puck may have gradually increased due to thermal conduction during the measurements.

A fluctuation in temperature is likely to be present with many in-situ lubricant measurements so the deviation found here permits a demonstration of the complex conditions which may be present during a measurement.

7.3.3. Viscosity Calibration

The temperature change of a liquid has a greater influence on the speed of sound than that of a solid component as the density and bulk modulus of a liquid have a greater propensity to change due to the physical nature of the state (Krautkrämer & Krautkrämer 1968). The effect of temperature on the measurement signal is a combination of several parameters, L, c_s, c_l, ρ, η and, α. To remove the effect of temperature, while obtaining the influence of viscosity change on S a viscosity calibration was completed.

Two cannon standard oils, S20 and N350 were measured, by placing the ELV containing the oil inside the oven, between 30 and 90℃. The viscosity range was 5 to 365 mPa.s for the range of temperatures analysed here. The peak amplitude of both a solid-ML-air and solid-ML-liquid signal for each oil can be seen in Figure 7-12.

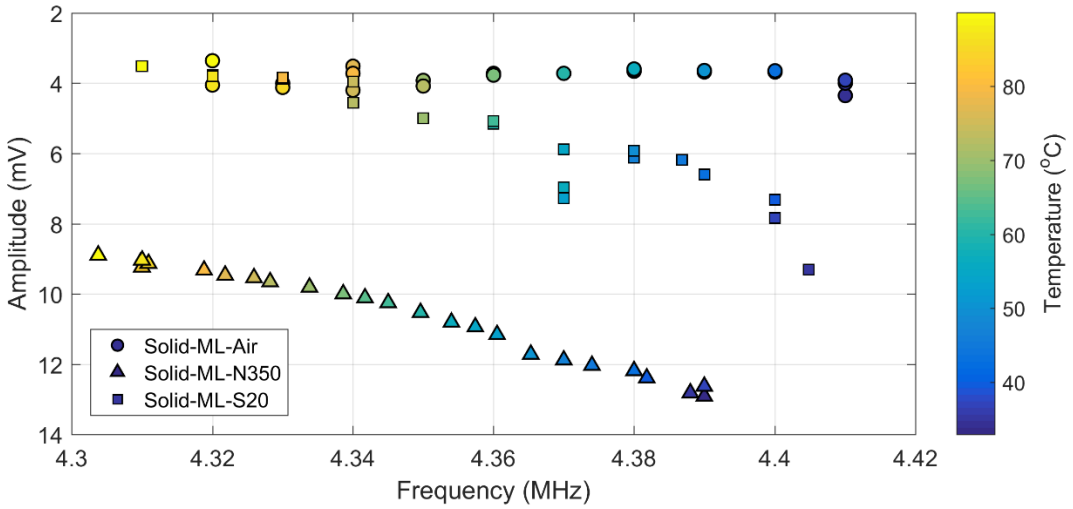

Figure 7-12: Solid-ML-air and solid-ML-liquid peak location and amplitude with temperature. Temperature is shown by the colour bar.

The amplitude of the solid-ML-liquid condition is lower than that of the reference signal due to the presence of the liquid at the interface. A calibration of this sort permits the full relationship between η and S to be found for the frequency peak in question. While the temperature of the component varies, S is calculated at each viscosity using values obtained at corresponding temperatures. This permits the complete removal of temperature from the

relationship, as the effect of the transducer and component in the reference condition are removed from the signal, leaving only the effect of the oil to influence S. Figure 7-13 shows the $S - \eta$ relationship for the ELV over the temperatures measured here using the data shown in Figure 7-12.

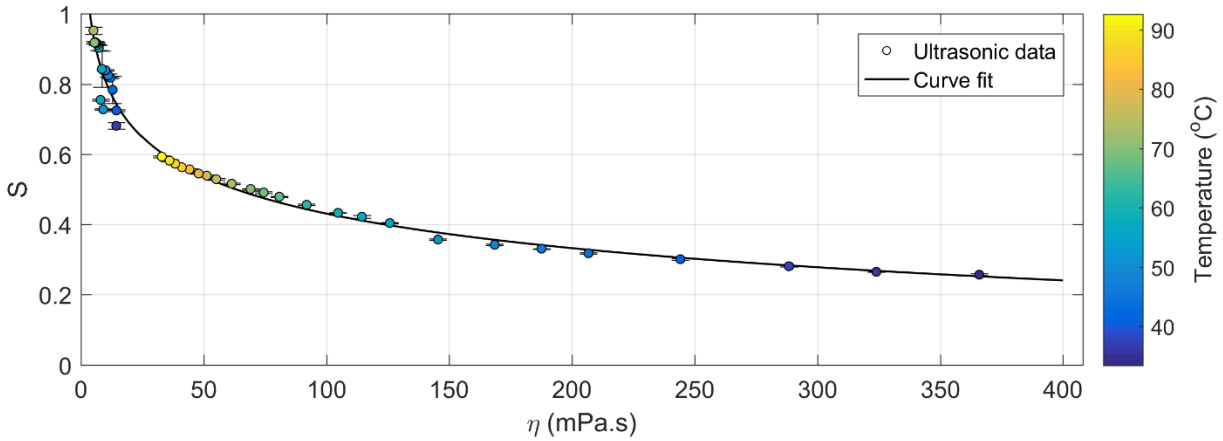

Figure 7-13: The S-η relationship using 4.3 to 4.4MHz antinode.

The viscosity calibration found using a power fit equation in Figure 7-13 has the experimental relationship.

$$\eta = 18.02S^{-2.221} - 15.38 \qquad \text{Equation 7-1}$$

This calibration curve allows the deduction of viscosity from a value of S which has been calculated by the direct comparison of A_r and A_m at the same temperature. Therefore the Equation 7-1 can be used to determine η from S at any temperature between 30 and 90℃ when S is found from the peak frequency between 4.3 and 4.4 MHz.

7.4. ELV Implementation

The ELV was firstly installed in an engine Lubricant Oil System Simulator (LOSS). This permitted the functionality of the device to be assessed, while minimising additional complications associated with the operation on a fully functional marine engine. After the success of measurements made on the LOSS rig, a second ELV was produced, and two ELV's were installed on the common rail lubricant line of a 6 cylinder RTX-6 marine diesel test engine during a scheduled test cycle.

7.4.1. Lubricant Oil System Simulator Rig

The LOSS test rig was developed by WinG&D to optimise lubricant injection spray patterns with the aim of reducing lubricant oil consumption. The quantity and mode of the injection can be optimised to achieve low wear rates while maintaining sufficient acid neutralisation capacity regulation within the cylinder. By monitoring the lubricant ultrasonically before the injection point, the viscosity of the oil injected can be measured. Figure 7-14 shows an image of this test rig.

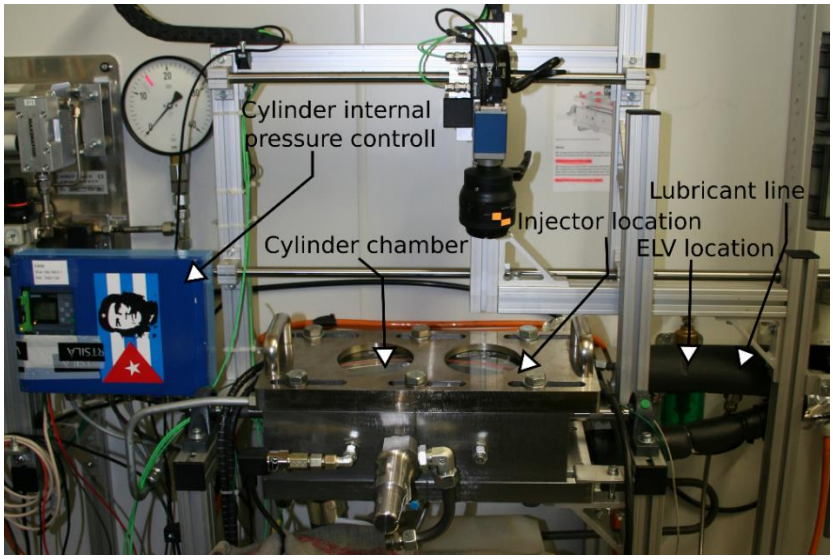

Figure 7-14: Arrangement of the chamber position in relation to the injector location and ELV. The ELV is encased in a thermally insulating sleeve in this image.

The LOSS rig used a simple quill with a non-return valve to control the lubricant oil spray pattern and oil distribution, which was mounted into the cylinder liner wall of a spray combustion chamber with optical access. The chamber was used by WinG&D to verify lubricant oil spray patterns and injector performance using a high speed camera to capture the distribution of oil. The rig had the capability to vary not only the lubricant pipe pressure but also the pressure inside the chamber, known as the vessel pressure, to determine how these factors influence the injection. The temperature of the oil used in the LOSS system was heated in an oil bath to the desired temperature, then pumped along the oil line to the injector. The oil within the lubricant line was surrounded by a heated sleeve then insulated up to the point of the injector.

Figure 7-15: a) The pressurised cylinder chamber, b) the lubricant line connected to the ELV positioned 15 cm before the injector.

The ELV was installed on the lubricant line of the LOSS rig 15 cm before the pipe connected to the injector, to measure the viscosity of the oil before it enters the injector. Three vessel pressures, three temperatures and three pipe pressures were produced, and the viscosity of the

liquid before the injection measured at each. The full range of pressure conditions (in the vessel and pipe) and temperatures tested are listed in Table 7-2. The expected change in viscosity due to the change in pressure within the pipe was calculated using the Barus Equation (Equation 2-7) with a pressure viscosity coefficient at 60℃ to determine the expected viscosity change. A change of 8 bar (0.8 MPa) resulted in a change of 0.1 mPa.s, hence the influence of pressure on η here is unlikely to be measurable (Williams 1994).

Table 7-2: Table of LOSS rig test parameters.

Pipe Temperatures tested (°C)	**Pipe Pressure (MPa)**	**Vessel Pressure (MPa)**
80	0.2, 0.5, 0.8	0.75
100	0.2, 0.5, 0.8	0.75
120	0.2, 0.5, 0.8	0.75

Tests were completed at each temperature in turn, from the lowest temperature to the highest. Equation 7-1 was used to find the viscosity of the oils from the S values measured using the ELV, where A_r at the same temperature as A_m was used to find S. Figure 7-16 shows the ELV viscosity measurements for all tests.

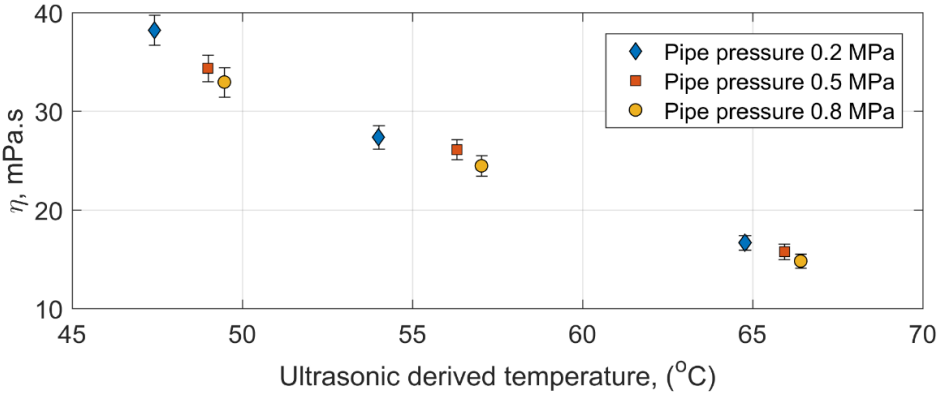

Figure 7-16: LOSS rig viscosity measurements at parameters outlined in Table 7-2.

Figure 7-16 shows the temperature indicated by the position of the peaks in the ultrasonic measurement, which was used as an indication of the trend of the lubricant temperature. As the measured temperature increases, the viscosity of the liquid decreases in all instances. Differences in viscosity due to pressure are likely to be negligible and so the principal factor affecting viscosity here is temperature.

The oil was then measured using a low shear Couette viscometer to determine the viscosity of the oil using a standard viscometer. The Couette results at a range of temperatures are shown in Figure 7-17 and equation fitted to the data shown in Equation 7-2.

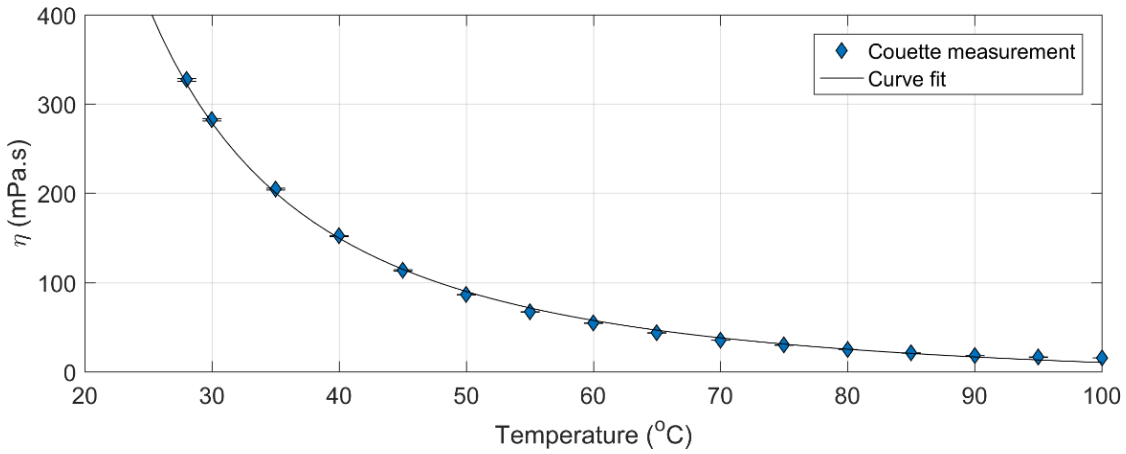

Figure 7-17: Couette measurements of the test oil.

$$\eta = 2.768e5 \times T^{(-2.002)} + (-16.49) \qquad \text{Equation 7-2}$$

The Couette viscosity of the oil was then calculated at the temperature which the oil was set to, (80, 100, 120℃), and the viscosity of the oil at the temperatures indicated by peak frequency. The viscosity of the oil, calculated using Equation 7-2 at 80, 100 and 120℃ is 26.4, 10.9 and 2.5 mPa.s and the viscosity at the temperatures indicated by the ultrasonic peak frequency are shown in Figure 7-18.

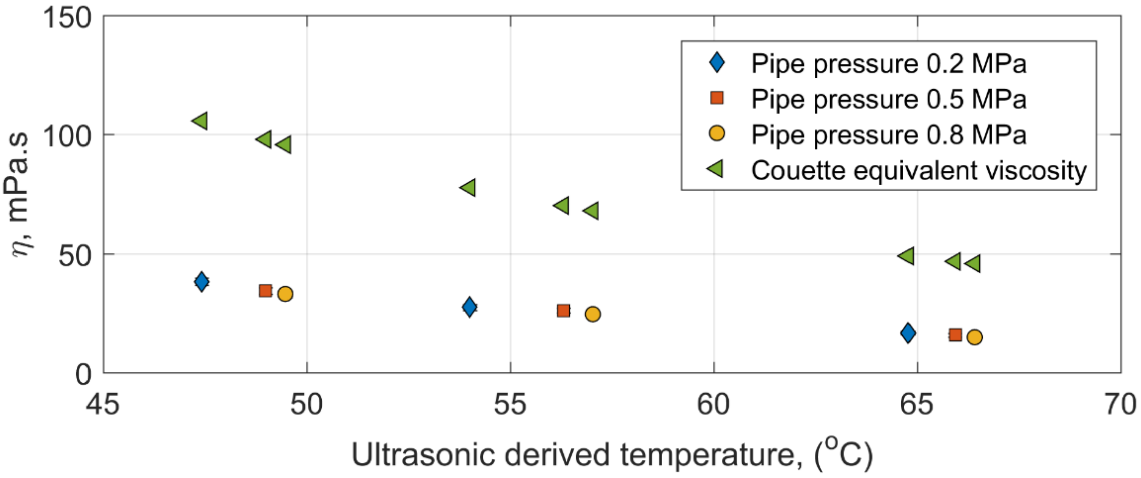

Figure 7-18: Ultrasonic viscosity and the viscosity calculated using Equation 7-2 at corresponding temperatures.

To summarise, the viscosity of the oil at 80, 100 and 120℃ is the target viscosity of the LOSS. The ultrasonic temperature is likely to be lower than the temperature of the oil due to conduction. As the temperature of the oil is expected to be higher, the actual viscosity of the oil may be lower than the Couette viscosity. The viscosity measured using the ELV is lower than the Couette viscosity at the equivalent temperature, and the effect of temperature is completely removed from ultrasonic measurements entirely. Hence the viscosity measured using the ELV is likely to be closest to the actual viscosity.

Installation and operation of the ELV was successful, with no obvious signal interference from the LOSS rig, while maintaining sufficient pressure of the oil. Success of this benchtop test, then lead to the installation of the ELV in the common rail lubricating system on a marine engine at the research facility.

7.4.2. Viscosity Measurement on the Lubricant Rail.

Following the successful installation into the LOSS, two ELV's were installed onto the common rail lubrication line of the test engine during down time. Results measured on the common rail system using the same ELV (ELV-A) used to measure the viscosity of oil in the LOSS rig will be considered here. The second ELV (ELV-B) was installed only as an indication of temperature as ELV-A was designed to include a second thermocouple located at the base of the puck, closer to the measurement surface. The aim of this was to give a clearer understanding of the temperature difference between the measurement surface of the puck and the transducer location. The ELV's from herein will therefore be known as ELV-A and ELV-B.

- ELV-A - Original ELV installed onto the LOSS rig to enable comparative measurements with one thermocouple (T1) located at the transducer interface.
- ELV-B - A second ELV with an additional channel drilled at the perimeter of the puck to determine the temperature 1mm away from the measurement surface. The location of the additional thermocouple is indicated in Figure 7-19 as T2 and the first thermocouple (T1) is located at the transducer interface.

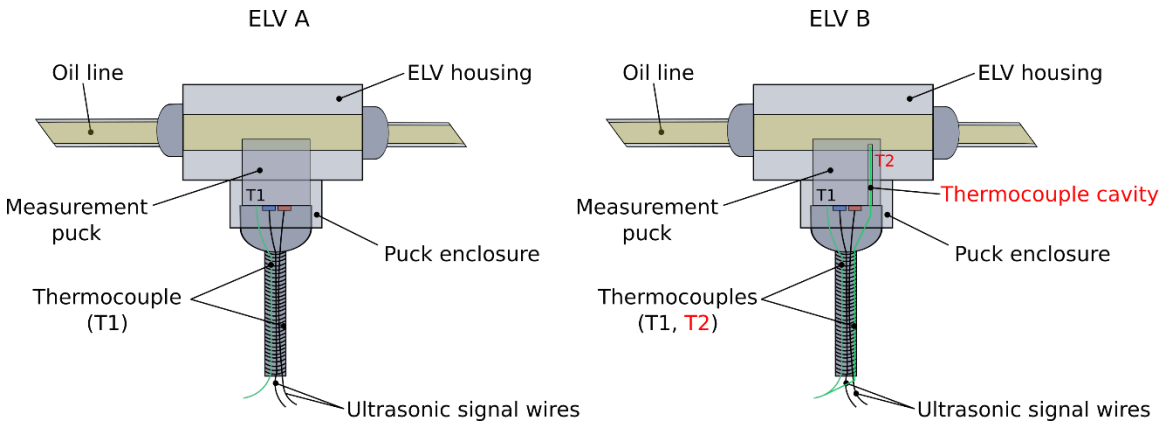

Figure 7-19: A schematic illustration of ELV-A and ELV-B installed onto the lubrication rail, highlighting differences between each in red.

The ELVs were both located 15 cm away from an injector on the same cylinder although a clear image of both ELV's was restricted due to obstructions of the surrounding supports of the liner, the position of each ELV are shown in Figure 7-20 highlighted in red circles.

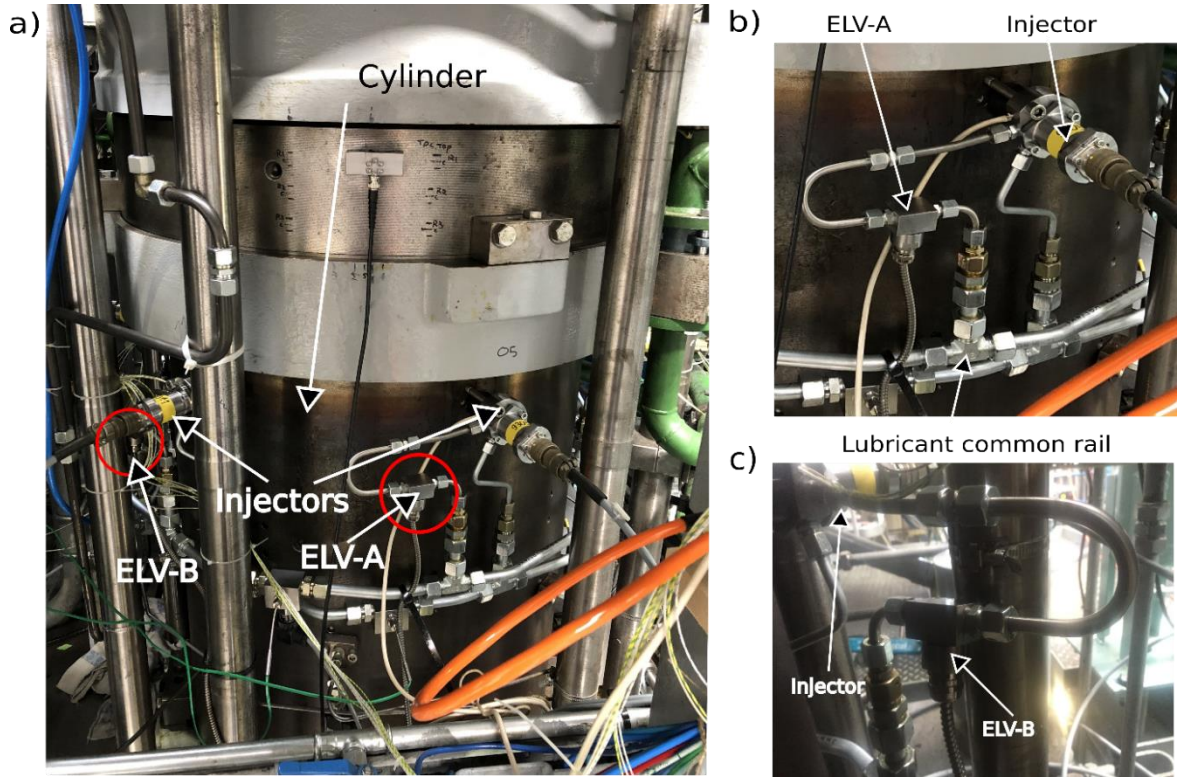

Figure 7-20: a) An image of the ELV locations on the common rail lubricant line, highlighted by red circles, b) ELV-A, c) ELV-B.

The lubricant viscosity was measured at three different engine loads, which each underwent variable lube oil feed rates. The test sequence completed by WinG&D on the day of testing is shown in Figure 7-21. The engine met 100% load at 10:25, ahead of schedule indicated by the markers on Figure 7-21.

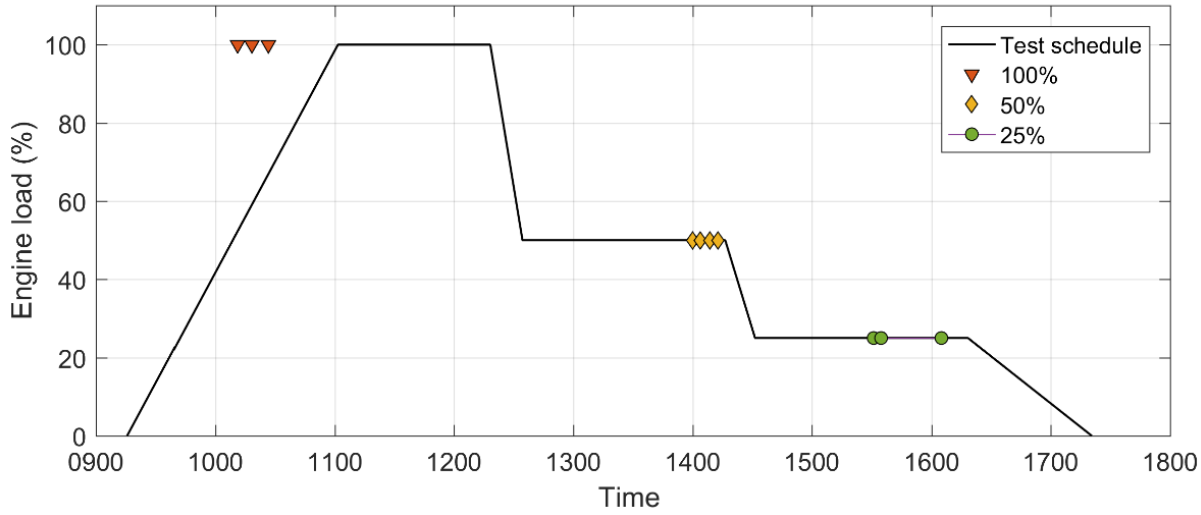

Figure 7-21: WinG&D test sequence.

The time at which the engine met the load in reality is shown by the additional markers in Figure 7-21. At these positions, the lube oil feed rate was varied manually by a control system as the desired engine load was met. At each specified load, the engine oil temperature set by

the facility also varied, this is shown in Table 7-3 alongside the corresponding load, and the time which these loads were actually met.

Table 7-3: Engine test parameters

Time (hours)	**Engine Load (%)**	**RPM**	**Lube oil feed rate (g/kWh)**	**Oil temp before injectors (℃)**
10:25	100	105.5	0.8	64.3
10:30	100	105.5	0.6	64.3
10:35	100	105.5	1.2	64.3
10:40	100	105.5	0.8	64.3
14:00	50	83.6	0.8	60.8
14:05	50	83.6	0.6	60.8
14:10	50	83.6	1.2	60.8
14:15	50	83.6	0.8	60.8
15:50	25	66.2	0.8	57.8
15:55	25	66.2	0.6	57.8
16:00	25	66.2	1.2	57.8
16:05	25	66.2	0.8	57.8

The temperature of each ELV was monitored for the duration of the test. The difference between the thermocouple temperature in ELV-B in location 1 and 2 can be seen in Figure 7-22. The temperature profile of the ELV's shows a delayed response to the load of the engine, as expected which is also highlighted in Figure 7-22.

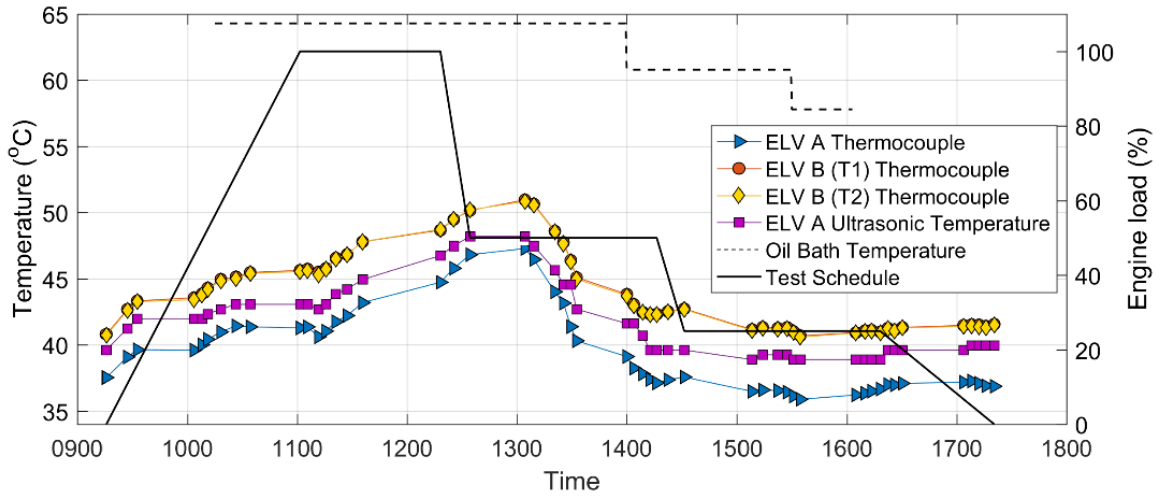

Figure 7-22: The difference in temperature between ELV-A and ELV-B thermocouple data taken while installed on the running engine at varying loads.

It is evident that the temperature recorded by ELV-A at the transducer interface (ELV A Thermocouple in Figure 7-22) differs from that of ELV-B at the transducer interface (ELV B (T1) Thermocouple). The temperature of ELV-A is consistently lower than ELV- B in the same

location. This may be due to the relative position around the circumference of the cylinder of the ELV devices. The cylinder upon which the ELV's were installed was the outer most accessible cylinder, hence it is anticipated that the temperature closest to the centre of the engine, is higher, due to reduced air flow and closer proximity to other cylinders. The location of ELV-A, as shown in Figure 7-20 and again schematically in Figure 7-23 is on the outermost area of the cylinder, whereas ELV-B is located underneath the cylinder support structures, shown clearly in Figure 7-23. The temperature of the surface of the cylinder for the duration of the tests varied between 140 and 110℃, measured using a contact thermocouple, which may also account for temperature variation of the ELV's.

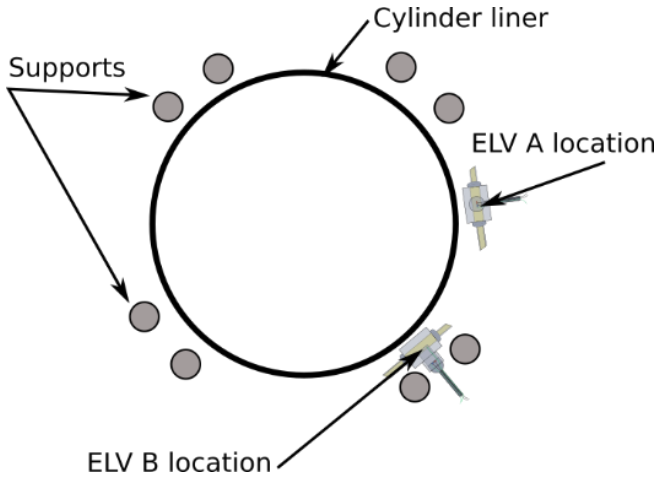

Figure 7-23: ELV locations around cylinders on the engine.

The temperature of the two thermocouples within ELV-B varied by less than 0.2℃. The error associated with the K-type thermocouples used within the ELV's was ±0.5℃, so the difference here is deemed negligible. This finding however suggests a small temperature gradient between these locations within the ELV, and so presents some uncertainties regarding the difference between the thermocouple measurement and ultrasonically predicted temperature of the pucks. A_r and A_m at the same temperature were used to find S, and the viscosity of the oil at each measurement was calculated, using Equation 7-1. The viscosity and associated error of each measurement are shown for the duration of the test schedule in Figure 7-24.

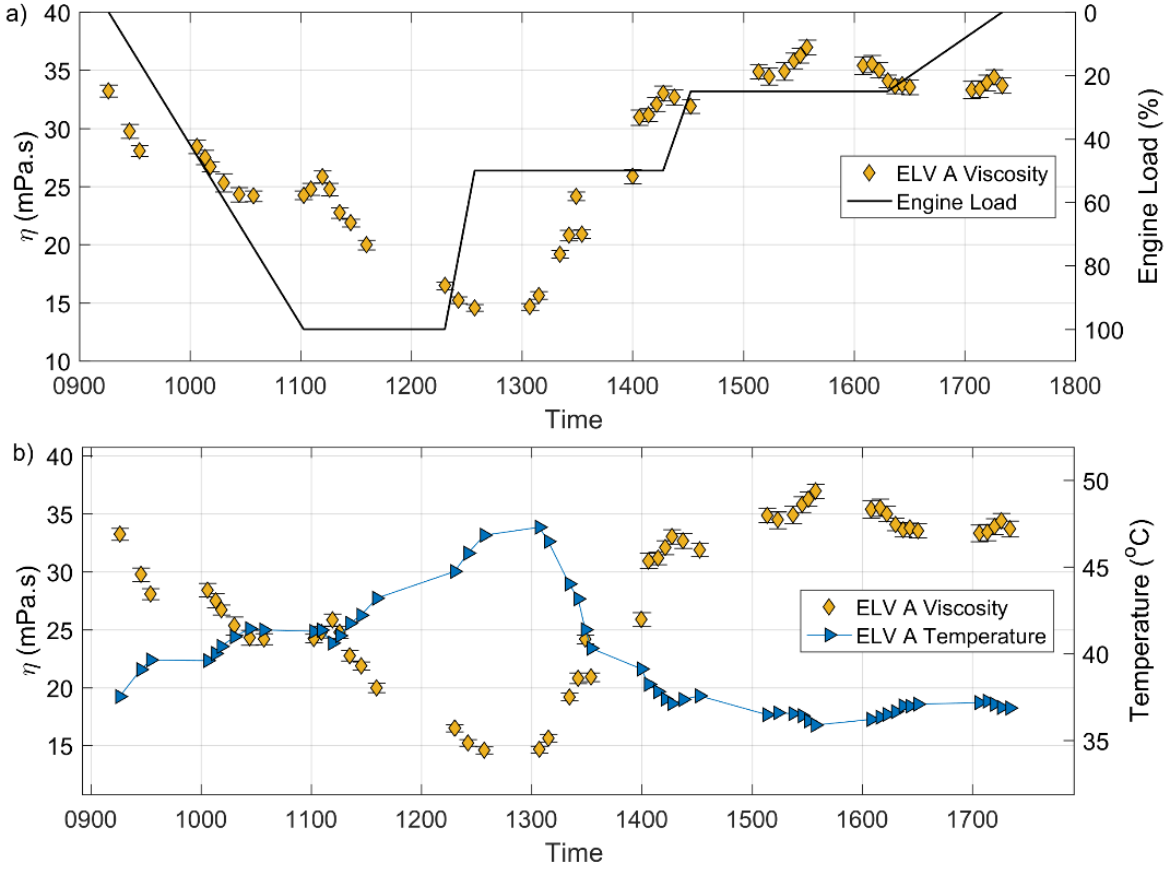

Figure 7-24: Viscosity measured using ELV A for the test schedule, with a) the engine load and b) temperature measured using ELV A.

At 10:40 the temperature of the oil supplied to the engine is reduced from 64.3℃ to 60.8℃ as the load of the engine increases. This is seen by a brief rise in viscosity at 11:00 and reduction in temperature before the effect of engine load increases the temperature of the cylinders in turn heating the oil, shown in Figure 7-24a and b. Engine load is then reduced to 50 then 25% which both result in an increase viscosity of the oil. At 15:50 the temperature of the oil is again reduced to 57.8℃, however this produces little change in viscosity as the temperature of the cylinders still dominates the temperature of the oil as the engine cools.

The viscosity of the oil changes with the temperature fluctuation, following a general inverse trend to that of the engine load change seen in Figure 7-21. The viscosity and temperature profile shown in Figure 7-24b highlight a delayed response from the test schedule shown in Figure 7-24a. The delayed temperature response may be due to thermal effects produced by the engine itself due to the large thermal mass which may be influenced by the load on the engine. The oil used for the engine test was then measured using a conventional viscometer, the results of which are shown in Figure 7-25. The curve fit of this data is shown in Equation 7-3. The viscosity of the oil from the temperature measured using ELV-A was then calculated using Equation 7-3, shown in Figure 7-26.

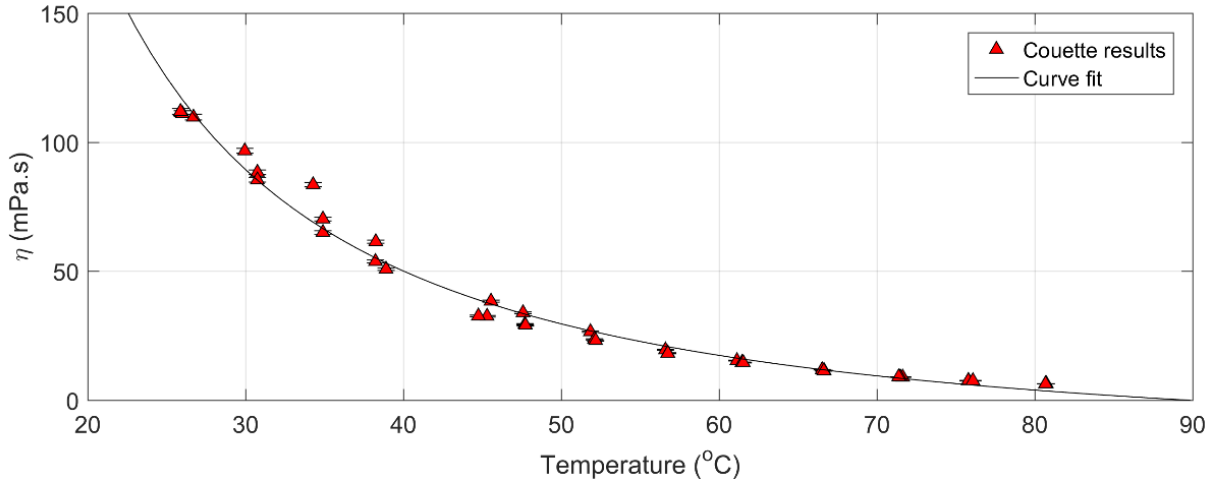

Figure 7-25: Brookfield Couette viscosity measurement of the engine oil.

$$\eta = 2.103e4T^{-1.546} - 20.09$$ Equation 7-3

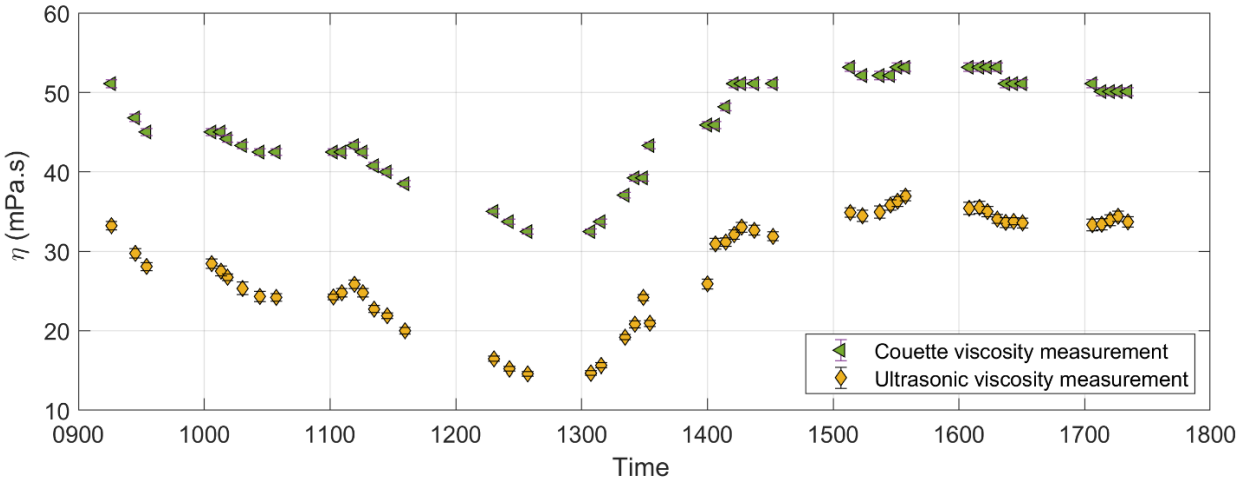

Figure 7-26: Ultrasonic and Couette viscosity using the temperature measured ultrasonically using ELV-A.

Ultrasonic and Couette viscosity measurement are shown in Figure 7-26, Couette measurements are higher than ultrasonic values. The values indicate a similar trend between the variation of viscosity with time between Couette and ultrasonic measurement, however Couette viscosity results are higher than ultrasonic. In addition it must be noted that the temperature measured at the ELV body is used to determine viscosity using Equation 7-3 for the Couette measurement.

Another consideration would be that of the shear rate used to measure the oil. The shear rate produced by the Couette viscometer ranged between 2.9 and 67 Hz, a shear rate which is significantly lower than that produced ultrasonically, which is in the MHz order. The results presented in Figure 7-25 could represent the viscosity of the oil at the first Newtonian plateau (previously discussed in Section 2.1.6) as engine oil is expected to show a non-Newtonian behaviour, the viscosity at the second Newtonian plateau was expected to be lower due to standard shear thinning behaviour of engine oils.

To verify this, a measurement to define where the Newtonian plateau exists in the viscosity shear rate diagram for this oil across a range of temperatures would be required. A potential route to measure this would be to use a high shear viscometer (the mechanisms of which are defined in Section 2.8.3.) in conjunction with a standard Couette viscometer for low shear measurements. The Cox-Merz rule would then be used to determine the ultrasonic shear rate. Measurements at these respective shear rates could then be used to verify that the Couette and ultrasonic viscosity measurements given in Figure 7-26 are each true in their own respect.

Work by (Rochefort et al. 1987, Yu & Gunasekaran 2001, and Bair et al. 2017) show the shear rate dependency on numerous liquids. In all cases presented, the viscosity of the liquid measured at a low shear rate is higher than the viscosity measured at a high shear rate. The shear rate investigated in (Yu & Gunasekaran 2001) shows a comparison of viscosity measured at 0.001Hz and 1.59 kHz. Both authors give structural breakdown of the liquid due to applied strain as an explanation for this behaviour. The high strain rate is said to result in a breakdown of inter and intra-molecular associations, producing the discrepancy in viscosity between measurements made at high and low viscosities. The shear thinning behaviour of the liquid measured by (Bair et al. 2017) is said to reside within the second Newtonian plateau. To determine whether ultrasonic measurements of the oil in question here are completed in the second Newtonian plateau, measurement at multiple frequencies would be required.

7.5. Conclusion

Design, fabrication, and installation of an in-line ultrasonic viscometer was successfully conducted, showing promising results for a robust viscometry device for in-situ viscosity measurements. Experimental results confirm liquid flow and liquid thickness have no effect on ultrasonic viscosity measurement when using the SW method, hence in-line SW measurements are independent of flow conditions and so the technique is suitable for common rail lubricant analysis.

The ELV was able to withstand the in-line pressures subject to the device during an industrial marine diesel engine test, confirmed by installation of the lube oil system simulator rig at WinG&D. Consistent and robust viscosity measurements were taken when the ELV was installed in-line and in real-time from the lubricant oil system simulator rig. The influence of temperature fluctuation on the ELV during the simulation was removed to reveal viscosity measurement alone.

The ELV was then installed on the common rail lubricant system of the engine, and the viscosity measured demonstrated how the load of the engine, temperature of the engine and temperature of the oil result in a unique viscosity profile of the oil. Accurate measurement of the lubricant before entering the injector permits a greater understanding of the spray mechanism of the injection onto the cylinder wall. A detailed understanding of the viscosity profile of the lubricant as the engine load is changed could permit a greater understanding of interim lubrication mechanisms between the cylinder and liner. The viscosity of the oil affects the injection spray pattern, hence feedback mechanisms could enable lubricant temperature adaptations to be fine-tuned to achieve optimum performance. ELV results show small errors, so high accuracy viscosity measurements, with an average error of $\pm$ 2.25% for all

measurements. This was achieved using a higher input voltage and by acquiring multiple signals at each measurement.

The ultrasonic standing wave with the matching layer was implemented here to produce the highest sensitivity possible, a capability shown previously in Chapter 4. After discussion with the industrial supervisor, a measurement capable of achieving measurements equal to that of conventional viscometers was deemed desirable. The sensitivity of the Couette viscometer used herein was ± 0.3 to 6%, and that of the vibrating wire method and capacitance methods discussed previously were $\pm 10\%$ and $\pm 1.5\%$ respectively (Schlumberger 2014, Shell 2012). The sensitivity of the standing wave method was on average $\pm 2.5\%$, hence a viable sensitivity was achieved by the method in comparison to other in-line viscometry techniques.

The ELV reached the peak temperature two hours after the maximum engine load was met, however the change in viscosity over the duration of the test followed the same behaviour as the temperature of the device, indicating that engine temperature has a greater influence on the temperature of the lubricant than the supply temperature of the lubricant. Although the viscosity of the oil can be calculated based on the temperature of the oil alone, ultrasonic viscosity measurements were calculated by removing the effect of temperature on the device entirely, hence the viscosity here is solely based on the ultrasonic reflection at the interface. In conclusion, the ELV's have the potential to measure viscosity regardless of temperature, oil condition (such as oxidation or degradation), and oil grade.

8. Conclusions

8.1. Newtonian Viscosity Measurement Using the Standing Wave Method.

The first aim of this research was to compare the capability of the standing wave and pulsed methods of Newtonian viscosity measurement. To do so a simple test apparatus was created to produce a viscosity measurement plate instrumented both with and without a matching layer in order to conduct two comparisons of each method. The oils measured were standard Newtonian oils which ranged from 3 to 1200 mPa.s. Results produced using an experimental calibration procedure for the SW method and a pulsed method were each shown to have the greatest sensitivity when using the matching layer arrangement. The accuracy of the standing wave method was higher than that of the pulsed method both with and without the matching layer.

Closer inspection also revealed that while both ultrasonic methods are incapable of any practical viscosity measurement above 200 mPa.s without a matching layer, the standing wave method produces a 50% error on average, whereas the pulsed wave method without a matching layer produces a 250% error. Use of the standing wave therefore is shown to improve the ultrasonic sensitivity to viscosity, and while 50% error is not acceptable, further development by materials selection and signal optimisation could potentially produce an acceptable response.

The nature of the standing wave method permits auto-referencing of the measurements, removing the requirement of a reference signal for each measurement. Auto-referencing with the SW method involves the use of a resonant peak which is least affected by viscosity to be used as the reference amplitude. The amplitude of the peak which changes most with respect to viscosity is then selected as the measurement peak. The auto-referencing analysis procedure was evaluated against a traditional solid-air interface with no significant difference in resulting viscosity values. Two variations of standing wave signal analysis were also conducted for the auto-referencing procedure. Individual peak selection was evaluated against a fixed frequency method, finding individual peak selection to be the optimal approach.

This chapter therefore presents novel ultrasonic measurements of viscosity using the standing wave method, where the capability of the technique is shown to be superior to conventional techniques. Using a standing wave generated within a solid component to measure a liquid on the surface is a concept which has not been documented previously, and so presents itself as the novelty of this work.

8.2. Development of an Analytical Model of the Standing Wave Method

The model was developed from an existing mathematical explanation of the standing wave method (Mills et al. 2017) with an analytical approach to gain a clearer understanding of the mechanisms which enable the standing wave method to measure viscosity. This was achieved by determining the amplitude of the signal by calculating the sum of n number of reflections within the component, for a range of frequencies at several different viscosities. Incorporation

of the complex three layer reflection coefficient within the model then allowed the matching layer technique to be simulated with the standing wave method.

The model was developed as a tool to find viscosity from an experimental standing wave reflection coefficient, but first the effect of several parameters was addressed. Increased frequencies showed greater sensitivity to viscosity, which conforms to ultrasonic principles, and increasing length of the component was found to increase the number of resonant peaks. The number of reflections within the component found to make a significant influence (to 3 decimal places) on S for the length of the component modelled here was 7 although it must be acknowledged that this value is specific for each case.

The influence of viscosity on the standing wave amplitude produced using the analytical model matched that of experimental results if assumptions of the model were considered. This was the case for the model with and without the matching layer. The model was then used to determine viscosity from two values of input information, these being the standing wave reflection coefficient and frequency.

8.3. Evaluation and Validation of the Standing Wave Model

Comparison of experimental and analytical results showed good agreement between both standing wave arrangements i.e. with and without a matching layer. The model produces a higher value of viscosity for a given S than that found experimentally for both models. The SW model was found to deviate on average 19%, while the matching layer model deviated on average 9.8% from experimental results. This behaviour was expected from the model as perfect model assumptions are made which are not often found experimentally, such as that of a perfect bond between the transducer and solid.

The position of the resonant peaks without the matching layer for the standing wave model agreed with those found experimentally for the frequencies investigated here, however at 6.4 MHz a deviation is seen. This effect is also seen with the matching layer model, but the matching layer model also shows good agreement with the experimental distribution of peaks.

The effect of parameters at the transducer interface were then investigated, however measurement of an equivalent system did not produce values which when input into the model improved agreement. The phase change at the transducer interface calculated using the principle relationship between materials is therefore used in the model. Measurement of R' provided useful information relating to the optimisation of the standing wave method, as the benefits of increasing R' were highlighted. Optimisation of the transducer-solid interface was identified as a key factor to improve the noise to signal ratio, as reducing the proportion of signal lost at this interface maintains a higher degree of wave energy to be incident upon the measurement interface at each passage through the solid. This could be achieved by impedance matching the transducer and solid component experimentally, or alternatively the model could also be adapted to examine and compare the sensitivity of different material combinations when using the standing wave technique.

No clear relationship between phase change in response to viscosity was found for the standing wave method experimentally, however with the addition of the matching layer, higher viscosities produced a greater phase change. This effect was also found analytically using the model, and fair agreement was found. Agreement between the models output and experimental results provides fair evidence of model validity for the standing wave method.

8.4. Application of the Standing Wave Method in an Engine Lubricating System

The standing wave method was then used in a bespoke engine lubricant viscometer designed to be installed on a marine diesel engine lubricating system. The engine lubricant viscometer was made to fully enclose the relatively delicate ultrasonic instrumentation, and so the outer casing was made from a steel body, enclosing the aluminium instrumented puck with a polyimide matching layer. Testing of the device was first completed on a lubricant oil system simulator rig to ensure no loss of pressure or interference from the device was present and after successful measurement and functionality was demonstrated, the engine lubricant viscometer was then installed onto the common rail lubricant line on a fired test engine.

The ELV was able to determine the lubricant viscosity over the test cycle of the engine for more than 8 hours. The viscosity measured here was produced through prior experimental calibration at a range of temperatures. The variation in temperature of the device over the test schedule and successful viscosity measurement demonstrate how the calibration technique can be applied to applications where temperature fluctuates.

The viscosity of the oil changed in response to the engine load and temperature. Although in this scenario, the viscosity of the lubricant could also be deduced from alternative conventional viscometry prior measurement, the engine lubricant viscometer offers to ability to determine the viscosity of the oil before the injectors if the oil used is an unknown grade. In the marine diesel industry, many different oils are often used as selection is based not only on the grade of the oil but increasingly on the price. Hence engine operators may choose an oil which is of a sub-optimal viscosity grade due to the quantity of oil required and may also find viscosity monitoring useful for liquid assurance when low sulphur fuels are exchanged due to imposed legislation regarding emission control areas of the sea. By the installation of an engine lubricant viscometer the optimum lubrication regime within the engine can be tuned by changing the temperature of the oil in real time.

8.5. Future Directions

The future work outlined here does not constitute an exhaustive list of possible applications. The body of the thesis has shown that, at a fundamental level, the standing wave method has the potential to be applied to many sensing challenges involving engineering interfaces. The suggestions presented offer potential directions for future research.

To develop this method into a commercially viable technique, the following factors would need to be assessed. Considerations of liquid measurement are firstly addressed, followed by an introduction into other potential areas of interest which may be suitable for this technique.

The natural progression of the work presented here would firstly be to extend the investigation to consider the behaviour of Newtonian fluids with viscosities outside the tested limits herein. To do this, Newtonian fluids with very low (< 1 mPa.s) and very high viscosities (>2000 mPa.s) could be investigated. The focus of this work would be to identify appropriate substrate-matching layer combinations and to determine where (in terms of viscosity) the requirement for a matching layer begins to improve sensitivity. A further extension would be to apply the standing wave method to a condition where a Newtonian fluid transitions from a liquid to a solid and so used to accurately determine material properties of a substance which cures over time. This could be of particular use in the construction of complex epoxy-composite structures where high inhomogeneity can restrict the applicability of pulse based ultrasonic techniques.

Though the primary objective of any further work would involve fully characterising the technique for use with Newtonian fluids, the use of the method to characterise non-Newtonian fluids would be of great benefit. The behaviour of non-Newtonian fluids (and Newtonian fluids at very high ($>10^6$) shear rates) when excited with shear waves at ultrasonic frequencies is an active topic, particularly in determining behaviours of relaxation and their dependence on shear rates. It is envisaged that the application of the standing wave method and the sensitivity advantages it offers may benefit investigations into these properties. The results of these investigations could then be used to further develop the analytical models by verifying the implementation of existing approaches, such as the non-Newtonian Maxwell Model.

The aforementioned work considers improvements to the understanding of how the ultrasonic measurements can be interpreted. In addition to this, however, the physical behaviour of the measurement interface during standing wave generation requires further investigation. Of particular interest would be the measurement of the true motion of the interface surfaces when excited by the shear stress wave. This could be measured using a laser interferometry based technique to determine the velocities and deflections of the surface both in and out of plane. Additionally, the extent of the 'measurement area' could be determined, which would be useful for practical applications where accurate knowledge of the location of viscosity measurement is important. An extension of the standing wave approach could therefore be to identify whether or not a component is in contact with another. Reduced signal amplitude would indicate contact between mating components. This approach could be used to measure conditions within intermittent contacts such as in rolling element bearings.

The material contained within this thesis relates to the specific use of the standing wave approach to measuring the viscometric properties of engineering fluids. However, the approach has the potential to be applied to many other applications. In the glass manufacturing industry for example, the viscosity of glass between its molten state and solid state is between 10 Pa.s and $10^{13.5}$ Pa.s (Hu 2015). The critical measurement point within this process is between the working and softening points where the glass has a viscosity between 10^{3} to $10^{6.6}$ Pa.s. The temperature of the glass at this stage is around 1500℃ and exhibits strong non-Newtonian behaviours. In-situ measurements of the glass viscosity has the potential to improve process control as this can be used as a proxy for other properties of the glass (such as refractive index). An obvious requirement of this work is to generate, transmit and receive ultrasound at high temperature, so a core part of this additional work would be to identify and develop suitable sensing strategies. For example, this could be achieved by using mechanical clamps to position the transducers, a technique previously shown to achieve stable transducer fixation at high temperatures in the petro-chemical industry (Cegla, F.B. Cawley, P. Allin, J. Davies 2010).

Methods to maximise the sensitivity of measurement required must also be considered, as demonstrated within this thesis. The standing wave method has been shown to be capable of viscosity measurement above 500 mPa.s with no matching layer, however the lowest viscosity of the glass within the manufacturing process is 10 Pa.s. Consideration of potentially viable matching layer-component arrangements could first be investigated within the system, as refractories that are used to contain the high temperature glass may possess properties or include existing coatings that can act as a suitable layer. Ceramic coatings are often considered for high temperature applications, a key part of this future work would look at the viability of these coatings for use as matching layers.

A further development of particular interest would be to adapt the approach to allow its use with EMAT (Electro-Magnetic Acoustic Transducer) techniques. These are useful for situations where direct contact of a transducer on the component are not desirable. One of the main limitations of EMAT's is the low conversion efficiency of electrical to strain energy when generating pulsed ultrasound. However, the amplification in sensitivity by applying the standing wave methodology may have the potential to offer benefits to their use. An example where this methodology could be highly effective is in the thickness measurement of high speed rolled stock (such as sheet metal), where both high temperatures and a need for non-contact sensing are crucial.

9. Appendix 1: Standing Wave Model Code

9.1. Standing Wave Mathematical Model Code

```
clear all
Ds=[865.8604    855.9064    851.5528    858.7608    864.2272    868.3592
837.4928    840.9272    844.0628];% density of oils at 24 degrees c
Vs= [0.0036567  0.0161918   0.0301912   0.0586455   0.1086943   0.2106982
0.3661707   0.6352365   1.1196]; %Viscosity vector of oils at 24 degrees c
df=0.005; % df (MHz)
f= 0:df:10; % Frequency (MHz)
nr =7;%number of reflections
%Pre allocate memory
MM = zeros(numel(Vs),length(f));
HH = MM;
KK = zeros(1,length(f));


for i = 1: length(Vs) %Loop for viscosity and density
    V = Vs(i);
    d=Ds(i);
for j = 1:length(f) %Loop for Frequency
    for n = 1:nr %Loop for number of reflections
        AA(n,:) = real(GG(n,f(j),V, d)); % Signal for sequential
reflections (real part)-measurement
        SS(n,:) = real(GR(n,f(j))); % signal for sequential reflections
(real part)-reference
    end
    CC = sum(AA); % Sum reflections of measurement signal
    DD = sum(SS); % Sum reflections of reference signal
    BB = sum(AA)/sum(SS); % Sum reflections at given time positions
    MM(i,j) = max(BB);% Calculating (Root Mean Square)RMS value of standing
waves
    HH(i,j) = max(CC);%Calculating RMS value of measurement
    KK(1,j) = max(DD); %Calculating RMS value of reference

end

end


function Ar = GR(n,f) %reference function
A0=1; % A0 incident amplitude
a=-0.4; % attenuation coefficient (Np/m)
L=7.33e-3; % Length of material (m)
f = f*1000000; % Convert MHz to Hz
w=2*pi*f; % Angular frequency
a1=16.856250e6; %Transducer acoustic impedance
b1=8.208e6; %aluminium acoustic impedance
R=abs((a1-b1)./(a1+b1)); %Reflection coefficient at the transducer-
Rm=1; %Reflection coefficient at the air interface
C=3040; % Shear speed of sound in aluminium (m/s)
Q=(2*L)/C;
X=Q/1000;
t=0:X:Q;
q=0.5*acos(1-(((1-R^2)^2)./(2+R^2))); %Phase shift at the transducer
interface
phi=0.5*acos(1-(((1-Rm^2)^2)./(2+Rm^2))); %Phase shift at the measurement
interface
```

```
Ar=A0*(exp(1i.*(w.*(((2*n*L)./C)-t))./(exp(n*phi)))./exp(((n-
1).*q)).*(Rm.^n).*(R.^(n-1)).*exp(2.*(n).*L.*a);
end

function [Am]=GG(n,f,V, d) % Measurement function
A0=1; % A0 incident amplitude
a=-0.4; % Attenuation coefficient (Np/m)
L=7.33e-3; % Length of material (m)
f = f*1e6; %(Hz)
w=2*pi*f; % Angular frequency
a1=16.856250e6; % Transducer acoustic impedance
b1=8.208e6; % Aluminium acoustic impedance
R=abs((a1-b1)./(a1+b1)); %Reflection coefficient at the transducer-
% d=d; % Density of oil at 23degrees C
C=3040; % Shear speed of sound in aluminium (m/s)
Q=(2*L)/C;
X=Q/1000;
t=0:X:Q;
q=0.5*acos(1-(((1-R^2)^2)./(2+R^2))); %Phase shift at the transducer
interface
c1=8.208e6; %Acoustic impedance of aluminium
c2=sqrt(1i*d.*w.*V); %Acoustic impedance of oil
Rm=abs((c2-c1)./(c2+c1));%Reflection coefficient at the measurement
interface
phi=0.5.*acos(1-(((1-Rm^2)^2)./(2+Rm^2))); %Phase shift at the measurement
interface
Am=A0*(exp(1i.*(w.*(((2*n*L)./C)-t))./(exp(n*phi)))./exp(((n-
1).*q)).*(Rm.^n).*(R.^(n-1)).*exp(2.*(n).*L.*a); % Measurement Equation

End

% Code to find S-viscosity relationship
B=[f;MM];
C=[[0,Vs]', B]
% save('F_S','B', 'Vs')
figure()
[peaks,locs]=findpeaks((-MM(2,:)'),f') %Finds troughs of S data when
inverted (becuase using peakfinder)
subplot(3,1,1)
plot(f,MM, locs,-peaks,'d') % plots data and peak locations
prompt = 'Input experimental frequency between 0 and 10MHz (in MHz) '; %
asks user to input desired frequency
F = input(prompt);% asks user to input desired frequency peak
[~,I] = min(abs(locs-F));
c = locs(I); %finds closest value to input value from peak locations in
model data
I=(c/df)+2; %Indexes the matrix of S values at the resonant frequency in
matlab code closest to input frequency
Collumn= C(:,int32(I)) %Indexing the integer value
Sf=Collumn(2:end); %Indexing S values of viscosity for given frequency
ModelFrequency=Collumn(1,:)
subplot(3,1,2)
plot(Sf,Vs) %plots S vs Viscosity
title (num2str(ModelFrequency))
xlabel('S')
ylabel('Viscosity')
Curve=fit(Sf,Vs','power1')
subplot(3,1,3)
plot(Curve,Sf,Vs')
hold on
```

```
prompt = 'Input experimental S value for given frequency '; % asks user to
input desired frequency peak
Sval = input(prompt);% asks user to input S value
ModelViscosity=Curve(Sval)
subplot(3,1,3)
plot(Sval, ModelViscosity,'d', 'MarkerSize',10,
'MarkerEdgeColor','red','MarkerFaceColor',[1 .6 .6])
```

9.2. Standing Wave Mathematical Model with the Matching Layer

```
clear all;
% Excitation frequency range
df = 100; % df (Hz)
f0 = 0.01e6; % Start frequency (Hz)
f = [f0:df:10e6];
w = f*2*pi; % Angular Frequency
Ds=[865.8604, 855.9064  851.5528    858.7608    864.2272    868.3592
837.4928    840.9272    844.0628];% density (kg/m3) of oils at 24 degrees c
Vs= [0.0036567, 0.0161918,0.0301912,0.0586455,0.1086943, 0.2106982,
0.3661707, 0.6352365,1.1196]; %Viscosity (Pa.s) of oils at 24 degrees c

% Material properties to calculate reflection coefficient at interface
z0 = 8.208e6; % Acoustic impedance of solid (Pa.s/m)
z1 = 1.4e6; % Acoustic impedance of ML (Pa.s/m)
L1 = 50e-6; % Thickness of matching layer (m)
c1 = 850; % ML speed of sound (m/s)
rho1a = 1.2; % Air density (kg/m3)
eta1a = 2e-5; % Air viscosity (Pa.s)

for i=1:length(Vs)
    V = Vs(i);
    d=Ds(i);
% Reflection coefficient conditions for reference (air) and measurement
 % (Liquid) conditions
for j = 1:length(f);
    z2 = sqrt(d*1i*w(j)*V); % Liquid acoustic impedance
    z2a = sqrt(rho1a*1i*w(j)*eta1a); % Air acoustic impedance
    z2A(j) = z2a; % Complex impedance (air) at each frequency
    % Three layer reflection coefficient (liquid)
    R0(j) = (((1-z0/z2)*cos(w(j)*L1/c1)+1i*((z1/z2-
z0/z1)*sin(w(j)*L1/c1)))/((1+z0/z2)*cos(w(j)*L1/c1)+1i*((z1/z2+z0/z1)*sin(w
(j)*L1/c1))));
    % Three layer reflection coefficient (air)
    R0a(j) =(((1-z0/z2a)*cos(w(j)*L1/c1)+1i*((z1/z2a-
z0/z1)*sin(w(j)*L1/c1)))/((1+z0/z2a)*cos(w(j)*L1/c1)+1i*((z1/z2a+z0/z1)*sin
(w(j)*L1/c1))));

end
% Substrate conditions:
% ---------------------
A0=1; % Initial amplitude
L0 = 7.38e-3;% Component length (m)
c0=3040;% Speed of(shear)sound in component (m/s)
a0 = -0.4;% Attenuation coefficient (Np/m)
p1 =0.442190380555790;% Phase shift at transducer interface (rad)
R1 = 0.345043238876088;% Reflection coefficient at transducer interface
N = 25;% Number of reflections
% Summation
% ---------
```

```
% Calculate S for each frequency in the sweep
for j = 1:length(w)
    for n = 1:N
        % Condition: Measurement is reflected conditions
        % Measurement (i.e. ML and liquid)
        X(n) = exp(-1i*(w(j)*(2*n*L0/c0)-(n-1)*p1))*(-1*R0(j))^n*R1^(n-
1)*exp(2*n*L0*a0);
        % Reference (ML and air)
        Y(n) = exp(-1i*(w(j)*(2*n*L0/c0)-(n-1)*p1))*(-1*R0a(j))^n*R1^(n-
1)*exp(2*n*L0*a0);

    end
    % Calculating the magnitude of (complex) S
    S(j, i) = abs(sum(X))/abs(sum(Y)); % Magnitude of S
    % Magnitude of numerator and denominator
    x(j, i) = abs(sum(X)); % (Numerator) measurement ML-liquid
    Pm(j,i) = angle(sum(X)); % Finds the phase of the complex sum of X
    y(j, i) = abs(sum(Y)); % (Denominator) reference ML-air
    Pr(j,i) = angle(sum(Y)); % Finds the phase of the complex sum of Y
end

end


% code to find S-Viscosity relationship to run after main code for ML.
Q=0.01;
B=[f*1e-6;y(:,1)'; x'];
Viscosity=[0;0;Vs'];
C=[Viscosity, B];
save('F_R','B', 'Vs')
figure()
subplot(3,1,2)
[peaksr,locsr]=findpeaks((y(:,1)),f*1e-6, 'MinPeakProminence',(Q)); %Finds
troughs of S data when inverted (becuase using peakfinder)
[peaks1,locs1]=findpeaks((x(:,1)),f*1e-6, 'MinPeakProminence',(Q)); %Finds
troughs of S data when inverted (becuase using peakfinder)
[peaks2,locs2]=findpeaks((x(:,2)),f*1e-6, 'MinPeakProminence',(Q)); %Finds
troughs of S data when inverted (becuase using peakfinder)
[peaks3,locs3]=findpeaks((x(:,3)),f*1e-6, 'MinPeakProminence',(Q)); %Finds
troughs of S data when inverted (becuase using peakfinder)
[peaks4,locs4]=findpeaks((x(:,4)),f*1e-6, 'MinPeakProminence',(Q)); %Finds
troughs of S data when inverted (becuase using peakfinder)
[peaks5,locs5]=findpeaks((x(:,5)),f*1e-6, 'MinPeakProminence',(Q)); %Finds
troughs of S data when inverted (becuase using peakfinder)
[peaks6,locs6]=findpeaks((x(:,6)),f*1e-6, 'MinPeakProminence',(Q)); %Finds
troughs of S data when inverted (becuase using peakfinder)
[peaks7,locs7]=findpeaks((x(:,7)),f*1e-6, 'MinPeakProminence',(Q)); %Finds
troughs of S data when inverted (becuase using peakfinder)
[peaks8,locs8]=findpeaks((x(:,8)),f*1e-6, 'MinPeakProminence',(Q)); %Finds
troughs of S data when inverted (becuase using peakfinder)
[peaks9,locs9]=findpeaks((x(:,9)),f*1e-6, 'MinPeakProminence',(Q)); %Finds
troughs of S data when inverted (becuase using peakfinder)
locs=[locsr', locs1', locs2', locs3', locs4', locs5', locs6', locs7',
locs8', locs9'];
peaks=[peaksr, peaks1, peaks2, peaks3, peaks4, peaks5, peaks6, peaks7,
peaks8, peaks9];

findpeaks((y(:,1)),f*1e-6, 'MinPeakProminence',(Q)); %Finds troughs of S
data when inverted (becuase using peakfinder)
findpeaks((x(:,1)),f*1e-6, 'MinPeakProminence',(Q)); %Finds troughs of S
data when inverted (becuase using peakfinder)
```

```
findpeaks((x(:,2)),f*1e-6, 'MinPeakProminence',(Q)); %Finds troughs of S
data when inverted (becuase using peakfinder)
findpeaks((x(:,3)),f*1e-6, 'MinPeakProminence',(Q)); %Finds troughs of S
data when inverted (becuase using peakfinder)
findpeaks((x(:,4)),f*1e-6, 'MinPeakProminence',(Q)); %Finds troughs of S
data when inverted (becuase using peakfinder)
findpeaks((x(:,5)),f*1e-6, 'MinPeakProminence',(Q)); %Finds troughs of S
data when inverted (becuase using peakfinder)
findpeaks((x(:,6)),f*1e-6, 'MinPeakProminence',(Q)); %Finds troughs of S
data when inverted (becuase using peakfinder)
findpeaks((x(:,7)),f*1e-6, 'MinPeakProminence',(Q)); %Finds troughs of S
data when inverted (becuase using peakfinder)
findpeaks((x(:,8)),f*1e-6, 'MinPeakProminence',(Q)); %Finds troughs of S
data when inverted (becuase using peakfinder)
findpeaks((x(:,9)),f*1e-6, 'MinPeakProminence',(Q)); %Finds troughs of S
data when inverted (becuase using peakfinder)
locs=[locsr', locs1', locs2', locs3', locs4', locs5', locs6', locs7',
locs8', locs9'];
peaks=[peaksr, peaks1, peaks2, peaks3, peaks4, peaks5, peaks6, peaks7,
peaks8, peaks9];

Cpk=[[0;Vs'], peaks'];
gg=[0,locsr];
ff=[gg;Cpk];
prompt = 'Input experimental frequency between 0 and 10MHz (in MHz)= '; %
asks user to input desired frequency peak
F = input(prompt);% asks user to input desired frequency peak
[~,I] = min(abs(locs(:,1)-F));
c = locs(I); %finds closest value to input value from peak locations in
model data
rr=ff(:,(I+1));
% I=(c/df)+2; %Indexes the matrix of S values at the resonant frequency in
matlab code closest to input frequency
% Collumn=rr(:,int32(I)) %Indexing the integer value
Sf=[(rr(3)/rr(2)), (rr(4)/rr(2)), (rr(5)/rr(2)),
(rr(6)/rr(2)),(rr(7)/rr(2)),(rr(8)/rr(2)),(rr(9)/rr(2)),(rr(10)/rr(2)),(rr(
11)/rr(2))]
% Sf=Collumn(2:end); %Indexing S values of viscosity for given frequency
ModelFrequency=rr(1,:)
subplot(3,1,2)
plot(Sf,Vs, 'd') %plots S vs Viscosity
grid on
legend (num2str(ModelFrequency))
xlabel('S')
ylabel('\eta')
Curve=fit(Sf',Vs','power1')
subplot(3,1,3)
plot(Curve,Sf,Vs')
legend (num2str(ModelFrequency))
grid on
hold on
prompt = 'Input experimental S value for given frequency ='; % asks user to
input desired frequency peak
Sval = input(prompt);% asks user to input desired frequency peak
ModelViscosity=Curve(Sval)
subplot(3,1,3)
plot(Sval, ModelViscosity,'d', 'MarkerSize',10,
'MarkerEdgeColor','red','MarkerFaceColor',[1 .6 .6])
xlabel('S')
ylabel('\eta')
```

10. Appendix 2: Associated Publications

O. F. Manfredi, R. S. Mills, M. M. Schirru, and R. S. Dwyer-Joyce, “Non-invasive measurement of lubricating oil viscosity using an ultrasonic continuously repeated chirp shear wave,” *Ultrasonics*, July, 2018. Available at: https://doi.org/10.1016/j.ultras.2018.08.002.

11. References

ASTM, 1998. Standard Practice for Calculating Viscosity Index from Kinematic Viscosity at 40 and 100°C. *ASTM International*.

ASTM International, 2007. ASTM 2270-04: Standard Practice for Calculating Viscosity Index from Kinematic Viscosity at 40 and 100 ° C 1 Liquid Petroleum Products and Opaque Liquids (and the Calculation of Dynamic Viscosity). , 91(95), pp.1–6.

Bair, S.S. et al, 2017. New EHL Modeling Data for the Reference Liquids Squalane and Squalane Plus Polyisoprene. *Tribology Transactions*, 0(0), pp.1–9.

Bair, S.S. et al, 2014. Oscillatory and steady shear viscosity: The Cox-Merz rule, superposition, and application to EHL friction. *Tribology International*, 79(October), pp.126–131.

Barlow, A.J. & Lamb, J, 1959. The Visco-Elastic Behaviour of Lubricating Oils under Cyclic Shearing Stress. *Proceedings The Royal Society London A*, 253, pp.52–69.

Barus, C., 1893. Isotherms, isopiestic and isometrics relative to viscosity. *Americal Journal of Science*, 45, pp.87–96.

Buckin, V. & Kudryashov, E, 2001. Ultrasonic shear wave rheology of weak particle gels. *Advances in Colloidal and Interface Science*, 89(90), pp.401–422.

Camara, V.C., Laux, D. & Arnould, O, 2010. Enhanced multiple ultrasonic shear reflection method for the determination of high frequency viscoelastic properties. *Ultrasonics*, 50(7), pp.710–715.

Cannon Instrument Company, 2018. *Certificate of Analysis*, STATE COLLEGE, PA 16803 USA.

Cegla, F.B. Cawley, P. Allin, J. Davies, J, 2010. *High temperature (> 500◦C) wall thickness monitoring using dry coupled ultrasonic waveguide transducers*. Imperial College London.

Courtney, C.R.P. et al, 2012. Manipulation of particles in two dimensions using phase controllable ultrasonic standing waves. *Proceedings of the Royal Society A: Mathematical, Physical and Engineering Sciences*, 468(2138), pp.337–360.

Crouch, R.F. & Cameron, A, 1961. Viscosity-temperature equations for lubricants. *Journal of the Institute of Petroleum*, 47, pp.307–313.

Desilets, C.S., Fraser, J.D. & Kino, G.S, 1978. The Design of Efficient Broad-Band Piezoelectric Transducers. *IEEE Transactions on Sonics and Ultrasonics*, 25(3), pp.115–125.

Doinikov, A.A, 1994. Acoustic Radiation Pressure on a Rigid Sphere in a Viscous Fluid. *Proceedings of the Royal Society A: Mathematical, Physical and Engineering Sciences*, 447(1931), pp.447–466.

Dwyer-Joyce, R.S, 2005. The Application of Ultrasonic NDT Techniques in Tribology. *Proceedings of the Institution of Mechanical Engineers, Part J: Journal of Engineering Tribology*, 219(5), pp.347–366.

Dwyer-Joyce, R.S. & Drinkwater, B.W, 2003. The measurement of lubricant-film thickness using ultrasound. *The Royal Society*, 459(2032), pp.957–976.

Eckart, C, 1948. Vortices and streams caused by sound waves. *Physical Review*, 73(1), pp.68–76.

Erwin, W.S. & Rassweiler, G.M, 1947. Ultrasonic Resonance Applied to Non-Destructive Testing. *American Institute of Physics*, 750, pp.1–5.

European Environmental Agency, 2015. Sulphur dioxide (SO2) emissions. Available at: https://www.eea.europa.eu/data-and-maps/indicators/eea-32-sulphur-dioxide-so2-emissions-1/assessment-3 [Accessed April 20, 2019].

Fuels Europe, 2018. Fuels Europe: Marine Fuels. Available at: https://www.fuelseurope.eu/policy-priorities/products/marine-fuels/ [Accessed April 20, 2019].

Gasparoux, J. et al, 2008. Large frequency bands viscoelastic properties of honey. *Journal of Non-Newtonian Fluid Mechanics*, 153(1), pp.46–52.

Ghosh, M.., Sarangi, M. & Majumdar, B, 2013. *Theory of Lubrication*, Tata McGraw Hill.

Greenwood, M.S, Adamson, J.D. & Bond, L.J, 2006. Measurement of the viscosity-density product using multiple reflections of ultrasonic shear horizontal waves. *Ultrasonics*, 44, pp.1031–1036.

Greenwood, M.S. & Bamberger, J.A, 2002. Measurement of viscosity and shear wave velocity of a liquid or slurry for on-line process control. *Ultrasonics*, 39(9), pp.623–630.

Habchi, W. et al, 2013. A film thickness correction formula for double-newtonian shear-thinning in rolling EHL circular contacts. *Tribology Letters*, 50(1), pp.59–66.

Haines, N.F., Bell, J.C. & McIntyre, P.J, 1978. The application of broadband ultrasonic spectroscopy to the study of layered media. *The Journal of the Acoustical Society of America*, 64(6), pp.1645–1651.

Hertz, T.G. et al, 1991. Viscosity measurement of an enclosed liquid using ultrasound. *Review of Scientific Instruments*, 62(2), pp.457–462.

IndiaMART, 2018. Glass Viscometers. Available at: https://dir.indiamart.com/impcat/glass-viscometer.html?biz=10 [Accessed November 5, 2018].

Kiełczynski, P. et al, 2008. New ultrasonic Bleustein-Gulyaev wave method for measuring the viscosity of liquids at high pressure. *Review of Scientific Instruments*, 26109(79), pp.1–4.

King, L. V, 1934. On the acoustic radiation pressure on spheres. *Proceedings of the Royal Society : Series A*, 147(1930), pp.212–240.

Kossoff, G, 1966. The Effects of Backing and Matching on the Performance of Piezoelectric Ceramic Transducers. *IEEE Transactions on Sonics and Ultrasonics*, 13(1), pp.20–30.

Krautkrämer, J. & Krautkrämer, H, 1968. *Ultrasonic Testing of Materials* 2nd ed., Springer-Verlag.

Kundt, A, 1868. III. Acoustic experiments. *The London, Edinburgh, and Dublin Philosophical Magazine and Journal of Science.*, 35(234), pp.41–48.

Lamb, H, 1917. On waves in an elastic plate. *Proceedings of the Royal Society of London. Series A.*, 93(648), pp.114–128.

Leedom, D, Krimholtz, R. & Matthaei, G, 1971. Equivalent Circuits for Transducers Having Arbitrary Even-or Off-Symmetry Piezoelectric Excitation. *IEEE Transactions on Sonics*

and Ultrasonics, 19(4), pp.427–435.

Manh, T. et al, 2014. Microfabrication of stacks of acoustic matching layers for 15 MHz ultrasonic transducers. *Ultrasonics*, 54(2), pp.614–620. Available at: http://dx.doi.org /10.1016/j.ultras.2013.08.015.

Markova, L. V. et al, 2010. On-line monitoring of the viscosity of lubricating oils. *Journal of Friction and Wear*, 31(6), pp.433–442.

Mason, W.P. et al, 1949. Measurement of Shear Elasticity and Viscosity of Liquids at Ultrasonic Frequencies. *Physical Review*, 75(6), pp.936–946.

Merz, E. & Cox, W, 1958. Correlation of dynamic and steady flow viscosities. *Journal of polymer science.*, 28(118), pp.619–622.

Mills, R.S., Dwyer-Joyce, R.S. & Marshall, M.B, 2017. Continuous Wave Ultrasound for Analysis of a Surface.

Morgan, J.D.N. & Wong, J.S.S, 2017. Quantitative Viscosity Mapping Using Fluorescence Lifetime Measurements. *Tribology Letters*.

NDT Resource Centre, NDT Resource Centre: Acoustic Tables. *NSF-ATE (Advanced Technological Education)*. Available at: https://www.nde-ed.org/GeneralResources/ MaterialProperties/UT/ut_matlprop_piezoelectrics.htm [Accessed April 18, 2018].

ONDA, ONDA Corporation: Tables of Acoustic Properties of Materials. *Putting Confidence in Ultrasound*. Available at: http://www.ondacorp.com/tecref_acoustictable.shtml [Accessed April 10, 2018].

Pau, M., Aymerich, F. & Ginesu, F, 2000. Ultrasonic measurements of nominal contact area and contact pressure in a wheel-rail system. *Proceedings of the Institution of Mechanical Engineers, Part F: Journal of Rail and Rapid Transit*, 214(4), pp.231–243.

Petersson, F. et al, 2005. Continuous separation of lipid particles from erythrocytes by means of laminar flow and acoustic standing wave forces. *Lab on a Chip*, 5(1), pp.20–22.

Rayleigh, L, 1885. On waves propagated along the plane surface of an elastic solid. *Proceedings of the London Mathematical Society*, 1(1), pp.4–11.

Reddyhoff, T. et al, 2005. The Phase Shift of an Ultrasonic Pulse at an Oil Layer and Determination of Film Thickness. *Proceedings of the Institution of Mechanical Engineers, Part J: Journal of Engineering Tribology*, 219(6), pp.387–400.

Roth, W. & Rich, S.R, 1953. A New Method for Continuous Viscosity Measurement. General Theory of the Ultra-Viscoson. *Journal of Applied Physics*, 24(7), p.940.

Schirru, M. et al, 2018. Development of a shear ultrasonic spectroscopy technique for the evaluation of viscoelastic fluid properties: Theory and experimental validation. *Ultrasonics*, (March).

Schirru, M, 2016. *Development of an Ultrasonic Sensing Technique to Measure Lubricant Viscosity in Engine Journal Bearing In-Situ*. The University of Sheffield.

Schirru, M.M. et al, 2015. Viscosity Measurement in a Lubricant Film Using an Ultrasonically Resonating Matching Layer. *Tribology Letters*, 60(3), pp.1–11.

Schirru, M.M. & Dwyer-Joyce, R.S, 2015. A model for the reflection of shear ultrasonic waves

at a thin liquid film and its application to viscometry in a journal bearing. *Proceedings of the Institution of Mechanical Engineers, Part J: Journal of Engineering Tribology*, 230(6), pp.667–679.

Schlumberger, 2014. InSitu Viscosity- Reservoir fluid viscosity sensor. Available at: slb.com/insitu.

Sheen, S.H, Chien, H.T. & Raptis, A.C, 1997. *Ultrasonic Methods for Measuring Liquid Viscosity and Volume Percent of Solids*. Energy Technology Division. U.S Department of Energy.

Shell, 2012. Shell lube analyst sensors. Available at: https://shell-lubeanalyst-sensors.com/.

Sriphutkiat, Y. & Zhou, Y, 2017. Particle manipulation using standing acoustic waves in the microchannel at dual-frequency excitation: Effect of power ratio. *Sensors and Actuators A: Physical*, 263, pp.521–529.

Tiefensee, F. et al, 2010. Nanocomposite cerium oxide polymer matching layers with adjustable acoustic impedance between 4 MRayl and 7 MRayl. *Ultrasonics*, 50(3), pp.363–366.

Turton, A, Bhattacharyya, D. & Wood, D, 2005. Liquid density analysis of sucrose and alcoholic beverages using polyimide guided Love-mode acoustic wave sensors. *Measurement Science and Technology*, 17, pp.257–263.

Waszczuk, K. et al, 2011. Chemical Application of piezoelectric tuning forks in liquid viscosity and density measurements. *Sensors & Actuators: B. Chemical*, 160(1), pp.517–523.

Wen, Y.H. et al, 2004. An experimental appraisal of the Cox-Merz rule and Laun's rule based on bidisperse entangled polystyrene solutions. *Polymer*, 45(25), pp.8551–8559.

Williams, J.A, 1994. *Engineering Tribology*, Oxford University Press.

WinG&D, 2018. Improving Efficiency - Engine Efficiency imporvements. Available at: https://www.wartsila.com/sustainability/innovating-for-sustainable-societies/improving-efficiency [Accessed November 7, 2018].

Woodward, J.G, 1953. A Vibrating-Plate Viscometer. *JOURNAL OF THE ACOUSTICAL SOCIETY OF AMERICA*, 25(1), pp.481–491.

YTC America Inc, 2008. Research and Development, Lead-free Piezoelectric Ceramics. Available at: http://www.ytca.com/lead_free_piezoelectric_ceramics [Accessed March 1, 2018].